A STUDY ON THE INFLUENCE OF MICROSTRUCTURE ON SMALL FATIGUE CRACKS

A Thesis
Presented to
The Academic Faculty

by

Gustavo M. Castelluccio

In Partial Fulfillment
of the Requirements for the Degree
Doctor of Philosophy in the
George W. Woodruff School of Mechanical Engineering

Georgia Institute of Technology
August 2012

A STUDY ON THE INFLUENCE OF MICROSTRUCTURE ON SMALL FATIGUE CRACKS

Approved by:

David L. McDowell, Committee Chair
George W. Woodruff School of
Mechanical Engineering
Georgia Institute of Technology

Richard Neu
George W. Woodruff School of
Mechanical Engineering
Georgia Institute of Technology

Olivier Pierron
George W. Woodruff School of
Mechanical Engineering
Georgia Institute of Technology

Ken Gall
School of Materials Science and
Engineering
Georgia Institute of Technology

Gregory Olson
School of Materials Science and
Engineering
Northwestern University

Date Approved: 1 May 2012

Patience, generosity, forgiveness, and much, much love.

Thanks for encouraging me to dream like a child, openly and limitless.

These pages are dedicated to you, Paula.

¿Qué es la vida? Un frenesí.

¿Qué es la vida? Una ilusión,

una sombra, una ficción,

y el mayor bien es pequeño;

que toda la vida es sueño,

y los sueños, sueños son.

Calderon de la Barca

PREFACE

We learn from an early age that, if we apply enough force to an object, we will eventually break it. However, we do not usually perceive that the repetitive application of much lower forces can also break the object. This fact turns to be important for rotating or alternating machinery, (e.g., motors, turbines) or structures undergoing vibrations (e.g., cars, planes, pipelines, bridges) among a myriad of examples that must endure thousands or millions of cycles.

For every good produced, either an everyday object or a complex machine, manufacturers must verify the integrity of their products to guarantee user safety and product reliability. When these conditions are not satisfied, the outcome may be unnoticed or it may cause tragedies such as the sinking of the Titanic or the crashing of an airplane. Such a broad range of outcomes explains why engineers study the mechanical properties of materials in an attempt to prevent failures. Indeed, millions of dollars are spent every year in research to improve materials and prevent unexpected failures.

In brief, this thesis analyzes how a piece of metal can be damaged by applying repetitive forces, or in other words, how fatigue damage evolves in metals. The results of this work provide computational tools to engineers for improving materials and better understanding of the fatigue phenomena.

GMC

ACKNOWLEDGEMENTS

I would like to express my gratitude to my advisor, Dr. David L. McDowell, whose considerable knowledge and patience were invaluable to the completion this work. His technical and editorial advice was essential for this dissertation. I would also like to extend my thanks to my reading committee, Dr. Ken Gall, Dr. Richard Neu, Dr. Greg Olson, and Dr. Olivier Pierron.

I arrived at Georgia Tech thanks to the great generosity of the Roberto Rocca Program and the guidance and support of my master's advisor, Dr. Hugo A. Ernst. Without this help, I would never have been able to complete my studies at this school. I am also grateful for the support provided by Questek Innovations, who trusted in my abilities to develop computational tools.

Once I started in the program, I found a warm and supportive environment from my fellow graduate students, many of whom have already moved on. I am indebted to Dr. Jason Mayeur and Dr. Rajesh Prasanna, for the countless number of times they helped me, and to Dr. Garritt Tucker, Dr. Nima Salajeheh, and Dr. Ryan Austin for their support. As time passed, I made new friends who patiently learned to tolerate my sour criticism of everything. I will miss the inane, but certainly inspiring and challenging discussions with Jeff T. Lloyd and Bill Musinski, interaction with Jin Song at crazy hours in the lab and guidance from Sam Britt on Linux issues. I also wish to mention the rest of my companions, Brett Ellis, Anirban Patra, Matthew Priddy, Shreevant Tiwari and Dr. Jagan Padbidri, with whom I spent many hours.

In 4+ years, I have received assistance from many people that should be acknowledged. First, I want to thank Glenda Johnson for her invaluable help and for caring about students. I also feel obliged to Cecelia Jones for her help, to Jane Chisholm and to Dr. Jeffrey Donnell for their guidance with my English, and to my former advisors Alejandro Yawny and Juan Perez Ipiña, for their advice. Furthermore, I want to recognize the immense help from

anonymous people by sharing their open source code.

Last and most importantly, I would like to thank my wife, Paula, and family, for their unwavering support and patience along this path. They receive my deepest gratitude for their understanding and encouragement. Finally, I leave Georgia Tech as a different, hopefully better, person. I wish the GT ME community the best of luck, hoping they take a moment to ponder the role and experiences endured by students.

TABLE OF CONTENTS

LIST OF TABLES

LIST OF FIGURES

LIST OF ABBREVIATIONS AND SYMBOLS

2D   Two-dimensional

3D   Three-dimensional

ALA   As-large-as

CEE   Cracked equivalent element

EBSD   Electron backscatter diffraction

EPFM   Elastic-plastic fracture mechanics

FCC   Face-centered cubic

FEM   Finite element method

FIP   Fatigue indicator parameter

FIP$_0$ Fatigue indicator parameter before extending the crack

GB   Grain boundary

HCF   High cycle fatigue

ISV   Internal state variable

LCF   Low cycle fatigue

LEFM   Linear elastic fracture mechanics

MSC   Microstructurally small crack

MSE   Mean square error

PSB   Persistent slip band

PSC   Physically small crack

RVE   Representative volume element

SEM   Scanning Electron Microscope

SFE   Stacking fault energy

SVE   Statistical volume element

TEM   Transmission Electron Microscope

UMAT   User Material Subroutine

UEXTERNALDB   User-defined external database subroutine

VHCF   Very high cycle fatigue

$\boldsymbol{\sigma}$ Cauchy stress

$\boldsymbol{\Delta}\textbf{CTD}$ Cyclic crack tip displacement

$\boldsymbol{\Delta}\textbf{K}$ Range of stress intensity factor

$\boldsymbol{\Delta}\textbf{J}$ Range of J-integral

$\dot{\gamma}^{\alpha}$ Slip rate for slip system α

$\boldsymbol{\phi}$ 2nd-rank damage tensor in the intermediate configuration

$\tilde{a}$ number of cracked grains in sequence

$\boldsymbol{C}$ 4th-rank elastic stiffness in the intermediate configuration

$\bar{\boldsymbol{C}}$ 4th-rank degraded elastic stiffness in the intermediate configuration

$\boldsymbol{D}$ 4th-rank damage tensor in the intermediate configuration

$\tilde{d},\ d_1$ Degree of degradation of the elastic stiffness

$\boldsymbol{E}^{ed}$ Elastic-damaged Green strain tensor in the intermediate configuration

$\boldsymbol{F}$	Deformation gradient
$\boldsymbol{F}^{ed}$	Elastic-damage part of the deformation gradient
$\boldsymbol{F}^{p}$	Plastic part of the deformation gradient
$\boldsymbol{I}$	Identity tensor
k	Fatemi-Socie constant
$\boldsymbol{L}$	Velocity gradient in the current configuration
$\boldsymbol{L}^{ed}$	Elastic-damage velocity gradient in the current configuration
$\boldsymbol{L}^{p}$	Plastic velocity gradient in the current configuration
$\boldsymbol{m}^{\alpha}$	Vector normal to slip plane α in the current configuration
$\boldsymbol{m}_{0}^{\alpha}$	Vector normal to slip plane α in the reference configuration
$\mathbf{N_f}$	Life to failure
$\mathbf{N_{Nuc}}$	Portion of fatigue life to nucleate a crack
$\mathbf{N_{LC}}$	Portion of fatigue life due to long crack growth
$\mathbf{N_{MSC}}$	Portion of fatigue life due to microstructurally small crack growth
$\mathbf{N_{PSC}}$	Portion of fatigue life due to physically small crack growth
$\boldsymbol{s}^{\alpha}$	Slip direction for slip system α in the current configuration
$\boldsymbol{s}_{0}^{\alpha}$	Slip direction for slip system α in the reference configuration
$\boldsymbol{T}$	Second Piola-Kirchhoff stress tensor in the intermediate configuration

SUMMARY

In spite of its significance in industrial applications, the prediction of the influence of microstructure on the early stages of crack formation and growth in engineering alloys remains underdeveloped. The formation and early growth of fatigue cracks in the high cycle fatigue regime lasts for much of the fatigue life, and it is strongly influenced by microstructural features such as grain size, twins and morphological and crystallographic texture. However, most fatigue models do not predict the influence of the microstructure on early stages of crack formation, or they employ parameters that should be calibrated with experimental data from specimens with microstructures of interest. These *post facto* strategies are adequate to characterize materials, but they are not fully appropriate to aid in the design of fatigue-resistant engineering alloys.

This thesis considers finite element computational models that explicitly render the microstructure of selected FCC metallic systems and introduces a fatigue methodology that estimates transgranular and intergranular fatigue growth for microstructurally small cracks. The driving forces for both failure modes are assessed by means of fatigue indicators, which are used along with life correlations to estimate the fatigue life. Furthermore, cracks with meandering paths are modeled by considering crack growth on a grain-by-grain basis with a damage model embedded analytically to account for stress and strain redistribution as the cracks extend.

The methodology is implemented using a crystal plasticity constitutive model calibrated for studying the effect of microstructure on early fatigue life of a powder processed Ni-base RR1000 superalloy at elevated temperature under high cycle fatigue conditions. This alloy is employed for aircraft turbine engine disks, which undergo a thermomechanical production process to produce a controlled bimodal grain size distribution. The prediction of the fatigue life for this complex microstructure presents particular challenges that are discussed and addressed.

The conclusions of this work describe the mechanistic of microstructural small crack. In particular, the fatigue crack growth driving force has been characterized as it evolves within grains and crosses to other grains. Furthermore, the computational models serve as a tool to assess the effects of microstructural features on early stages of fatigue crack formation and growth, such as distributions of grain size and twins.

CHAPTER I

INTRODUCTION

1.1 Importance of fatigue failure

The production of parts and goods requires the qualification of their structural integrity to guarantee the safety of the users and adequate functioning and reliability. When these conditions are not satisfied, the outcome may range from being unimportant and unnoticed to causing deaths. Such a broad range of outcomes justifies the need for understanding the mechanical properties of materials and evaluating of risks of failure. In particular, this thesis focuses on the analysis of fatigue damage on metallic materials.

Although infrequent, catastrophic failures such as railway axes in the 19th century [208], crashes of de Havilland Comet airplanes in the mid-20th century [192], and the recent failure of a turbine [12] in the world's largest passenger aircraft, show the need for understanding the fatigue phenomena the purpose of preventing human and economic losts. Indeed, the economic impact of fatigue failures on industry is in the billions of dollars, a problem that prompts the development of strategies that mitigate the problem.

To moderate fatigue damage, engineers have traditionally attempted to either redesign parts or search for better fatigue-resistant materials. In the last decade, this latter approach has received particular attention with the introduction of computer-based models for designing materials. These models provide an efficient tool for testing strategies that improve the desired property of a material without intense experimental work.

1.2 Outcomes

The core of this work is dominated by a critical review of extensive experimental data, which is later translated into informed decisions for the design of computer simulations. This approach allows the construction of physics-based models that contribute to the scientific community in two main ways: connecting areas of studies and length scales and contributing

to engineering applications.

1.2.1   Connection to areas of study and length scales

As a result of the complexity of the fatigue problem, any attempt to characterize the early fatigue growth of cracks needs to be supported by an understanding of the fundamental physics involved. Certainly, in the past two centuries, many disciplines have approached the problem, leading to contributions that sometimes seem disconnected. One of the reasons for such a disconnection is that fatigue damage can be studied as a macroscopic phenomenon that leads to cracks or as the accumulation of defects on an atomic scale. This wide range falls outside the domain of validity for most fatigue models and requires an approach that uses a multiscale model. Thus, this thesis will analyze multiscale models that estimate the early fatigue growth of cracks as a function of the underlying microstructure.

1.2.2   Contribution to engineering applications

Apart from analyzing the fundamental mechanics of fatigue, this thesis will also develop computational tools that will assist in designing fatigue-resistant alloys. These tools will be designed according to the needs of an industrial partner that will employ the computational tools to assess the initiation of fatigue cracks in turbine disks. Because of this partner, the models will be based on the commercial finite element software ABAQUS, which is a common language for transferring computer-based tools to industry. Furthermore, the computational work will aim to run for up to a day on a USS 2000 computer to comply with industrial preferences.

1.3   Thesis organization

This thesis starts with a broad view of the early fatigue problem crossing multiple materials and loading conditions. Throughout the chapters, the content becomes more detailed with regard to materials, loading conditions, and damage mechanisms, facilitating the testing of the models proposed with data from real materials.

The next chapter overviews theoretical models and experimental data regarding the

nucleation and early growth of fatigue cracks, and the influence of strain localization and microstructures. This general review of the current understanding examines multiple failure mechanisms for multiple metals under a wide range of loading conditions. One conclusion of the review is that many strategies that predict the failure of materials do not consider adequately the local driving forces for crack growth at the crack tip. Hence, Chapter 3 will focus on reviewing a variety of measures of the fatigue driving force that are compared in FEM simulations of Cu single crystals, which is among the most studied material under cyclic loading. These results provide confidence about the quality of the driving forces at the crack tip that will be employed in simulations of small cracks.

Chapter 4 starts by discussing possible correlations between the fatigue life of small cracks and fatigue indicator parameters. Due to the local character of the driving forces, the simulations would require intense computational work that updates the local fields after some extent of crack growth. To avoid such demanding work, a novel mesoscale model will provide the fundamental shortcuts that allow crack growth to be simulated along multiple grains and hundreds of microns. The basis and limits of the mesoscale model assumptions are discussed extensively. This analysis concludes that the stress and strain redistribution due to crack growth cannot be ignored and needs to be accounted explicitly. Hence, the chapter further introduces a fully anisotropic damage model that can simulate crack growth.

This study then continues applying the mesoscale model on a specific material: the RR1000 alloy, which is a nickel-based superalloy employed in turbines for planes. This alloy is currently of interest for the turbine industry and needs to resist thousands of loading cycles that result from landing and taking off. Hence, Chapter 5 introduce the main characteristics of superalloys and their relation to fatigue failure. Furthermore, a crystal plasticity model for RR1000 is discussed in relation to experimental stress-strain data, which is employed in the calibration of the model. Additionally, the fatigue driving force for RR1000 is characterized and the results are compared to those in Chapter 3 for Cu.

Following this, the mesoscale model is adjusted for the analysis of RR1000 alloys. Such a task implies fitting the constants and the construction of a sub-grain model that predicts the evolution of the driving force while the crack grows within a grain, which is not

explicitly considered by the mesoscale model. The results show that the sub-grain behavior is predictable and follows a law that cannot be deduced from previous approaches in the field. Indeed, these results are a fundamental explanation of why theories such as singularity-based fracture mechanics fail in describing the small crack problem.

Chapter 7 focuses on applying the mesoscale model to predict the early fatigue life of RR1000 microstructures with ALA grains, which correspond to materials that have big grains surrounded by smaller grains. This bimodal distribution of grain size affects the fatigue life in ways that can be studied with the tools developed in the previous chapters. Finally, this thesis concludes with a summary of the most relevant conclusions from this work and future additional work. In addition, the appendix section provides further information about the computational implementation and some details of the numerical scripts developed.

CHAPTER II

OVERVIEW: MICROSTRUCTURALLY SMALL CRACKS

For more than a 150 years, engineers and scientists have been concerned about fatigue damage of metals, which they still consider a matter of high priority as shown by the number of conferences related to fatigue damage. Indeed, the complexity of the nucleation and growth of a fatigue crack has called the attention of researchers from multiple disciplines ranging from applied engineering to theoretical physics, involving studies about cyclic loading, crack formation, plastic deformation, and slip localization among the most important aspects. Hence, the challenge is to combine the understanding from these sources.

2.1 Approaching the problem

Among the multiple approaches developed to study small fatigue cracks, three perspectives stand out for their importance with regard to understanding the problem of microstructurally small cracks (MSCs):

- Fatigue life estimation,

- Fracture mechanics, and

- Plastic deformation.

2.1.1 Fatigue life estimation

More than 100 years ago, Wöhler (see the excellent historical review by Walter [208]) pioneered the study of the fatigue failure on railway components by correlating the number of cycles to failure with the applied stress amplitude, today are know as S-N curves. These curves were later plotted in logarithmic scale, which inspired Basquin [15] to fit a power law with two material constants (i.e., a line in logarithmic scale) to correlate the total life to the applied stress range. Since metals do not show a macroscopic plastic deformation

in the high cycle fatigue (HCF) regime, the stress applied is a natural magnitude to assess the fatigue damage. However, when plastic deformation is macroscopically apparent (e.g., low cycle fatigue (LCF) and notches), the strains that develop are a better magnitude to describe fatigue damage.

Coffin and Manson independently proposed a power-law correlation between plastic strain and life that was later combined with the Basquin model into a single *strain-life relation*:

$$\frac{1}{2}\Delta\epsilon = \frac{\sigma'_f}{E}(2N)^b + \epsilon'_f(2N)^c, \tag{1}$$

in which σ'_f, b, ϵ'_f and c are material constants that depend on the chemistry of the material, but they can also depend on the microstructure processes, loading conditions and environment among many. Most fatigue life models cannot predict theoretically the value of the material constants, but they require experimental tests to calibrate the parameters. Hence, this *post facto* methodology can be adequate to characterize materials, but they are not fully appropriate to assist in the design of microstructures for newer fatigue-resistant engineering alloys.

Power law correlations such as that in Equation 1 were introduced between 50 to 100 years ago, and they are still of relevance to engineering applications. Certainly, Equation 1 has inspired a myriad of power law correlations to estimate the fatigue life under multiple testing conditions. However, the total life approach disguises the nature of fatigue damage by assuming one temporal scale (the total life) and one length scale (the entire specimen cross-section) associated with the failure process; in other words, it does not distinguish the stages of fatigue life. Indeed, the damage tolerant approach born from fracture mechanics in the 60's recognize the need to understand the evolution of fatigue damage represented by the crack growth rate.

2.1.2 Fracture mechanics

The classical fracture mechanics approaches quantify the local driving force for fatigue crack growth in terms of far field magnitudes (e.g., ΔK, ΔJ-integral, $\Delta CTOD$). Even though traditional homogeneous material fracture mechanics provides useful tools for the

assessment and characterization of long cracks (e.g., the Paris Law [192]), it fails when dealing with MSCs. Certainly, experiments have revealed an "anomalous" growth of cracks until they become longer than some characteristic length related to the microstructure [73, 66, 194, 199]. The works of Tanaka and Akiniwa [194] or Tokaji and Ogawa [199] provide clear experimental evidence of the correlation between the microstructure and the crack speed. For example, Figure 1 [199] presents the crack growth rate measured from a MSC in steel on the surface of the specimen and the corresponding microstructure crossed by the crack.

As shown in Figure 1, the growth rate of MSCs decreases substantially as the crack tip approaches a grain boundary (GB), where it may even arrest. After crossing the GB, the crack may accelerate rapidly and then decelerate until reaching the next GB. This cycle repeats until the crack becomes "long," which can be defined as the required length for applicability of linear elastic fracture mechanics (LEFM), which includes homogeneity, similitude and small scale yield requirements. The current challenge is to model this oscillatory behavior and the transition into a long crack as a function of the underlying 3-dimensional microstructural attributes.

MSCs grow with different kinetics that usually depend on the length of the crack relative to the microstructure lengths scale [130], rendering local-global singularity-based fracture mechanics valid only for longer cracks. Among the many reasons for this behavior is that the mesoscale material inhomogeneity and the directional character of slip invalidate the similitude assumption, leading to a disconnect between the apparent driving force far from the crack tip and that at the crack tip. In other words, the highly localized and anisotropic plastic zones of small cracks do not resemble those predicted by crack singularity models based on homogeneous plasticity [178, 117]. Second, the small scale yielding requirements of LEFM are often violated by MSCs. Third, the cycle plastic zone and damage process zone must engage a suitably large number of grains to achieve statistical homogeneity of the crack growth response along the entire crack front. Additionally, virtually all of the common driving forces (e.g., ΔK, ΔJ, $\Delta CTOD$) are not of thermodynamic character when used in fatigue applications.
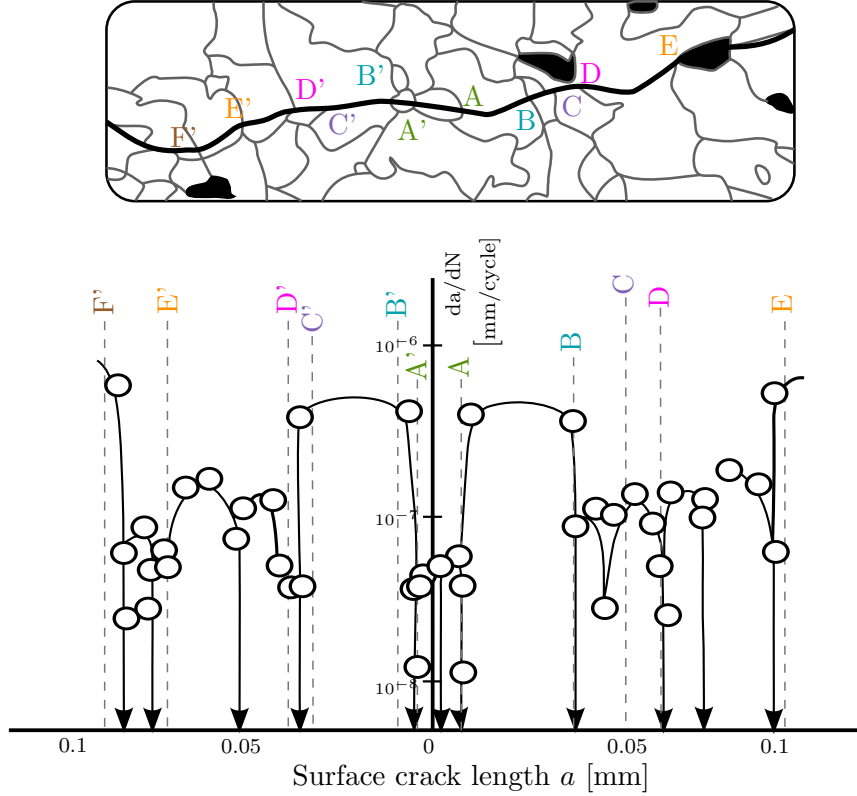
Figure 1: An example of experimental fatigue crack growth rate for a MSC in low carbon steel. Note the correlation with the microstructure shown above. (Adapted from [199]).

These reasons point to the lack of accuracy of traditional fracture mechanics theory and suggest the need for a microstructure-sensitive approach [131]. Since the MSC regime is dominant in HCF, comprising a significant portion of the fatigue life [81], improvements in current life prediction schemes require an understanding of the early stages of damage, progressing from the first grain up to hundreds of grains. Novel microstructure-sensitive schemes should represent the most significant features of the underlying physics over different length scales [119, 121].

2.1.3 Plastic deformation

Ewing and Humfrey [52] were among the first to ascertain that in HCF of iron, plastic deformation accumulates on certain favorably oriented grains (constrained microplasticity) in the form of slip bands that cross entire grains. Indeed, Figure 2, published in 1903 [52], shows iron grains crossed by slip bands that orient along the least slip-resistant directions.
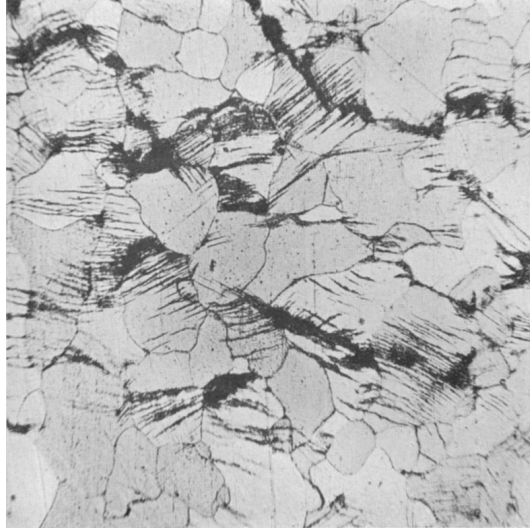
Figure 2: Slip bands found in iron in 1903 by Ewing and Humfrey [52]. A century has passed and scientists are still trying to understand and model the role of these bands.

The bands comprise organized dislocation structures that appear during the early stages of fatigue life as a result of thermodynamically irreversible interactions among crystalline defects [92], causing extrusion and intrusions at free surfaces [17, 140, 164]. These intrusions are usually accepted as necessary precursors of cracks at free surfaces [109]; in addition, the environment plays a major role that is almost independent from the plastic deformation [79]. Moreover, these basic observations of the fatigue process are especially prevalent in the LCF regime.

The correlation between fatigue crack directions and slip bands was further noticed by Forsyth [60], who classified fatigue damage in two stages depending on the path followed by the crack:

- Stage I corresponds to the initial phase in which plastic deformation occurs predominantly by single slip along a favorably oriented slip plane that usually becomes the site where cracks nucleate; the loading of the cracks is predominantly mode II. Thus, Stage I cracks propagate following well defined crystallographic planes.

- Stage II is characterized by slip along multiple crystallographic planes that allows for cracks to grow through many slip planes, which results in a net noncrystallographic opening mode and the formation of fatigue striations. Because cracks grow from

9
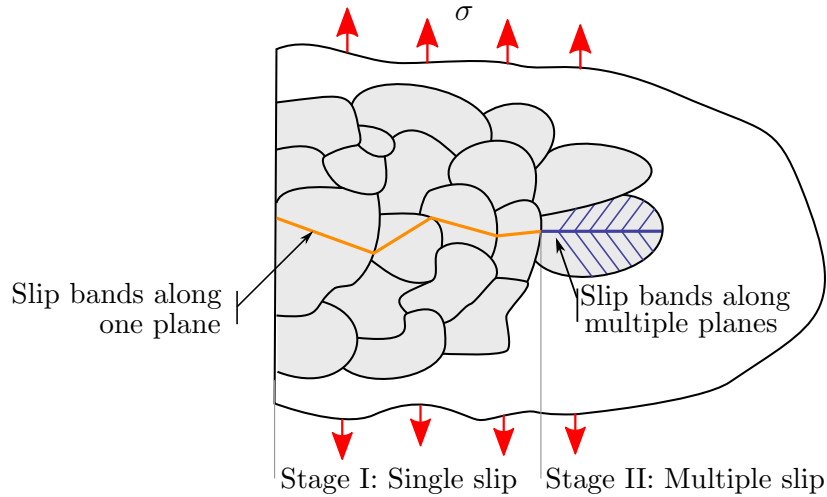
Figure 3: Schematic representation of transition from fatigue Stages I to II. This simple description exemplifies the intrinsic correlation between subgrain plastic deformation structures and crack growth directions.

the contribution of multiple slip planes, the macroscopic plane of the crack can turn towards maximum mode I loading.

The work of Forsyth is among the first to relate the orientation of cracks to the plastic deformation substructure, showing that the direction of cracks is initially defined by the orientation of slip bands, as depicted in Figure 3. Later investigations showed that the bands reappear at the same location after repolishing the metal, so they were named persistent slip bands (PSBs).

2.1.3.1 Stress and strain evolution

Multiple researchers have characterized the evolution of the cyclic stress-strain curve, whose area is a measure of the irreversibility of the process. Mughrabi [140] was among the first to show that Cu single crystals present a plateau in the saturation stress with increasing applied cyclic strain. The plateau corresponds to the localization of plastic strain in persistent slip bands and extends up to the formation of cell structures. Such a behavior is not particular of Cu; it is generally found in most low-to-medium stacking fault energy (SFE) FCC metals loaded for single slip [97, 104].

Secondly, single crystal experiments of low-to medium SFE metals and alloys have shown
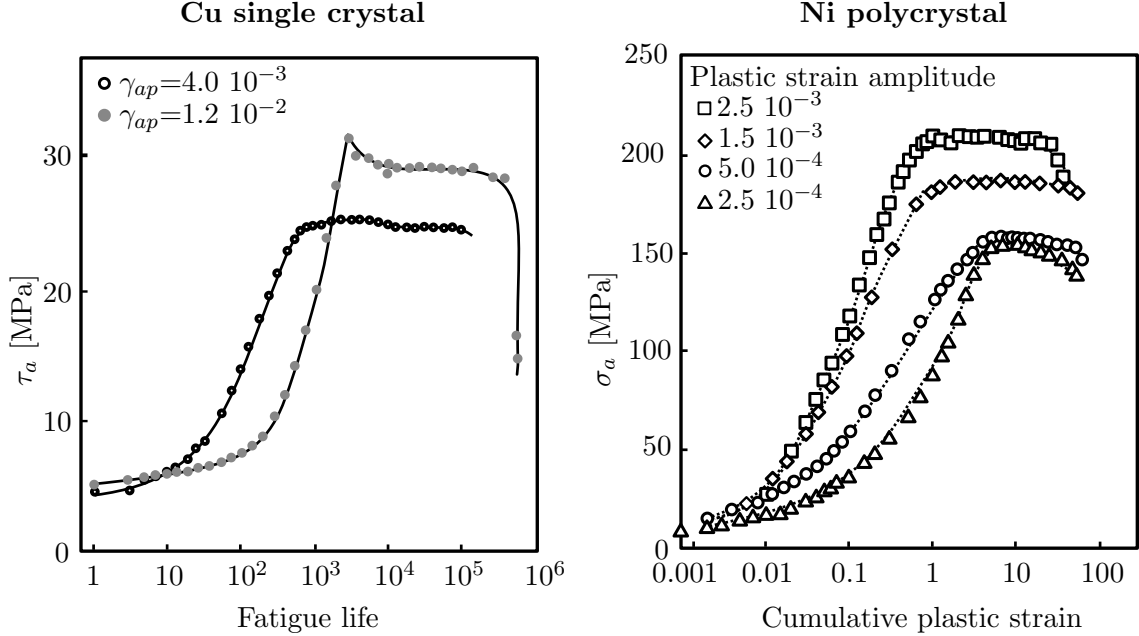
Figure 4: Examples of the development of stress plateaus after plastic strain has localized for multiple loading amplitudes in the HCF regime. (left) Cu single crystal (adapted from [167]). (right) Ni polycrystal (adapted from [137]).

that plastic strain localization can limit the material hardening when cycled in the HCF regime. Indeed, after localization occurs, stress-cycle or stress-accumulated strain diagrams present plateaus [167, 219, 202, 212], as exemplified by Figure 4 (left). Since localized plastic strain can accommodate a limited amount of strain, further cycling can develop new areas of localized plastic strain [211]. These mechanisms of plastic deformation in FCC single crystals are also usually found on individual grains in polycrytalline materials [168, 137, 104]. As a result, FCC polycrystalline metals can present plateaus after the most favorably oriented grains have localized plastic stain, as shown in Figure 4 (right).

Although plastic strain may localize with a variety of dislocation substructures for different materials, Figure 4 is representative of FCC metals and alloys with low-to-medium SFE cycled under the HCF regime. Such an evolution of the shear stress suggests that crack nucleation and early growth can occur under almost constant stress. Indeed, analyses of the dislocation substructures (e.g., slip bands) close to the crack tip have shown that crack embryos may not alter dislocations substructures [88, 3], and therefore, the strains around the crack are accommodated by slip bands without further hardening.

11

2.2 Physics and models for early fatigue damage

2.2.1 Driving forces and irreversibility

Multiple studies have shown that, at an atomic scale, the irreversible migration of point and line defects is responsible for crack growth; for example, the nucleation of fatigue cracks (i.e., extrusions and intrusions, particle decohesion) has been attributed to the intense production of vacancies in slip bands [7, 165, 201]. In contrast, fatigue crack growth is usually dominated by dislocations that are emitted from a stress concentrator (a crack embryo) and that are not annihilated after a stress cycle [76, 153, 151, 54]. Indeed, the remaining dislocations trapped by wells of potential (e.g., foreign atoms, point defects, forest dislocations, second-phases) cause a permanent change in crack tip displacement range (ΔCTD), which has been employed as a the crack driving force by Tanaka et al. [195] and references therein. In other words, crack growth corresponds to the accumulation of net Burgers vectors at the crack tip [177, 163].

The introduction of a line defect can be reversed by its annihilation with another defect or at a surface; for example, in the mesoscale, cracks developing in a vacuum can reweld and disappear [148, 211]. To characterize this feature, fatigue models should distinguish between the driving force and the degree of mechanical irreversibility. The former measures the production of defects (i.e., degree of plastic deformation) and depends mainly on the constitutive behavior and loading conditions. The latter quantifies the irreversibility of the crack tip dislocation migration (net crack growth), and it is strongly affected by interaction with the environment. Although the driving force and irreversibility are conceptually different and usually almost independent, they can influence each other in multiple ways. For example, strain localization can enhance diffusion of foreign atoms from the environment (creating fast-paths) and embrittle atomic layers close to the crack surface, while irreversibility affects the number of cycles to failure, and equivalently, the accumulated plastic strains until failure [214].

2.2.2 Crack nucleation models driven by dislocations

This section will address a variety of models that consider the irreversibility of line defects and point defects within a crack tip damage zone [113].

2.2.2.1 Crack nucleation at free surfaces

In a foundational approach, May [116] developed a model for crack nucleation based only on irreversible random slip planes that form valleys deep enough to be considered as cracks. Later, Rosenbloom and Laird [179] were able to model the surface roughening observed experimentally after a certain number of cycles, but they could not account for the fact that cracks tend to nucleate at the interface between the slip band and the matrix and that a net amount of material is extruded from the slip band.

In a different approach, Lin and Ito [107] attempted to model slip bands by using only two very close slip planes, one activated during forward loading and the other during reverse loading (Figure 5). A drawback of the model is the *ad hoc* assumption that plastic strain localization in slip planes produces a stress field in which resolved shear stresses vary linearly from positive in a given slip plane to negative in the adjacent one. This assumption has not been supported by experimental evidence or independent simulations.

Tanaka and collaborators [193, 196] further explored the idea of very close parallel layers that accumulate deformation by modeling irreversible dislocation pileups of different signs against a GB, as shown in Figure 6. They used continuously distributed continuum dislocations and LEFM to deduce a dependence on the grain size of the threshold the stress intensity factor range (ΔK_{th}) and the fatigue life. Their results constitute a theoretical basis for the power-law fatigue life models.

Following this approach, Navarro and de los Rios [147] employed a 2D elastic-plastic model based on dislocation pileups and cyclic crack tip displacement range to assess the effect of slip band blockage on successive grains. Their results showed that the constraint on slip caused by the grains contributed to oscillatory crack growth rates close to those observed for small cracks as depicted in Figure 7. This work emphasized that both strain localization and GB blockage affect the driving force for fatigue crack growth.
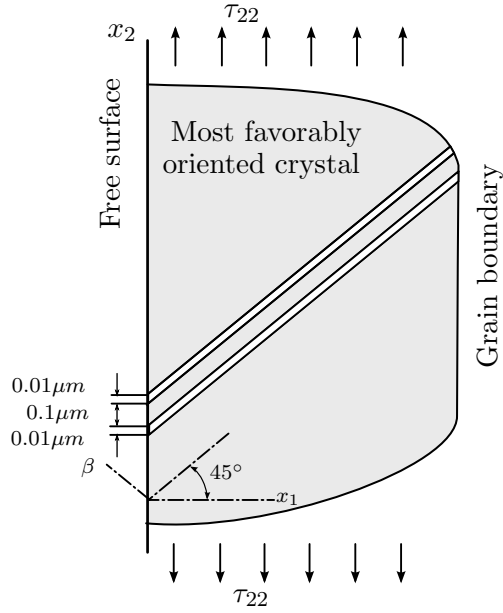
Figure 5: Schematic representation of the model proposed by Lin and Ito. The 45° bands contain dislocations that are activate at opposite loading directions. (Adapted from [107, 113].)
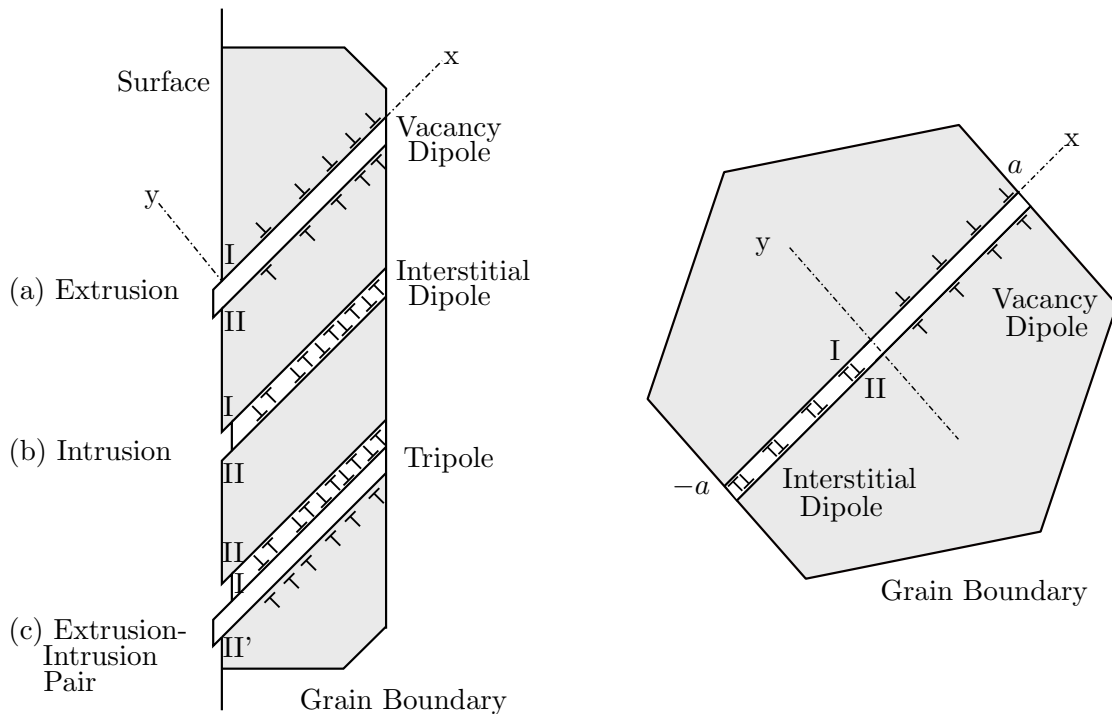
Figure 6: Schematic representation of Tanaka an Mura model for a surface grain (left) or an embedded grain (right). Dislocation pileups along bands modulate the driving force to nucleate cracks. Adapted from [196].

Using another approach, Mura and colleagues [203, 142] proposed fatigue crack initiation formulations based on energy considerations using the elastic theory of dislocations and dipoles. This work assumes that dislocation dipoles accumulate as a result of irreversible dislocation motion along different favorably oriented slip planes, which become active in tension or in compression. As a result, the elastic energy increases until it is relieved by the crack initiation along PSBs. Thereafter, Sangid, Sehitoglu and colleagues [182, 181, 180] also analyzed fatigue crack initiation at slip bands and GBs using energy-based models enriched with atomistic simulations that account for the role of GBs. Their work developed a methodology to compute the energy balance for a PSB and employed a failure criterion based on the minimization of the PSB energy with respect to plastic deformation.

The studies based on energy considerations were successful in explaining the evolution of the fatigue driving force to nucleate cracks as a function of the dislocation accumulation process; however, they rely either on pile-up mechanisms, PSBs with ladder structures or other predefined dislocation structure without considering arbitrary complex dislocation organization within slip bands and multislip effects. Moreover, they ignore crack growth aspects and the role of the environment in the nucleation of cracks.

More recently, improvements in computational capacity have allowed researchers to model plastic deformation by explicitly inserting, tracking, and removing dislocations represented by line singularity fields in a linear elastic solid. The so-called discrete dislocation dynamics method was successful in describing strain localization [48] and also surface relief [47]. Similarly, atomistic simulations proved useful in revealing the irreversible interactions among defects and foreign environmental atoms at the crack tip that are responsible for crack growth.

Although dislocation dynamics and atomistic approaches are promising, they are computationally too demanding for engineering applications; more importantly, they are usually based on limited, simplified assumptions regarding the representation of dislocations. These simplifications render such models more qualitative (e.g., two-dimensional, no mixed character, no cross-slip nor climb, extremely rapid loading, and approximate potentials), so other continuum models still retain substantial importance.
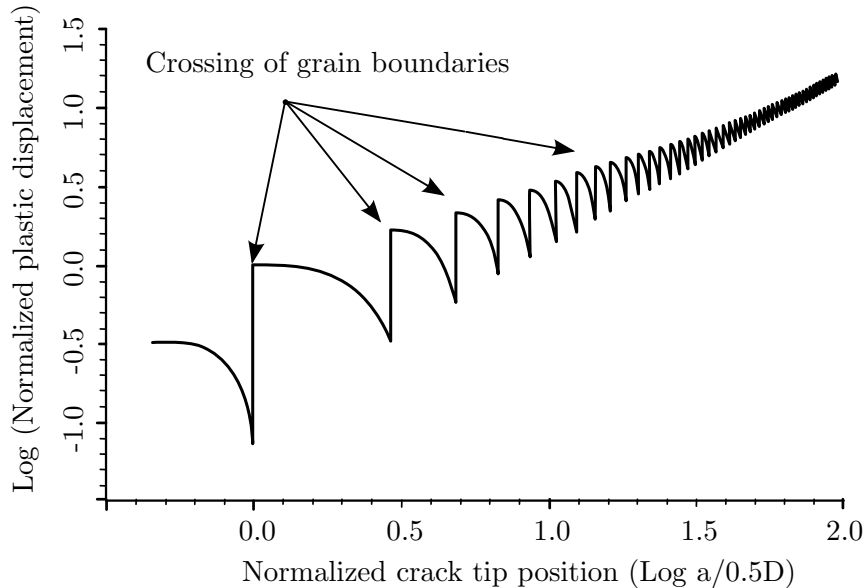
Figure 7: Variation of the crack driving force in crossing many grains. When the crack crosses a new GB, the driving force jumps instantaneously and continues decreasing up to the next GB. Adapted from [147].

2.2.2.2 Crack nucleation at interfaces

Several experimental studies on bicrystals and polycrystals have shown that GBs are sometimes favorable sites for cracks to nucleate [209, 78, 138]. Zhang and Wang [225] reviewed the accumulation of plastic deformation in Cu bicrystals and concluded that intergranular failure is promoted for medium and large misorientation angles. Furthermore, they showed that the impingement of slip bands on GBs produces strain concentrations that initiate cracks at multiple locations along a GB; this is also observed in a variety of FCC metals [202], as exemplified by Figure 8. These studies are in agreement with the experiments developed by Mughrabi et al. [141], who concluded that cracks could form along GBs in Cu polycrystals via the Zener-Stroh mechanism. In this mechanism, when dislocations blocked by obstacles pile up (e.g., at GB), they can develop stresses high enough to render a crack more energetically favorable [190, 191]. Following the work from Zener, Stroh initially proposed that around 1000 dislocations on a slip plane were require for coalescence to occur [190], but recognizing that so many dislocations could not be found in experiments, he later argued that a few hundred would be enough if multiple slip planes were allowed

16
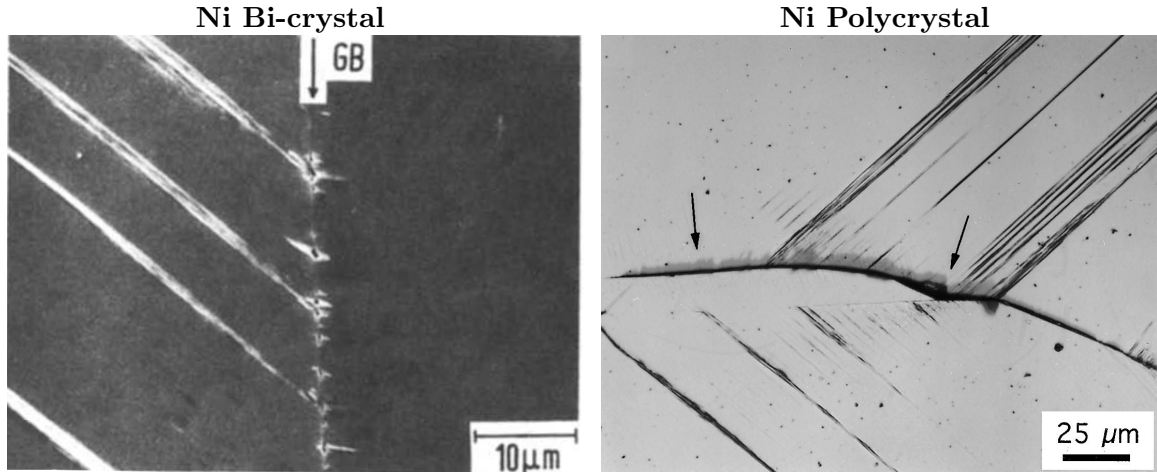
Figure 8: Intergranular cracking caused by the impingement of slip bands on GBs in Ni. Note the distributed character of the damage, which originates cracks at several locations along a GB. (Left) Adapted from [202]. (Right) Adapted from [138]

[191]. More recently, Cherepanov concluded that cracks at interfaces of different anisotropic elastic materials could be formed with just a few dislocations [40].

Fan [53] reviewed the behavior of cracks at the interfaces of anisotropic elastic materials and concluded that the Zener-Stroh mechanism relates to the behavior of smaller cracks while the traditional Griffith theory [6] is valid for larger cracks. Furthermore, Fan also argued that the energy release rate for Zener-Stroh cracks loaded with external stress has contributions from a plasticity factor (super-dislocation Burgers vector) and a stress factor (normal stress to the interface). Although these conclusions are valid for "brittle-type" boundaries that cannot emit dislocations from crack embryos, their validity for ductile metals depends on the misorientation between grains that regulate the fast diffusion of foreign atoms (typically from the environment), enhancing the brittle character of the boundaries.

2.2.3 Crack nucleation models assisted by vacancies

Low amplitude strain cycling of metals leads to plastic strain localization, which is characterized by an intense dislocation activity within constrained regions. Antonopoulos and co-workers [8] showed that the production and the annihilation of dislocations results in an extensive generation of point defects, among which vacancies dominate in terms of number density. Furthermore, they argued that vacancies accumulate within the dislocation

structure in the slip band (i.e., dipole walls) and produce long-range tensile effects on slip bands. This hypothesis was later used by Brown and Ogin [27] who, instead of modeling dislocation pileups as per Tanaka and Mura [196], accommodated the boundary mismatch strain by assuming a uniform array of dipoles. The model results in a singular stress at the intersection of the slip band with the surface, which drives the crack growth.

The EGM model (Essmann-Gossele-Mughrabi) [51] also assumed that dislocation annihilation generates high concentrations of vacancies that migrate, depending on the temperature; however they proposed that vacancies accumulate along the slip band-matrix interface. The boundary mismatch strain is again accommodated by an array of dipoles under compression, which is not in agreement with the results from Brown and Ogin [27]. Polak further developed the EGM model [164, 169] by extending the production and migration of vacancies to the entire volume of the slip band. Later, Hsiung and Stoloff [77] indeed observed evidence of vacancy diffusion towards the slip band interface and proposed a function that would estimate the number of cycles to nucleate a crack between the slip band and the matrix; their estimate depends on the vacancy concentration, which drives crack nucleation.

Although point-defect-based models have traditionally been formulated only for describing early crack nucleation at intrusions, these models recognize that the fatigue driving force may depend on the production and the migration of point defects along localized bands. In fact, atomistic simulations have shown that crack growth due to vacancy condensation is a feasible mechanism at that scale [151, 54]. Moreover, the nucleation of cracks under creep conditions at GBs has long been recognized to occur at high temperature due to coalescence of vacancies depending on the temperature and the strain energy release rate [61]. Such a mechanism might also be expected to occur for vacancies produced under fatigue conditions as a result of the interaction among dislocations at slip bands impinging on GBs.

2.2.4   Crystal plasticity and FEM approach

Since crack nucleation and crystal orientation are connected in transgranular failure of metals with planar slip, any constitutive law employed for simulating crack initiation and
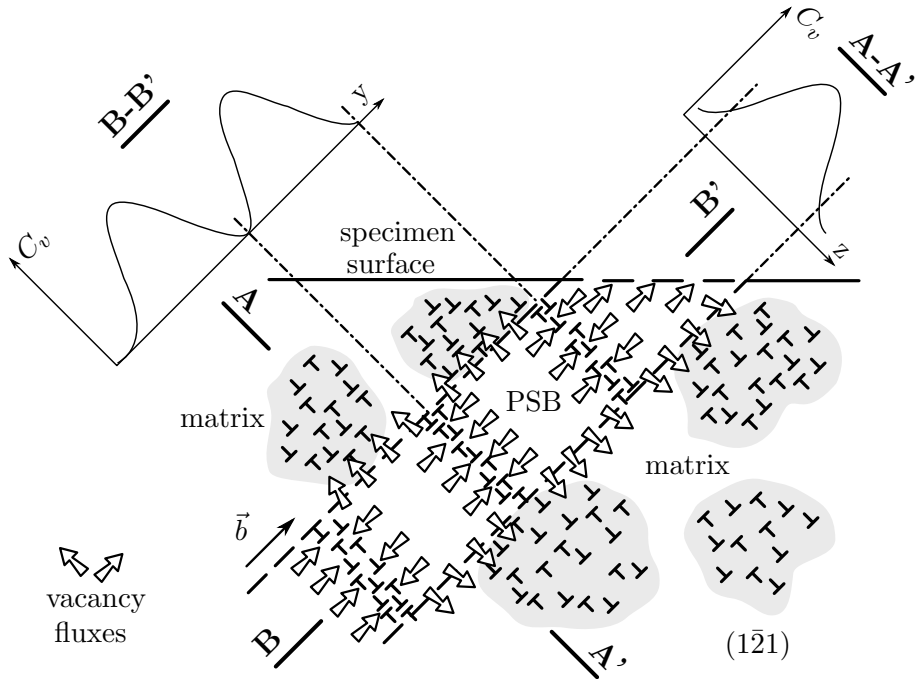
Figure 9: Fluxes of vacancies in a ladder-type slip band in Cu proposed by Polak. Note the complexity of modeling the interaction of dislocation substructures and vacancies. Adapted from [113].

early growth needs to account for crystallographic slip geometry. In this sense, crystal plasticity constitutive formulations [9, 10] are among the simplest and least computationally demanding models that can describe crystal orientation by allowing plastic deformation to occur only along a finite number of slip planes. Certainly, these models have been extensively used in crack initiation analyses. In an early study, Gall et al. [64] investigated variability in crack nucleation by modeling a notch with a crystal plasticity scheme. Their model varied the orientation of only two slip planes and characterized the deviation of the nucleation driving force. Later, Bennett and McDowell [19, 20] employed models with explicit cracks to study the effect of different crystallographic orientations of the neighboring grains on the CTD, an approach also employed by Ferrie and Sauzay [57].

Some recent works avoided representing cracks with refined meshes and employed indicators of fatigue damage. Dunne et al. [49] reproduced the grain morphology in a crystal plasticity model of a Ni-base superalloy and tried to predict the site of formation of a crack. Although they successfully described the slip pattern found in experiments, cracks did not

form in the highest plastic strain regions, suggesting the need for Fatigue Indicator Parameters (FIPs) that do not depend just on plastic strain [121]. Kirane and Ghosh [90, 91] also examined crack nucleation in simulations that accounted for realistic distributions of grain size, shape and crystallographic orientation of Ti alloys undergoing dwell fatigue. They proposed a fatigue crack nucleation criterion that depends on the local stresses and the length of the neighboring pile-ups in order to measure the non-local accumulated plastic strain on neighboring grains.

The importance of these investigations is that they showed the influence on fatigue crack initiation of the stress and strain concentration that occurs within grains and at GBs, as previously mentioned as one of the features in Tanaka's model. Nevertheless, Tanaka's models localize the inelastic strain on infinitesimally close planes, while traditional crystal plasticity models employ a diffuse inelastic strain treatment. For the sake of completeness, Repetto and Ortiz [174] investigated the effect of vacancy generation and diffusion by proposing a decomposition of the deformation gradient that included vacancy generation, and their results resemble those found in crack nucleation experiments. However, the role of vacancies is not usually explicitly addressed within FEM models due to poor current understanding of their behavior, and to the increase in computational complexity.

2.2.5 Driving force and FIPs

During crack nucleation and the early growth processes, the local driving force is affected by the microstructure, which has particular implications for MSCs. Hence, the driving force for early fatigue damage needs to be characterized using FIPs that describe the local fields (i.e., not the far field described by the stress intensity factor in LEFM). In the past fifty years, a myriad of formulations have been proposed to correlate early fatigue crack growth based on stress, strain or energy concepts [188]. The sheer number of formulations shows that a single continuum model cannot capture the nature of all metals fatigue under multiaxial conditions. Thus, the choice of a FIP is necessarily linked to the kind of deformation mechanism involved in the material and the loading conditions to analyze.

Fatemi and Socie [56] proposed a FIP based on the critical plane approach of the general

form

$$\text{FIP}_{\text{FS}} = \Delta\gamma^p_{max}\left[1 + k\frac{\sigma^{max}_n}{\sigma_y}\right], \tag{2}$$

in which $\Delta\gamma^p_{max}$ is the maximum cyclic plastic shear strain, σ^{max}_n is the maximum normal stress on the maximum plastic shear range plane normalized by the yield strength σ_y, and k is a constant, usually between 0.5 and 1. FIP_{FS} correlates well with the early fatigue behavior of metals that exhibit planar slip and provides a useful quantitative characterization of the early crystallographic crack growth phenomena [188, 55].

The value of such a parameter was explored by Reddy and Fatemi [173] and McDowell and Berard [120], who postulated that FIP_{FS} represents the fatigue driving force and plays a role similar to that of the ΔK or the ΔJ-integral in predicting fatigue crack nucleation. In particular, McDowell and Berard [120] and McDowell [118] showed that the Fatemi-Socie parameter in Eq. (2) behaved over a broad range of multiaxial loading conditions in a manner very similar to the ΔJ-integral of elastic-plastic fracture mechanics, which is of course closely related to the fatigue crack growth driving force. Afterwards, several investigators have successfully employed approaches akin to the Fatemi-Socie parameter along with crystal plasticity formulations for studying the effects of microstructure on fatigue life [220, 185, 223, 171].

2.3 Preliminary conclusions

This review of the current understanding of the development of small fatigue crack supports these propositions:

- Traditional homogeneous-based fracture mechanics cannot describe the early behavior of fatigue cracks because the models are based on far-homogeneized fields magnitudes and not local measurements. Instead, an adequate description of the fatigue driving force requires the characterization of the local fields, which could be carried out by FIPs that depend on the damage mechanism.

- Mechanically irreversible processes are the original cause of fatigue damage, either as point or line defects, although the nature of the damage may change along the fatigue

life. Even though fatigue models may not consider atomic scale processes explicitly, they should represent the homogenized effect of those processes.

- When the amount of loading is below yield strength, the microstructure can greatly affect plastic deformation orientation and continuity among grains. This variability is then transferred to the fatigue lives of components.

Hence, the prediction and comparison of the fraction of fatigue life associated with the growth of MSCs is still an open challenge [119]. **This impacts mechanical design by necessitating an increase in the safety factor due to uncertainty, which points to the utility of the present research**. The proposed investigation employs the finite element method and crystal plasticity formulations to study the fatigue life of MSCs in 3D polycrystals. It does this by explicitly rendering the grain structure of FCC metals with low-to- medium SFE that manifest planar slip. The preferred approach avoids explicit modeling of cycle-by-cycle crack extension with explicit nodal release; Instead, it employs FIPs to estimate the driving force for small crack growth.

CHAPTER III

SINGLE CRYSTAL ANALYSIS

3.1 Overview

The fact that the transgranular growth of MSC is affected by the character of the GBs suggests that models homogenized above a grain scale would not capture the intrinsic variability of small crack growth. This focuses attention on the simulation of explicit microstructures. Moreover, fatigue crack formation has long been associated with the localization of plastic strain, which suggests that subgrain slip localization plays a role in defining the driving force for MSC crack growth. Limited experimental evidence has shown "anomalous" growth rates in single crystals ([111, 23, 224]) even in the absence of a clear intrinsic microstructural length scale associated with the minimum crack growth rate. Due to the anisotropy and heterogeneity of single slip, the influence of strain localization is expected to be more significant in Stage I crystallographic crack growth, which comprises a significant portion of the life under high cycle loading conditions (low strain amplitudes).

Although the localization of cyclic plastic strain (i.e., not induced by geometric stress concentration) has long been recognized in experimental work as a precursor to fatigue damage, its influence on the crack tip driving force has not been studied extensively by theoretical or computational models. Indeed, most studies have avoided the additional complexity of introducing a crack and have attempted to describe either the formation or the deformation of regions with localized plastic strains (i.e., slip bands). Winter [213] was among the first to model a slip band as a different material embedded in a matrix. His work assumed that the composite material deforms following the rule of mixtures. This approach was employed by many to characterize the cyclic evolution of pure metals, and more recently the same basic idea was employed in modeling slip bands as a different material in a crystal plasticity framework [228, 183].

One of the most detailed studies to date that considers effects of slip bands on the

crack driving force is the work by Hutchinson and Tvergaard [82]. Their investigation considered the effect of slip bands on cracks using a 2D fracture mechanics approach under small scale plasticity, and it showed that the driving force can be improperly estimated using homogeneous plasticity. These results are relevant for interpreting single crystal experiments in which plastic strain localizes. Hence, this chapter studies the driving force for fatigue crack growth in single crystals by modeling short cracks under Stage I. The simulations employ FEM crystal plasticity models containing an idealized slip band with material properties that differ from the matrix. Two measures of the driving force are compared, ΔCTD and FIPs, in order to establish the degree to which they can be related under remote multiaxial displacement/strain-controlled loading. The final goal is to learn from the simulation of single crystals to extrapolate those lessons to individual grains in simulations of polycrystals.

3.2   Fatemi-Socie-based FIP and ΔCTD

The damage-tolerant approach assumes the presence of a crack and calculates its crack growth rate by means of the range of stress intensity factor (ΔK), the range of the J-integral (ΔJ) or the ΔCTD. These measures attempt to characterize the driving force for crack growth under cyclic loading of metals, and their generalized success has prompted their use in situations well beyond the limits of the underlying hypotheses [178, 117]. As mentioned in the previous chapter, the complexity of studying MSC fatigue driving forces lies in correctly describing the local fields, which are assumed *a priori* in the similitude hypothesis of LEFM and EPFM.

The use of the ΔCTD as a driving force introduces the need to conduct detailed FEM simulations that capture the influence of load history and microstructure in the vicinity of the crack tip. The CTD is typically computed using the displacement of two nodes just behind the crack tip, decomposing the displacement into an orthogonal basis parallel (giving the crack tip sliding displacement, CTSD) and normal (giving the crack tip opening displacement, CTOD) to the notch plane. The ΔCTD approach has been extensively and successfully employed in fracture mechanics experiments and theoretical modeling [16], but

it has the drawback of requiring detailed meshes that are computationally demanding.

More recent approaches have emerged that attempt to estimate the local driving force of small fatigue cracks under complex loading sequences. A myriad of FIPs used to correlate multiaxial fatigue crack initiation have been based on stress, strain or energy concepts [188], with the caveat that a single continuum parameter cannot correlate the fatigue crack initiation behavior of all metals under multiaxial conditions. In other words, the choice of a FIP is linked to the material-specific deformation and fatigue damage mechanism(s). Several studies have employed approaches akin to the Fatemi-Socie parameter instead of the ΔCTD for studying the effects of microstructure on fatigue crack formation and early crystallographic growth [185, 223, 171].

A primary objective of this research is to explore whether such a FIP can achieve a linear correlation with the ΔCTD for a crack within a single grain/crystal. Accordingly, the FIP attained over the third loading cycle will be compared to the corresponding ΔCTD in cracked single crystals for several stationary crack lengths (no consideration of crack growth and corresponding wake effects) employing a crystal plasticity constitutive model for Cu with a variety of meshes, loading conditions, and plastic strain localization scenarios as follows:

- Shear and mixed mode loading: Transgranular small fatigue cracks evolve from shear-dominated growth to opening-dominated growth; hence, an adequate driving force must represent the behavior of the crack tip under multiaxial loading conditions. This study evaluates ΔCTD and FIPs under imposed remote shear and mixed mode loading conditions.

- Plastic strain localization: The effect of plastic strain localization on ΔCTD and FIPs is analyzed by modeling cracks lying at the interface of idealized slip bands with a matrix having different material properties. For comparison, two slip band thicknesses are modeled, and the driving forces are computed for models without slip bands.

- Parametric study of normal stress coefficient, k: The literature does not provide a clear method to estimate the value of the constant k in the Fatemi-Socie FIP; this

chapter undertakes a parametric study to understand the sensitivity of the FIP and its correlation with ΔCTD.

- Mesh refinement: Cyclic plastic strain depends on the volume over which it is evaluated, and the maximum FIP attained changes with the size of the FEM mesh employed. Hence, the effect of the mesh is assessed in terms of mesh refinement, FIP averaging volume, and crack tip shape/geometry.

3.2.1 Modeling single crystals with cracks

Simulations of single crystals with cracks were performed using 3D finite element models in ABAQUS [1] with a user-material subroutine (UMAT) for Cu crystal plasticity based on McGinty's work [123]. The choice of Cu for simulations is based on the extensive characterizations of the slip bands and fatigue evolution in the literature. Five models with stationary cracks lengths of 2 μm, 5 μm, 7.5 μm, 10 μm and 15 μm were analyzed with an initial spacing between parallel crack surfaces of 0.2 μm, as shown in Figure 10. This initial opening is about one order of magnitude smaller than any other dimension, and should be interpreted as a rough approximation of experimental observations [100, 37, 176]. The models contain about 3000 reduced 8-node brick elements (C3D8R) constructed with ABAQUS visual interface to introduce some refinement in the element size towards the tip and slip band. Note that the latter requirement introduced asymmetries in the mesh, although their effect was negligible. The crack tip geometry was initially chosen as semicircle with a minimum of 10 elements along the perimeter, which follows the recommendations by Anderson [6] for fracture mechanics FEM simulations of elasto-plastic materials.

In one set of simulations the entire single crystal was allowed to undergo plastic deformation following the crystal plasticity constitutive model developed by McGinty [123]; these simulations are referred to as *homogeneous* and do not employ an explicit slip band of localized plastic deformation. A second set of simulations involved single crystals in which only the region immediately above and parallel to the crack (refer to Figure 10) had no restriction in deforming plastically other than specification of potentially active slip systems; this region is referred to as the "slip band". This band is considered as idealized as it

26

Table 1: Displacements applied to the top face in μm for the different cases analyzed. The displacement of the bottom face had the same magnitude and opposite direction/sense.

	Shear 1	Shear 2	Shear 3	Mixed 1	Mixed 2	Mixed 3
X axis	0.005	0.010	0.050	0.00354	0.00707	0.03540
Y axis	0	0	0	0.00354	0.00707	0.03540
Nominal peak strain	0.05%	0.1%	0.5%	0.05%	0.1%	0.5%

does not attempt to represent in detail the complex structure and mechanics of an actual persistent slip band in Cu single crystals. The width of the slip band was set at either 1 μm or 2 μm, which corresponds to the minimum width usually measured in cyclic loading experiments on pure Cu ([59]); below this length-scale, cell structures become energetically favorable [88, 108]. The crystal was oriented for single slip in remote shear loading, parallel to the crack and the slip band (X-direction, or $< 110 > (111)$) slip direction, but the remaining planes are not symmetric with respect to the crack front. The model is employed to determine the extent to which plastic strain localization in a slip band adjacent to a crack affects the driving forces as a function of remote load amplitude and mixed mode character.

3.2.2 Applied loading

The loading sequence consisted of quasistatic relative displacement of the upper and lower boundary planes of the crystal in Figure 12 under shear or mixed mode loading to achieve nominal overall model peak strains of 0.05%, 0.1%, and 0.5%. These values were chosen to provide plastic strains between 10^{-4} to 10^{-1}, typical of the HCF to LCF transition regimes. The magnitudes of the displacement vector (D) in Figure 13 were equivalent for loading cases with similar number in Table 1 (e.g., Shear 1 and Mixed 1). Furthermore, the out-of-plane displacement (Z axis) of the boundary planes was null, but they were allowed to move freely along the (Y axis). Three cycles were applied between zero and maximum displacement (i.e., $R_\epsilon = 0$) after which the fatigue driving forces were evaluated, as depicted in Figure 13.
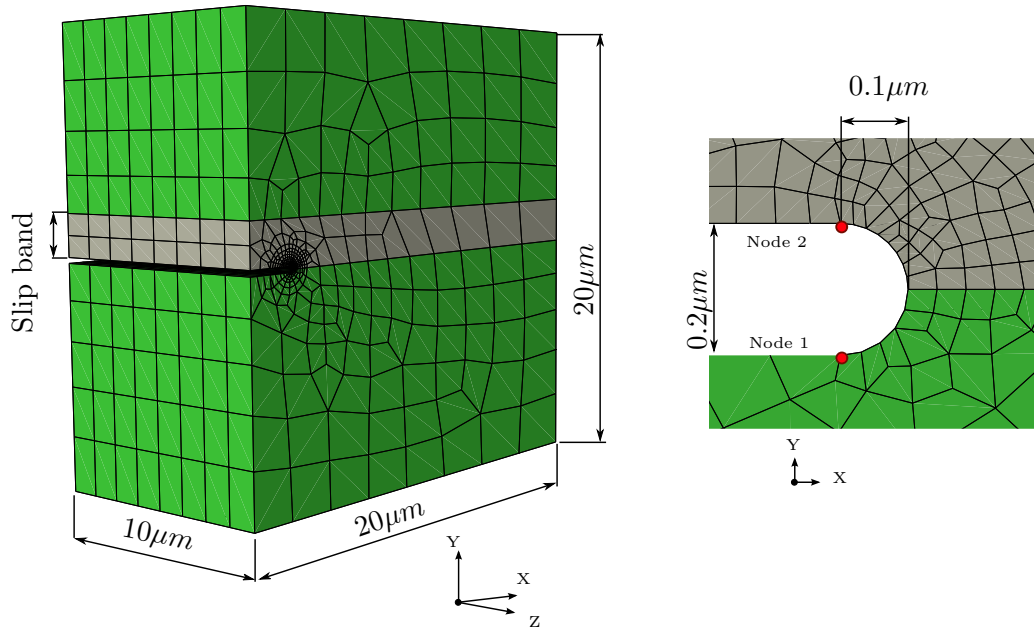
Figure 10: Cracked single crystal employed to evaluate FIPs and ΔCTD measured between nodes 1 and 2 at the mid-thickness. Similar models were analyzed with longer stationary cracks.
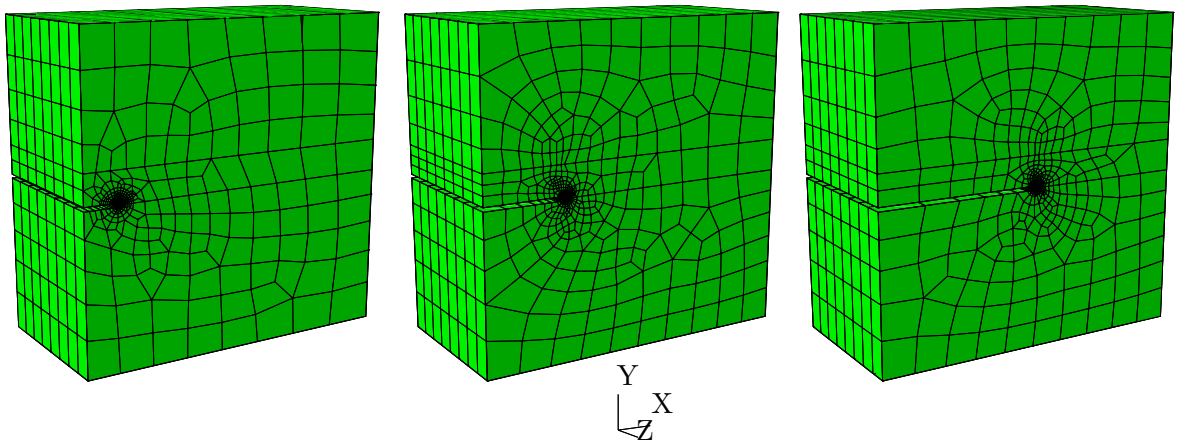
Figure 11: Example of three stationary crack lengths modeled. From left to right, $2\mu m$, $5\mu m$ and $10\mu m$ respectively.
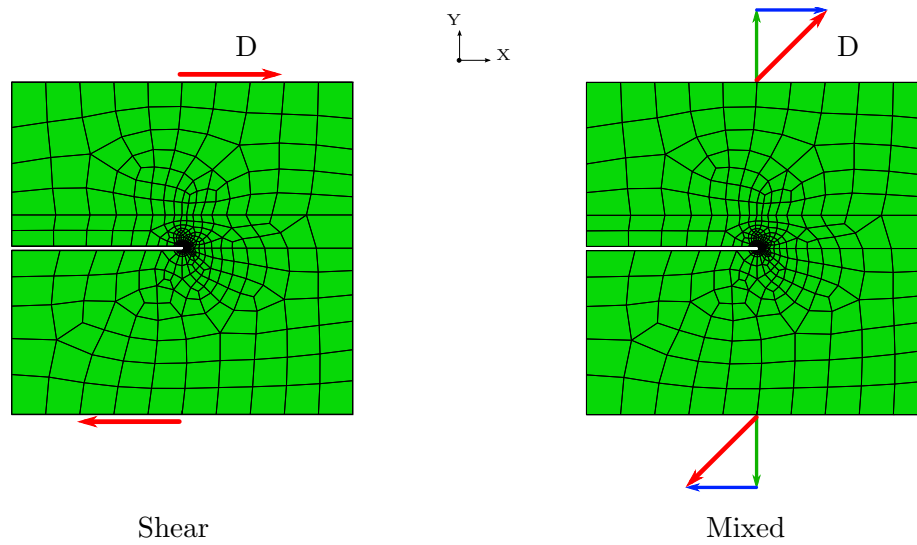
Figure 12: Applied boundary displacements. Both loading cases employed the same magnitude of the displacement vector (D).
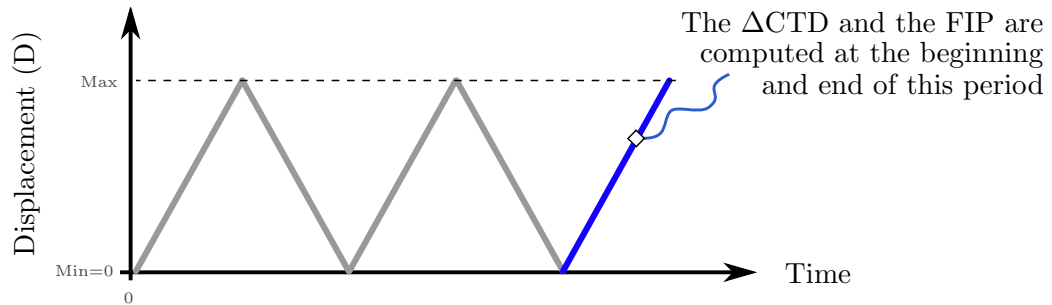
Figure 13: Magnitude of the displacement (D) applied to the upper and lower boundary planes of the single crystal as a function of time. The driving force is computed over the loading portion of the third loading cycle

3.2.3 Constitutive model for Cu

The continuum theory of crystal plasticity (cf. [43, 89]) was implemented in ABAQUS using a UMAT for Cu at room temperature. The numerical scheme is an extension of the implicit integration method outlined by Cuitiño and Ortiz [43], and was initially developed for Cu by McGintiy [123]. The formulation combines anisotropic elasticity along with the flow rule

$$\dot{\gamma}^{(\alpha)} = \dot{\gamma}_0 \left| \frac{\tau^{(\alpha)} - \chi^{(\alpha)}}{g^{(\alpha)}} \right|^m \text{sgn}(\tau^{(\alpha)} - \chi^{(\alpha)}), \tag{3}$$

where $\dot{\gamma}^{(\alpha)}$ is the shearing rate for slip system α, $\dot{\gamma}_0 = 0.001 s^{-1}$ is the reference shearing rate, $m = 50$, $\tau^{(\alpha)}$, $\chi^{(\alpha)}$ and $g^{(\alpha)}$ are the corresponding slip system shear stress, back stress and drag stress, respectively. The slip system back stress was neglected for all planes ($\chi^{(\alpha)} = 0$) and the drag stress had an initial value of $g_0 = 13MPa$, and evolves according to

$$\dot{g}^{(\alpha)} = H_{dir}\dot{\gamma}^{(\alpha)} - H_{dyn}g^{(\alpha)}|\dot{\gamma}^{(\alpha)}|, \tag{4}$$

in which $H_{dir} = 225MPa$, $H_{dyn} = 2.25MPa$. For further details see Ref. [123].

This constitutive formulation was employed in the homogeneous specimen and in the slip band region. The matrix that surrounds the slip band used the same constitutive model, except that the initial drag stress was specified as $g_0 = 100MPa$, which delays the onset of plastic deformation.

3.2.4 Calculation of the driving force parameters

3.2.4.1 ΔCTD

The ΔCTD was evaluated by measuring the displacement between nodes 1 and 2 at the mid-thickness (see local X-Y axis in Figure 10, right) over the loading portion of the third loading cycle. The total crack tip displacement range was calculated using [112, 19, 20]

$$\Delta\text{CTD} = \sqrt{\Delta\text{CTOD}^2 + \Delta\text{CTSD}^2} \tag{5}$$

The ΔCTOD and the ΔCTSD were calculated as the change in distance between nodes 1 and 2 in Figure 10, resolved along the X and Y axis directions, respectively, which follows the methodology outlined by Shih [186] and has been extensively employed in fracture mechanics [26].

As described by McDowell [119], FIPs offer an attractive and efficient means to estimate the driving force for small fatigue crack growth because they avoids the direct measurement or computation of the ΔCTD. The maximum cyclic plastic shear strain range on any plane is computed to evaluate the FIP in Equation (2) using the ordered principal cyclic plastic strain ranges over a cycle $(\Delta\epsilon_i^p)_{cyc}$, for $i = 1, 2, 3$, as $\frac{1}{2}\Delta\gamma_{max}^p = \frac{1}{2}[(\Delta\epsilon_1^p)_{cyc} - (\Delta\epsilon_3^p)_{cyc}]$. These principal plastic strain ranges correspond to the principal values of the plastic strain tensor range, $\Delta\boldsymbol{E}^p = \boldsymbol{E}_{final}^p - \boldsymbol{E}_{initial}^p$. For proportional loading with a positive peak plastic strain, we may estimate $\Delta\gamma_{max}^p$ based on the unloading half cycle from the peak load to the minimum point in the cycle, such that $\Delta\boldsymbol{E}^p = \boldsymbol{E}_{max}^p - \boldsymbol{E}_{min}^p$. Here, subscripts max and min relate to the peak and minimum points in the cycle, respectively. The unit normal vector to the plane of maximum plastic strain range $(\boldsymbol{\pi})$ is defined by the eigenvectors associated with $(\Delta\epsilon_1^p)_{cyc}$ and $(\Delta\epsilon_3^p)_{cyc}$, $\boldsymbol{\nu}_1$ and $\boldsymbol{\nu}_3$, i.e.,

$$\boldsymbol{\pi} = \frac{\boldsymbol{\nu}_1 + \boldsymbol{\nu}_3}{||\boldsymbol{\nu}_1 + \boldsymbol{\nu}_3||} \tag{6}$$

The normal stress to the plane of maximum range of plastic shear strain is then given by $\sigma_n = max(\pi_i\sigma_{ij}\pi_j)$. The constant $k = 1$ is assigned in Equation 2, and the polycrystalline yield strength (σ_y) is taken as 150 MPa.

3.3   Results of the simulations

3.3.1 ΔCTD and maximum FIP

This section presents the results of multiple measurements of the fatigue driving forces in single crystals. As explained in section 3.2.4.1, the ΔCTD corresponds to the net displacement of two nodes, while the FIP is computed for every element using Equation (2). However, the fatigue driving force based on FIPs could be evaluated in several ways: the simplest case is to employ the maximum FIP computed among those elements near the crack tip. A second option is to define a non-local region and then average the FIP computed for each element in that volume. In this case the driving force is referred to as an average FIP.

Figure 14 illustrates the ΔCTD, computed from simulations over the loading portion of the third loading cycle, as a function of the stationary crack length for shear (left) and mixed mode (right) loading. Overall, the ΔCTD exhibits a monotonic increase with decreasing slope as the crack length increases. For specimens with slip bands under shear, differences with the homogeneous case become more significant with increasing nominal peak strain. Furthermore, the value of the ΔCTD is dominated by the ΔCTSD for shear loading, which is typically an order of magnitude larger than the ΔCTOD in this case. When mixed mode loading is applied, the ΔCTD has significant contributions from both the ΔCTSD and ΔCTOD; homogeneous and localized plasticity cases show a similar monotonic increase with crack length, differing in the magnitude of the ΔCTD for increasing nominal peak strain.

The dependence of the ΔCTD on slip bands varies with the crack length and load amplitude. In the presence of a slip band, shorter cracks under low loading amplitude (shear/mixed 1 and 2) exhibit larger ΔCTD while homogeneous specimens with longer cracks show the opposite trend. Additionally, for shear and mixed loading, the results show that the thickness of the slip bands exerts only a secondary influence on the crack driving force, also found by Sauzay and Gilormini [183].

Figure 15 is equivalent in essence to Figure 14, save that it considers the maximum FIP. Overall, the trends in both figures are comparable, but the maximum FIP shows differences between models with and without slip bands. The similarities between Figures 14 and 15 suggest that the FIP and the ΔCTD may be correlated.

Figure 16 cross plots the maximum FIP near the crack tip versus the ΔCTD for all cases studied, with and without slip bands, for all crack lengths and applied displacement amplitudes. In all cases, the maximum FIP was located in proximity to the crack tip, and the correlation to ΔCTD had a slope on the order of unity in logarithmic coordinates. However, shear loading seems to shift the FIPs of the homogeneous specimens towards lower values (blue dots). Furthermore, the FIP seems to lose the correlation with ΔCTD for very low values of ΔCTD, suggesting a threshold value when the applied displacement amplitude is decreased (also found in mixed mode loading with lower nominal peak strain, although
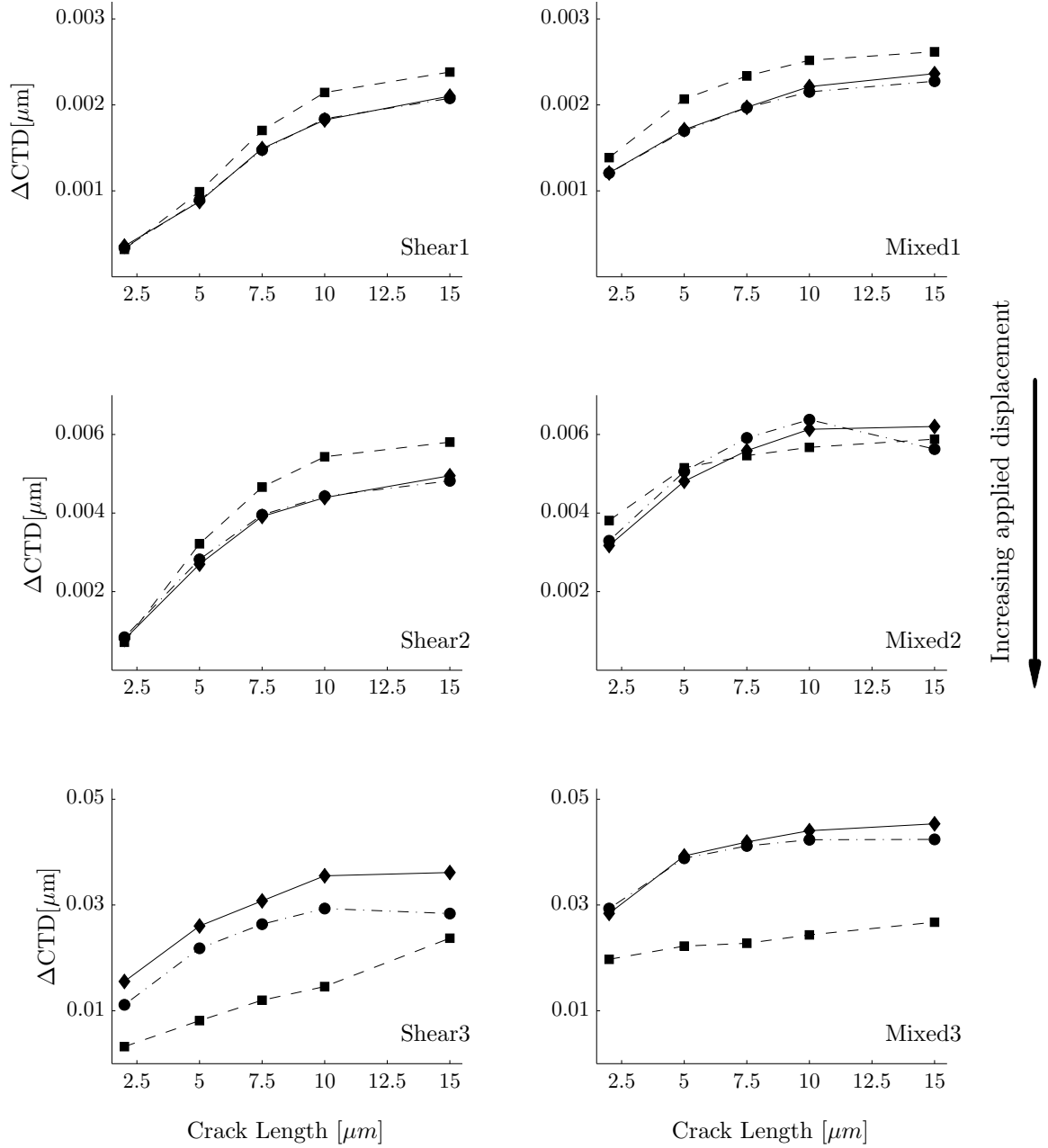
Figure 14: ΔCTD measured from models with increasing static crack lengths for shear (left) and mixed (right) mode loading. The numbers next to the loading mode correspond to the applied displacement defined in Table 1. Symbol legend: ◆ 1 μm band, ● 2 μm band, ■ Homogeneous.
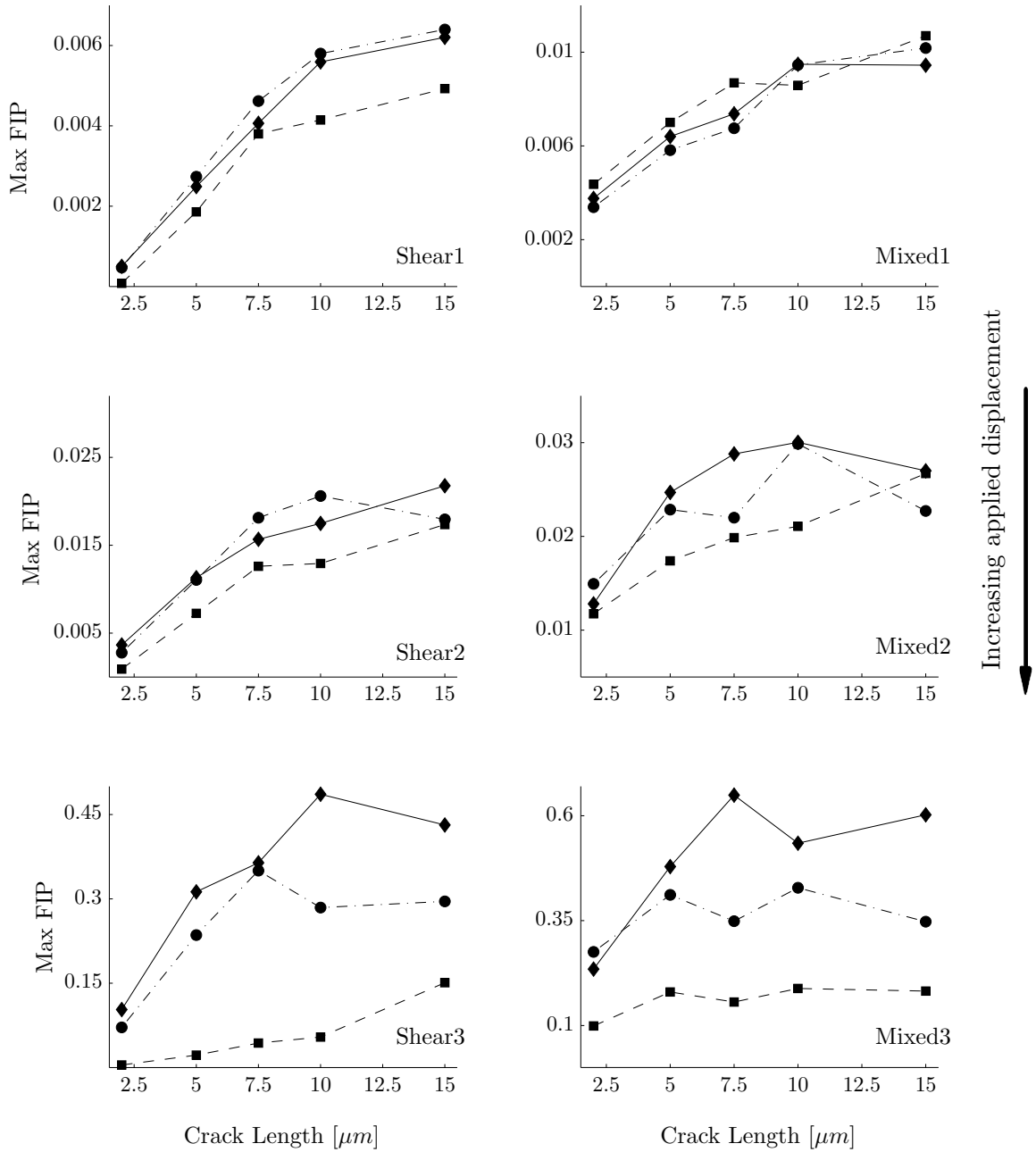
Figure 15: Maximum FIP as a function of static crack lengths for shear (left column) and mixed mode (right column) loading. The numbers next to the loading mode correspond to the applied displacement defined in Table 1. Symbol legend: ♦ 1 μm band, ● 2 μm band, ■ Homogeneous.
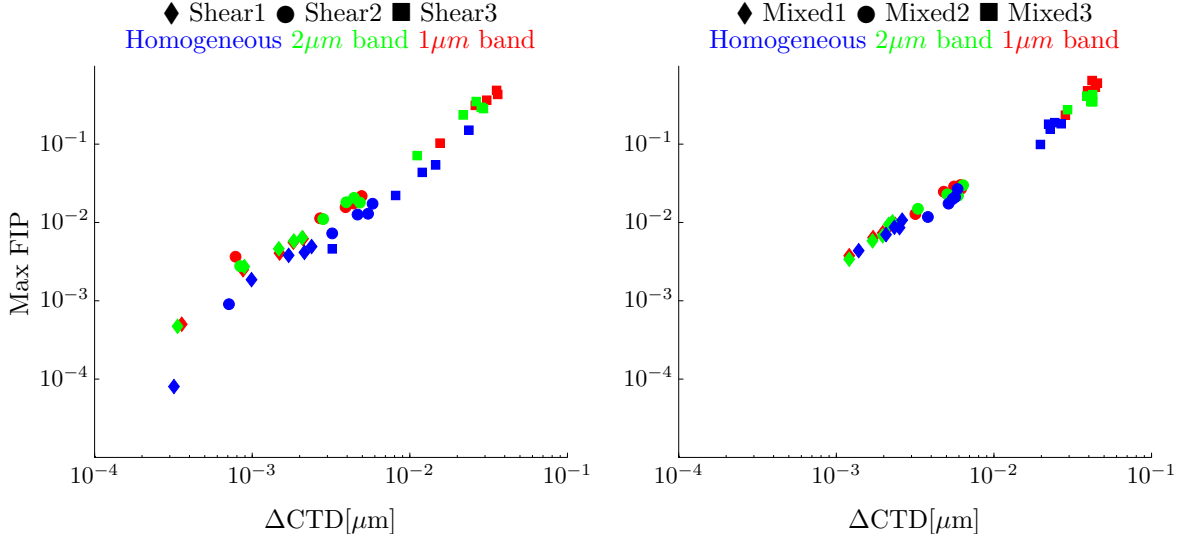
Figure 16: Maximum FIP reached close to the crack versus ΔCTD for shear (left) and mixed mode (right) loading. The numbers next to the loading mode correspond to the applied displacement defined in Table 1.

not shown here). This threshold is expected since the comparison is made between a FIP based on cyclic plastic deformation and the total ΔCTD (which includes elastic and plastic components).

To avoid the threshold and extend the correlation between the FIP and the ΔCTD over broader domains, either the elastic component of the ΔCTD should be subtracted or the FIP should additionally account for elastic strain. The latter option is preferred, in view of the complexities in resolving the elastic part of the ΔCTD. Figure 17 presents the maximum FIP among all elements but calculated using the full strain tensor to compute $\Delta\gamma_{max}$. In this case, the results do not show the threshold presented in Figure 16, and the correlation between the total-strain FIP and ΔCTD extends for the entire load range studied. The shift of the data relative to homogeneous specimens still persists in shear loading. Clearly, the plastic strain range dominates the FIP near the crack tip, as expected.

3.3.2 Volume averaged FIPs

As a means of arriving at mesh insensitive measures of FIPs and respecting the finite volume of the fatigue damage process zone [119], nonlocal (volume averaged) measures of cyclic plastic shear strain range and normal stress are adopted. This is also justified
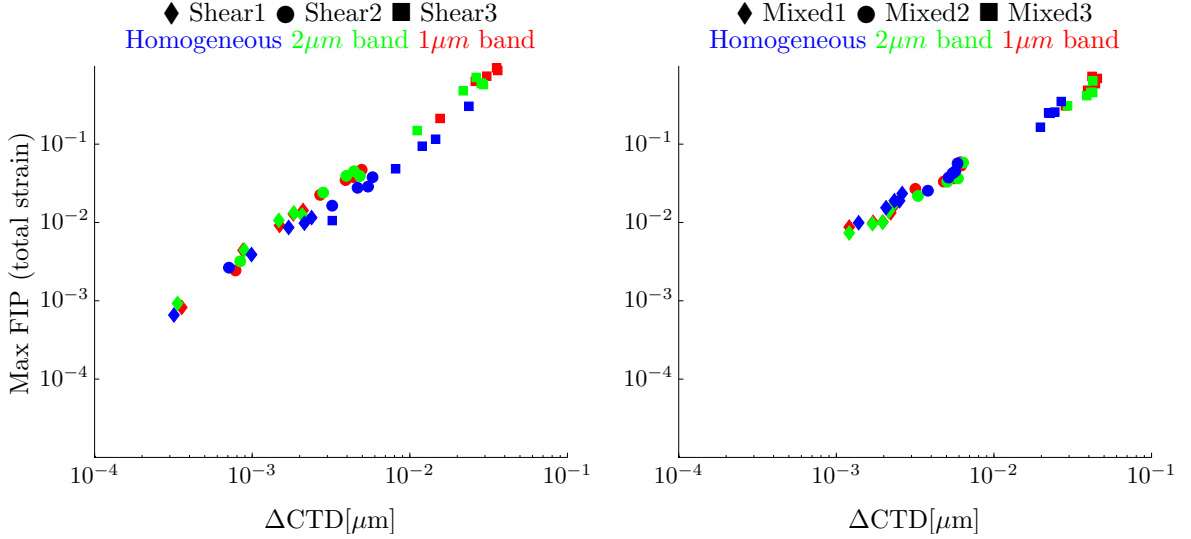
Figure 17: Maximum total-strain FIP reached close to the crack versus ΔCTD for shear (left) and mixed mode (right) loading. The numbers next to the loading mode correspond to the applied displacement defined in Table 1.

by the fact that dislocation substructures and crack nuclei of finite scales form on the order of a μm; for example, plastic deformation and fatigue damage are intrinsic non-local processes [21, 114, 119, 121]. In view of the strong gradients of inelastic deformation and the presence of a physical damage process zone at the tip of an advancing fatigue crack, it is to be expected that the characteristic volume for averaging FIPs (see Section 3.2) should somehow relate to the geometry of the crack tip, cyclic plastic zone size, and so forth. For example, when a single slip band has developed, the crack driving force depends on the length of the ligament up to the GB and not the volume of the grain [114]. To evaluate the effect of the averaging volume on the driving force, the FIP was averaged based on values from each element in homogeneous specimens over the following volumes:

- Spheres of either $3\mu m$ or $5\mu m$ in diameter, randomly placed in the single crystal. The average FIP corresponds to the maximum value found among all of the spheres among 50 locations/samples near the notch root,

- Bands of either $1\mu m$ or $2\mu m$, similar to the volume occupied by slip bands. These averaging volumes are parallel to the slip plane that is expected to activate the most, so the average value should represent the behavior of the entire slip plane,

- The entire volume of the crystal.

To avoid averaging over essentially elastic deformation regions, only the elements within each volume that have FIP values above 10^{-8} were considered.

The effect of the averaging volume FIPs on homogeneous specimens is assessed in Figure 18, which compares the FIP averaged over a variety of domains. All the averages follow the same trend, but the average over spheres seems to exhibit higher variability, which is expected since as the limit of the sphere size approaches zero, the maximum FIP values should be recovered. Additionally, the location of the spheres adds a degree of freedom that contributes to the variability of the results.

Regarding the average over bands, the change from 1 μm to 2 μm bands does not seem to affect the results significantly, but they differed from averaging the FIPs over the entire crystal, especially for low amplitude loading. The fact that differences decrease with decreasing loading amplitude suggests that for small loading amplitude, the plastic deformation in homogeneous specimens did not extend outside the band, but localized within it.

The good behavior of the band average in Figure 18 suggests that the average FIP on the volume defined by the slip bands can moderate the variability of the results. In the case of the simulation of homogeneous specimens, the averaging volume chosen corresponds to a band of $2\mu m$, similar to that occupied by slip bands. Hence, the rest of this and the following chapters will employ FIPs averaged along bands that are parallel to the most activated slip plane, and they will be referred as to averaged FIPs.

Figure 19 presents the results of the averaged FIP for the simulations introduced in section 3.3.1 as a function of static crack lengths. The comparison with Figures 14 and 15 shows that the evolution of the averaged FIPs is smoother than that of maximum FIP values, and resembles the evolution of the ΔCTD.

Figure 20 depicts the comparison between the nonlocal FIPs averaged along bands and the ΔCTD; It shows that both parameters have almost a one-to-one correlation with slightly less variability than in the case of maximum FIP vs ΔCTD. Additionally, the correlation between the nonlocal FIP and the ΔCTD does not appear to be affected by the presence
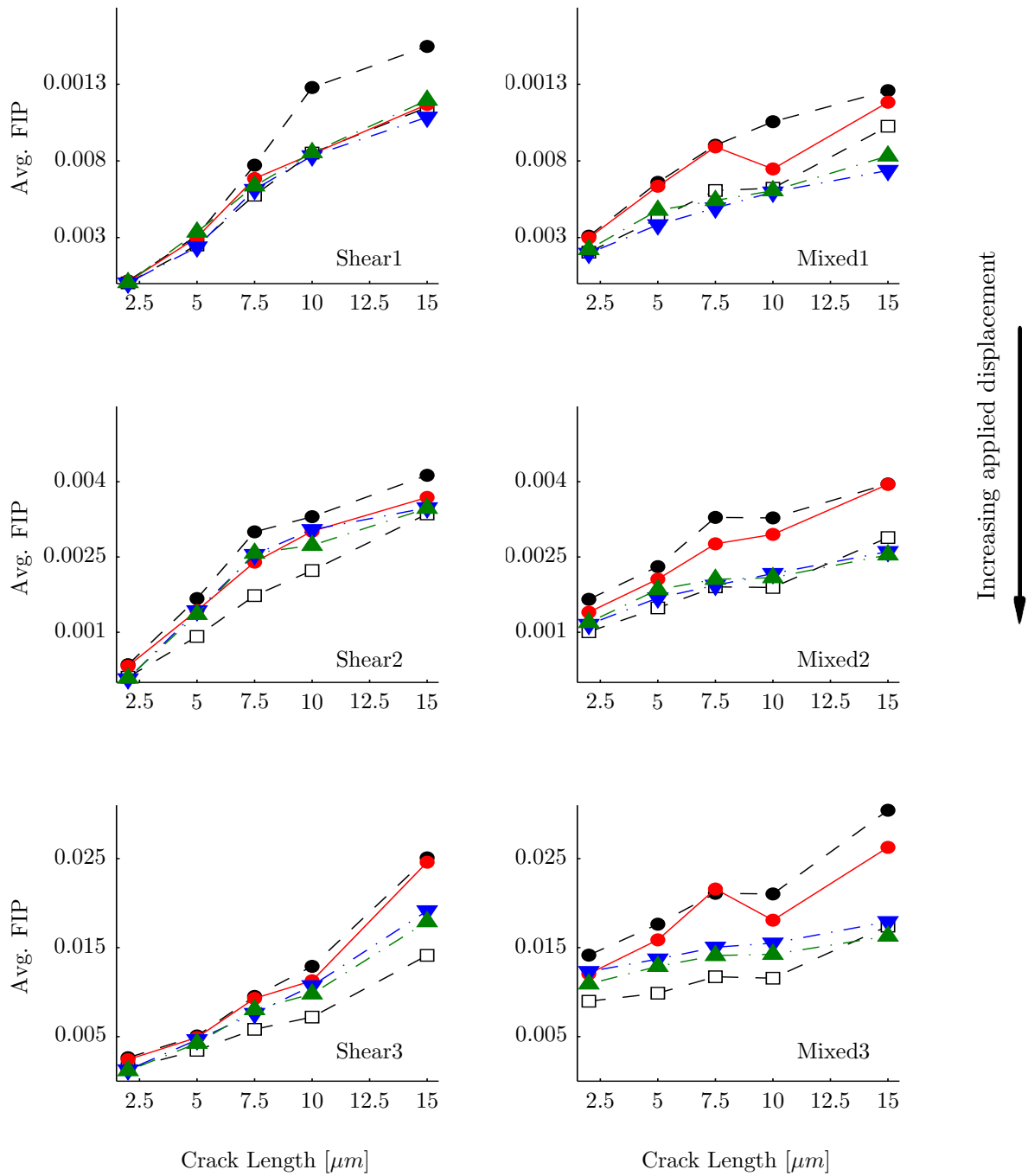
Figure 18: Comparison of the FIP averaged over spheres, bands or the entire crystal for homogeneous specimens as a function of static crack lengths. Symbol legend: ● 3 μm sphere, ● 5 μm sphere, ▼ 1 μm band, ▲ 2 μm band, □ entire crystal.
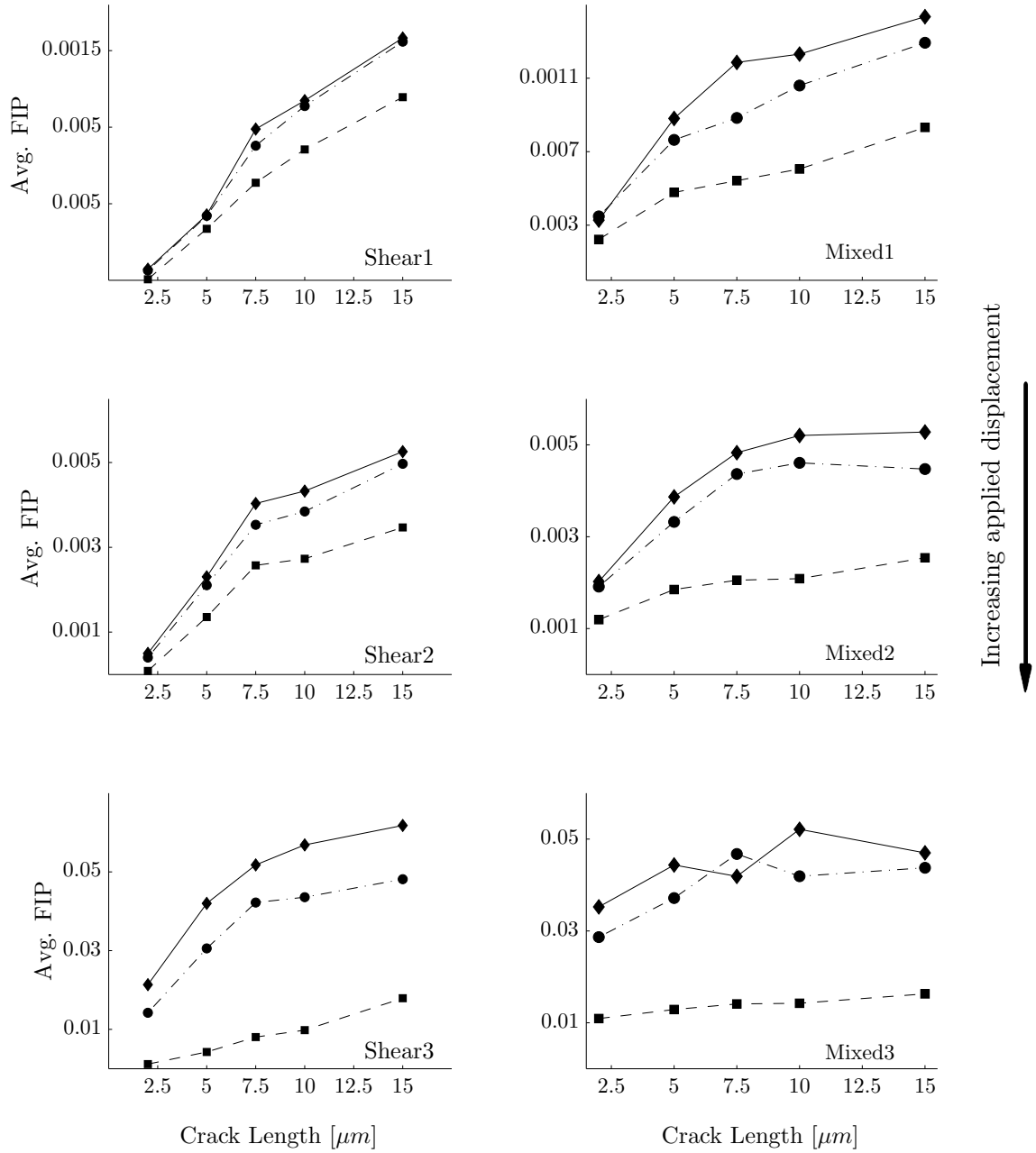
Figure 19: Averaged FIP as a function of static crack lengths for shear (left column) and mixed mode (right column) loading. Symbol legend: ♦ 1 μm band, ● 2 μm band, ■ Homogeneous.
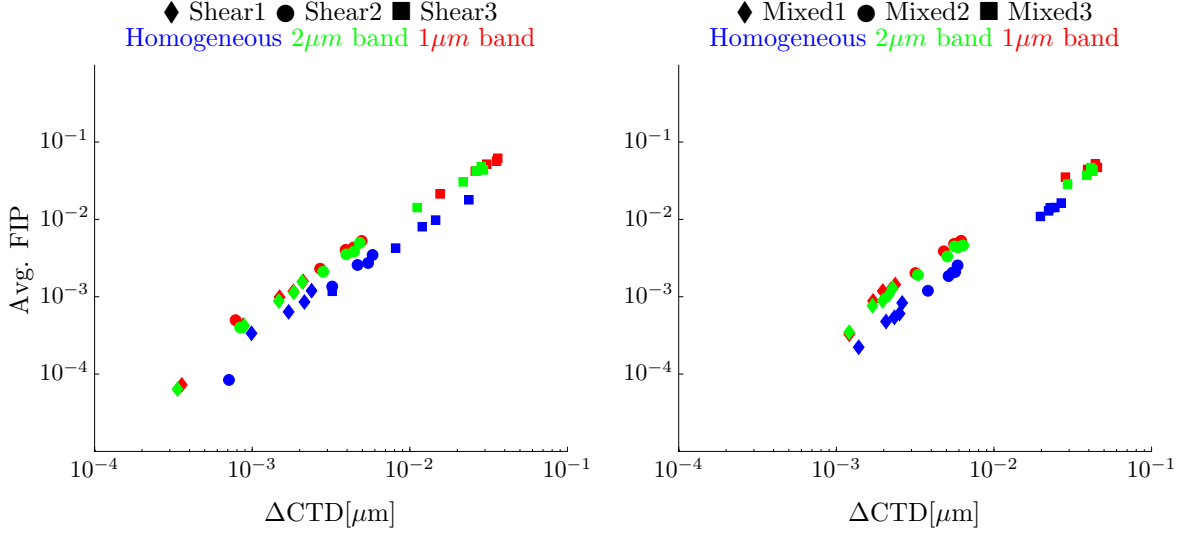
Figure 20: FIP averaged over bands parallel to the crack versus ΔCTD for shear (left) and mixed mode (right) loading.

of a slip band, and all results in Figure 20 follow a single power law.

3.3.3 FIP calculation assessment

For proportional loading, the methodology to calculate the FIP introduced in section 3.2.4.2 is simpler than the approach employed by McDowell and coworkers [171], which is described in further details in Appendix A. This methodology requires calculation of four eigenvalues (instead of two) and computes the plastic shear range by subtracting the plastic shear calculated at maximum and minimum loading, $\Delta\gamma^p_{max} = \gamma^p_{max} - \gamma^p_{min}$, using that,

$$\gamma^p_{max} = \left|\epsilon^p_1|_{max} - \epsilon^p_3|_{max}\right| \, \mathrm{sgn}(\epsilon^p_1|_{max}),$$

$$\gamma^p_{min} = \left|\epsilon^p_1|_{min} - \epsilon^p_3|_{min}\right| \, \mathrm{sgn}(\epsilon^p_3|_{min}), \tag{7}$$

in which $(\epsilon^p_i)_{cyc}$, for $i = 1, 2, 3$ are the ordered principal plastic strains, and the subscripts *max* and *min* refer to the peak and minimum points in the cycle, respectively. The value of $\Delta\gamma^p_{max}$ is then employed to compute the FIP along with the stress acting normal to the plane of γ^p_{max}, following the procedure described in section 3.2.4.2

To assess the equivalence of both methodologies, a set of fully reversed simulations ($R_\epsilon = -1$) were developed for Shear and Mixed loading as described in Table 1. This type

Table 2: Displacements applied to the top face in μm for the different cases analyzed. The displacement of the bottom face had the same magnitude and opposite direction.

	Tensile 1	Tensile 2	Tensile 3
X axis	0	0	0
Y axis	0.005	0.010	0.050
Nominal peak strain	0.05%	0.1%	0.5%

of loading is only employed in this section for comparing FIP calculations methodologies. Additionally, tensile loading cases were analyzed in which $R_\epsilon = -1$ and the displacement vector D was along the Y direction, as described in Table 2. The calculations used only homogeneous specimens (all the elements hold the same constitutive model), but the volume occupied by $2\mu m$ slip bands was employed to compute an averaged FIP. Figures 21 and 22 compare the maximum FIPs and the FIPs averaged along $2\mu m$ bands computed with both methodologies. The results show good agreement among the calculations; only a slight bias was observed with increasing loading, which supports the calculations in section 3.2.4.2.

3.3.4   Influence of the constant k in the FIP definition

Little guidance exists regarding the value of the constant k in the Fatemi-Socie parameter of Equation (2), which controls the influence of normal stress to the plane of maximum plastic shear strain range. The form of the FIP is loosely related to the models from Brown and Miller [28, 87] and Findley (see Ref. [188]) that argue for the role of normal stress (or strain) to the crack plane in enhancing the crack driving force (cf. [118]). Thus, the effect of this constant on the correlation between the total-strain FIP and ΔCTD was analyzed by varying k from 0 to 2 and then pursuing linear regression in log-log plots, which was performed by using a Matlab subroutine [99] to minimize the mean square error (MSE) in correlation with the ΔCTD. The slope of the linear regression represents the exponent b in the power law

$$\mathrm{FIP}(k) = C\Delta\mathrm{CTD}^b, \tag{8}$$

while the intersection with the vertical axis represents the $log(C)$. Figure 23 presents an example of the linear regression using k=1, and is representative of all the cases analyzed.
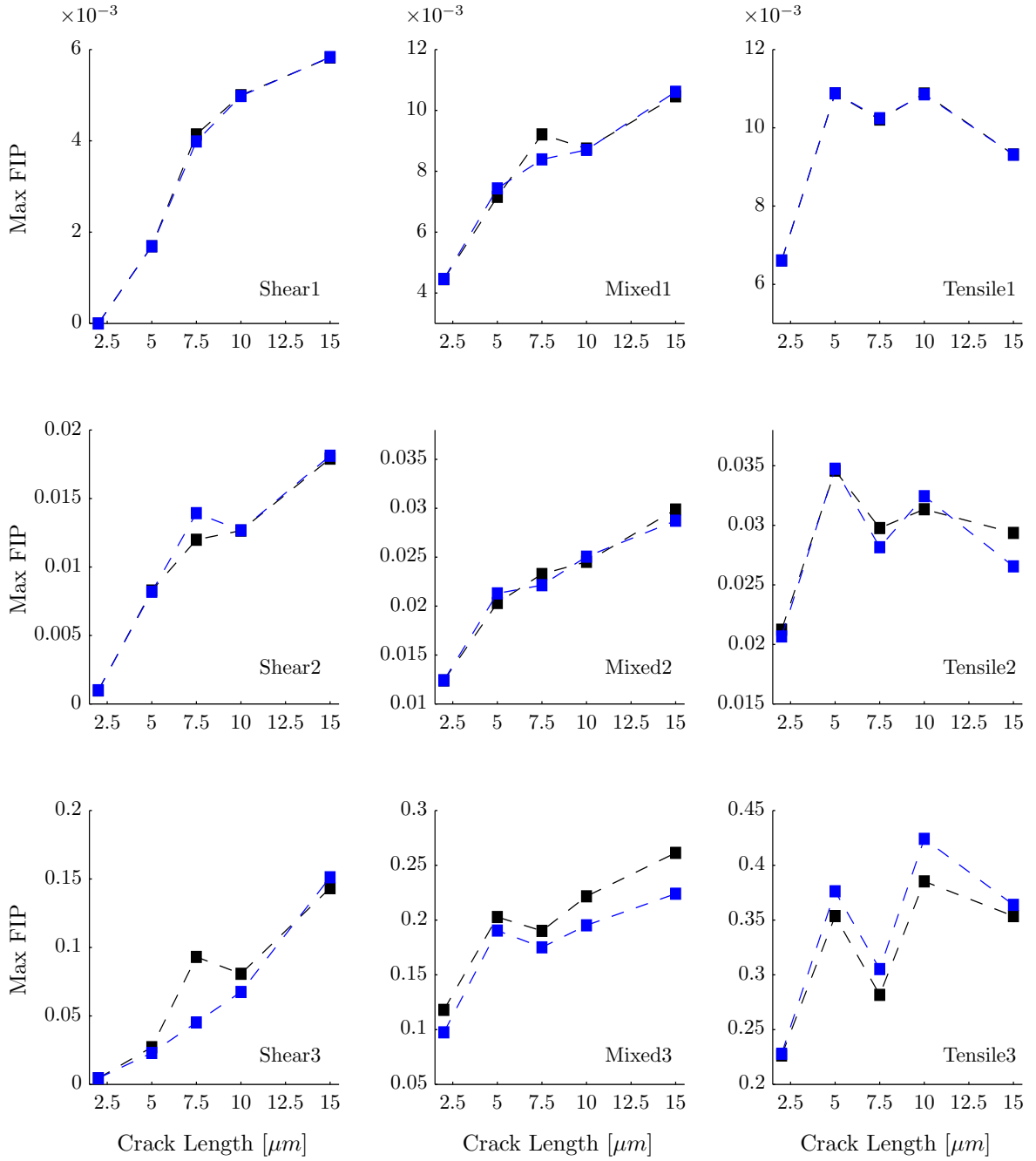
Figure 21: Comparison of the max FIP calculation as a function of static crack lengths for shear (left), mixed (center), and tensile (right) mode loading.
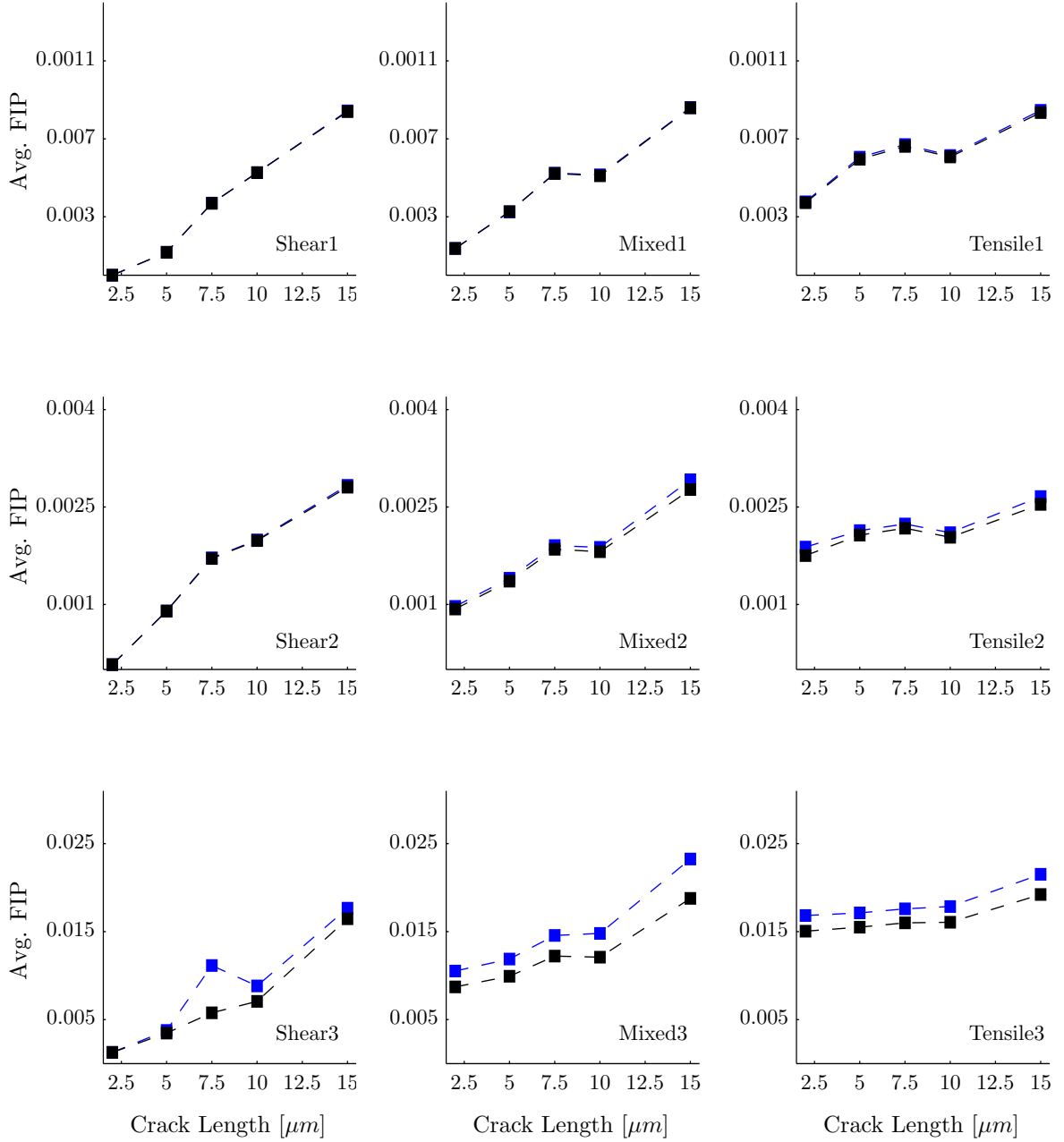
Figure 22: Comparison of the averaged FIP calculation as a function of static crack lengths for shear (left), mixed (center), and tensile (right) mode loading.
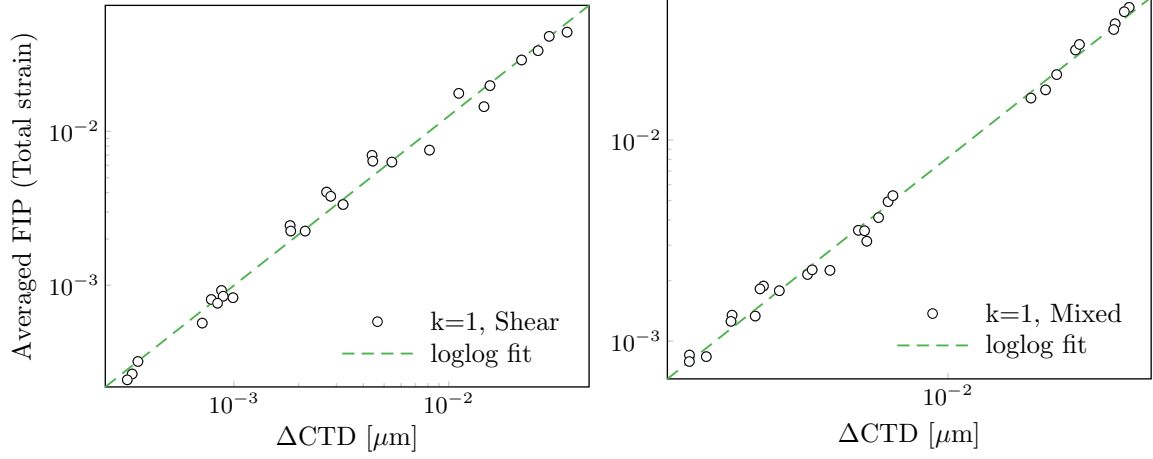
Figure 23: Linear regression of the averaged total-stain FIP vs ΔCTD. Shear loading (left). Mixed loading (right).

Figure 24 presents the constants b and C, as calculated using the linear regression of the averaged total-stain FIP, including the data from all the models (i.e, with and without slip bands). For the entire range of k, the correlation is almost one-to-one (i.e., b $\approx$ 1) for both shear and multiaxial loading. Coefficient C evolves in similar ways for both shear and mixed loading, but the latter is slightly lower than the former. Finally, the bottom plots in Figure 24 show the MSE of the linear regression, which increases with k, and which thus suggests that the dependence on the normal stress may be slightly nonlinear, as suggested by other models [188]. Note that the quality of the correlation may be improved by fitting data from simulations conducted either with or without slip bands.

The previous analyses consider linear regressions of shear and mixed mode loading data independently. Both loading conditions resulted in an approximately one-to-one correlation ($b = 1.1 \pm 0.1$), but the coefficient C showed a larger relative difference. Figure 25 describes the ratio of the coefficients b and C for shear and mixed mode loading. Interestingly, the coefficients for the shear and mixed modes become more similar with increasing value of k, for which the MSE increases. Thus, the quality of a single correlation for multiaxial loading conditions needs to balance these two opposite trends; consequently the optimum k is not the value associated with minimum MSE. Further loading condition data would be necessary to determine the best correlation between the FIP vs ΔCTD for a general loading
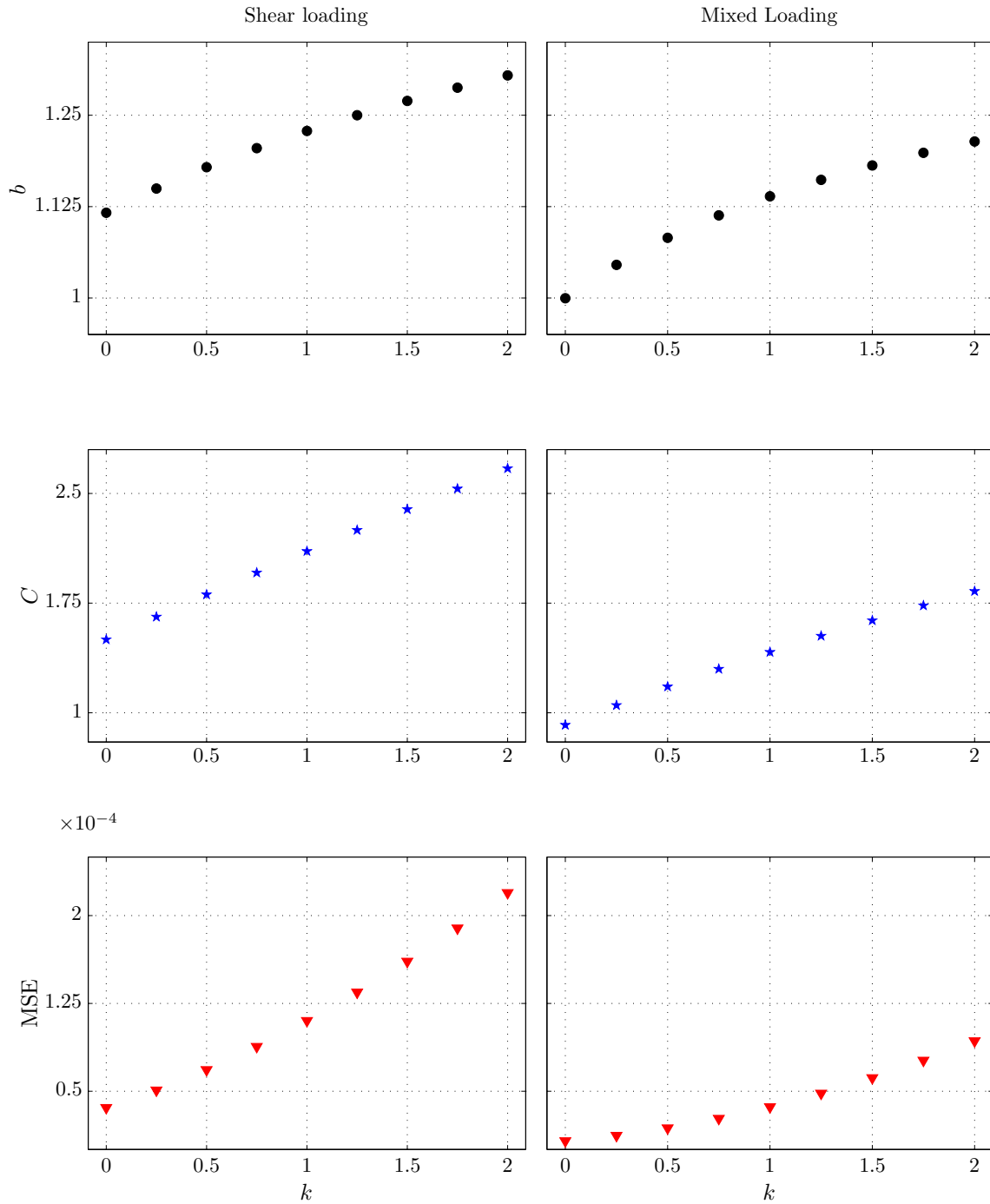
Figure 24: Linear regression of the averaged total-stain FIP vs ΔCTD. b, C correspond to Equation (8). Shear loading (left). Mixed loading (right).
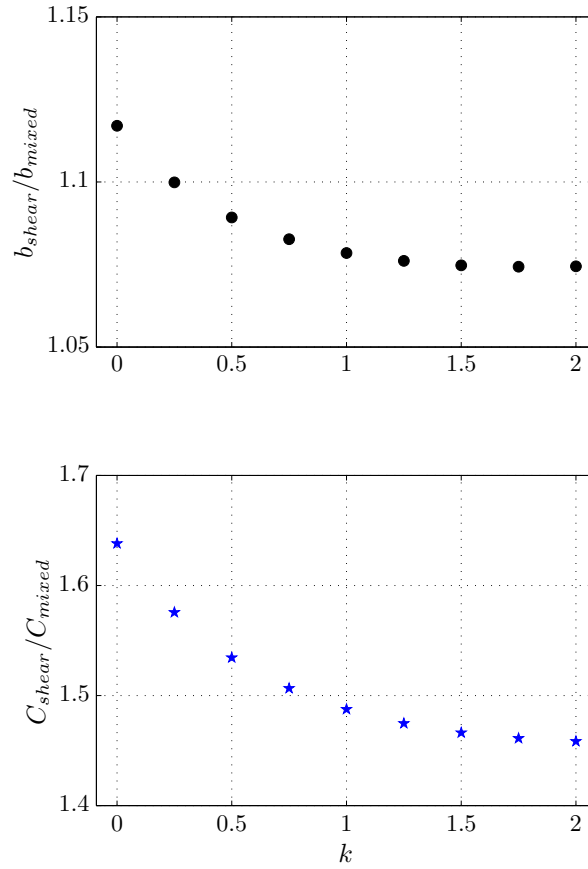
Figure 25: Relation between the regression coefficients that were determined independently for shear and mixed mode loading. Note that increasing k makes the coefficients more similar, which would be ideal for single multiaxial correlation between the FIP and ΔCTD. b and C correspond to Equation (8).

situation, but the point is made that exponent b showed smaller variations than coefficient C for different loading modes.

For completeness, regression analysis was performed with the maximum FIP data instead of the average FIP, and the results are presented in Figure 26. In this case, fitting parameters for Equation (8) are significantly different between shear and mixed loading, while the MSE is much larger than in the averaged case. Thus, these results support the use of averaged values instead of local maximum magnitudes to characterize the driving force with a single correlation law for multiple loading conditions.
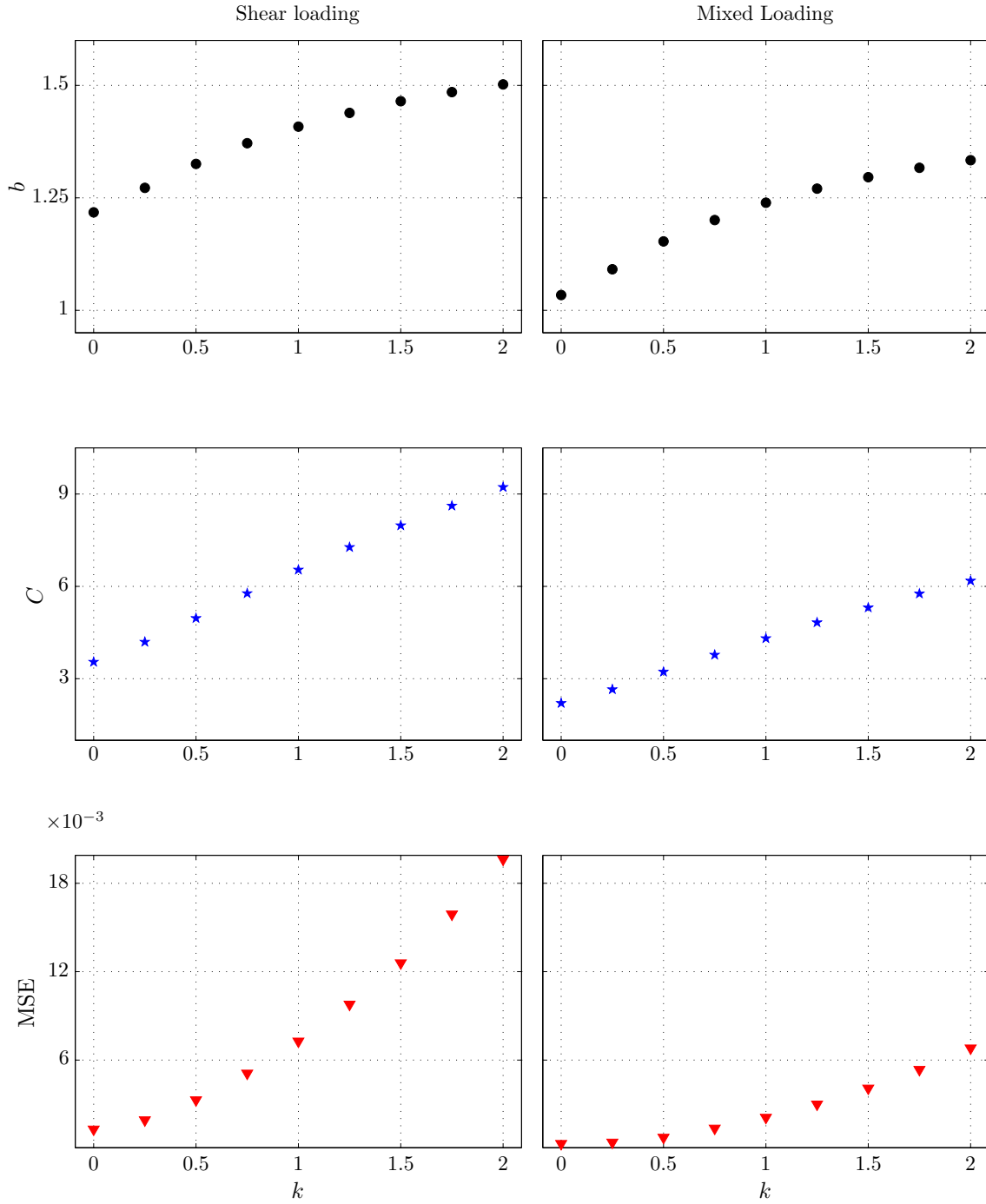
Figure 26: Linear regression of the Max FIP vs ΔCTD. b and C correspond to Equation (8). Shear loading (left). Mixed loading (right).

3.4 Influence of the model geometry

With the objective of generalizing the results, this section presents additional simulations that are similar to the those previously introduced, but with particular differences in geometry, i.e., the initial spacing of the faces of the crack, the crack tip geometry, and the mesh refinement. The loading conditions, the material and the crystallographic orientation are identical, but the analyses only consider cracks adjacent to a 2 μm slip band and homogeneous specimens, because the results showed that the thickness of slip bands plays a secondary role on the driving forces.

3.4.1 Initial crack face spacing

To evaluate whether the initial separation between the faces of the crack (initial opening) affects the results, a new set of simulations was developed using an initial crack opening of $0.05\mu m$ (compared to $0.2\mu m$).

Figures 27 and 28 present the evolution of the ΔCTD and the band averaged FIP with the crack length, respectively, and they depict trends similar to those found for an initial crack face spacing of $0.2\mu m$ (Figures 14 and 15). In particular, the localization of plastic strain in a $2\mu m$ band enhances the driving force for high and low displacement amplitudes, and the homogeneous specimens with shorter cracks present slightly higher driving forces for crack growth, especially for mixed loading. Figure 29 exhibits the FIP averaged over $2\mu m$ bands as a function of the ΔCTD for simulations with an initial opening of $0.05\mu m$, for shear and mixed loading. These results show a shift of the FIP to lower values for the homogeneous specimens, and an almost one-to-one relation between the FIP and the ΔCTD, similar to the results shown in Figure 20.

3.4.2 Effect of crack tip geometry

A primary drawback of using ΔCTD as the fatigue crack growth driving force is that it requires the analysis of the details of the crack tip geometry and the choice of location at which to measure/compute the displacements. The simulations described in the previous sections have presented cracks with circular tip geometry. For comparison, this section
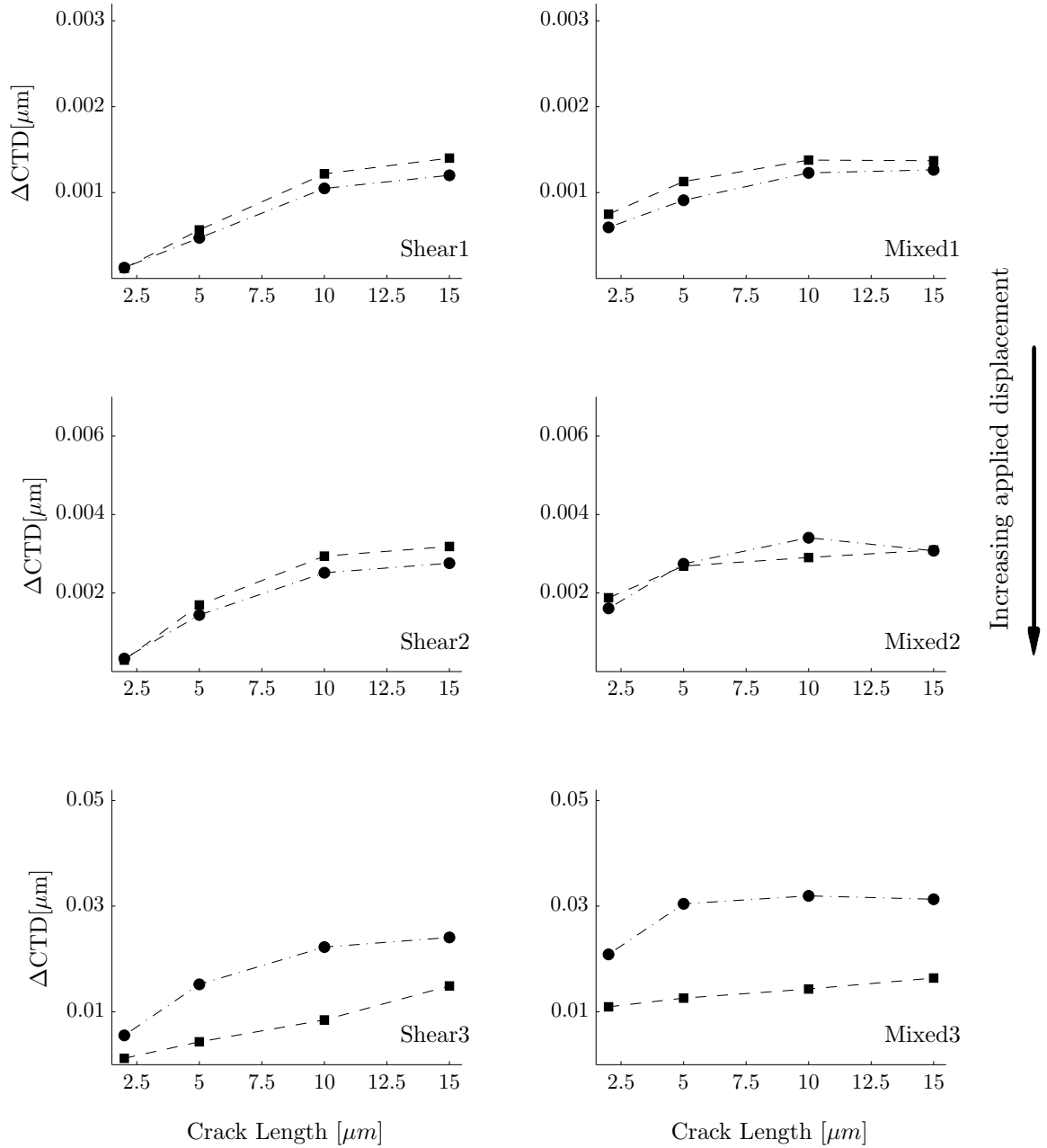
Figure 27: ΔCTD as a function of crack length for an initial crack face spacing of $0.05\mu m$. Shear loading (left). Mixed mode loading (right). Symbol legend: ● 2 μm band, ■ Homogeneous.
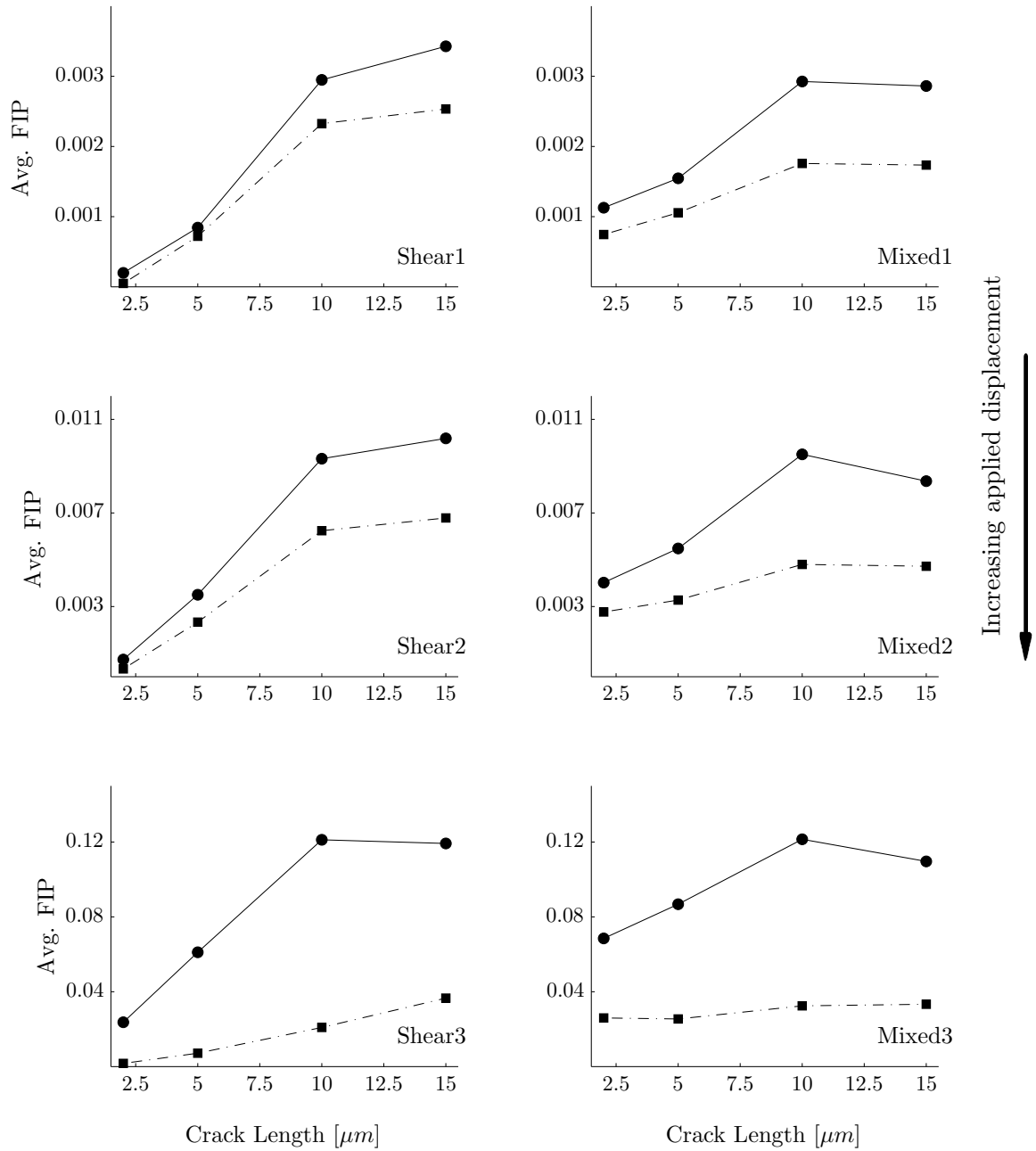
Figure 28: Averaged FIP as a function of crack length for an initial crack face spacing of $0.05\mu m$. Shear loading (left). Mixed mode loading (right). Symbol legend: • 2 μm band, ■ Homogeneous.
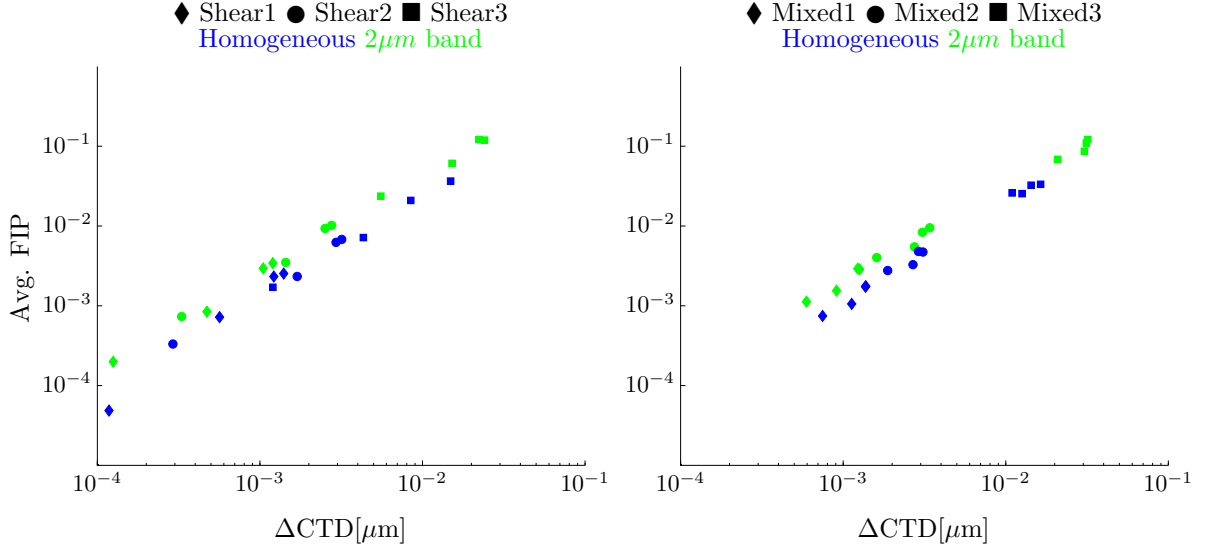
Figure 29: Comparison between ΔCTD and the averaged FIP for an initial crack face spacing of $0.05\mu m$. Shear loading (left). Mixed mode loading (right).

assesses single crystals with a $90°$ triangular crack tip, as depicted by Figure 30. The load history is similar to that shown in Figure 13, but only two nominal peak strain cases were analyzed, 0.1% and 0.5% (shear/mixed mode 2 and 3). In this case, the driving force is also measured over the loading portion of the third loading cycle, and the FIP is calculated as stated in section 3.2.4.

In Figure 31 the ΔCTD for homogeneous and 2 μm slip band specimens that were shown in Figure 14 are reproduced in solid symbols; These are compared with the results for triangular crack tips in hollow symbols and thicker lines. The ΔCTD does not appear to be significantly affected by changing the shape of the tip geometry, and, more importantly, the differences are consistent for all the load histories and meshes analyzed. Thus, the change from a circular to a triangular crack tip shape may justify a consistent bias of around 10% in ΔCTD. Figure 32 presents the FIP versus ΔCTD for the circular tip (solid symbols) and triangular tip (hollow symbols), for the two loading conditions analyzed, showing that the shape of the crack tip affects to some extent the maximum FIP and ΔCTD correlation, especially for higher driving forces.

However, the correlation between the averaged values of the FIP and the ΔCTD does not appear to be affected by changing the shape of the crack tip, as shown in Figure 33.
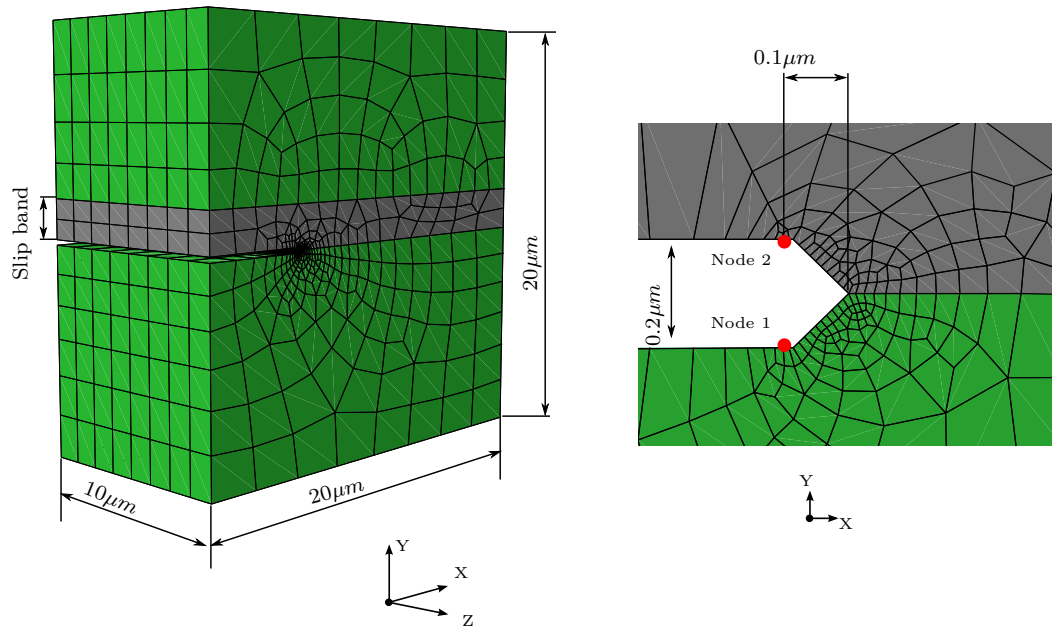
Figure 30: Cracked single crystal with a 90° triangular crack tip. The ΔCTD is measured between nodes 1 and 2.

Indeed, there is a good agreement between the results for both crack tip geometries in shear and mixed mode loading in several respects:

1. The threshold at low driving force,

2. The effect of a $2\mu m$ slip band in the driving force, and

3. A similar level of variability in the correlation between the FIP and the ΔCTD.

Finally, Figure 34 presents the results obtained by using the averaged FIP calculated using the total strain tensor (including both elastic and plastic components); it supports the conclusion that the crack tip geometry exerts only a secondary influence on the correlation between the FIP and ΔCTD when the FIP is computed as averaged rather than as a pointwise maximum in the mesh.

3.4.3 Mesh refinement

As mentioned previously, use of the maximum pointwise FIP has been avoided in previous works by McDowell (2007,2010) in part due to its inherent mesh sensitivity; continued
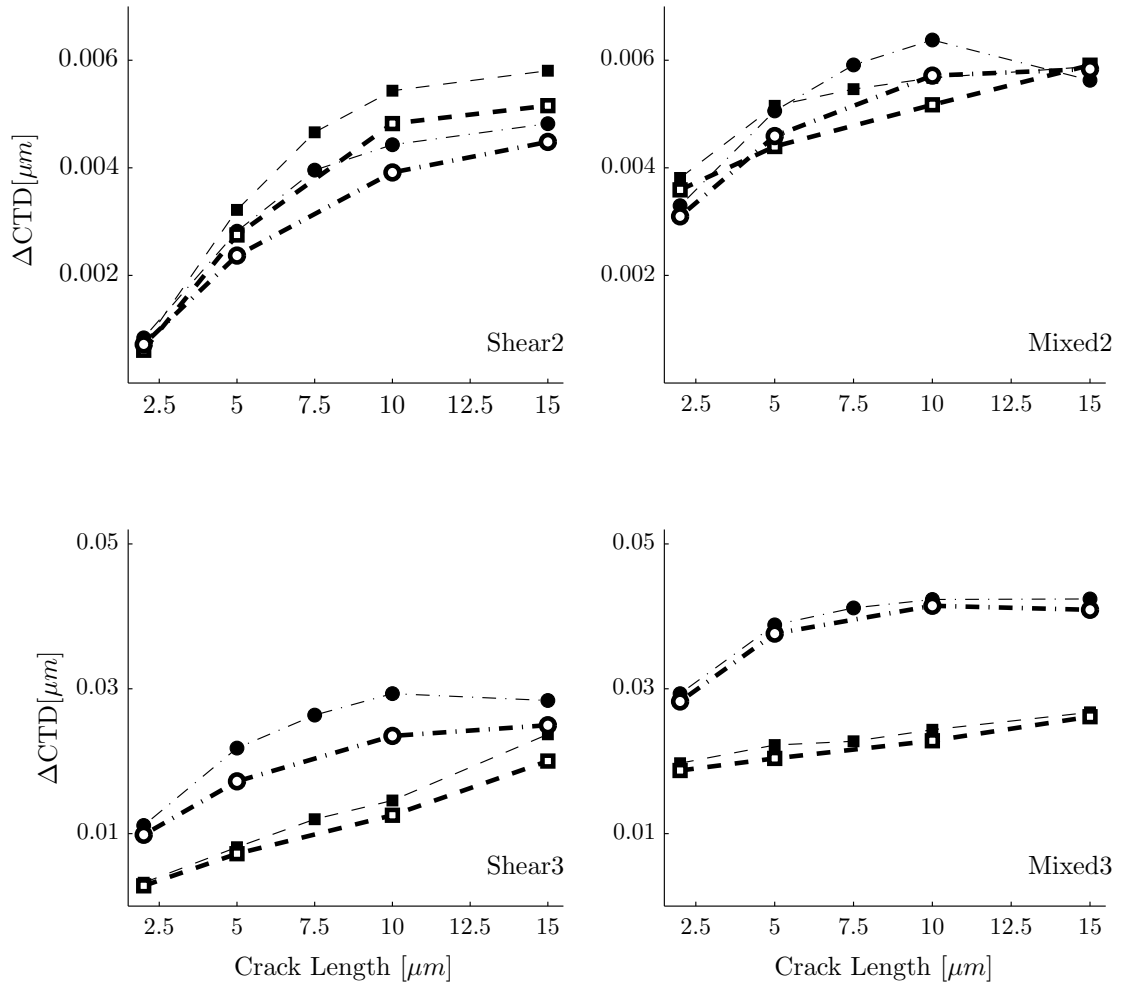
Figure 31: ΔCTD as a function of stationary crack lengths for shear (left column) and mixed mode (right column) loading. Data in solid symbols correspond to homogeneous and $2\mu m$ slip band specimens in Figure 14, while the results for triangular crack tips are shown in hollow symbols and thicker lines. Symbol legend: • 2 μm band, ▪ Homogeneous.
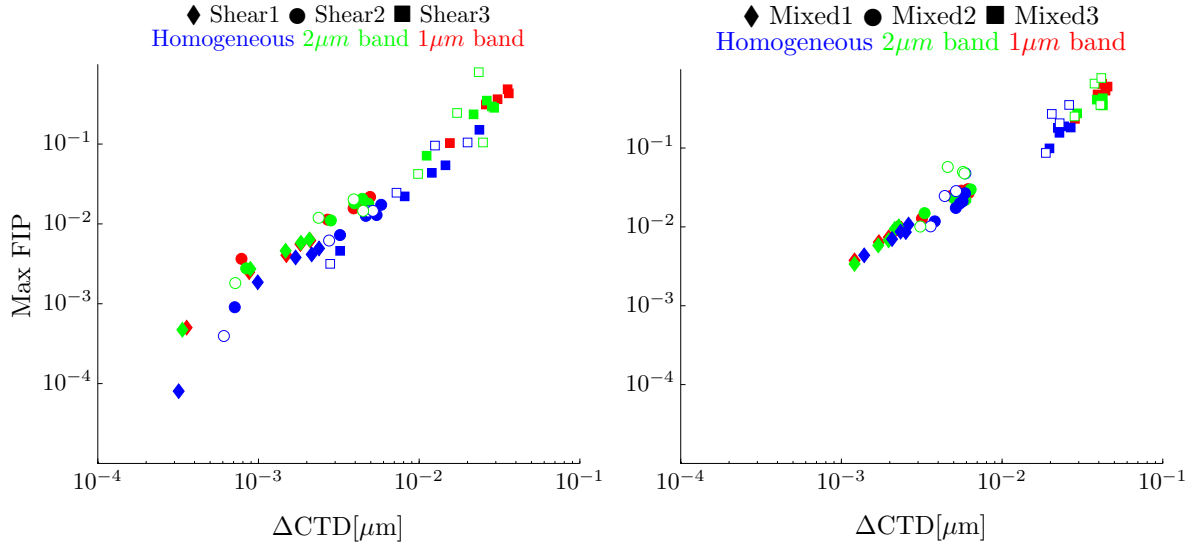
Figure 32: Maximum FIP close to the crack ΔCTD for shear (left) and mixed mode (right) loading. Solid symbols: circular crack tip. Hollow symbols: triangular crack tip.
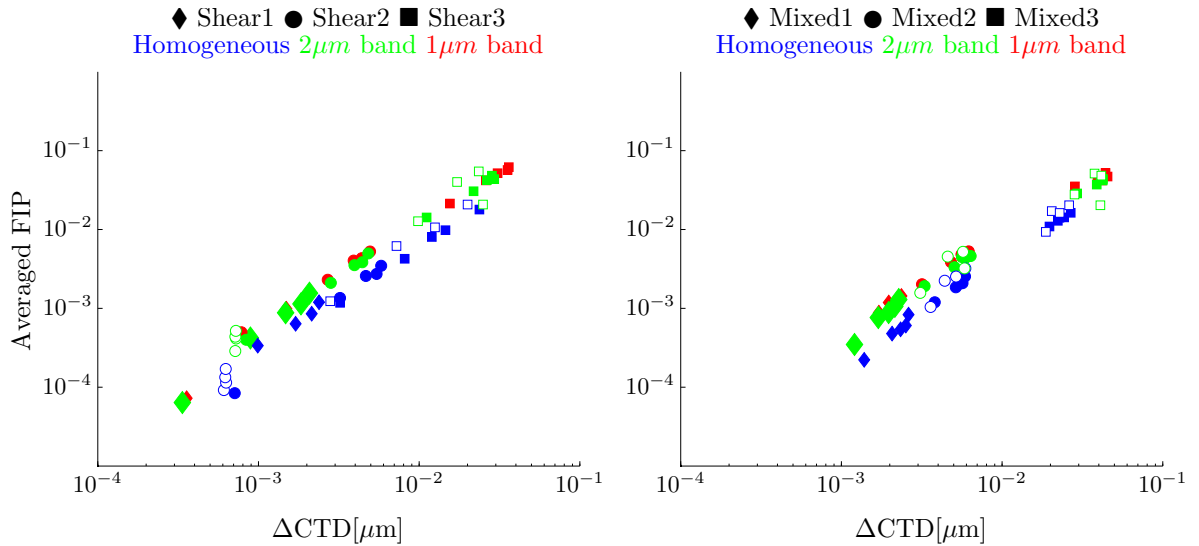
Figure 33: Averaged FIP versus ΔCTD for shear (left) and mixed mode (right) loading. Solid symbols: circular crack tip. Hollow symbols: triangular crack tip.
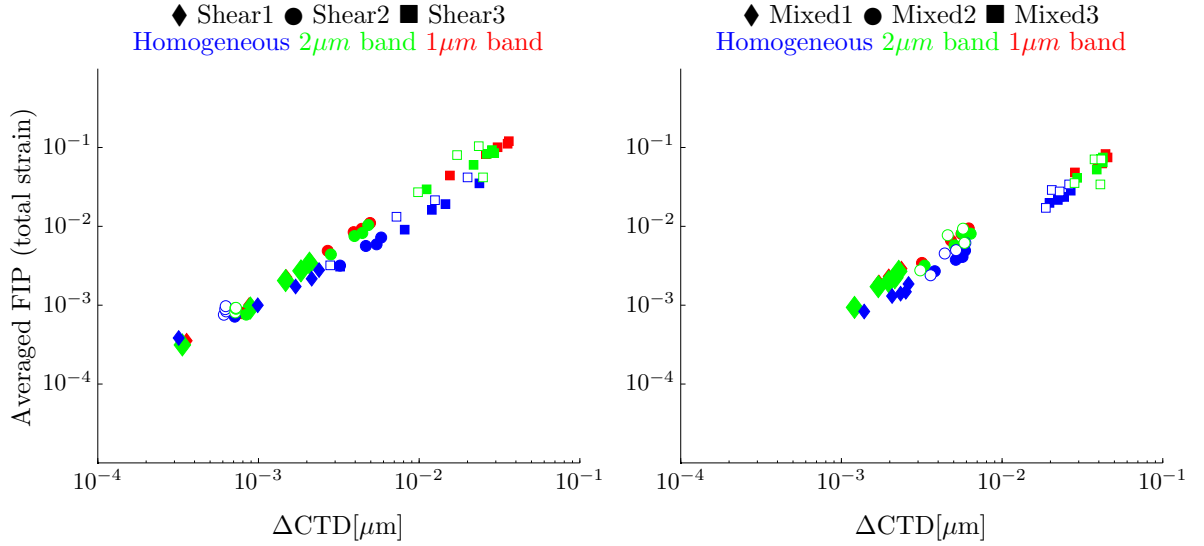
Figure 34: Averaged FIP versus ΔCTD for shear (left) and mixed mode (right) loading. Solid symbols: circular crack tip. Hollow symbols: triangular crack tip.

mesh refinement results in higher maximum FIPs in the proximity of a sharp crack tip. To investigate the effect of mesh refinement on the driving force, the meshes for the circular and triangular tip geometries with crack lengths of $2\mu m$ were refined, approximately doubling the number of elements at the crack tip each time, as shown in Figures 35 and 36. Upon refinement, the number of elements increased from about 3000 to 10000 for the circular crack tip models and from about 2500 to 100000 for the triangular crack tip models. The refinement is not homogeneous but is more intense towards the crack tip, which defines better the strain fields where plastic deformation is the highest; hence, some mesh sensitivity should be expected.

The refinement of models increases the computational time by orders of magnitudes (from hours to weeks); therefore, further refinement would not be applicable in engineering applications with current computation capabilities. Furthermore, the smaller element size is about $4nm$, which is about 10 Burgers vectors, additional refinement could affect the validity of continuum theories. To reduce the computational work, the analysis of refined meshes considered only a nominal peak strain of 0.1% (Shear2 and Mixed2), as described in Table 1. Moreover, the models have homogeneous properties or a $2\mu m$ band parallel to the crack.

15 elements   30 elements   60 elements
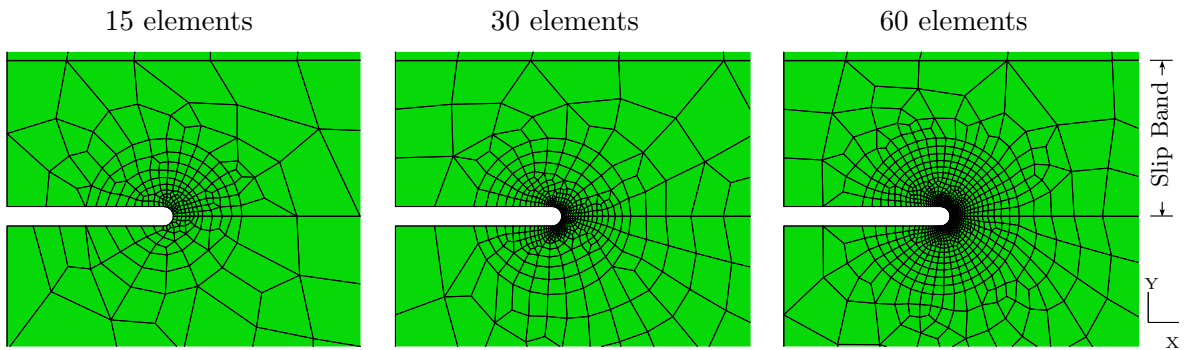
Figure 35: Mesh refinement analysis for the circular crack using 15, 30, 60 elements at the crack tip and a crack length of $2\mu m$.

10 elements   25 elements

40 elements   80 elements
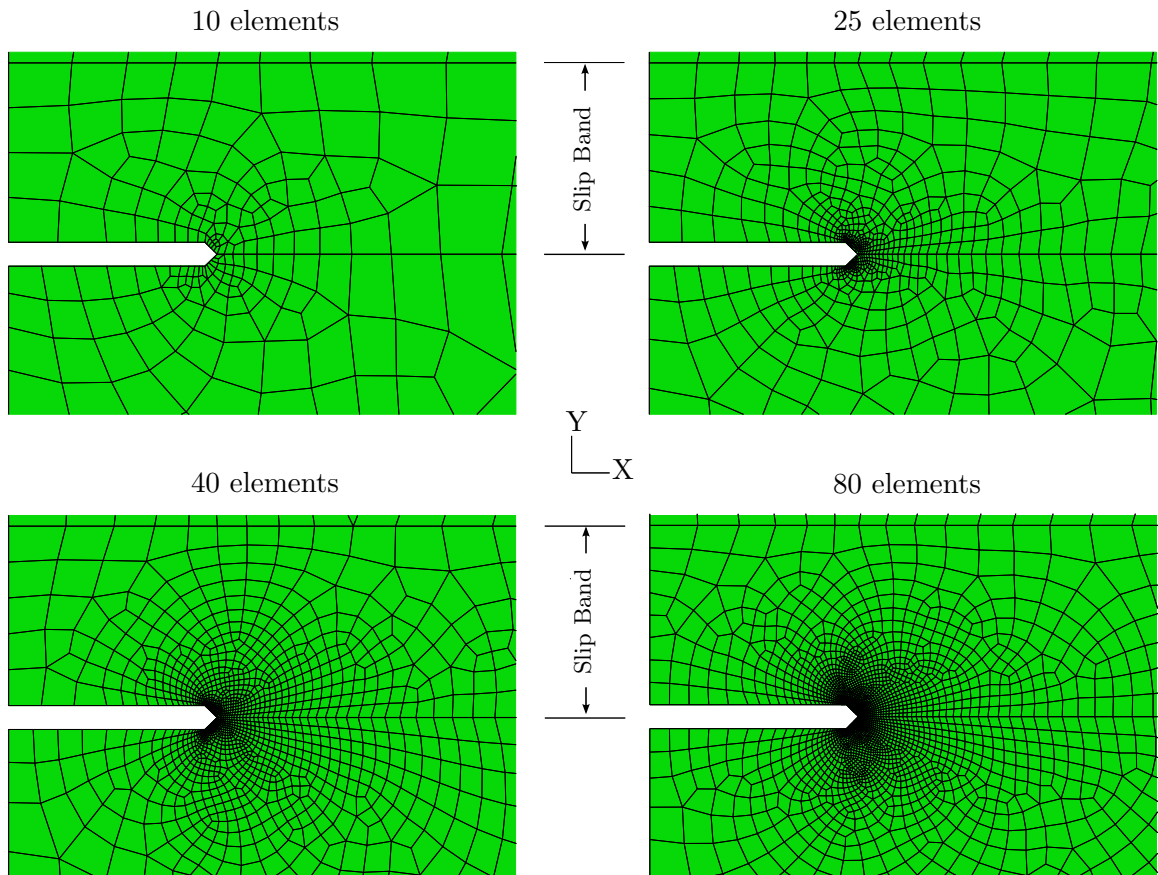
Figure 36: Mesh refinement analyzed for the triangular crack tip with 10, 25, 40 and 80 elements at the crack tip, respectively, and a crack length of $2\mu m$.
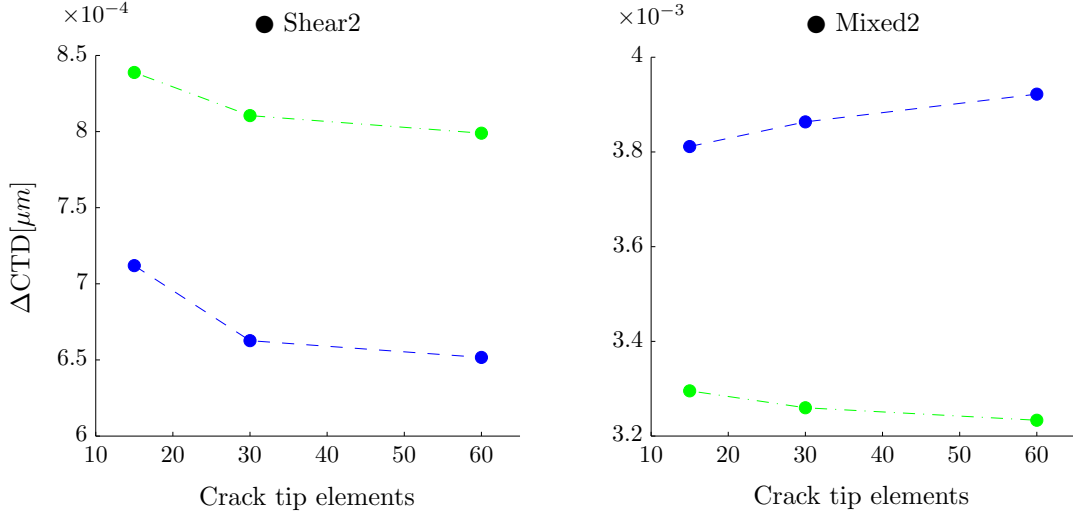
Figure 37: ΔCTD with increasing mesh refinement for Shear2 (left) and Mixed2 (right) loading for the circular crack tip geometry. • Homogeneous, • $2\mu m$ band.

Figure 37 shows that for circular and triangular crack tip geometries and for both loading modes, the value of the ΔCTD appears to be converging with increasing mesh refinement for models with and without slip bands. Furthermore, the influence of a slip band is significant and consistent among all the simulations. Hence, these results again show the lack of influence of the crack tip geometry on the ΔCTD and the possible effect of strain localization on small fatigue crack driving force.

Figures 39 and 40 illustrate the FIP-based driving forces as a function of increasing mesh refinement for the circular and triangular crack tip geometries, respectively. The trends are similar between circular and triangular tip geometries and show that FIPs increase monotonically with increasing refinement. As expected, the maximum FIPs are more sensitive to the refinement, and their values increased between 2 to 4 times, while averaged FIPs exhibit less sensitivity, especially under single slip loading.

Overall, shear loading (with a single, dominant octahedral plane activated) seems to be less affected by the crack tip mesh refinement, especially with regard to the averaged FIPs. The results for mixed mode loading are affected by coarse meshes, but upon refining the mesh the averaged FIPs varies in less than 15% when the number of elements in the model is increased by a factor of 10. Thus, the mesh sensitivity can be mitigated with adequate refinement, given the nonlocal scheme for estimating FIPs.
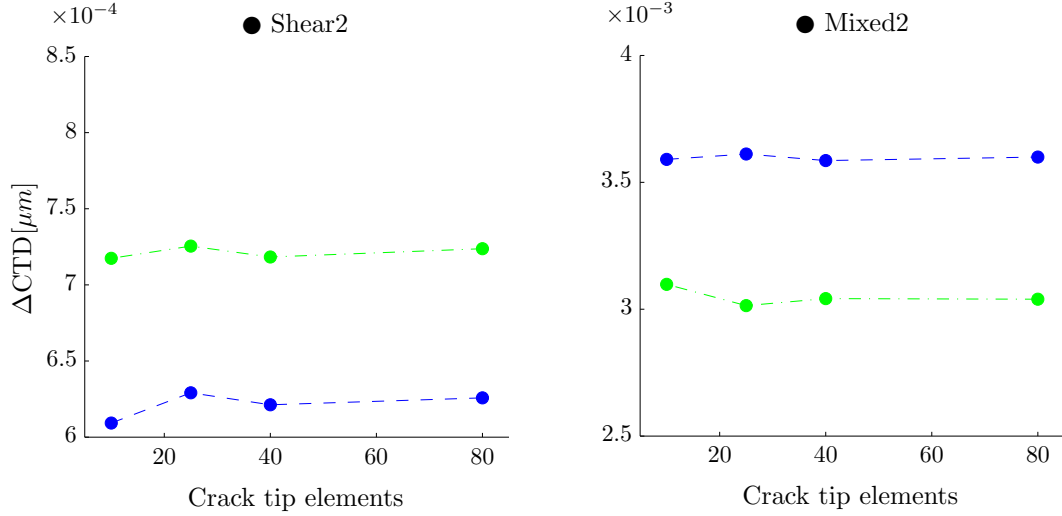
Figure 38: ΔCTD with increasing mesh refinement for Shear1 (left) and Mixed1 (right) loading for the triangular crack tip geometry. • Homogeneous, • $2\mu m$ band.

Maximum FIP values show almost no differences, qualitatively and quantitatively, whether the elastic strains are considered or not (compare Max FIP with Max FIP(t-s)), which suggests that plastic strains dominate. On the contrary, averaged values are more affected if the elastic strains are employed in the calculation of the FIP, particularly for shear mode loading.

When comparing shear and mixed mode loadings, the latter seems to be more affected by mesh refinement. For example, ΔCTD exhibits higher values in homogeneous crystals under Mixed2 conditions, although this trend is not consistently found in FIP calculations. This lack of agreement among simulations is found for circular and triangular crack tips, and may suggest that the averaging volume should include two slip bands, corresponding to the two most active planes.

It is emphasized that the procedure of averaging FIPs is not intended to entirely eliminate mesh sensitivity, but rather to regularize mesh sensitivity compared to the local maximum FIP case and to provide a measure of driving force that is consistently applied (in terms of the averaging volume that corresponds roughly to a crack tip damage process zone). Hence, the fact that such averaged FIPs conform, with higher confidence than pointwise maximum FIPs, to a linear correlation with ΔCTD is a most relevant point of the present study.
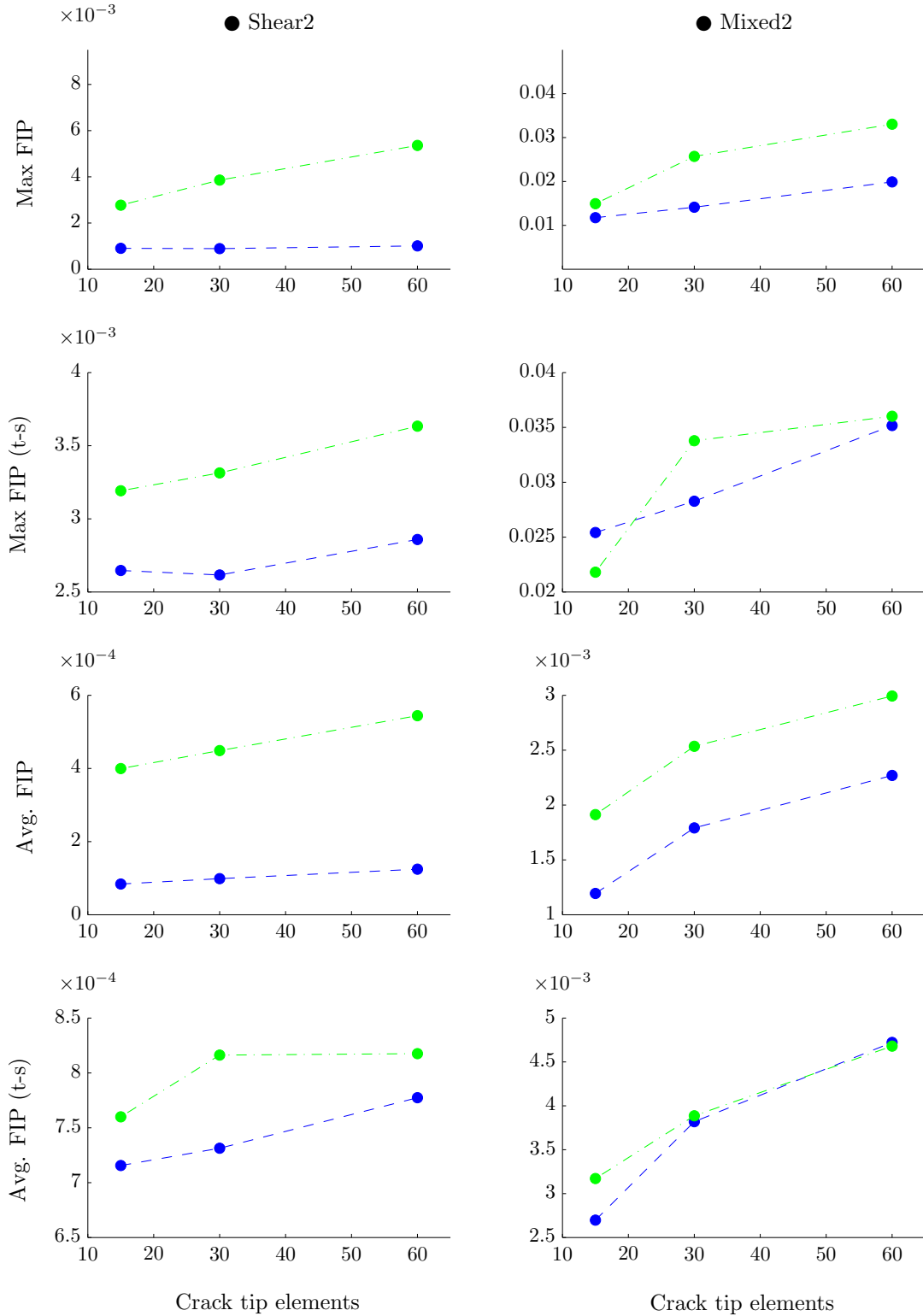
Figure 39: Different FIP as a function of mesh refinement for Shear1 (left) and Mixed1 (right) loading for the circular crack tip geometry. Here, (t-s) refers to total strain calculations. • Homogeneous, • $2\mu m$ band.
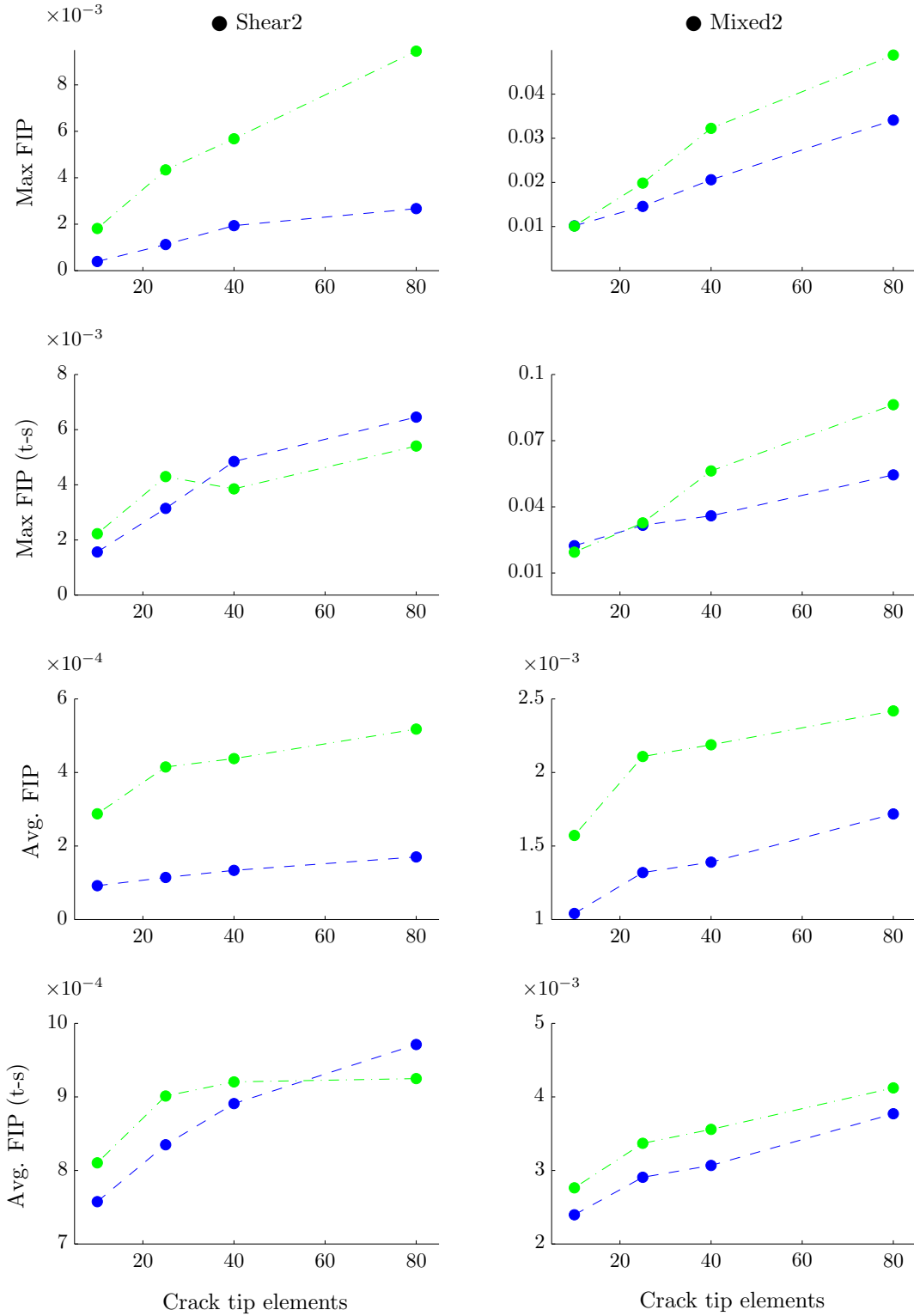
Figure 40: Different FIP as a function of mesh refinement for Shear1 (left) and Mixed1 (right) loading for the triangular crack tip geometry. Here,(t-s) refers to total strain calculations. • Homogeneous, • $2\mu m$ band.

3.5 Preliminary conclusions

This chapter considered the short fatigue crack driving force for cracks in single crystals, with and without idealized slip band heterogeneities, by analyzing the ΔCTD, the Fatemi-Socie FIP, and the correlation between the two for several multiaxial loading conditions. The results support the following conclusions:

- The localization of plastic strain in a slip band can exert significant influence on the ΔCTD, particularly for higher values, and appears to affect the threshold ΔCTD. This observation suggests that fatigue models that do not consider slip band strain localization, when relevant, may lead to inaccurate estimation of the small crack growth driving force.

- The ΔCTD was successfully correlated with the Fatemi-Socie FIP (either maximum or averaged values), suggesting that these measures of the fatigue crack driving force may be interchangeable under certain conditions. Furthermore, the quality of the correlation was not noticeably affected by introducing slip bands (with dimensions much larger that the CTOD), and the crack tip geometry exerted only a secondary influence on the driving forces.

- For values of the constant k in the Fatemi Socie FIP between 0 and 1, the correlation of the averaged FIP and ΔCTD is almost one-to-one (e.g., b $\approx$ 1.1), and the mean square errors present local minima for both remote shear and multiaxial loading conditions. The evolution of the proportionality constant C is also similar between shear and mixed loading, but its value differed for both cases.

- Averaged FIP values showed lower variability and dependence on the mesh refinement than local maximum magnitudes. In particular, averaged FIPs under shear mode loading showed lower dependence and consistent results, which is attributed to the fact that the averaging volume (the slip band) is parallel to the most activate and dominant slip plane. Mixed mode loading may be improved by averaging the FIP along two slip bands, each corresponding to the two most active planes

- Mesh refinement affects slightly the value of computed FIPs to a greater extent than ΔCTD, and the effect is more intense for mixed loading. Averaged FIPs demonstrate reduced sensitivity, but the point is made that the goal is not to entirely eliminate mesh sensitivity, but to achieve a consistency in the estimation of the driving force.

These findings offer fundamental support for simulation of small fatigue cracks using FIPs, since they demonstrate that ΔCTD and Fatemi-Socie based FIPs are correlated measures of the driving force. Furthermore, FIPs can be employed even in cases when strain localization develops, and its correlation to ΔCTD is almost identical to the that in homogeneous materials.

The following chapter will discuss the use of FIPs to evaluate fatigue crack growth rates and later on, in Chapter 5, simulations with single crystals will be revisited employing a different constitutive model and FIP averages along multiple bands.

CHAPTER IV

NUCLEATION AND EARLY GROWTH OF FATIGUE CRACKS

To this point, this research has compared measures of the driving forces for early fatigue crack growth in single crystals, and the results support the use of volume-averaged FIPs in the analysis of Stage I MSC fatigue crack growth. This work continues by correlating FIPs with fatigue life, considering explicitly the simulation of crack growth and the consequent redistribution of stresses and strains. These effects were previously considered by comparing different stationary crack lengths with meshes rendering cracks with predefined paths, but a more general strategy is required for assessing the nucleation of cracks at arbitrary locations in polycrystals.

4.1 Local and mesoscale models for crack growth

4.1.1 FIP formulations

Because multiple FIPs could be formulated to account for different types of failure mechanisms, the choice of a FIP to characterize the driving force for fatigue crack growth depends on the mechanism involved in the fatigue damage process. Since the FIPs are designed to characterize failure mechanisms, they are not necessarily specific for a certain alloy and can be applied to ranges of materials that share the same damage mechanisms.

This work focuses on FCC metals with low to moderate SFE and proposes to quantify the driving force for transgranular failure with a version of the Fatemi-Socie parameter that has been adapted to evaluate the FIP on each octahedral slip plane, i.e.,

$$\text{FIP}^\alpha = \frac{\Delta\gamma_p^\alpha}{2}\left(1 + k\frac{\sigma_n^\alpha}{\sigma_y}\right),\tag{9}$$

where $\Delta\gamma_p^\alpha$ is the cyclic plastic shear strain on slip plane α, σ_n^α is the peak stress normal to the slip plane α, σ_y is the cyclic yield strength, and k is a factor between 0.5 and 1, as proposed by Fatemi-Socie [56]. For each slip plane α, this FIP is assumed to correlate with the ΔCTD. The choice of evaluating FIPs for individual slip planes is supported by the

fact that the early stages of low amplitude fatigue are dominated by strain localization in single slip (Stage I), and fatigue crack growth is usually limited to only a single or a small number of crystallographic planes.

4.1.2 FIP correlation with transgranular fatigue life

A hierarchical (multistage) approach to fatigue modeling partitions the number of cycles to failure (N_f) into several regimes. Although the damage mechanisms involved may depend on the material and loading conditions, N_f has been divided in four regimes [119, 122]: nucleation, MSC, physically small crack (PSC) and long crack growth, i.e.,

$$N_f = N_{nuc} + N_{msc} + N_{psc} + N_{lc} \tag{10}$$

4.1.2.1 Nucleation

The nucleation regime in pure metals has been interpreted in multiple ways, but many authors have defined this regime as the number of cycles required to develop certain geometric features–angle of an intrusion [79], height of the extrusion [42], a specific critical length [150]. Such an interpretation is broad enough to be applicable to engineering alloys, even when cracks nucleate at voids, second phases or foreign particles. For example, when cracks start at inclusions, the nucleation regime includes an incubation period, which refers to the cycles required for debonding or cracking an inclusion from the matrix [75]. Although this period is usually short in comparison with the life of the specimen (particles may debond in one cycle or particles can even be partially debonded during the materials processing), it affects the initial conditions of the subsequent nucleation regime.

The difficulty in defining the nucleation regime lies in differentiating a stress concentrator from a crack. One approach to avoid the ambiguity is to associate each regime with a damage mechanism. Thus, the nucleation regime is defined as a period in which mechanical irreversibility is not characterized by a single well-understood mechanism (i.e., formation of sub-grain dislocation structures, fluxes of vacancies, intrusion formation). These irreversible processes disrupt the initial smooth geometry and create stress concentrators that start emitting dislocations from a region of a few atomic layers (typically about 1 to 100). When

64

the mechanical irreversibility at this hot spot spikes (becomes larger than the mechanical irreversibility of the bulk) due to the lack of reabsorption of defects, it may be considered that a crack embryo has been formed. This lack of reabsorption mechanism will typically dominate fatigue crack growth for the rest of the life, so the transition into the PSC and long crack can be defined based on the size of the irreversible processes, i.e., the fatigue damage process zone. The proposed definition does not intend to be applicable in a general sense more than transgranular fatigue crack nucleation, since different mechanisms may become active during the fatigue life of different materials. For example, in some cases [25] the nucleation mechanism may be dominated by brittle fracture of inclusions rather than plastic slip.

Based on the definition proposed for the nucleation regime, the estimation of this period will require,

1. The determination of the number of cycles to develop a stable mesoscale dislocation structure.

2. The prediction of the evolution of the geometry (i.e., extrusions and intrusions) by considering the influence of point and line defects.

3. The comparison of the local irreversible processes and the prediction that dislocation emission dominates.

The work by Repetto and Ortiz [174] on Cu is among the most detailed models that attempts a formal simulation of the nucleation regime, though the results are disputed by Polak and Sauzay [169]. Indeed, the mechanisms involved in the nucleation of cracks are so complex that today no models are capable of reproducing the physics of the process, not even for simple alloys such as Cu. Furthermore, the models based on energy consideration ([142, 180]) are approximate and arguable solutions, applicable to specific materials and dislocation structures. Hence, the number of cycles required to nucleate a crack in the bulks of a grain may only be estimated using correlations with experimental data. For example, one relation is the power-law based on the simplified dislocation model by Tanaka

and Mura [196],i.e.,

$$N_{nuc} = \frac{\alpha_g}{d_{gr}}(\text{FIP}^\alpha)^{-2}, \tag{11}$$

which was further extended by Chan [36] and Shenoy [185]. Here, d_{gr} is a length scale representative of the microstructure that could be the size of the first grain to crack (typically the largest grain at or near the surface), the size of an inclusion or some other defect; α_g is a measure of the mechanical irreversibility of dislocation activity at surface intrusions, precipitate surfaces or bulk of grains and depends strongly on the environment.

Equation (11) has been extensively employed in fatigue modeling [185, 4] and has been supported by experimental evidence [79, 139]. For example, Hunsche and Neumann [79] performed experiments using single crystals and concluded that the life to nucleate the crack was proportional to the inverse of the square of the plastic shear strain accumulated in PSBs. Moreover, since the nucleation regime is dramatically affected by several factors such as the environment, the loading conditions or the surface roughness, Equation (11) can be reformulated to include an explicit dependence of these effects [83].

However, Equation (11) does not provide the value of the crack length by the end of the nucleation regime, suggesting that the change into MSC regime may occur at some point inside the grain. Hence, the number of cycles required to crack the first grain is formed by the nucleation regime plus the growth up to the GB. Furthermore, the physical mechanisms in the nucleation process (e.g., crack growth due to point defect coalescence) may reappear as dominant over dislocation emission in cases where the crack crosses into another grain and does not have enough driving force to transmit or emit new dislocations across the boundary. In such a situation, the crack would need to nucleate again at the new grain. The likelihood of this scenario decreases after a few grains have been cracked, since the average driving force tends to increase.

4.1.2.2   MSC regime

Although the nucleation period may last for thousands of cycles, depending on the stress amplitude, in typical HCF applications a significant portion of the life is spent in very early stages of crack growth. Following the nucleation period, the crack growth rate is assumed

to be controlled by the mechanical irreversibility of dislocations emitted from an embryonic crack. Indeed, it is noticeable that most vacancies models concern only the localization of a crack and not the extension, which was further reinforced in a personal communication with Professor Polak, who stated that "in crack propagation the role of vacancies is probably not as important as in crack nucleation [166]."

The MSC crack growth rate is proportional to the number of dislocation emitted and not annihilated after a cycle, or equivalently the ΔCTD [122], i.e.,

$$\frac{da}{dN}\bigg|_{msc} = \phi\langle\Delta\text{CTD} - \Delta\text{CTD}_{\text{th}}\rangle, \tag{12}$$

where $\Delta\text{CTD}_{\text{th}}$ is the threshold ΔCTD that recognizes a minimum required driving force for dislocation emission, and the Macaulay brackets satisfy that $\langle a\rangle = a$ if $a > 0$ or $\langle a\rangle = 0$ if $a \leq 0$.

The proportionality factor ϕ in Equation (12) measures the mechanical irreversibility of the dislocation activity in the process zone and depends on the environment, the loading amplitude, and the temperature among many factors. The quantification of mechanical irreversibility has been attempted using a variety of measurements that usually result in values on the order of 0.01 to 0.1 [187]. Hence, about 1% to 10% of the dislocations created at the crack tip remain after a full loading cycle.

Although it might be desirable to explicitly calculate and track ΔCTD values during simulations, the evaluation of the ΔCTD would require a detailed representation of the geometry of cracks. FIPs can more efficiently take the place of ΔCTD in Equation (12), as shown in Chapter 3. Since plastic deformation in the MSC regime is characterized by slip on only a few activated planes, the transgranular crack growth rate within a grain is proposed to follow

$$\frac{da}{dN}\bigg|_{msc}^{\alpha} = \phi\langle A(\beta_i)\text{FIP}^{\alpha} - \Delta\text{CTD}_{\text{th}}\rangle, \tag{13}$$

in which A is a scaling constant that may depend on microstructural attributes, referred to as β_i, and $\Delta\text{CTD}_{\text{th}}$ represents a threshold below which no dislocations are emitted from a crack, i.e., the Burgers vector. Notice that this formulation proposes that crack growth rates differ among slip planes.

When the cyclic plastic zone ahead of the crack is large enough to engulf many grains, and EPFM theory becomes valid, the crack has reached the PSC regime. For such a regime, the transgranular crack growth rate is proposed to follow

$$\frac{da}{dN}\bigg|_{psc} = \tilde{\phi}\left\langle \tilde{A}(\beta_i)\left(\frac{\Delta\sigma}{S_u}\right)^{m_1} - b \right\rangle, \tag{14}$$

which is based on the work of Alexandre et al. [4]. $\tilde{A}$ and $\tilde{\phi}$ are constants analogous to in Equation 13. Equation 14 is an homogenized averaged crack growth rate from the cyclic elasto-plastic process zone.

The long crack growth rate can be characterized, for R=0, by the ΔK via the Paris Law [6], i.e.,

$$\frac{da}{dN}\bigg|_{lc} = C\Delta K^m = C(Y\sigma\sqrt{\pi a})^m, \tag{15}$$

in which C and $m \neq 1$ are material constants, Y depends on the geometry, and σ is the far field stress. Equation (15) can integrated for the specific geometry of interest between a transition crack length to the long crack regime and the maximum allowed crack length or critical crack length. Furthermore, the choice of material constants in this formulation reflects the type of failure mode (transgranular vs. intergranular). Since the PSC and the long crack regimes can usually be addressed successfully using continuum homogenized theories (EPFM and LEFM), this investigation focuses on the MSC regime.

4.1.3   Intergranular failure

The literature that deals with driving forces for MSC intergranular crack growth is not extensive, but a few authors have characterized the far field driving force by means of ΔK [86], ΔJ and C* [155] depending on the loading conditions. Thus, the relation between ΔJ and the Fatemi-Socie parameter found by Berard and McDowell [120] justifies the use of an FIP$^\alpha$ based on critical plane theories, but in the case of intergranular decohesion, the orientation of the GBs plays a role in determining the local driving force if a Zener-Stroh mechanism is assumed.

The driving force for intergranular Zener-Stroh decohesion depends on the accumulated directional plastic strain at a GB and the stress normal to that boundary. In the spirit of the energy release rate formulated by Fan [53], this work proposes a FIP_{int} that is the result of multiplying two factors: the first factor relating to the number of dislocations impinging on the GB and the second to the stress normal to the boundary, i.e.,

$$\mathrm{FIP}_{\mathrm{int}} = \left[\sum_{\alpha} \left| \frac{\gamma_p^{\alpha}}{2} \left(1 + k_{tran} \frac{\sigma_n^{\alpha}}{\sigma_y} \right) \right| \right]^{\lambda_1} \left(\frac{\sigma_n^{GB}}{\sigma_y} \right)^{\lambda_2}, \tag{16}$$

in which λ_1 and λ_2 are material constants and σ_n^{GB} is the peak stress normal to the GB. The first factor on this equation is similar to FIP^{α} except that the directional plastic shear strain and not the range of plastic shear strain, is introduced.

Even though cracks may nucleate intergranularly for low loading frequencies or high temperatures [154], this research focuses on the MSC regime and accounts for the transgranular and intergranular failure transition after cracks have nucleated. Then, it is assumed that cracks can only nucleate in a transgranular manner, and subsequently the intergranuar and transgranular failure modes are assessed. Indeed, GB nucleation is more prevalent at higher strains [38], which may be achieved at the crack tip of longer cracks. To estimate the intergranular crack growth of MSCs, this study employs an expression similar to that proposed by Miller et al. [132], i.e.,

$$\frac{da}{dN}\Big|_{msc}^{inter} = \phi_{int} exp \left\{ -\frac{Q - B\langle PS \rangle}{RT} \right\} \Delta t^{(1/2 - \xi)} \mathrm{FIP}_{\mathrm{int}}, \tag{17}$$

This formulation accounts for the fact that the diffusion of foreign atoms controls intergranular cracking, as proposed in [132]. Δt is a time range representing the portion of the cycling period at high strain and stress, Q is the activation energy, and PS is the maximum principal stress; ξ and B are assumed to be constants that may depend on the type of failure mechanism.

4.2 Mesoscopic fatigue life prediction

To this point, this chapter has introduced local measurements of the driving force for small fatigue crack growth based on the physics at the grain scale. These measurements are valid,

69

theoretically, up to the limit in which the continuum representation is valid (typically on the order of tens of Burgers vectors [11]). However, the study of realistic microstructures demands the prediction of the small crack driving forces over tens or hundreds of microns and thousands of cycles, which limits the achievable refinement in the crack growth rates calculations, even when using hundred of processors in computer clusters. Hence, a feasible mesoscale scheme is required; it should be capable of extrapolating the response of the material over distance and time. The extrapolation must be dual, in the sense that it needs to predict the cycles required to extend a crack and the updated driving force on the crack without applying hundreds of loading cycles or detailed cycle-by-cycle evaluation of stress redistribution.

4.2.1 Cycle-averaged FIPs

Although a cycle-by-cycle analysis would be desirable, it is currently computationally unfeasible to reach hundreds of thousands of loading cycles using crystal plasticity constitutive models at a scale of hundreds of grains. These competing demands can be addressed by assuming that, except for the FIP, the magnitudes in Equation (13) do not not depend on the number of cycles or the crack length. This simplification requires that values of β_i be approximately constant, which means that the microstructure and the strain localization mechanisms should not change significantly over the life (e.g., no significant GB shift, no drastic rotation of the crystal lattice within the grain, and no growth of voids, etc). Furthermore, since the irreversible processes at the crack tip depend on the stress that changes constantly over the cycle, the irreversible factor should average this effect by introducing a dependence on the shape of the loading cycle. This requirement implies that the mechanical irreversibility varies for different shapes of the loading cycle, but it does not change cycle after cycle.

The mesoscale model should further assume that the FIPs calculated after a few cycles (typically three to ten loading cycles) can represent the effect of the microstructure on the mean FIP over thousands of cycles and can correlate with life estimations for a grain. Such a simplification can be justified, in the small crack regime dominated by single slip, by the

following arguments:

1. Winter [213] first proposed that the accumulated plastic strain in Cu slip bands was constant. Although this assumption was later shown not to be accurate [17], it is still a good approximation for individual slip bands (not macro PSBs formed by multiple slip bands [98]). Indeed, once a grain localizes plastic deformation and nucleates a crack, dislocation structures within the grain do not change significantly, even when a crack is propagating along the grain [88].

2. As discussed in section 2.1.3.1, several authors [167, 212] have characterized that the stress amplitude (in plastic strain-controlled tests) remains almost constant during a significant portion of the fatigue life of single crystals under HCF. This can also be assumed to apply to individual grains [168, 137, 104] as shown in Figure 4. Note that some investigators [212] have argued that some low SFE single crystals may not have a saturation stress when cycled at high plastic strain amplitude; in these metals, the simplifications proposed in this research may be applied to low plastic strain cycling.

Thus, once plastic deformation is localized, stress fields are almost constant, and plastic shear strains evolve slowly, as long as the specimen geometry remains constant. However, when a crack grows inside a grain, the redistribution of stress would modify the crack driving force, or equivalently, the current FIP value. To account for this effect, this work seeks to develop simpler models that do not require damage to be introduced at a microscopic scale (element-by-element), but at a mesoscopic scale (grain-by-grain). This objective is based on the hypothesis that the evolution of the driving force on each grain is proportional to the initial averaged FIP (i.e., before cracking), and it follows some law dependent on the crack length (a). Such a function may depend on the microstructure, but an average behavior can be explored by comparing the multiple crack growth laws proposed in the literature. For example, Hobson and coworkers [73, 74] proposed that the crack growth rate for small cracks followed the equation

$$\frac{da}{dN} = C(d-a)^{1-\alpha}a^{\alpha} \tag{18}$$

71

in which d is a microstructural length scale, and C and α are experimental constants. In this equation, the crack growth rate has two competing factors, one that decreases the driving force when the crack approaches the microstuctural barrier $(d - a)$, and another that dominates for larger crack lengths, (a^α). More recently, Miller [130] worked extensively on predicting the crack growth rates, which he summarized as three different regimes, i.e.,

$$\frac{da}{dN} = A\Delta\gamma^\alpha(d - a) \tag{19}$$

$$\frac{da}{dN} = B\Delta\gamma^\beta a - D \tag{20}$$

$$\frac{da}{dN} = C(\Delta\gamma\sqrt{\pi a})^n \tag{21}$$

Interestingly, for the first regime Equation (19), Miller replaced the factor (a^α) in Hobson's model with the range of plastic deformation $(\Delta\gamma)$, which is involved in all the regimes. These equations resemble the fracture mechanics approach, which has a factor representing the applied loading and a factor involving the crack length. Indeed, similar approaches have been developed for small cracks based on the applied stress and not strains. For example, Nisitani et al.,[152] and many Japanese researchers have employed small crack growth laws of the form,

$$\frac{da}{dN} = C\sigma_a^n a \tag{22}$$

Hence, this investigation proposes that a $\text{FIP}^\alpha_\text{meso}$ can be formulated as the product of a magnitude that represents the initial applied loading and a function that predicts the influence extending the crack i.e.,

$$\text{FIP}^\alpha_\text{meso} = \text{FIP}^\alpha_o \cdot g(a) \tag{23}$$

Here, $g(a)$ carries the influence of the crack length and is valid over a limited mesoscale domain and FIP^α_o represents the plastic deformation before cracking. The $\text{FIP}^\alpha_\text{meso}$ can be understood as a measure of the driving force for the Microstructural Fracture Mechanics proposed by Miller [130]. In comparison, for LEFM the FIP^α_o simply becomes the far field stress and $g(a)$ is equivalent to $\sqrt{\pi a}$, which is valid for any crack length.

In the case of MSCs, it is hypothesized that the $\text{FIP}^\alpha_\text{meso}$ evolution can be predicted within a grain using a single type of law, such as Equation (23). The individual evolution in

each grain are summed up to contribute to a macroscopic crack growth rate that, depending on the microstructure, may present an evolution different from Equation (23). Consequently, $g(a)$ represents the crack length dependence of the crack growth within the grain, and it should follow some decreasing driving force law, similar to the first regime proposed by Miller (Equation (19)). Furthermore, the crack length should be taken as the normalized crack length within a grain i (a_i, $0 \leq a_i \leq 1$), and not the entire length of the crack. The dependence of the FIP with the total crack length is captured by the FIP_o^α, whose mean statistical value among grains should increase as the cracks grow.

4.2.2 Mesoscale averaging volumes for FIPs

To regularize numerically the FEM discretization and also to represent the physical scale of the process zone for crack formation, the FIPs calculated at each integration point in the FEM need to be averaged over mesoscale volumes. To a certain degree, the selection of averaging domains for estimating FIPs is arbitrary and is related to the level of computational work, but the physics of the problem ultimately guides the choice. For example, one natural choice is to average transgranular FIPs over the entire volume of grains [185], which results in a coarse and non-crystallographic measure of the driving force, or over a regular fraction of the grain volume [222]. Other authors have proposed one-dimensional domains connecting integration points to average the FIPs [75].

Due to the intrinsic planar slip of low to medium SFE metals and precipitate strengthened alloys, transgranular failure occurs along bands parallel to slip planes with little diffusion of damage normal to the slip planes. This scenario resembles the damage accumulated along slip bands due to dislocation substructures in pure metals [168, 138] or to localized shearing of γ' precipitates in superalloys [216, 189]. Furthermore, as explained in Chapter 2, several theoretical models [107, 196, 147] have described the fatigue crack nucleation process evaluating the plastic deformation along favorably oriented planes or bands. Thus, this investigation will average FIPs representing transgranular failure on bands of width W parallel to slip directions across an entire grain, as depicted in Figure 41. From a computational standpoint, the value of W should be at least the size of the finite element; based

on the physics of the problem, W should be at least the spacing between slip bands, which has been described by several empirical laws summarized in [5]. An additional feature of averaging along bands is that it naturally introduces a sub-grain length scale for localized deformation, even when the constitutive equation is not capable of self-localizing plastic strain.
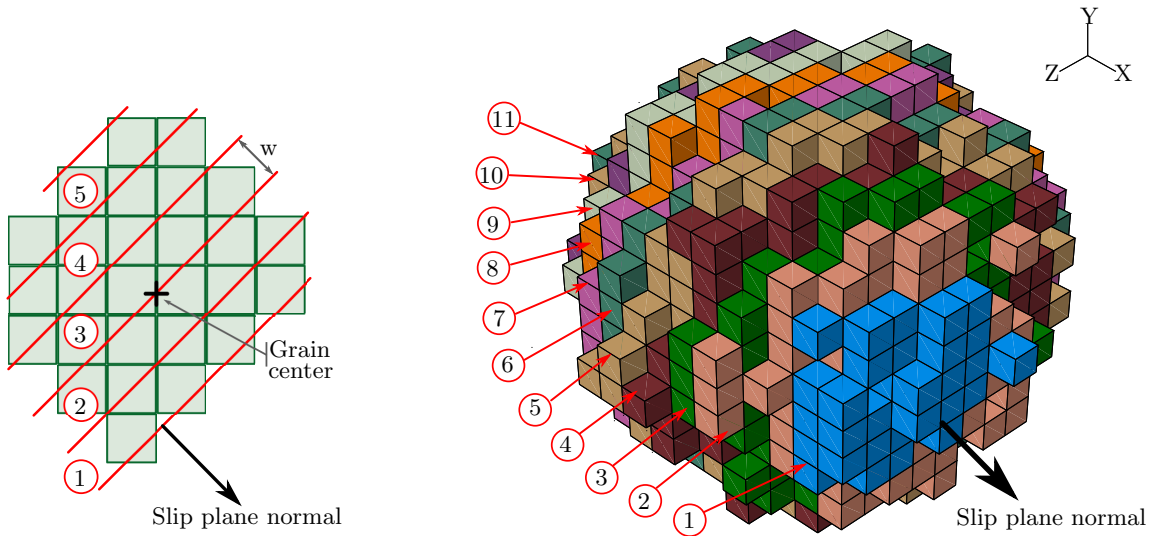
Figure 41: Schematic representation of the bands in which FIPs are averaged to estimate transgranular failure. The figure on the left represents the assignment of each element of the mesh to a band of width W. On the right, the implementation in a FEM model is presented. The bands in one grain are highlighted with different colors and numbers for one slip plane normal.

Intergranular decohesion depends on the plastic deformation impinging on the GB and on the misorientation of the grains; thus, a natural choice is to calculate the driving force for intergranular failure on every GB sector shared by two grains. Regarding FEM mesh, this research proposes to estimate the intergranular fatigue life in two sets of neighboring elements separately. Each set represents the GB sector on each on the neighboring grains, and it is composed by the first neighbor elements to the GB, as highlighted with a more intense color in Figure 42.

Since the nature of the Zener mechanism allows nucleating multiple cracks on the same GB sector (each due to the impingement of a different slip band as shown in Figure 8) that afterwards grow and interconnect, the life of each element on a GB is computed using the
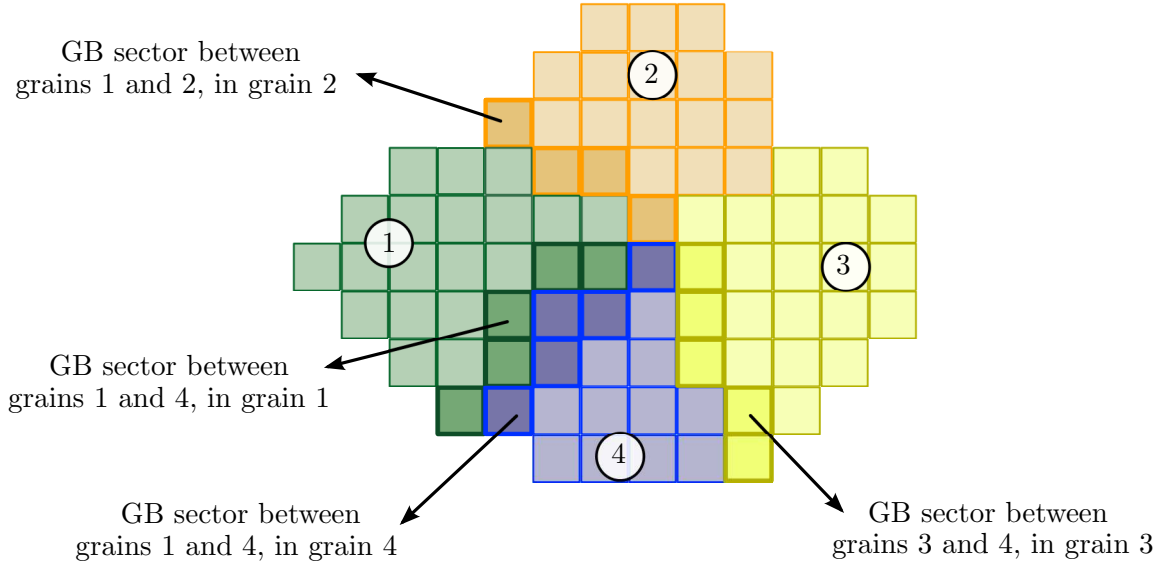
Figure 42: 2D representation of a mesh with numbered grains and some of the GB sectors highlighted with a more intense color. For each element in the GB sector, the FIP_{int} and intergranular life are computed, and the latter is averaged on each of two GB sectors in each grain independently.

FIP_{int}. Then, the mean life of each GB sector results from the average value of the life of the elements within. These averages are computed on both GB sectors independently, and the minimum of those averages defines the intergranular fatigue life of the GB. This calculation is slightly different from that used for transgranular failure in which the FIPs are averaged before calculating the life because the Zener-Stroh mechanism has a "distributed character" rather than a clear crack tip localization.

4.2.3 Grain-by-grain fatigue life estimation

Since this research focuses on the interaction between small fatigue cracks and the microstructure at a mesoscale level, the minimum length scale employed to evaluate the number of cycles to failure is related to the grain size; therefore, the mesoscale scheme developed in this thesis will estimate the fatigue life considering the bands grains as the minimum units that fail in transgranular crack growth. Although the transition from nucleation to MSC regime may occur while the crack lies inside a grain, the model will assume that the nucleation regime extends until the first grain has cracked, and the possible crack growth direction inside a grain is a straight path along any of the bands defined for averaging the

FIP. Since each grain has many bands over which the FIP is averaged, the number of cycles required to nucleate a crack is estimated for each band; the minimum life among all bands defines the life to nucleate a crack in a grain and the direction of cracking. Similarly, the comparison among multiple grains defines in which grain a crack will nucleate first.

After determining the nucleation life, the model computes the MSC life for bands that are in contact with the crack, and the crack extends along the band with the minimum MSC life. The condition of being in contact means that a band has at least one element that is within one element of distance to the crack, which will also be referred as a band neighboring the crack. Since the MSC regime considers only bands that neighbor the crack, the number of bands involved in the MSC life assessment increases with the perimeter of the crack. Furthermore, the number of bands assessed in the MSC regime is significantly smaller than that in the nucleation regime, which considers all the bands in the model.

Another caveat of the mesoscale model is that Equations (13) and (17) define the MSC crack growth rates and not a value for the MSC life of a grain; therefore, these equations need to be integrated to estimate the MSC life of each grain. In order to integrate analytically the crack growth rates, an explicit dependence of the FIP_{meso} on the crack length within each grain is necessary. This situation will be reviewed in the following chapters, where the function $g(a)$ in Equation (23) is derived for a specific material.

4.3 *Crack growth and stress redistribution*

Once a fatigue crack has grown over a grain the stress intensification at the crack tip and tortuous path of the crack may influence the driving force. To account for such an effect, this section develops a theoretical methodology to extend the crack in FEM simulations. Myriad strategies available in the literature account for crack growth stress redistribution— continuous, weakly and strongly discontinuous kinematic fields—with an ample range of complexity in the FEM implementation: embedded cracks, cohesive elements, and remeshing [206, 84, 85], etc. Among those methodologies, the most appropriate should,

- minimize computational overhead,

- represent the decohesion of small cracks,

- be applicable to any crack growth path (either intergranular or transgranular failure), and

- be able to represent crack closure.

4.3.1 Traditional approached to simulate crack growth

One possibility to simulate crack growth that has been extensively employed in fracture mechanics modeling (available in ABAQUS) is an enriched finite element method (e.g., XFEM). Such a technique usually enriches the FEM formulation with discontinuity-based functions that are typically compatible with the elastic singular fields of LEFM; for example, the enriched displacement approximation may have the following interelement interpolation [124, 67]:

$$\mathbf{u}^{XFEM}(\mathbf{x}) = \sum_i N_i(\mathbf{x})\mathbf{u}_i + \sum_i N_i(\mathbf{x})H(\mathbf{x})\mathbf{a}_i + \sum_i N_i(\mathbf{x})\sum_{\alpha=1}^{4}\left[\Phi_\alpha(\mathbf{x})\mathbf{b}_i\right] \qquad (24)$$

Here, $\mathbf{u}^{XFEM}$ is the enriched displacement vector at position $\mathbf{x}$, $N_i(\mathbf{x})$ is the nodal shape function, $H(\mathbf{x})$ is the Heaviside function that represents the opening of a crack, Φ_α are the asymptotic functions that resemble LEFM crack tip displacement fields, and a_i and b_i are the extra degrees of freedom associated with the Heaviside and asymptotic functions, respectively. The standard enriched formulation can successfully recreate the strain/stress fields surrounding cracks that result from elastic singularity-based models, but its application to small fatigue crack simulations is arguable and inaccurate, since small cracks do not present the singularity fields corresponding to LEFM. Although it would be conceptually possible to formulate "small crack enrichment functions," such a formulation is not known to have been proposed and verified. Moreover, enrichment functions aimed at addressing small cracks would be greatly complicated by the need to consider nonlocality, lack of self-similarity, and crystallographic slip anisotropy. There is no clear path in this direction, which would be largely expensive for cycle by cycle crack extension.

The cohesive element model is a feasible alternative that does not assume a predefined strain field, and thus can be applied to the small crack problem [136]. Multiple cohesive

element models are available in ABAQUS, but they require the definition of the cohesive region in the mesh. Thus, if the crack path is not predefined, either the entire volume needs to be filled with cohesive elements or remeshing is required at each increment of crack length. Either case increases the computational burden substantially, especially the latter one. One variation is to employ embedded cohesive elements [156, 157], but this type of model requires the modification of the finite element formulation and is not amenable with standard FE codes. Moreover, the orientation of the cohesive zone is predefined, so without remeshing this model does not allow reorientation along a specific direction (e.g., crystallographic plane). Finally, cohesive zone models can suffer from non-regularized localization of plastic deformation, which adds complexities without clear solution.

A simpler method that is also available in ABAQUS is to remove the element from the calculation; however, this technique does not allow the resistance to be reaffirmed under crack closure. An alternative for the simulation of fields redistribution due to crack growth is the implementation of a damage mechanics model that is able to degrade the elastic stiffness tensor. Furthermore, the elastic stiffness can be reaffirmed to simulate the tension-compression asymmetry caused by crack closure. Within the mesoscale framework, the crack extends on a grain-by-grain basis by decreasing the elastic stiffness tensor of the elements on a band along the entire cross section of the grain. After degrading the stiffness in a new grain, a few cycles should be applied to update the FIPs before predicting to which grain the crack will extend to.

The degradation of stiffness only affects the crystal plasticity algorithm in the calculation of the stress tensor, which makes use of the elastic stiffness tensor. Indeed, this calculation is performed after the kinematic evolution is solved (i.e., elastic and plastic strains). Therefore, the change of the elastic stiffness tensor does not interfere with the core of the crystal plasticity algorithm, and it should not affect the convergence of the plastic components. Hence, the elastic-damage approach strategy is chosen to account for crack growth, as developed in the following subsections.

4.3.2 Overview of damage mechanics

By the end of 1950's, Kachanov's work on creep gave birth to damage mechanics as a discipline; this soon became a volume-averaged alternative to the individual dominant crack character of fracture mechanics. Indeed, both theories attempt to describe the behavior of solids in the presence of defects with different approaches, and the choice of either depends on the application, and whether a single dominant crack is expected.

Several damage mechanics formulations rely on the assumption that a fictitious un-damaged configuration (Figure 43 c) evolves due to a fictitious deformation gradient [144]. Figure 43 represents the evolution of an initially undamaged bar (a) that becomes damaged with a reduced effective cross-section after being loaded uniaxially (b). This damaged state is assumed to be mechanically equivalent to a fictitious undamaged bar (c) subject to the applied load t with the cross-sectional area $\bar{A}$, called the fictitious undamaged state, which involves a non-zero damage variable D.
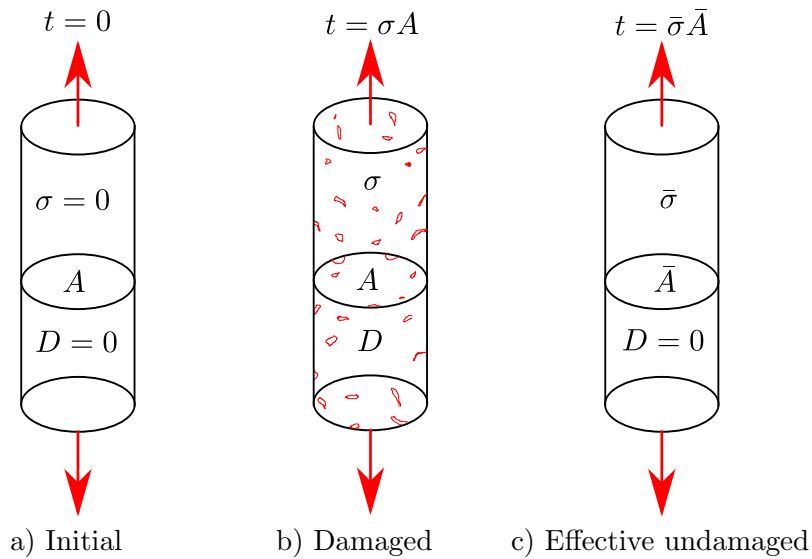
Figure 43: Damage in a bar under uniaxial tension. a) to c) represents the three possible stages.

The basis of damage mechanics can be understood with a simple thought exercise consisting of a system of similar parallel bars loaded in tension, as shown in Figure 44. Initially, all the bars sustain some stress, and the total applied force is distributed (Figure 44 a). Thus, the nominal stress on each bar is,
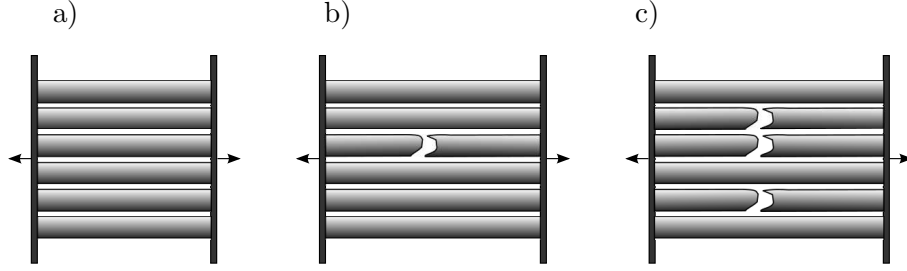
Figure 44: Parallel bars model. The number of broken bars increases with increasing applied force (a to c).

$$\sigma = \frac{P}{A}.$$
(25)

Here, P is the applied force, and A is the total load-carrying area (i.e., the number of bars times the cross-section). Upon an increment in the load, some bars may break, and the resulting force redistribution due to a decrease in area $(\bar{A})$ will increase the stress on the remaining bars, $\bar{\sigma}$. However, if the stress is calculated without an update in the load-carrying area, there will be no change in the stress. Thus, it can be stated that

$$P = \bar{\sigma}\bar{A} = \sigma A,$$
(26)

in which $\bar{\sigma}$ and $\bar{A}$ are considered as "effective" quantities, different from the nominal quantities. Furthermore, by assuming that each bar has elastic deformation up to a perfectly brittle failure, the effective stress satisfies

$$\bar{\sigma} = E\epsilon$$
(27)

Thus,

$$\sigma = \frac{\bar{A}}{A}\bar{\sigma} = \frac{\bar{A}}{A}E\epsilon = (1-d)E\epsilon,$$
(28)

which still holds in more general situations in which d can be interpreted as a damage parameter indicating no damage if $d = 0$ and full fracture if $d = 1$.

Despite the simplicity of the unidirectional model, it presents some of the distinctive features of more general cases. For example, it correctly represents the reduction in stiffness, experimentally verified upon unloading damaged dog-bone or fracture mechanics specimens. A straightforward and simple extension to multiaxial states assumes that damage is isotropic and represented by a single scalar parameter [2], i.e.,

$$\boldsymbol{\sigma} = (1 - d)\bar{\boldsymbol{\sigma}}, \tag{29}$$

in which d is an internal scale variable that represents the damage evolution used to relate damaged and undamaged configurations. More detailed formulations employ 2nd rank damage tensors, $\boldsymbol{\phi}$, to characterize the effective stress, i.e.,

$$\boldsymbol{\sigma} = (\boldsymbol{I} - \boldsymbol{\phi}) \cdot \bar{\boldsymbol{\sigma}}. \tag{30}$$

However, the most general formulation requires the damage to be characterized with a 4th rank damage tensor $\boldsymbol{D}$, i.e.,

$$\boldsymbol{\sigma} = (\boldsymbol{I} - \boldsymbol{D}) : \bar{\boldsymbol{\sigma}}. \tag{31}$$

Depending on the shape of the tensor, the induced evolution can be isotropic or anisotropic; i.e., if $\boldsymbol{\phi}$ or $\boldsymbol{D}$ are represented with a diagonal matrix, the resulting damage is isotropic. Furthermore, in the general case the stress tensor can become unsymmetric in the damage configuration, thus entering the realm of polar continua.

Considering an elastic material, different hypotheses are usually proposed to derive transformation relations between configurations in Figure 43. The hypotheses most commonly studied and used for elastic damage theories are,

- *The principle of strain equivalence* [102], which states that both the nominal and effective applied stress produces the same strain i.e.,

$$\epsilon = \bar{\boldsymbol{C}}^{-1} : \boldsymbol{\sigma} = \boldsymbol{C}^{-1} : \bar{\boldsymbol{\sigma}}, \tag{32}$$

  in which $\bar{\boldsymbol{C}}$ is the damaged elastic stiffness tensor, and in the most general case, it can be related to the undamaged elastic stiffness tensor via the 4th rank damage tensor

$(\boldsymbol{I} - \boldsymbol{D})$, i.e.,

$$\bar{\boldsymbol{C}} = (\boldsymbol{I} - \boldsymbol{D}) : \boldsymbol{C}, \tag{33}$$

which can lead to non-symmetric damage elastic stiffness tensor, $\bar{\boldsymbol{C}}$.

- *The principle of energy equivalence* [41], which assumes that the elastic energy of the effective and nominal stresses and strains are equal, i.e.,

$$w = \frac{1}{2}\boldsymbol{\sigma} : \boldsymbol{\epsilon} = \frac{1}{2}\bar{\boldsymbol{\sigma}} : \bar{\boldsymbol{\epsilon}} \tag{34}$$

One consequence of this principle is that the effective elasticity tensor is symmetric since

$$w = \frac{1}{2}\boldsymbol{\sigma} : \boldsymbol{\epsilon} = \frac{1}{2}\boldsymbol{\sigma} : \boldsymbol{C} : \boldsymbol{\sigma}, \tag{35}$$

and

$$w = \frac{1}{2}\bar{\boldsymbol{\sigma}} : \bar{\boldsymbol{\epsilon}} = \frac{1}{2}\bar{\boldsymbol{\sigma}} : \bar{\boldsymbol{C}} : \bar{\boldsymbol{\sigma}} = \frac{1}{2}\boldsymbol{\sigma} : \boldsymbol{M}^T : \bar{\boldsymbol{C}} : \boldsymbol{M} : \boldsymbol{\sigma}, \tag{36}$$

where $\boldsymbol{M} = (\boldsymbol{I} - \boldsymbol{D})^{-1}$. Consequently

$$\boldsymbol{C} = \boldsymbol{M}^T : \bar{\boldsymbol{C}} : \boldsymbol{M} \quad or \quad \bar{\boldsymbol{C}} = \boldsymbol{M} : \boldsymbol{C} : \boldsymbol{M}^T, \tag{37}$$

which proves the symmetry of $\bar{\boldsymbol{C}}$.

For completeness, it is worth mentioning that Voyiadjis and Kattan [206] proposed a *generalized hypothesis of strain transformation* that considers the previous principles as particular cases. In this approach, the nominal and effective strain tensor are related through the transformation law

$$\bar{\boldsymbol{\epsilon}} = \boldsymbol{L}(\boldsymbol{\varphi}^{(8)}) : \boldsymbol{\epsilon} \tag{38}$$

in which $\boldsymbol{L}(\boldsymbol{\varphi}^{(8)})$ is a 4th rank tensorial function of the 8th rank damage tensor, $\varphi^{(8)}$. Then, by defining $\boldsymbol{L}(\boldsymbol{\varphi}^{(8)}) = \boldsymbol{I}$ or $\boldsymbol{L}(\boldsymbol{\varphi}^{(8)}) = \boldsymbol{M}^{-T}$, the strain equivalence principle or the energy equivalence principle are recovered, respectively. Noticeably, this formulation can be postulated without the concept of the effective stress space, just as a relation that evolves the process of degradation of the elastic stiffness.

4.3.2.3 Symmetrization of the damage tensor

Since the principle of strain equivalence does not guarantee that the effective stress is symmetric, the "machinery" of polar continua (e.g., micromorphic, microstretch or micropolar) would be required. To avoid such complication, strategies involving the symmetrization of the stress tensor can be implemented. The three most commonly adopted strategies for symmetrization are as follows [101, 207]:

$$\bar{\boldsymbol{\sigma}} = (\boldsymbol{I} - \boldsymbol{\phi})^{-\frac{1}{2}} \cdot \boldsymbol{\sigma} \cdot (\boldsymbol{I} - \boldsymbol{\phi})^{-\frac{1}{2}} \tag{39}$$

$$\bar{\boldsymbol{\sigma}} = \frac{1}{2} \left(\boldsymbol{\sigma} \cdot (\boldsymbol{I} - \boldsymbol{\phi})^{-1} + (\boldsymbol{I} - \boldsymbol{\phi})^{-1} \cdot \boldsymbol{\sigma} \right) \tag{40}$$

$$\boldsymbol{\sigma} = \frac{1}{2} \left(\bar{\boldsymbol{\sigma}} \cdot (\boldsymbol{I} - \boldsymbol{\phi}) + (\boldsymbol{I} - \boldsymbol{\phi}) \cdot \bar{\boldsymbol{\sigma}} \right) \tag{41}$$

in which $\boldsymbol{\phi}$ is the 2nd rank damage tensor proposed by Murakami [143].

Although a variety of other symmetrization techniques have been proposed, only the one defined by Cordebois and Sidoroff [41] (Equation (39)) can be used to obtain a simple and condensed 4th rank damage tensor that has the form [207],

$$\boldsymbol{M} = (\boldsymbol{I} - \boldsymbol{\phi})^{-\frac{1}{2}} (\boldsymbol{I} - \boldsymbol{\phi})^{-\frac{1}{2}}, \tag{42}$$

Indeed, Equation (40), which has been extensively employed by Murakami [144], does not result in a general 4th rank damage tensor. Note that the three symmetrization techniques produce frame-indifferent stress tensors as required for constitutive equations [101].

Voyiadjis and Kattan [206] stated that the three symmetrization techniques result in qualitatively similar damage tensors, except for some oscillations in one coefficient when using Equation (39); they thus recommended the other two methods. However, other studies analyzed the first two symmetrization techniques and concluded that the symmetrization results were not equivalent since the results were affected by the technique employed [215]. Thus, the reliability of the symmetrization techniques is still a matter of contention.

Another strategy for avoiding non-symmetric stress tensors was proposed by Cauvin [33]; it assumed the validity of the equivalence strain principle and deduced necessary conditions on the damage tensor to render the elastic stiffness tensor "partially" symmetric. This approach is based on a set of constraints on $\boldsymbol{D}$ such that the undamaged and damaged elastic

tensors satisfy $C_{ijkl} = C_{jikl}$, $C_{ijkl} = C_{ijlk}$ and $\bar{C}_{ijkl} = \bar{C}_{jikl}$, $\bar{C}_{ijkl} = \bar{C}_{ijlk}$, guaranteeing the symmetry of the stress tensor. Thus,

$$\bar{C}_{ijkl} = (I_{ijrs} - D_{ijrs})C_{rskl} = \bar{C}_{jikl} = (I_{jirs} - D_{jirs})C_{rskl}, \tag{43}$$

which implies

$$D_{ijrs} = D_{jirs}, \tag{44}$$

and also

$$\bar{C}_{ijkl} = (I_{ijsr} - D_{ijsr})C_{srkl} = (I_{ijsr} - D_{ijsr}) : C_{rskl} = (I_{ijrs} - D_{ijrs})C_{rskl}, \tag{45}$$

which implies

$$D_{ijsr} = D_{ijrs}. \tag{46}$$

Equations (44) and (46) are sufficient conditions to guarantee the symmetry of the stress tensor, but they do not guarantee that $\bar{C}_{ijkl} = \bar{C}_{klij}$ nor $D_{ijkl} = D_{klij}$ [34]. Indeed, the most general damage tensor has 36 independent variables, which can be written in matrix (Voigt) notation as

$$[\boldsymbol{D}] = \begin{pmatrix} D_{1111} & D_{1122} & D_{1133} & 2D_{1123} & 2D_{1131} & 2D_{1112} \\ D_{2211} & D_{2222} & D_{2233} & 2D_{2223} & 2D_{2231} & 2D_{2212} \\ D_{3311} & D_{3322} & D_{3333} & 2D_{3323} & 2D_{3331} & 2D_{3312} \\ 2D_{2311} & 2D_{2322} & 2D_{2333} & 2D_{2323} & 2D_{2331} & 2D_{2312} \\ 2D_{3111} & 2D_{3122} & 2D_{3133} & 2D_{3123} & 2D_{3131} & 2D_{3112} \\ 2D_{1211} & 2D_{1222} & 2D_{1233} & 2D_{1223} & 2D_{1231} & 2D_{1212} \end{pmatrix} \tag{47}$$

4.3.3 Damage accumulated on slip planes in metals

Despite the fact that the fundamentals of damage mechanics were established between the 1980's and 1990's, a description of the damage accumulated on slip planes in metals is still not thoroughly developed. One important deficiency of most damage models is that they do not usually involve microstructural information, which is the reason why damage mechanics and micromechanics have diverged in the past 20 years. Indeed, many damage models have been developed for brittle-type materials such as concrete, for which the damage evolution

usually depends only on thermodynamic forces (e.g., the orientation of maximum stress) while the effect of the microstructure is dimly reflected in the damage constants. Note that microplane theories define director vectors [32, 31] that are not based on the microstructure or the physics of crack extension *per se.*

Because metals undergoing limited cyclic plastic deformation develop damage along a few activated slip planes that eventually lead to crack formation, the evolution of damage is strongly correlated with the underlying microstructure and needs to be reflected by the damage law. Hence, this research will employ a crystal plasticity model that assumes a decomposition of the total deformation gradient in an elastic-damage ($\boldsymbol{F}^{ed}$) part and a plastic-damage ($\boldsymbol{F}^{pd}$) part:

$$\boldsymbol{F} = \boldsymbol{F}^{ed} \cdot \boldsymbol{F}^{pd}, \tag{48}$$

as shown in Figure 45. This approach assumes the existence of the following configurations:

C^o: Initial undeformed configuration.

C^t: Current elasto-plastically deformed and damaged configuration.

C^{pd}: Plastically-damaged configuration after elastic unloading, which has damage.

Each of the deformation gradients $\boldsymbol{F}^{ed}$ and $\boldsymbol{F}^{pd}$ may be further decomposed as $\boldsymbol{F}^{ed} = \boldsymbol{F}^e \cdot \boldsymbol{F}^{d_e}$ and $\boldsymbol{F}^{pd} = \boldsymbol{F}^{d_p} \cdot \boldsymbol{F}^p$ to form:

$$\boldsymbol{F} = \boldsymbol{F}^e \cdot \boldsymbol{F}^{d_e} \cdot \boldsymbol{F}^{d_p} \cdot \boldsymbol{F}^p \tag{49}$$

in which $\boldsymbol{F}^{d_e}$ and $\boldsymbol{F}^{d_p}$ are associated with elastic and plastic deformation as enhanced by damage, respectively, but for simplicity this separation will not be pursued.

The proposed kinematic representation implies that,

- Plastic deformation can cause damage, which is assumed to occur sequentially after plastic deformation, preserving the isoclinic character. Such sequence is found, for example, in vacancy production followed by clustering, which is thought to be an important contribution for crack initiation [44][201]. Moreover, Repetto and Ortiz [174] have attempted to characterize vacancy evolution by decomposing the deformation gradient.
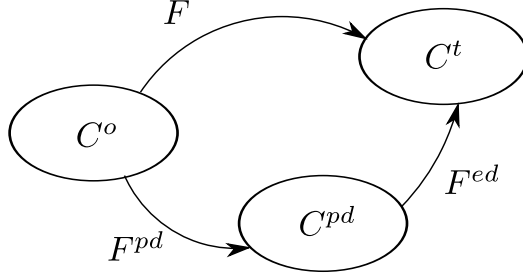
Figure 45: Proposed representation of elasto-plastic-damage deformation configurations.

- Damage may appear without the need of plastic deformation, since it can be the result of irreversible elastic release of energy; this makes it necessary to decompose the damage contribution on the deformation gradient. Indeed, elastic damage can be interpreted as the introduction of elastic constants that depend on some parameter.

To account for the effect of voids, Potirniche and coworkers [170] proposed an intermediate deformation gradient that would be equivalent to $\boldsymbol{F}^v = \boldsymbol{F}^{d_e} \cdot \boldsymbol{F}^{d_p}$ and coupled it with crystal plasticity. Although they successfully modeled isotropic damage effects with crystal plasticity, they do not account for the orientation of damage. Furthermore, they showed that

$$\boldsymbol{F}^v = \frac{1}{(1-d)^{\frac{1}{3}}} \boldsymbol{I} \tag{50}$$

in which d is the isotropic damage that represents the evolution of porosity.

By pulling back from the current configuration to the undamaged elasto-plastically deformed configuration (where crystal plasticity is defined), the stress becomes

$$\boldsymbol{\Sigma} = det(\boldsymbol{F^e} \cdot \boldsymbol{F^v})(\boldsymbol{F^e} \cdot \boldsymbol{F^v})^{-1}\boldsymbol{\sigma}(\boldsymbol{F^e} \cdot \boldsymbol{F^v})^{-T} = \frac{1}{(1-d)^{\frac{1}{3}}}det(\boldsymbol{F^e})(\boldsymbol{F^e})^{-1}\boldsymbol{\sigma}(\boldsymbol{F^e})^{-T}, \tag{51}$$

and since the shear stress satisfies

$$\boldsymbol{\tau}^\alpha = \boldsymbol{\Sigma} : s^\alpha \otimes m^\alpha, \tag{52}$$

we can interpret that by introducing the deformation gradient $\boldsymbol{F}^v$, the shear stress becomes an effective shear stress:

$$\bar{\boldsymbol{\tau}}^\alpha = \frac{1}{(1-d)^{\frac{1}{3}}}\boldsymbol{\tau}^\alpha, \tag{53}$$

86

Recently, Vladimirov et al. [205] studied the anisotropic creep damage in superalloys by tracking a damage accumulation on each slip plane; they proposed what could be described as an effective resolved shear stress on each slip plane, which depends on a pseudo-isotropic damage parameter (ω^α) for each slip plane α:

$$\tau^\alpha = \frac{1}{1 - \omega^\alpha} \boldsymbol{\Sigma} : s^\alpha \otimes m^\alpha, \tag{54}$$

Here, ω^α is the damage accumulated on each slip plane. Although it was not noticed on the publication, this approach is a generalization of the work from Potirniche et al. for crystal plasticity, by assuming a combined plastic-damage deformation gradient, $\boldsymbol{F}^{pd}$.

Although the original objective was only to propose a methodology that represents the separation of crystallographic planes, section 4.3.3 discussed a general framework that combines crystal plasticity with elastic and plastic damage. The damage associated with the plastic deformation gradient can be connected, for example, with vacancies and voids creation, as mentioned before [170, 205]. However, a formulation still needs to be developed for the elastic deformation gradient associated with the directional stress and strain redistribution of fatigue crack growth.

4.3.4 A model for crack surface separation along crystallographic planes

This section presents a model to represent the crack surface separation based on the degradation of the elastic stiffness tensor $\boldsymbol{C}$, referred to the orientation of the crack along a crystallographic direction. The general approach proposed by Voyiadjis and coworkers [206] and presented in Section 4.3.2.2 is interesting mainly from a theoretical standpoint as a general principle, but it is less applicable due to the complexities involved in defining the function in Equation (38). Similarly, although the energy equivalence principle assures symmetry of the damage tensor, the difficulty lies in defining the 4th-rank damage tensor, which cannot be identified with any general anisotropic elastic stiffness tensor. Moreover, the symmetrization techniques also introduce concerns about this approach. Consequently, this investigation follows the path proposed by Cauvin [33], who assumed the strain equivalence principle and imposed constraints on the shape of the degraded elastic stiffness tensors to guarantee the symmetry of the stress tensor.
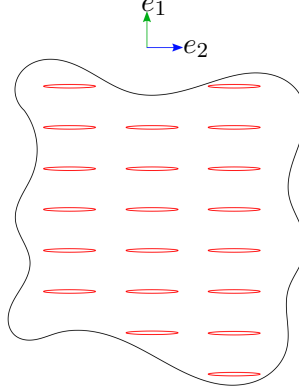
Figure 46: Schematic array of parallel cracks.

The simple coupling between stress and strain introduced by the strain equivalence principle allows the user to guess the effects of a certain damage tensor by simple inspection. In this research, the damage tensor should represent the separation of the crack surfaces along a crystallographic plane, which is intrinsically anisotropic. One alternative is to employ the following 4th rank tensor that describes the damage of the regular arrangements of cracks in Figure 46 [34, 103]. The description of the 4th rank damage tensor is simplified by using a 6x6 matrix representation in Equation (55), similar to the Voigt representation for elasticity, i.e.,

$$
\left[\boldsymbol{D}\right] = \begin{pmatrix}
d_1 & 0 & 0 & 0 & 0 & 0 \\
d_2 & 0 & 0 & 0 & 0 & 0 \\
d_2 & 0 & 0 & 0 & 0 & 0 \\
0 & 0 & 0 & 0 & 0 & 0 \\
0 & 0 & 0 & 0 & d_5 & 0 \\
0 & 0 & 0 & 0 & 0 & d_5
\end{pmatrix},
\tag{55}
$$

By comparing Equations (55) and (47), we can find the 4th rank damage tensor that represents a crack whose surface normal is oriented towards direction 1 and that preserves the symmetry of the stress tensor. The components of the damage tensor are zero except for:

$$
D_{1111} = d_1,\ D_{2211} = d_2,\ D_{3311} = d_2
$$

$$D_{1212} = \frac{d_5}{2},\ D_{2112} = \frac{d_5}{2},\ D_{1221} = \frac{d_5}{2},\ D_{2121} = \frac{d_5}{2}$$
$$D_{3131} = \frac{d_5}{2},\ D_{1331} = \frac{d_5}{2},\ D_{3113} = \frac{d_5}{2},\ D_{1313} = \frac{d_5}{2}$$

Here, d_1, d_2 and d_5 are parameters associated with the degradation of the elastic stiffness tensor that in a general situation may be independent. However, in the interest of describing the separation of crack surfaces and the stress redistribution in HCF, this study proposes that those parameters are not independent but are constrained as follows:

- $d_2 = \alpha d_1$ with α constant. This functional dependence gives the property that when the cracked element is loaded normal to the crack plane, normal and transverse stresses go to zero.

- $d_5 = \beta d_1$, with β constant. d_5 controls the resistance under shear loading and represents the interference or friction between surfaces of the cracks, which is expected to be insignificant for Stage I fatigue cracks [66, 162]. Note that surface roughness interference due to meandering crack growth can still be accounted for by explicitly simulating crack growth through grains.

Consequently, a single parameter for each slip system $d_1^{(\alpha)}$ controls the resistance normal to the slip plane. The degraded elastic stiffness tensor represents the response of a cracked equivalent element (CEE) shown in Figure 47. To verify that the theorized behavior is actually obtained, a MATLAB$^{\copyright}$ script computed the degradation of the elastic constants and the stress tensor that follows from different damage coefficients and applied elastic strain tensors. The elastic constants represent the elastic stiffness tensor for RR1000 superalloy [105] with cubic symmetry, $C_{11} = C_{22} = C_{33} = 166.2 GPa$, $C_{12} = C_{13} = C_{23} = 66.3 GPa$, $C_{44} = C_{55} = C_{66} = 138.2 GPa$, rotated so that one slip plane normal is along axis 1. This calculation represents the case in Figure 47, in which the crack surface normal is oriented along direction 1.

Table 3 presents the cases analyzed and the resulting stress tensor (in Voigt notation), which results in the expected behavior for a CEE. The values $\alpha = 0.398917$ and $\beta = 1$ were determined for the specific elastic constants employed so that, when an oriented CEE is
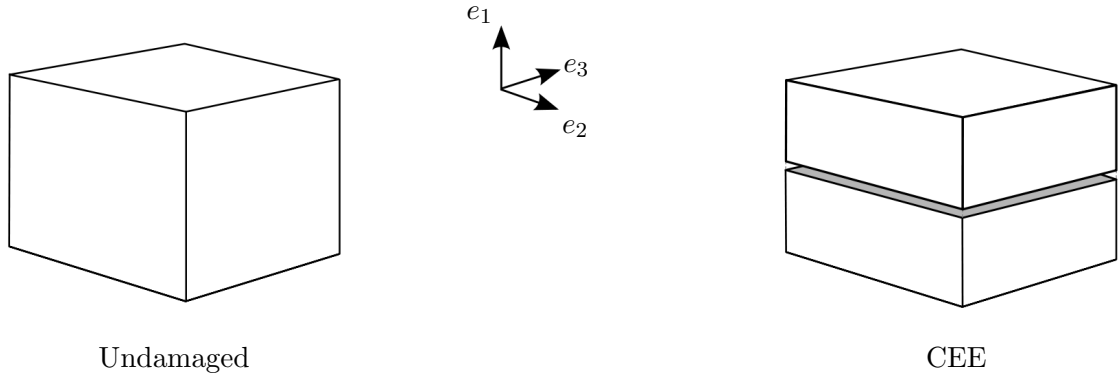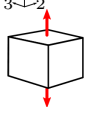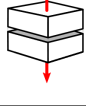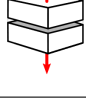
Figure 47: The effect of degrading the elastic stiffness tensor is equivalent cracking an oriented CEE.

loaded in tension parallel to the crack, the resulting stress in that direction is not affected by the degradation (this situation is reviewed in the 4th example in Table 3). These results are for a crack normal with a specific direction (1-axis); therefore, in a general case the 4th rank damage tensor should be accordingly rotated to orient the crack with the crystallographic plane.

4.3.4.2 Roughness friction and closure

The parameter d_5 controls the friction resistance between surfaces of the cracks in a CEE. For Stage I fatigue cracks where shear loading dominates, experiments [66, 162] have shown that MSC growth rates resemble the results from longer cracks with large fatigue ratio R$\sim$ 1. Since this type of loading conditions minimizes the friction of the crack surfaces because the cracks remains open most the time, it is reasonable to assume that MSCs should also experience limited friction. For simplicity, the simulations will assume that parameter d_5 takes a value of 0.99 when the crack is open, which implies that only 1% of the shear resistance is maintained; hence, there is no attempt to address roughness induced closure effects emerging from crack face frictional contact. However, it is noted that d_5 could be formulated as a function of the normal stress to the crack to introduce a friction law between the faces of the crack.

Table 3: Effect of damage coefficients (d_1, d_2 and d_5) on the stress tensor σ for different strain tensors in elastic materials. The crack surface normal is along direction 1 (Figure 47). "Any" means that the results are invariant with respect to that damage coefficient.

Elastic strain applied	Damage	Resulting elastic stress	Case studied
$\begin{pmatrix} 1 & 0 & 0 \\ 0 & 0 & 0 \\ 0 & 0 & 0 \end{pmatrix}$	$d_1 = 0$ $d_2 = 0$ $d_5 = 0$	$\begin{pmatrix} 16.6\text{x}10^4 & 0 & 0 \\ 0 & 6.6\text{x}10^4 & 0 \\ 0 & 0 & 6.6\text{x}10^4 \end{pmatrix}$	No damage. Normal stresses are obtained upon tensile loading.
$\begin{pmatrix} 0 & 1 & 0 \\ 1 & 0 & 0 \\ 0 & 0 & 0 \end{pmatrix}$	$d_1 = 0$ $d_2 = 0$ $d_5 = 0$	$\begin{pmatrix} 0 & 27.6\text{x}10^4 & 0 \\ 27.6\text{x}10^4 & 0 & 0 \\ 0 & 0 & 0 \end{pmatrix}$	No damage. Shear stresses are obtained upon shear loading.
$\begin{pmatrix} 1 & 0 & 0 \\ 0 & 0 & 0 \\ 0 & 0 & 0 \end{pmatrix}$	$d_1 = 0.9999$ $d_2 = 0.3989$ d_5, any	$\begin{pmatrix} 16.6 & 0 & 0 \\ 0 & < 10^{-2} & 0 \\ 0 & 0 & < 10^{-2} \end{pmatrix}$	Fully Damaged. All stresses decrease upon tensile loading normal to the crack.
$\begin{pmatrix} 0 & 0 & 0 \\ 0 & 1 & 0 \\ 0 & 0 & 0 \end{pmatrix}$	$d_1 = 0.9999$ $d_2 = 0.3989$ d_5, any	$\begin{pmatrix} 6.6 & 0 & 0 \\ 0 & 1.4\text{x}10^5 & 0 \\ 0 & 0 & 4\text{x}10^4 \end{pmatrix}$	Fully Damaged. The stress normal to the crack decreases upon tensile loading parallel to the crack.
$\begin{pmatrix} 1 & 0 & 0 \\ 0 & 0 & 0 \\ 0 & 0 & 0 \end{pmatrix}$	$d_1 = 0.5$ $d_2 = 0.3989$ d_5, any	$\begin{pmatrix} 8.4\text{x}10^4 & 0 & 0 \\ 0 & < 10^{-2} & 0 \\ 0 & 0 & < 10^{-2} \end{pmatrix}$	Partially Damaged. Stresses decrease upon tensile loading normal to the crack.
$\begin{pmatrix} 0 & 0 & 0 \\ 0 & 1 & 0 \\ 0 & 0 & 0 \end{pmatrix}$	$d_1 = 0.5$ $d_2 = 0.3989$ d_5, any	$\begin{pmatrix} 3.3\text{x}10^4 & 0 & 0 \\ 0 & 1.4\text{x}10^5 & 0 \\ 0 & 0 & 4\text{x}10^4 \end{pmatrix}$	Partially Damaged. Only the stress normal to the crack decreases upon tensile loading parallel to the crack.
$\begin{pmatrix} 0 & 1 & 0 \\ 1 & 0 & 0 \\ 0 & 0 & 0 \end{pmatrix}$	d_1, any d_2, any $d_5 = 1$	$\begin{pmatrix} 0 & 27.6 & 0 \\ 27.6 & 0 & 0 \\ 0 & 0 & 0 \end{pmatrix}$	Fully Damaged. Stresses go to zero upon shear loading parallel to the crack.
$\begin{pmatrix} 0 & 0 & 1 \\ 0 & 0 & 0 \\ 1 & 0 & 0 \end{pmatrix}$	d_1, any d_2, any $d_5 = 1$	$\begin{pmatrix} 0 & 0 & 27.6 \\ 0 & 0 & 0 \\ 27.6 & 0 & 0 \end{pmatrix}$	Fully Damaged. Stresses go to zero upon shear loading parallel to the crack.
$\begin{pmatrix} 0 & 0 & 0 \\ 0 & 0 & 1 \\ 0 & 1 & 0 \end{pmatrix}$	d_1, any d_2, any d_5, any	$\begin{pmatrix} 0 & 0 & 0 \\ 0 & 0 & 27.6\text{x}10^4 \\ 0 & 27.6\text{x}10^4 & 0 \end{pmatrix}$	Fully Damaged. Stresses are obtained upon shear loading normal to the crack.
$\begin{pmatrix} 0 & 1 & 0 \\ 1 & 0 & 0 \\ 0 & 0 & 0 \end{pmatrix}$	d_1, any d_2, any $d_5 = 0.5$	$\begin{pmatrix} 0 & 13.8\text{x}10^4 & 0 \\ 13.8\text{x}10^4 & 0 & 0 \\ 0 & 0 & 0 \end{pmatrix}$	Partially Damaged. Stresses decrease upon shear loading parallel to the crack.

When the stress normal to the crack plane is in compression, the crack should be considered to be as closed and the elastic stiffness is fully recovered (both elastic tensile and shear resistance). Crack closure can be caused by the wake of plastic deformation as the crack grows, or by the meandering crack path among crystallographic planes in multiple grains. The former is considered by the present framework since plastic deformation is still included in the constitutive formulation after the degradation of the elastic stiffness tensor. The decrease of elastic stiffness prevents further development of plastic deformation because the stresses can be lower than the threshold for slip activation, but the accumulated plastic strains remain unaltered.

The meandering path of a crack, exemplified in Figure 1, is taken into account in the model by explicitly considering grains and bands oriented with the slip planes. Therefore, a crack will develop some roughness on the cracked surface with an intrinsic length scale that depends on the grain size. The surface can suffer additional plastic deformation in compression (e.g., deformation of peak), but the formulation does not consider surface friction.

4.3.4.3   Positive definiteness of the elastic stiffness tensor

An additional verification is that the elastic energy w^e remains positive for all damage d_1, i.e.,

$$w^e = \frac{1}{2}\boldsymbol{\sigma} : \boldsymbol{E}^e = \boldsymbol{E}^e : \bar{\boldsymbol{C}} : \boldsymbol{E}^e > 0 \ \ \forall \ \ d_1 \tag{56}$$

The elastic stiffness tensor in Voigt notation has the property to maintain the energy equivalence:

$$w^e = \frac{1}{2}\boldsymbol{E}^e : \boldsymbol{\sigma} = \frac{1}{2}\{\hat{E}^e\}\{\hat{\sigma}\}e = \frac{1}{2}\{\hat{E}^e\}[\hat{C}]\{\hat{E}^e\} > 0 \ \ \forall \ \ d_1 \tag{57}$$

in which $\{\hat{\sigma}\}$, $\{\hat{E}^e\}$, $[\hat{C}]$ refer to the stress, strain and elastic stiffness tensor matrices in Voigt notation, respectively. Equation (57) implies that the elastic stiffness matrix should be positive definite, which is equivalent to saying that the eigenvalues of $[\hat{C}]$ are all greater than zero. Then, the eigenvalues of the elastic stiffness tensor in Table 3 (written in Voigt notation) were computed for a range of damage parameter d_1 as shown in Table 4. From

these results we can infer that the degraded elastic stiffness tensor is positive definite and satisfies Equation (57).

Table 4: Eigenvalues of the degraded elastic stiffness tensor in Table 3 computed for multiple values of the $\tilde{d}$.

d_1	Eigenvalues					
	λ_1	λ_2	λ_3	λ_4	λ_5	λ_6
0	0.9990	0.9990	2.7640	2.7640	2.7640	2.9980
0.1	0.9551	0.9990	2.7640	2.4826	2.4876	2.8128
0.3	0.8389	0.9990	2.7640	1.9348	1.9348	2.4908
0.5	0.6726	0.9990	2.7640	1.3820	1.3280	2.7640
0.7	0.4462	0.9990	2.7640	0.8292	0.8292	2.0072
0.9	0.1610	0.9990	2.7640	0.2764	0.2764	1.8541
0.99	0.0166	0.9990	2.7640	0.2764	0.2764	1.8014
0.9999	0.000166	0.9990	2.7640	0.0002764	0.0002764	1.7961

4.4 Elastic stiffness degradation in the mesoscale model

The mesoscale approach introduced in section 4.2 assumes that the crack is extended along an entire band within a grain in correspondence with the number of cycles computed for this amount of extension to occur based on the grain-level FIP values. Hence, the degradation of the elastic stiffness tensor is performed in such an incremental fashion to achieve proper description of stress redistribution with crack growth. The stress and strain fields and the fatigue driving force are later updated with further cycling.

However, an instantaneous decrease of stiffness can affect the convergence rate of the FEM, and it requires a gradual increase of coefficient d_1 on the elements to achieve convergence. In this case, the rate of degradation of stiffness is only dictated by the rate of convergence of the FEM algorithm. Furthermore, in order to account for crack closure, the stiffness tensor should be reestablished if the stress normal to the crack is negative (compression), which implies decreasing d_1 up to zero. The assessment of the stress sense is performed for each element in a cracked band (i.e., allowing partial crack closure), and

when one of those elements presents a compressive stress normal to the crack, d_1 is decreased gradually to achieve convergence. All these tasks are performed in ABAQUS by the UMAT, which is the subroutine that can control the evolution of the stiffness tensor for each element and at each time increment.

4.4.1 Issues with the degraded stiffness tensors

The damage mechanics model proposed to degrade the stiffness tensor is a flexible strategy to simulate the decohesion of cracked surfaces along directions that do not need to be predefined when the FEM mesh is created. It is also adequate to model either transgranular or intergranular cracks or to represent the crack separation along a single or multiple slip plane. Another benefit is that the stress and strain redistribution can be partially evaluated by not fully degrading the stiffness tensor. This methodology would reduce significantly the computational work, while the results could still be a good approximation of more detailed simulations.

However, the model relies on strongly anisotropic stiffness tensors that presented a much slower rate of convergence compared to the undamaged case. Furthermore, the rate of convergence was noticeably decreased when the parameter d_1 approached a value of one (typically $d_1 > 0.75$) or when the nominal applied strain increased. As argued in the literature [210], this slow convergence could have multiple origins:

- Depending on the orientation and value of d_1, the degraded elastic stiffness could present a high degree of anisotropy, and under the finite deformation formulation, it could lead to a non-convex elastic potential energy over the entire space of admissible loading conditions [69]. Under such circumstances, the underlying principle of virtual work in FEM may be affected, causing a lack of convergence.

- The convergence of the constitutive model could be affected by the misalignment of stresses and nodal forces due to strong anisotropic properties [197] or an elastic snap-back instability (the softening behavior in which both strain and stress decrease with further loading) [65] among multiple possibilities. Thus, if the stiffness tensor is

degraded too rapidly, it could cause a strong change in some of the stress components, affecting the convergence of the crystal plasticity model FE.

4.4.2 Simplification of the elastic stiffness degradation model

The possible causes for the low convergence rate of the degraded stiffness model are indeed complex, and their solution would require a detailed and exhaustive analysis of the model to be implemented, first in FEM environment, second in ABAQUS, and finally, in coordination with the crystal plasticity model. Hence, in order to maintain the focus of the thesis on the study of the small fatigue crack problem, this research will employ a simplified model in which the stiffness tensor varies following isotropic degradation, i.e.,

$$\bar{C} = \left(1 - \tilde{d}\right) C \tag{58}$$

being $\tilde{d}$ a scalar that varies from 0 to 0.99, at which point fully surface decohesion is assumed. To further simplify the implementation and reduce computational time, crack surface separation is only considered for transgranular failure (i.e., along transgranular bands and not GB sectors), which does not affect the characterization of the early transition between failure modes. In other words, intergranular fatigue life is assessed, but cracks are not extended along GBs.

4.4.2.1 Gradual degradation of the elastic stiffness tensor to achieve convergence

In simulations with isotropic degradation of the stiffness tensor, the abrupt increase of the damage parameter $\tilde{d}$ from zero to 0.99 can affect the convergence. For example, in some cases ABAQUS attempted to reduce the time increment in orders of magnitude after increasing $\tilde{d}$, but simulations did not converge even after having converged easily, with relatively large time increments, on the preceding steps. If the maximum time step in the input file was reduced, simulations showed an improvement in convergence. However, this strategy affects the entire loading step and not only during the degradation of the stiffness tensor. An improved strategy is to control the degradation of the stiffness tensor for those elements in a cracked band using a feedback from the current time increment, i.e.,

$$\tilde{d}_{(i+1)} = \tilde{d}_i \pm \nu \, \mathsf{d}t_i \tag{59}$$

for $\tilde{d}$ ranging between 0 (initial) to 0.99 (fully cracked). Here, $\mathsf{d}t_i$ is the ith time increment that is passed to the UMAT for each new increment, and ν is a factor that depends on the cycling period and overall convergence of the crystal plasticity model. Thus, to fully degrade the stiffness tensor in one loading cycle (t_{cycle}), ν should satisfy that $0.99/\nu \leq t_{cycle}$.

For example, for loading cycles of 2 seconds, a value of $\nu = 2$ was enough to increase $\tilde{d}$ up to 0.99 by the end of the loading step, hence assuming total separation of the crack surfaces. The plus sign corresponds to the case in which the stress normal is positive and the stiffness tensor should be degraded (crack extension). In contrast, if the stress normal to the crack is negative (in compression), the crack is assumed to be closed, and the stiffness is reestablished by decreasing $\tilde{d}$ up to zero. Figure 48 presents a schematic description of the loading sequence, the instances in which $\tilde{d}$ is increased and some possible evolutions for $\tilde{d}$ in one random realization. For simplicity, Figure 48 assumes only one $\tilde{d}$ parameter per band, but the simulations actually track the value of $\tilde{d}$ for each element in the cracked bands, which allows for partial crack closure within a grain. In all cases, the increase or decrease of $\tilde{d}$ occurs after predicting the path of the crack along the next grain, and it is controlled by Equation (59) to achieve a good convergence rate.

Equation (59) does not relate the stiffness degradation rate to the fatigue driving force *per se*, but it is an artifact to introduce a crack in bands with an acceptable convergence rate of the overall simulation. Indeed, Equation (59) decreases the stiffness tensor in proportion to the time increment, so if the simulation has a large time increment (because it is converging easily), it will decrease the stiffness tensor significantly, which will further tend to slow down the rate of convergence. This modification of the degradation model limits the softening of the elastic stiffness tensor, and it is consistent with other regularization solutions (such as artificial viscosity [18]), that modify the time-scale of the damage process.

Furthermore, $\tilde{d}$ increases up to 0.99 and not to 1, to increase the speed of the simulations and avoid numerical instabilities due to strain localization; a value of 0.99 means that the resisting stress on the elements that are cracked is about two orders of magnitude smaller than without a crack. Bammann and coworkers [14] proposed a similar limit of the damage
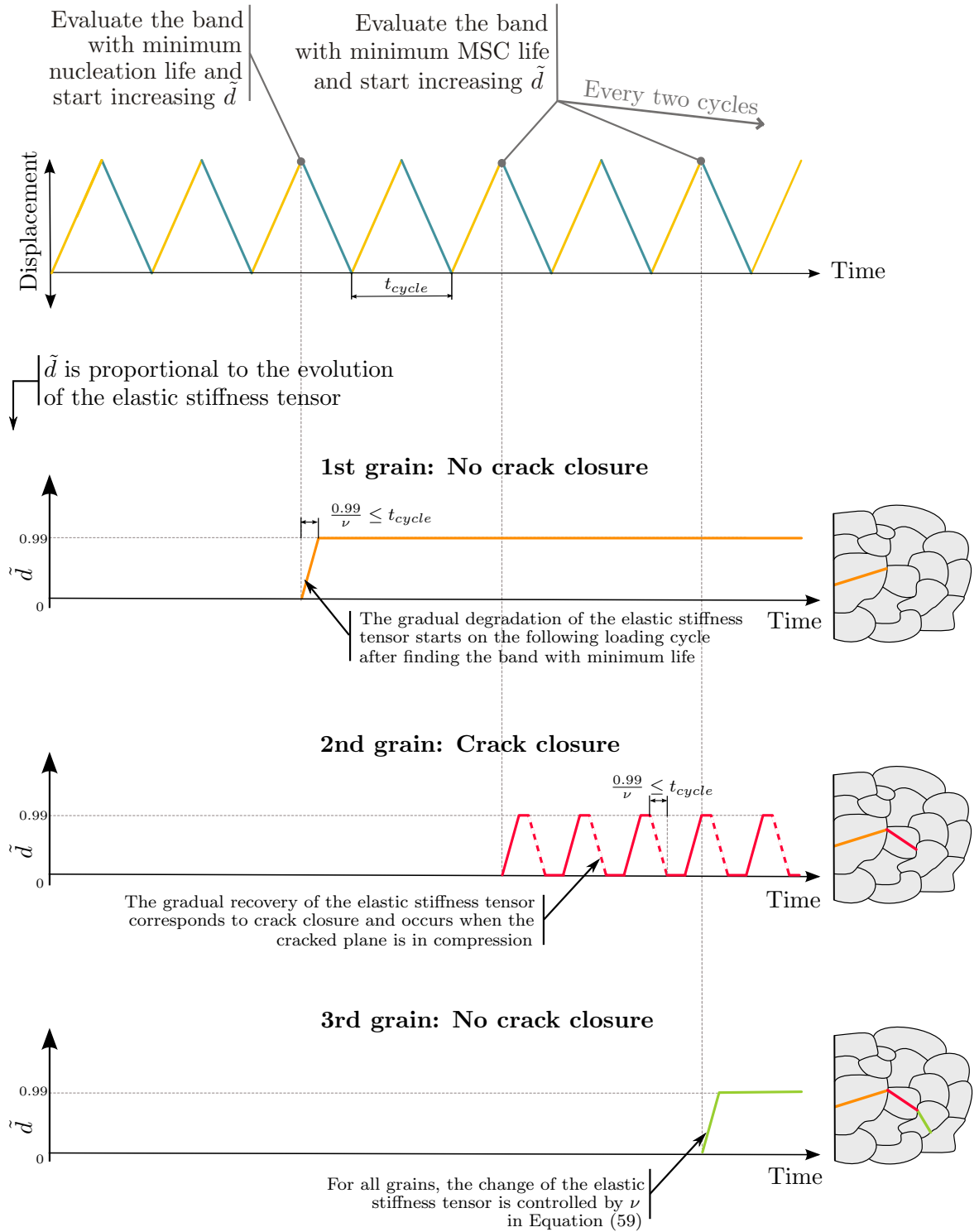
Figure 48: Schematic description of the possible time evolution of $\tilde{d}$ in different bands; $\tilde{d}$ is proportional to the degradation or recovery of the stiffness tensor. For simplicity the figure describes a single value of $\tilde{d}$ for each band, but the simulations actually degrade the elastic stiffness tensor for each element in cracked bands. The parameter ν in Equation (59) controls the rate of degradation of the elastic stiffness tensor, and it should satisfy that $0.99/\nu \leq t_{cycle}$ to fully crack a grain in one loading cycle.

parameter to avoid numerical problems. Despite the fact that the addition of damage may temporarily require reduced time increments, the simplifications implemented improve considerably the convergence rate and reduce the number of simulations that exhibit abnormal termination.

4.4.3 Mesoscale life estimation algorithm

Figure 49 presents a summary of the mesoscale scheme devised for assessing the fatigue crack formation and early growth in microstructures. The algorithm starts by calculating the values of the FIPs and their average on every band in every grain after applying a few cycles (i.e., three to ten cycles), and it proceeds calculating the number of expected cycles to nucleate crack on all bands for all grains using Equation (11). Once the band with the lowest number of cycles to nucleate a crack is found and the elements within are marked as "cracked," the model applies again a few cyclic loading and updates the values of the parameters in Equations (12), (13) and (17). It is during this loading cycle that the stiffness tensor is degraded ($\tilde{d}$ increased) in those elements marked as cracked in a rate that follows Equation (59), which improves the convergence of the FEM model.

Thereafter, the algorithm computes the MSC life of bands or GB sectors for transgranular and intergranular failure, respectively. The implementation then finds the band neighboring the crack with minimum MSC life, and renders the elements within as cracked. The simulation proceeds by applying further loading cycles, in which the stiffness tensor is degraded on the cracked elements, and the MSC life is evaluated again on the remaining grains. By repeating the procedure, the model can calculate the path of a crack among several grains, estimate the number of cycles to failure and account for competition between transgranular and intergranular growth; The simulation ends when a certain number of grains have been cracked. This approach is limited to represent a single dominant crack.

Create FEM model

- Create a regular (voxellated) mesh containing microstructural attributes e.g., grain size, orientation distribution.
- Subdivide each grain in bands and assign elements to them.
- Create sets with the elements neighboring another grain.

Apply several loading cycles

- Typically 3 to 10 cycles are enough to develop stress-strain flields close enough to saturation conditions.

Evaluate the Nucleation life

- Calculate FIPs for each element.
- Calculate the average FIP for each band.
- Estimate the life of each band. The nucleation life corresponds to the lowest life among all bands.
- Set the band with lowest life as "cracked", which means that the crack spans the entire grain.

Apply some loading cycles

- The stiffness tensor is degraded at a rate defined by Equation (59) for the elements on all the cracked bands.
- 2 to 5 loading cycles are typically enough to update the stress and strain fields due to crack growth and crack closure.

Evaluate the MSC life

- Updates the FIPs for each element.
- Updates each band average of the FIP.
- Estimates the life of each non-cracked bands. The MSC life corresponds to the lowest life among all bands.
- Sets the band with lowest life as "cracked", which means that the crack spans the entire grain.

Reached the max number of grains to crack?

No

- The algorithm continues calculating MSC lives and extending the crack until a predifined number of grains are cracked.

Yes

Finish the simulation

Figure 49: Flow chart showing the algorithm to calculate the life until a certain number of grains are cracked.

4.5 Preliminary conclusions

This chapter introduced local correlations between crack growth rates and FIPs based on a hierarchical approach to fatigue modeling that allows the estimation of the life consumed in different stages as the crack extends.

To limit the computational demands, a mesoscale framework was introduced that enables modeling of crack growth over many grains. The mesoscale scheme takes the grain as the minimum unit that can crack (instead of an element) and assumes that the evolution of the driving force inside grain i scales with a function, $g(a_i)$ that depends on the normalized length of the crack within the grain, a_i, $(0 \leq a_i \leq 1)$.

Once the crack has extended over one or more grains, the stress and strain redistribution can affect the driving force on the neighboring uncracked grains. To account for this effect, various strategies were reviewed, among which the damage mechanics approach was preferred. This methodology degrades the elastic stiffness tensor without affecting the crystal plasticity calculations.

A general anisotropic damage formulation was developed for finite deformation based on a 4th rank damage tensor that guarantees a symmetric stress tensor. However, the implementation in ABAQUS of such model showed very low convergence rate. Hence, to maintain the focus of this thesis on the fatigue problem, a simplified model was implemented to extends cracks along grains. The simplified isotropic degradation of the stiffness tensor presents acceptable convergence rates when combined with an algorithm that adjusted dynamically the decrease of elastic stiffness.

CHAPTER V

APPLICATION: MODELING RR1000

The previous chapters have presented a physically-based model to predict fatigue life at the grain scale with a broad focus on FCC metals. To compare the model with experimental data, this investigation will apply the multi-stage framework to predict the early stages of the fatigue life in turbine disks made of the RR1000 alloy. This alloy corresponds to a third generation of powder-processed Ni-base superalloy with a dual microstructure (large grains surrounded by small grains), strengthened by γ' precipitates [133]. The distribution of grain sizes results from a thermomechanical process aimed at improving different mechanical properties at different locations.

The premise is that the fatigue initiation life of a relatively new alloy can be estimated for different microstructures by combining current general knowledge of fatigue damage and plastic deformation at multiple scales with limited experimental information. Such an objective is expected to be achieved by including the most significant aspects of the physics of the fatigue problem and is not a mere fitting of data.

5.1 Significant aspects of Ni-base superalloys

Synthesizing the physics of crystallographic plastic deformation relevant to fatigue damage is one of the main goals of this thesis. The following characteristics of superalloys are relevant to the fatigue resistance of RR1000 alloy:

- Planar slip: Because Ni-base superalloys for disk applications have an FCC arrangement, octahedral planes are the most dense, and at low to medium temperatures, plastic deformation occurs mainly by planar slip along those planes. In addition, starting in the range between 600°C and 700°C, many superalloys deform along the cube plane directions in the matrix, often attributed to a zig-zag cross-slip mechanism depicted by Figure 50 [22, 115].

- Cyclic strain localization: A characteristic shared by low to medium SFE FCC alloys (e.g., Cu-Al alloys, certain stainless steels and many superalloys) [13, 29, 71, 218] is the development of thin slip bands in fatigue ($\sim$ 100 nm in thickness). This process is closely connected to the formation and growth of cracks in the small crack regime and indicates that transgranular fatigue crack growth tends to follow octahedral planes [70, 110].

- Constitutive modeling: To capture relaxation and creep effects at medium to high temperature, the Chaboche [35] and crystal plasticity [9] models have been most commonly employed. The first is a macroscopic model that does not account for the crystallographic orientation, while the second is more relevant for small crack growth analysis, since plastic deformation develops on a finite number of slip planes along which cracks grow within individual grains.

- Environmental effects: Because it augments crack tip irreversibility and weakens GBs [80, 96], the content of oxygen in the environment affects the fatigue crack growth rates in metals and is detrimental for many FCC metals. Furthermore, several authors [133, 93] have concluded that oxygen diffusion can trigger intergranular crack growth in superalloys (including RR1000), which can reduce the fatigue life by orders of magnitude.

- Nucleation and transition to a MSC: Turbine parts (e.g., disks) may present a microstructure with a wide statistical dispersion of grain sizes in which the largest grains are often the most favorable sites for crack transgranular nucleation [62, 46], followed by inclusions or GBs.
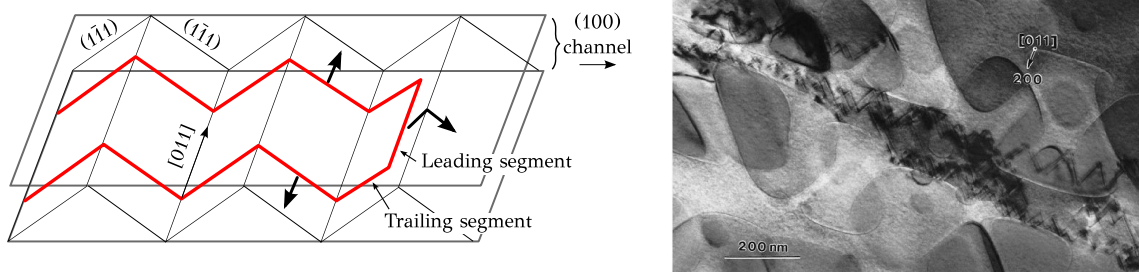
Figure 50: Zig-zag dislocation mechanism in superalloys at 650C [22]

5.1.1 Microstructure of RR1000 alloy for disk applications

Only a few studies in the literature have focused on RR1000 alloy, but they provide useful insights. Some studies [135, 133, 134, 63] have analyzed the microstructure evolution of turbine disks as a function of thermal history. The heat treatment is designed to produce a dual-microstructure [133], which optimizes the grain size at different locations, based on service requirements. For example, the bore region undergoes tensile and fatigue loading at relatively low temperature and achieves the best of performance with fine grain microstructures. However, the rim region requires good creep and high temperature fatigue crack growth resistance, which are achieved with coarse grain microstructures, as shown in Figure 51.

Turbine disk

Bore: Fine grains   Rim: Coarse grains
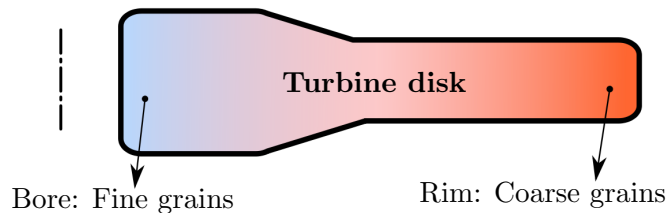
Figure 51: Sketch of the cross section of a turbine disk. Red/blue color indicates the last/first region to cool down in the manufacturing process, which results in a dual microstructure.[133]

Mitchell et al. [133] characterized quantitatively the change in grain size and the γ' volume from the bore to the rim, as a function of the maximum temperature achieved while processing. Furthermore, at 750°C they showed evidence of localized planar deformation, typical of low SFE materials, and precipitates cut by dislocations. Stocker et al. [189] performed several TEM analyses confirming the localized planar deformation in the form of slip bands along with some climb at 650°C, as shown in Figure 52. Interestingly, they compared the results with specimens deformed at room temperature and found that "dislocation patterns were broadly similar for samples tested under pure fatigue and combined fatigue creep loading conditions." Furthermore, the study also reported planar slip character of the deformation, and none of these studies mentions either cube slip or microtwining [95, 204], although they were not searching for them specifically.
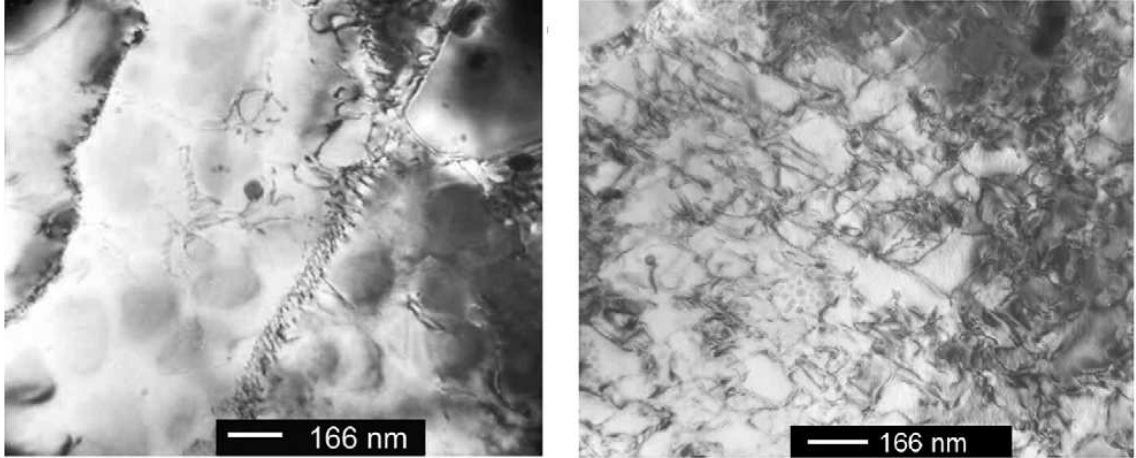
Figure 52: TEM micrographs for RR1000 after 2% deformation, 0.5%/s and hold time 100s. (left) Planar slip deformation. (right) Shearing between γ' particles and dislocations. [189]

The thermal gradient from the heat treatment produces bore and rim regions that can be considered as formed by unimodal grain size distribution with different mean values. However, in between lies the so-called transition region that has a bimodal distribution with small and large grain sizes coexisting. The shape of the distribution determines the probability of having an "as-large-as" (ALA) grain of a certain size [133, 62, 63], which plays a major role in limiting the fatigue life. The transition zone is most critical and prone to failure because the dual microstructure renders ALA grains close to those in the rim. Thus, a deep understanding of the microstructural effects on fatigue life (e.g., effect ALA grains) is needed in order to design a microstructure that will be adequate and that can be realized with thermomechanical processing.

5.2 Grain size distribution and FE mesh generator

An important step in modeling the influence of the microstructure on fatigue life is to provide an accurate description of the grain size and texture. For the HCF and HCF-LCF transition regimes, the extreme values of the distributions should be considered with regard to minimum fatigue life, rather than the mean values. Then, models should reproduce distributions of grain size with more detail towards the larger grain size tail (e.g., ALA grains). Based on the analysis of Lin et al. [106], the smallest representative volume element

(RVE) for the constitutive modeling of RR1000 with unimodal grain size distribution would contain on the order of 100 grains. This estimation involves only the macroscopic stress-strain behavior, so an RVE for fatigue analysis based on extreme values would include an even larger number of grains. Indeed, the wide scatter in HCF simulations and experiments shows that true RVEs are larger than the volumes usually employed in specimens.

Since bimodal distributions of grains have a larger number of significant statistical moments than unimodal distributions, RVEs of dual microstructures should include larger numbers of grains. If we consider RR1000 dual microstructures as being formed by two independent unimodal distributions (each similar to the bore and rim), we would expect that an RVE should contain at least 100 grains of each distribution. Furthermore, RR1000 disks typically contain ALA grains in the rim that are about ten time larger than the ALA in the bore [133, 62]. Then, assuming that ALA grains in the bore are formed by one element, rim ALA grains would have about 4000 elements, and a RVE would need about 400000 elements! Such a large number of elements is outside the scope of this research because it would demand extensive computational resources, so an alternative solution should be found. One alternative would be to create meshes with variable element sizes, but this approach will not be pursued because it introduces additional complexities such as non-homogeneous meshes with variable accuracy in FIP calculations from grain to grain. A second solution is to perform a statistical analysis of the simulations using models with one rim ALA grain surrounded by smaller bore-size grains. This solution is preferred because it demands an amount of computational work that can be scaled with the available resources and desired accuracy.

Each model is aimed to represent a statistical volume element (SVE) of sufficient size to capture the lower order moments of the cyclic-plastic evolution [171]. Therefore, the simulations are allowed to nucleate only one crack, after which the crack extends in the MSC regime. Each simulation represents the behavior of a dominant crack that can extend through crystallographic planes, and can branch at GBs (i.e., not inside a grain)

5.2.1 Mesh generator

Before conducting FE simulations, the information about the microstructure needs to be defined and incorporated into ABAQUS [1] either via the input file or additional files read by user subroutines. Such tasks are performed by the Mesh Generator program, which is a Matlab script based on the framework originally created by Musinski [146] for assigning grain size distributions. The Mesh Generator program was designed to allow the user to define all the parameters involved in the FE simulations (from the constitutive model to the fatigue life model) under a single user-friendly graphical interface.

The objective of the Mesh Generator is to create all that is required to run a simulation, which demands that several calculations be performed before the input files are written. The program initially creates a regular cubic mesh of reduced 8-node linear brick elements (C3D8R) using ABAQUS python commands (called from the Matlab code) and defines regions occupied by spherical grains with lognormal grain size distributions. The lognormal distribution is described by

$$f(x; \mu, \sigma) = \frac{1}{x\sigma\sqrt{2\pi}}\exp\left[\frac{-(ln(x) - \mu)^2}{2\sigma^2}\right], \qquad (60)$$

and it has been employed to fit IN100 superalloy [185, 217, 68] using $\mu = -0.1$ and $\sigma = 0.4$. Due to the lack of quantitative data about the specific grain size distributions for rim and bore regions in RR1000, they are assumed to follow a lognormal distribution.

The number of grains is calculated as the ratio of the volume of the cubic mesh divided by a slightly reduced average grain size that accounts for the spherical packing factor; this factor represents the open spaces in between randomly packed spheres [146]. The unassigned elements in between spheres are afterwards added to the closest grains, and the result is an approximately equiaxed grain structure. The crystallographic orientation of the grains is defined with three Euler angles (in Bunge notation [50]), which are selected randomly to achieve no initial texture. The program also provides the chance to specify the size of three grains that are located at the center, bottom-center and left-center of the mesh (Figure 53, right); these grains correspond to ALA grains surrounded by smaller grains that follow a lognormal distribution. This work focuses on the influence of one ALA grain, and will not
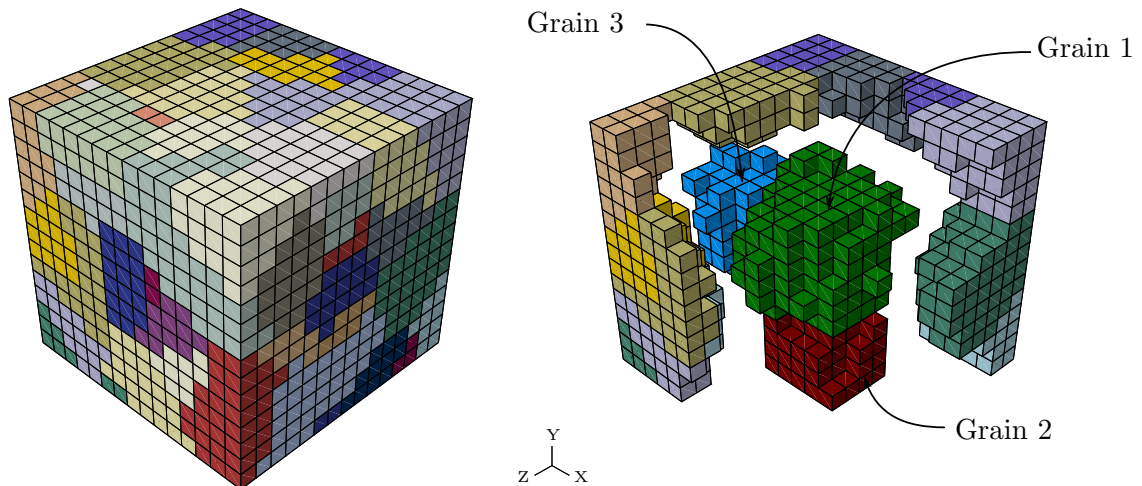
Figure 53: An example of a mesh created. On the left the entire model is shown. On the right a detail of grains 1, 2 and 3, which were given grain radius larger than the rest. The model has periodic boundary conditions and strain is applied along the Z axis.

consider the cases of two or three ALA grains in the same simulation.

Once all the elements are assigned to grains, the Mesh Generator subdivides each grain, starting from the center of the grain, in consecutive bands of similar width (as shown in Figure 41, Chapter 4) and lists the elements whose centroids lie within the bands. This task is repeated four times, each corresponding to a different slip plane normal, and these sets of elements will later be used for averaging FIPs. Similarly, a series of sets is defined, listing the elements neighboring another grain that will later be employed to assess the intergranular failure of GBs. Each boundary between two grains is represented by two sets of elements, each belonging to one of the grains. Furthermore, the model has boundaries achieved by imposing that the sum forces and moments on opposite faces of the cubic are equal to zero. Note that the meshes are not truly periodic, since grain distributions on opposite faces are not identical. Finally, all the sets and boundary conditions are written in the input file, so they are available for visualization in the ABAQUS graphical interface.

Apart from the standard ABAQUS input file, the user subroutines require further information about the microstructure that is defined during the creation of the mesh. This information is passed to ABAQUS in the form of text files that are read by the user subroutines and usually stored in local (dynamic) or global (static) memory. Among the files

created by the Mesh Generator are,

- *Definitions.txt*: Defines the value of the constants used in the prediction of the life, i.e., irreversibility factors, $\Delta \mathrm{CTD}_{th}$.

- *Geom_Def.txt*: Defines several variables employed by the user subroutines, mainly concerned to the geometry and microstructure of the model, i.e., number of elements and grains, mesh size, width of the bands within which to average FIPs, and number of grains to crack (i.e., maximum crack length).

- *Grain.txt*: Lists the size of the grains and the Euler angles that define the orientation of the grain.

- *Min_dist.txt*: Defines the connectivity among bands in which the FIP is averaged. This information is stored as a logical variable array (possible values are 0 or 1) and usually corresponds to the largest variable stored, easily reaching gigabytes in size when hundreds of grains are involved.

- *Neighbor_grains.txt*: Contains in line number $(2i - 1)$ how many neighbor grains has grain i, and in line $2i$ lists the actual number each of those neighboring grains separated by commas.

5.3   Crystal plasticity constitutive model

5.3.1   Kinematics of crystal plasticity for large deformations

This section presents an overview of the crystal plasticity formulation for large strains employed in simulations. Further details about the generalities of crystal plasticity models can be found in Ref [89].

Considering an infinitesimal element, the deformation gradient defines the transformation between two configuration, i.e.,

$$d\boldsymbol{x} = \boldsymbol{F} \cdot d\boldsymbol{X} \tag{61}$$

where $\boldsymbol{x}$ and $\boldsymbol{X}$ are the current and initial coordinate of a material particle, respectively. The deformation gradient is decomposed into an elastic-damaged, $\boldsymbol{F}^{ed}$, and plastic $\boldsymbol{F}^p$ such

that

$$\boldsymbol{F} = \boldsymbol{F}^{ed} \cdot \boldsymbol{F}^{p} \tag{62}$$

which takes into account the degradation of the elastic stiffness tensor as discussed in the previous Chapter, but does not include any damage in the plastic part. $\boldsymbol{F}^{p}$ describes the kinematics of plastic deformation without any rigid rotation of the lattice, which is considered in $\boldsymbol{F}^{ed}$. Figure 54 represents the slip direction ($\boldsymbol{s}^{\alpha}$) and the slip plane normal ($\boldsymbol{m}^{\alpha}$) in the initial, intermediate and current configurations.
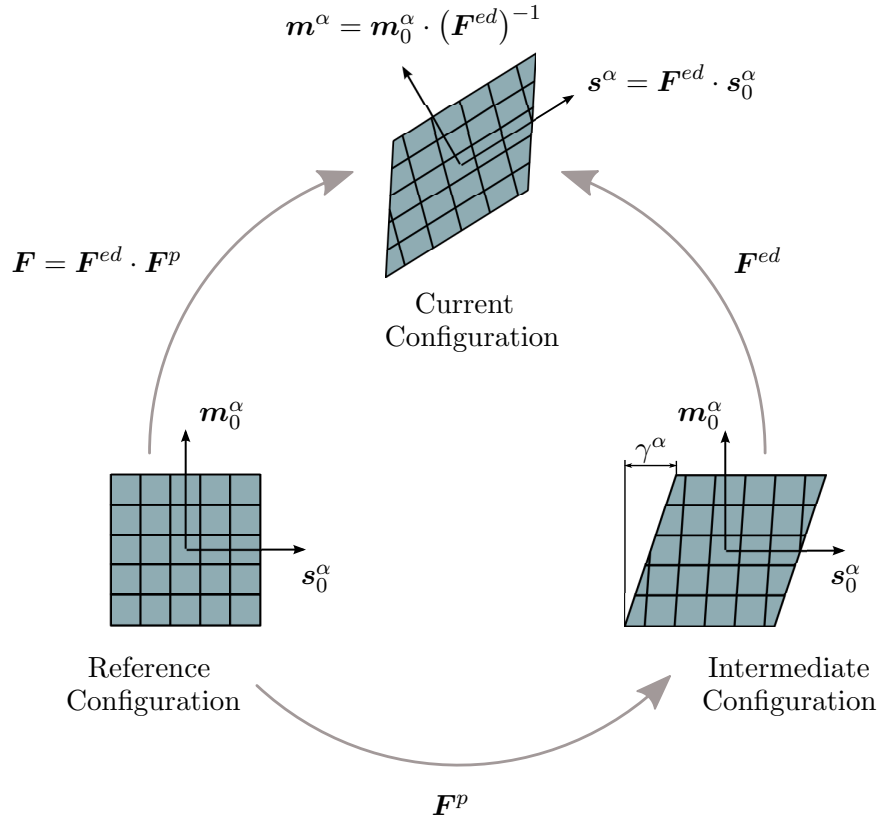
Figure 54: Schematic representation of the elastic-damaged and plastic deformation gradients in a crystalline solid.

According to Rice [175], if dislocation motion is the only deformation process, the time derivative of the plastic deformation gradient $\dot{\boldsymbol{F}}^{p}$ can be expressed as,

$$\dot{\boldsymbol{F}}^{p} = \left(\sum_{\alpha=1}^{N_{\alpha}} \dot{\gamma}^{\alpha} \boldsymbol{s}_{0}^{\alpha} \otimes \boldsymbol{m}_{0}^{\alpha} \right) \cdot \boldsymbol{F}^{p} \tag{63}$$

in which N_{α} is the number of active slip systems and $\dot{\gamma}^{\alpha}$ is the shearing rate for slip system

α.

The plastic velocity gradient $\boldsymbol{L}_0^p$ in the intermediate configuration satisfies

$$\boldsymbol{L}_0^p = \dot{\boldsymbol{F}}^p \cdot (\boldsymbol{F}^p)^{-1} = \left(\sum_{\alpha=1}^{N_\alpha} \dot{\gamma}^\alpha \boldsymbol{s_0^\alpha} \otimes \boldsymbol{m_0^\alpha} \right) \tag{64}$$

and in the current configuration plastic velocity gradient follows,

$$\boldsymbol{L}^p = \boldsymbol{F}^{ed} \cdot \boldsymbol{L}_0^p \cdot (\boldsymbol{F}^{ed})^{-1} \tag{65}$$

while the elastic velocity gradient in the current configuration is given by

$$\boldsymbol{L}^{ed} = \dot{\boldsymbol{F}}^{ed} \cdot (\boldsymbol{F}^{ed})^{-1} \tag{66}$$

Finally, the velocity gradient in the current configuration can be computed as the sum of Equations (65) and (66),

$$\boldsymbol{L} = \dot{\boldsymbol{F}} \cdot (\boldsymbol{F})^{-1} = \boldsymbol{L}^{ed} + \boldsymbol{L}^p \tag{67}$$

In the intermediate configuration, the second Piola-Kirchoff stress $\boldsymbol{T}$ satisfies that,

$$\boldsymbol{T} = \bar{\boldsymbol{C}} : \boldsymbol{E}^{ed} \tag{68}$$

in which $\boldsymbol{E}^{ed}$ is the Green strain tensor:

$$\boldsymbol{E}^{ed} = \frac{1}{2} \left[(\boldsymbol{F}^{ed})^T \cdot \boldsymbol{F}^{ed} - \boldsymbol{I} \right] \tag{69}$$

being $\boldsymbol{I}$ the 4th rank identity tensor. The Cauchy stress $\boldsymbol{\sigma}$ in the current configuration is obtained as

$$\boldsymbol{\sigma} = \frac{1}{det(\boldsymbol{F}^{ed})} \boldsymbol{F}^{ed} \cdot \boldsymbol{T} \cdot (\boldsymbol{F}^{ed})^T \tag{70}$$

Finally, the resolved shear stress, τ^α, for system α is computed using that

$$\tau^\alpha = \boldsymbol{\sigma} : \left(\boldsymbol{s_0^\alpha} \otimes \boldsymbol{m_0^\alpha} \right) \tag{71}$$

5.3.2 RR1000 crystal plasticity model

Zhan et al. performed an experimental evaluation of RR1000 [220, 221], including monotonic and fatigue tests at 650°C using different strain rates (0.5%/s, 0.05%/s, 0.005%/s) and dwell

periods. In order to describe the constitutive behavior including creep effects, these results were later employed to fit a Chaboche model. Overall, the model was fit to the data with acceptable error for industrial applications, but in experiments with dwell periods the stress relaxation predicted exceeded grossly the experimental measurements after the first cycle. The experimental data were later employed to fit a model that tracked the diffusion of oxygen in order to predict crack growth rates [227].

Recently, Lin et al. [105] fit Zhan's RR1000 experimental data to 2-D FEM simulations that explicitly describe grain orientation and to a crystal plasticity scheme based on the work by Meissonnier et al. [125]. The model was implemented in ABAQUS using a fully-implicit implementation based on the Newton-Raphson iterative method and the backward-Euler integration scheme. The constitutive model employs the flow rule

$$\dot{\gamma}^{(\alpha)} = \dot{\gamma}_0 \exp\left[-\frac{F_0}{kT}\left\langle 1 - \left\langle \frac{\left|\tau^{(\alpha)} - B^{(\alpha)}\right| - S^{(\alpha)}\mu/\mu_0}{\widehat{\tau}_0\mu/\mu_0}\right\rangle^p\right\rangle^q\right] sgn(\tau^{(\alpha)} - B^{(\alpha)}), \qquad (72)$$

where $\dot{\gamma}^{(\alpha)}$ is the shearing rate of slip plane α, $\tau^{(\alpha)}$ is the associated resolved shear stress, T is absolute temperature, $F_0, \widehat{\tau}_0, p, q, \dot{\gamma}_0, \mu, \mu_0$ are constants that may differ for octahedral and cube slip planes, and k is the Boltzmann constant. This formulation is based on the work from Busso [30] that is related to the work of Kocks [94] and considers 12 octahedral and 6 cube slip systems. The constants were adjusted by simulating a sheet with grains under cyclic loading, with and without dwell times at multiple strain rates at 650°C [105].

The flow rule in Equation (72) includes, for each crystallographic plane, a directional slip resistance term ($S^{(\alpha)}$) that functions as a threshold stress below which no plastic deformation develops and a back stress ($B^{(\alpha)}$) that accounts for directional hardening and Bauschinger effects. The evolution laws for slip resistance and back stress in Equations (73) and (74) follow, respectively:

$$\dot{S}^{(\alpha)} = \left[h_S - d_D\left(S^{(\alpha)} - S_0^{(\alpha)}\right)\right]\left|\dot{\gamma}^{(\alpha)}\right| \qquad (73)$$

$$\dot{B}^{(\alpha)} = h_B\dot{\gamma}^{(\alpha)} - r_D^{(\alpha)}B^{(\alpha)}\left|\dot{\gamma}^{(\alpha)}\right| \qquad (74)$$

in which $r_D^{(\alpha)} = \dfrac{h_B \mu_0}{S^{(\alpha)}} \left\{ \dfrac{\mu'_0}{f_c \lambda} - \mu \right\}^{-1}$ and $S_0, h_B, h_S, d_D, \mu'_0, f_c, \lambda$ are constants that are different for octahedral and cube slip planes. Both equations follow a hardening-dynamic recovery type of evolution [103], but they differ in the initial values of the stresses, namely S_0 for the slip resistance and $B_0^{(\alpha)} = 0$ for the back stress.

Since this formulation does not account for dislocation transmission across GBs, the plastic deformation generated within one grain cannot be transferred into a neighboring grain. Furthermore, the constitutive model does not have an intrinsic length scale, so two identical FEM models but one ten times larger will result in exact same stresses and strains. Both limitations of the constitutive formulation will be partially mitigated by the fatigue model.

5.3.3   Constitutive model implementation

The model was implemented as a UMAT in ABAQUS 6.9 [1] by modifying Shenoy's original crystal plasticity implementation for IN100 [184], which is also an implicit scheme based on the Newton-Raphson and the backward-Euler methods. As discussed by McGinty [123], power law flow rules can produce numerical instabilities that would require exceptionally small time steps when using explicit algorithms. Since the exponential flow rule proposed by Lin et al. [105] can be approximated by a sum of power terms, an implicit scheme is judged as the most reliable path to calculate the plastic shearing rate.

With the beginning of a new time increment Δt, the subroutine evaluates the discrete plastic shear rate for each slip system, i.e.,

$$\dot{\gamma}^{(\alpha)} = \dot{\gamma}_0 \exp\left[-\frac{F_0}{kT} \left\langle 1 - \left\langle \frac{\left| \tau_{t+\Delta t}^{(\alpha)} - B_{t+\Delta t}^{(\alpha)} \right| - S_{t+\Delta t}^{(\alpha)} \mu/\mu_0}{\widehat{\tau}_0 \mu/\mu_0} \right\rangle^p \right\rangle^q \right] \mathrm{sgn}(\tau_{t+\Delta t}^{(\alpha)} - B_{t+\Delta t}^{(\alpha)}), \quad (75)$$

and the slip resistance $S^{(\alpha)}$ and the back stress $B^{(\alpha)}$ are discretized using Euler differences,

$$S_{t+\Delta t}^{(\alpha)} = \frac{S_t^{(\alpha)} + \left(h_S + d_D S_0^{(\alpha)} \right) \left| \dot{\gamma}^{(\alpha)} \right| \Delta t}{1 + d_D \Delta t \left| \dot{\gamma}^{(\alpha)} \right|} \tag{76}$$

and

$$B_{t+\Delta t}^{(\alpha)} = \frac{B_t^{(\alpha)} + h_B \dot{\gamma}^{(\alpha)} \Delta t}{1 + r_D^{(\alpha)} \Delta t \left| \dot{\gamma}^{(\alpha)} \right|} \tag{77}$$

Since Equations (75), (76), and (77) are coupled and nonlinear, a Newton-Raphson algorithm is employed to solve for the set of equations by iteratively solving the function $f^{(\alpha)}$ defined as,

$$f^{(\alpha)} = \sum_{(\beta)=1}^{N_{sys}} \frac{\partial f^{(\alpha)}}{\partial \dot{\gamma}^{(\beta)}} \Delta \partial \dot{\gamma}^{(\beta)} =$$

$$\frac{\dot{\gamma}^{(\alpha)}}{\dot{\gamma}_0} \text{sgn}(\tau^{(\alpha)} - B^{(\alpha)}) - \exp\left[-\frac{F_0}{\kappa\theta}\left\langle 1 - \left\langle \frac{\left|\tau^{(\alpha)} - B^{(\alpha)}\right| - S^{(\alpha)}\mu/\mu_0}{\widehat{\tau}_0\mu/\mu_0}\right\rangle^p\right\rangle^q\right] =$$

$$\frac{\partial}{\partial \dot{\gamma}^{(\beta)}}\left\{\frac{\dot{\gamma}^{(\alpha)}}{\dot{\gamma}_0}\text{sgn}(\tau^{(\alpha)} - B^{(\alpha)}) + \exp\left[-\frac{F_0}{\kappa\theta}\left\langle 1 - \left\langle \frac{\left|\tau^{(\alpha)} - B^{(\alpha)}\right| - S^{(\alpha)}\mu/\mu_0}{\widehat{\tau}_0\mu/\mu_0}\right\rangle^p\right\rangle^q\right]\right\}\Delta\partial\dot{\gamma}^{(\beta)}$$

$$(78)$$

The first term of the last equation equals,

$$\frac{\partial}{\partial \dot{\gamma}^{(\beta)}}\left\{\left[\frac{\dot{\gamma}^{(\alpha)}}{\dot{\gamma}_0}\text{sgn}\left(\tau^{(\alpha)} - B^{(\alpha)}\right)\right]\right\}\Delta\partial\dot{\gamma}^{(\beta)} = \text{sgn}\left(\tau^{(\alpha)} - B^{(\alpha)}\right)\frac{\delta^{(\alpha\beta)}}{\dot{\gamma}_0} \qquad (79)$$

The second term equals zero when $\dfrac{\left|\tau^{(\alpha)} - B^{(\alpha)}\right| - S^{(\alpha)}\mu/\mu_0}{\widehat{\tau}_0\mu/\mu_0} \leq 1$. Note that this condition is sufficient for both Macaulay brackets. For any other case,

$$\frac{\partial}{\partial \dot{\gamma}^{(\beta)}}\left\{\exp\left[-\frac{F_0}{\kappa\theta}\left\langle 1 - \left\langle \frac{\left|\tau^{(\alpha)} - B^{(\alpha)}\right| - S^{(\alpha)}\mu/\mu_0}{\widehat{\tau}_0\mu/\mu_0}\right\rangle^p\right\rangle^q\right]\right\}\Delta\partial\dot{\gamma}^{(\beta)} =$$

$$\exp\left[-\frac{F_0}{\kappa\theta}\left\langle 1 - \left\langle \frac{\left|\tau^{(\alpha)} - B^{(\alpha)}\right| - S^{(\alpha)}\mu/\mu_0}{\widehat{\tau}_0\mu/\mu_0}\right\rangle^p\right\rangle^q\right]\left(1 - \left(\frac{\left|\tau^{(\alpha)} - B^{(\alpha)}\right| - S^{(\alpha)}\mu/\mu_0}{\widehat{\tau}_0\mu/\mu_0}\right)^p\right)^{q-1}$$

$$\left(\frac{\left|\tau^{(\alpha)} - B^{(\alpha)}\right| - S^{(\alpha)}\mu/\mu_0}{\widehat{\tau}_0\mu/\mu_0}\right)^{p-1}\frac{q\,p}{\widehat{\tau}_0\mu/\mu_0}\left[\left(\frac{\partial\tau^{(\alpha)}}{\partial\dot{\gamma}^{(\beta)}} - \frac{\partial B^{(\alpha)}}{\partial\dot{\gamma}^{(\beta)}}\right)\text{sgn}\left(\tau^{(\alpha)} - B^{(\alpha)}\right) - \frac{\mu}{\mu_0}\frac{\partial S^{(\alpha)}}{\partial\dot{\gamma}^{(\beta)}}\right]$$

$$(80)$$

The derivatives for the discrete implicit scheme have the following shape

$$\frac{\partial B_{t+\Delta t}^{(\alpha)}}{\partial \dot{\gamma}^{(\beta)}} = \frac{\left[h_B - r_D^{(\alpha)}B_t^{(\alpha)}\text{sgn}\left(\dot{\gamma}^{(\alpha)}\right)\right]\delta^{(\alpha\beta)}\Delta t}{1 + r_D^{(\alpha)}\Delta t\left|\dot{\gamma}^{(\alpha)}\right|} \qquad (81)$$

$$\frac{\partial S_{t+\Delta t}^{(\alpha)}}{\partial \dot{\gamma}^{(\beta)}} = \frac{\left[h_S - d_D\left(S_t^{(\alpha)} - S_0^{(\alpha)}\right)\right]\text{sgn}\left(\dot{\gamma}^{(\alpha)}\right)\delta^{(\alpha\beta)}\Delta t}{1 + d_D\Delta t\left|\dot{\gamma}^{(\alpha)}\right|} \qquad (82)$$

113

The Newton-Raphson method is usually an efficient solving technique, but it does not guarantee the convergence of the calculation, especially if the initial guess is far from the solution. For this problem, the initial guess corresponds to the ISVs from the previous time step, which may vary significantly over a time step. Therefore, after the Newton-Raphson method is executed; a line search algorithm aids in the convergence of the equations [123]. In certain cases the line search algorithm does not assure convergence, so the time increment is then refined into subincrements within the UMAT to integrate the constitutive equations, in a process that is transparent to the underlying FEM algorithm. To summarize the functioning of the algorithm, Figure 55 presents a flow chart with the computations performed by the UMAT for each time step; this is a modified version of the scheme described by McGinty [123].

Furthermore, Figure 56 outlines the interaction between the ABAQUS FEM algorithm and the UMAT. For each time increment, ABAQUS passes to the UMAT the deformation gradients at the beginning $\boldsymbol{F}_t$ and end $\boldsymbol{F}_{t+\Delta t}$ of the time increment. After resolving the kinematics of plastic deformation, the elastic deformations, the Jacobian and the Cauchy stresses (see Ref. [123] for further details), the UMAT updates the Euler angles, and the ISVs–plastic stains, back stress, slip resistance–, and returns to the FEM algorithm controlled by ABAQUS.

The integration scheme is always subject to improvement; for example, the power functions employed by Shenoy et al. [184] for the IN100 constitutive formulation are less stiff than the exponential function in Equation (72), which can lead to an abnormal abortion of the simulations caused by a diverging number of time subincrements. One strategy to avoid an unbounded number of time subincrements has been to set a low limit to the maximum time increment in the FEM computations. This strategy is highly undesirable since it imposes limits on time increments for the entire FEM code that cannot be modified based on the variable convergence requirements of the constitutive model. In other words, if the constitutive model requires a small limit in the time increment to be able to converge at a specific point in the loading history (e.g., the initial steps of a dwell period, at the onset of plastic deformation or after changing the loading direction), that small time increment

114
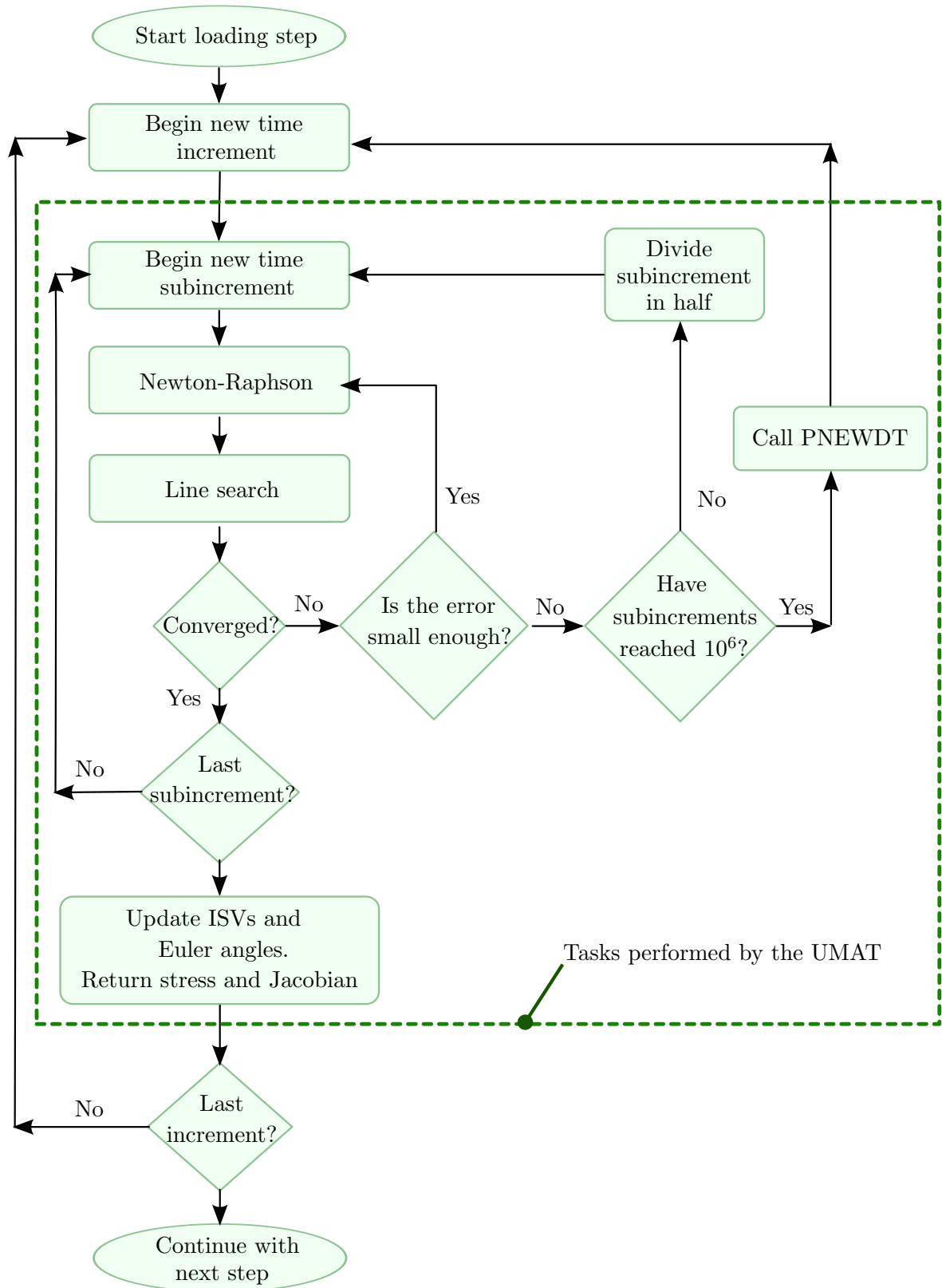
Figure 55: Flow chart showing the numerical integration scheme of the constitutive model for each loading step. Adapted from [123].
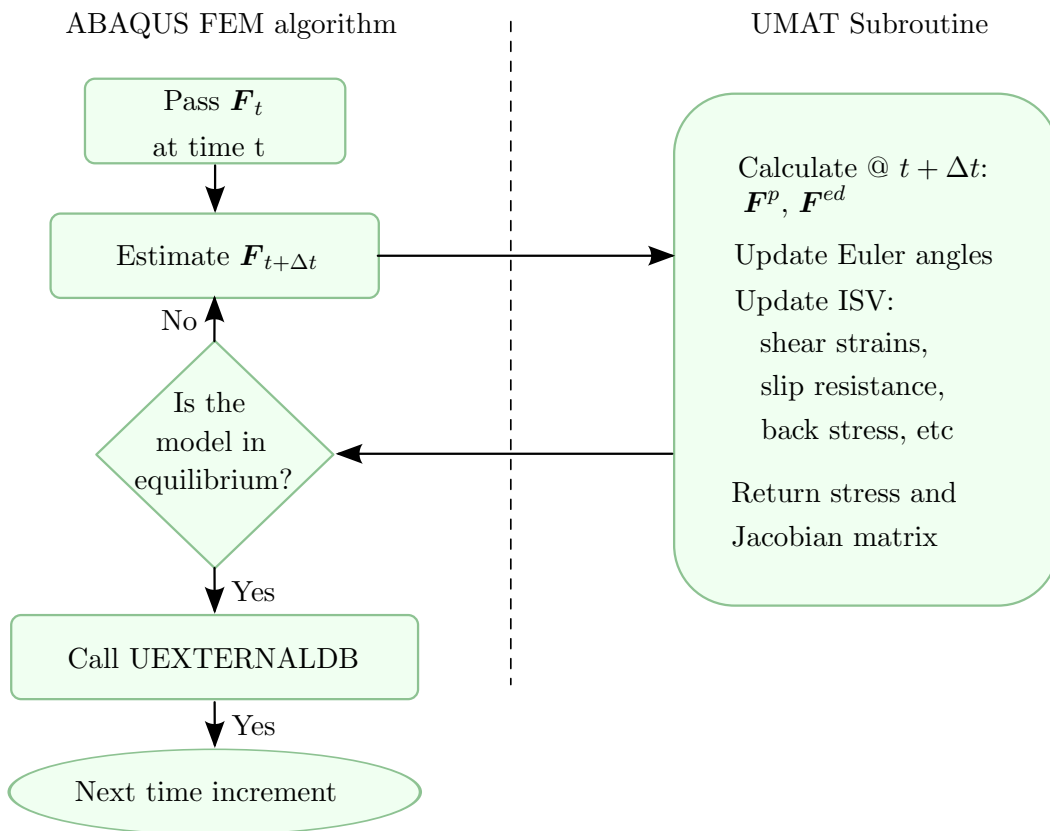
Figure 56: Flow chart showing the interaction of ABAQUS finite element algorithm with the UMAT subroutine. Adapted from [123].

becomes the maximum possible increment for the entire step.

A more adequate strategy to avoid the problem is to limit the maximum number of subdivisions (e.g., lower than 10^6) and restart the analysis of the current step with a smaller time increment; this means that the sub-incrementation is not entirely transparent to the FEM algorithm. This methodology has been implemented using the ABAQUS command "PNEWDT", which restarts the analysis of the current step with a smaller time increment every time the number of subdivisions reaches $1x10^6$, as shown in Figure 55. This strategy demonstrated that the maximum time increment was not a limiting factor, and the running time of the simulation decreased sharply (for example, simulations with hold time run about one order of magnitude faster).

5.3.4 Calibration of the constitutive model for RR1000 superalloy

The constitutive model was exercised using a mesh similar to that shown in Figure 53 with unimodal grain size distribution, rendering about 30 grains, created with the Mesh Generator. Loading consisted of applying a low-amplitude cyclic displacement along the Z direction and periodic loading conditions in which the sum of forces and moments on opposite faces was equal to zero. Table 5 presents the values of the constants, which are similar to those used by Lin [105] at 650°C and strain rates of 0.5%/s, 0.05%/s and 0.005%/s., except for a 15% increment in the initial values of the threshold stress (S_0).

The results are compared to experimental data in Figures 57, 58, and 59, which show the red squares from the simulations overlapping the experimental data in black circles. These results suggest that the calibration by Lin et al. [105] for a 2-D model works adequately. However, the analysis of the parameters points out that the initial value of the threshold stress for the cube slip is about an order of magnitude smaller than that of the octahedral slip. Such a fact does not seems to be reasonable from a physical standpoint if we consider that the cube slip mainly represents the zig-zag meandering of dislocations along octahedral planes. Even though cube slip via a zig-zag cross-slip mechanism has not been explicitly observed in RR1000 alloy, a limited amount is expected to develop, but this argument would not justify the difference in the initial value of the threshold stresses.

117

Table 5: Initial values of the parameters of the constitutive model.

Parameter	Octahedral slip	Cube slip
F_0 $(kJmol^{-1})$	295	295
p	0.31	0.99
q	1.8	1.6
$\dot{\gamma}_0$ (s^{-1})	120	4
$\widehat{\tau}_0$ (MPa)	810	630
S_0 (MPa)	400	55
h_B (GPa)	400	100
h_S (GPa)	160	4.5
d_D (MPa)	6024	24
μ'_0 (GPa)	72.3	28.6
f_c	0.42	0.18

Other parameters: $C_{11} = 166.2 GPa$, $C_{12} = 66.3 GPa$, $C_{44} = 138.2 GPa$, $\lambda = 0.85$, $\mu_0 = 192 GPa$.
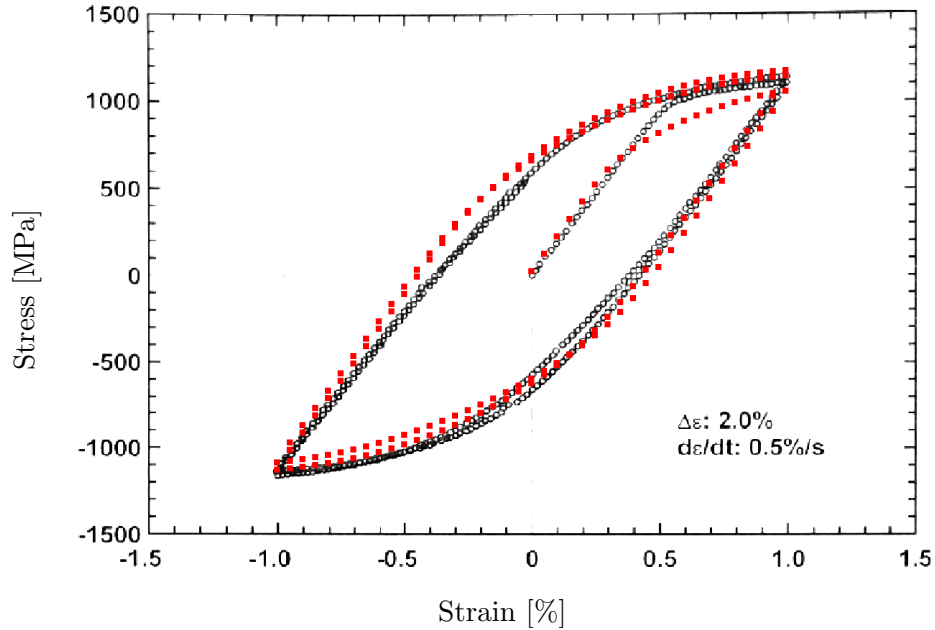
Figure 57: Stress-strain results for the cubic mesh undergoing 2% cyclic displacement-controlled loading at 0.5%/s strain rate: simulations (red) and experiments (black) [220].
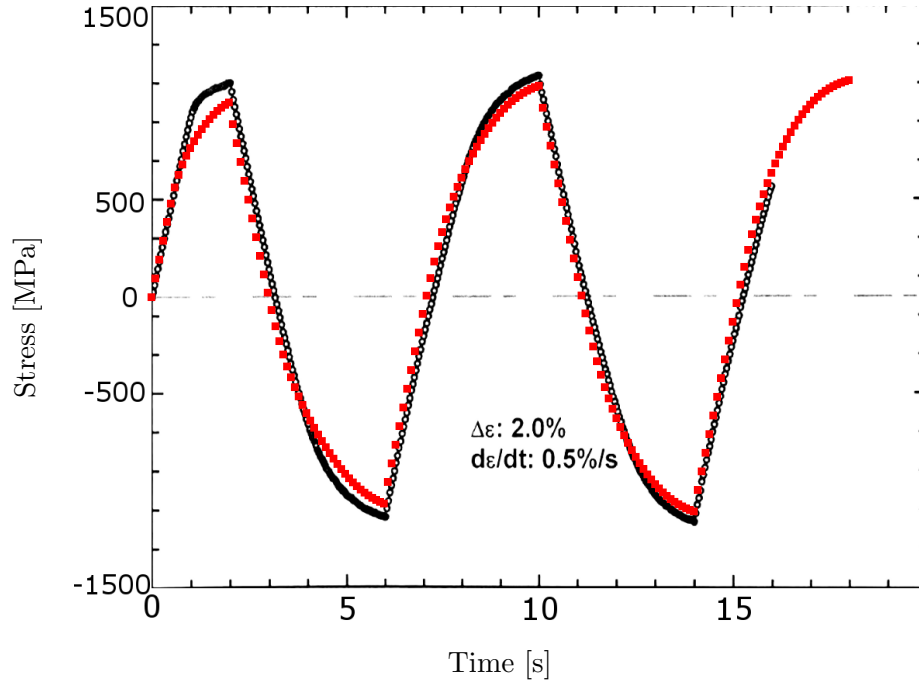
Figure 58: Stress-time results for the cubic mesh undergoing 2% cyclic displacement-controlled loading at 0.5%/s strain rate: simulations (red) and experiments (black) [220].

The partition of plastic strain between octahedral and cube planes can be quantified by comparing the equivalent plastic strain, $\epsilon_{eq}^{pl} = \sqrt{2/3 \sum \epsilon_{ij}^{pl}}$ calculated based on either the contribution of the octahedral planes or the cube planes, i.e.,

$$E_{Oct}^{pl} = \sum_{\alpha=1}^{12} \gamma_{Oct}^{(\alpha)}(\boldsymbol{s}_0^{(\alpha)} \otimes \boldsymbol{m}_0^{(\alpha)}) \text{ and } E_{Cub}^{pl} = \sum_{\alpha=1}^{6} \gamma_{Cub}^{(\alpha)}(\boldsymbol{s}_0^{(\alpha)} \otimes \boldsymbol{m}_0^{(\alpha)}),$$

in which $\boldsymbol{s}_0^{(\alpha)}$ and $\boldsymbol{m}_0^{(\alpha)}$ are the slip plane normal and the slip plane direction in the intermediate configuration respectively.

To reproduce the work by Lin et al.[105] as closely as possible, a set of simulations were designed rendering planar sheets of one element thickness and explicit circular grains. The resulting octahedral and cube equivalent plastic strains after five loading cycles are depicted in Figure 60. These results suggest that at 650°C the contribution from octahedral and cube slip are comparable, which is not in agreement with the general behavior expected for Ni-base superalloys at that temperature. This discrepancy is caused by the lack of uniqueness of the constants for the constitutive model when they are fitted to macroscopic tensile

119
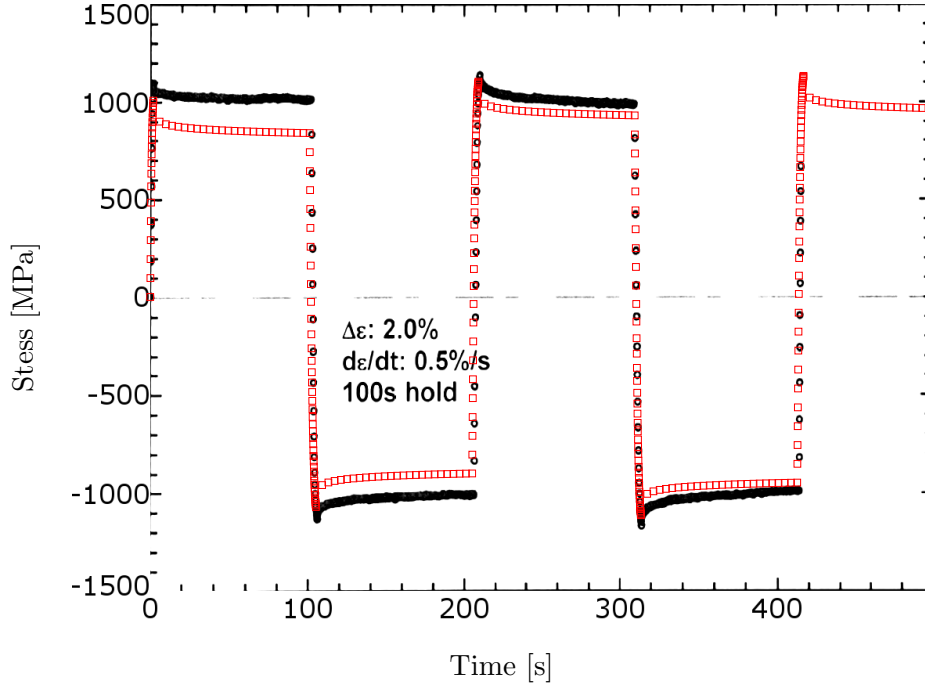
Figure 59: Stress-time results for the cubic mesh undergoing 2% cyclic displacement-controlled loading at 0.5%/s strain rate with 100s hold time: simulations (red) and experiments (black) [220].

experiments of polycrystals. Furthermore, even though the macroscopic behavior might match the experiments, the local overestimation of cube slip may affect fatigue assessment by predicting lower values of octahedral strains. Currently, there is no accepted methodology to fit the constitutive model with cube slip originated by the zig-zag mechanism. Therefore, since the zig-zag mechanism requires dislocations to move along octahedral planes, the best guidelines for defining the values of the parameters are that octahedral slip dominates and that the initial value of the threshold is, at least, larger for the cube than for the octahedral slip planes.

Testing single crystals oriented for octahedral and cube slip activation would not resolve the calibration problem since the cube slip in the model represents mainly octahedral slip with a zig-zig mechanism. Further research needs to be done to introduce proper calibration methodologies that convey the physics of dislocation cross-slip along octahedral planes, resulting in plastic deformation along cube planes. However, a relatively simple procedure

120
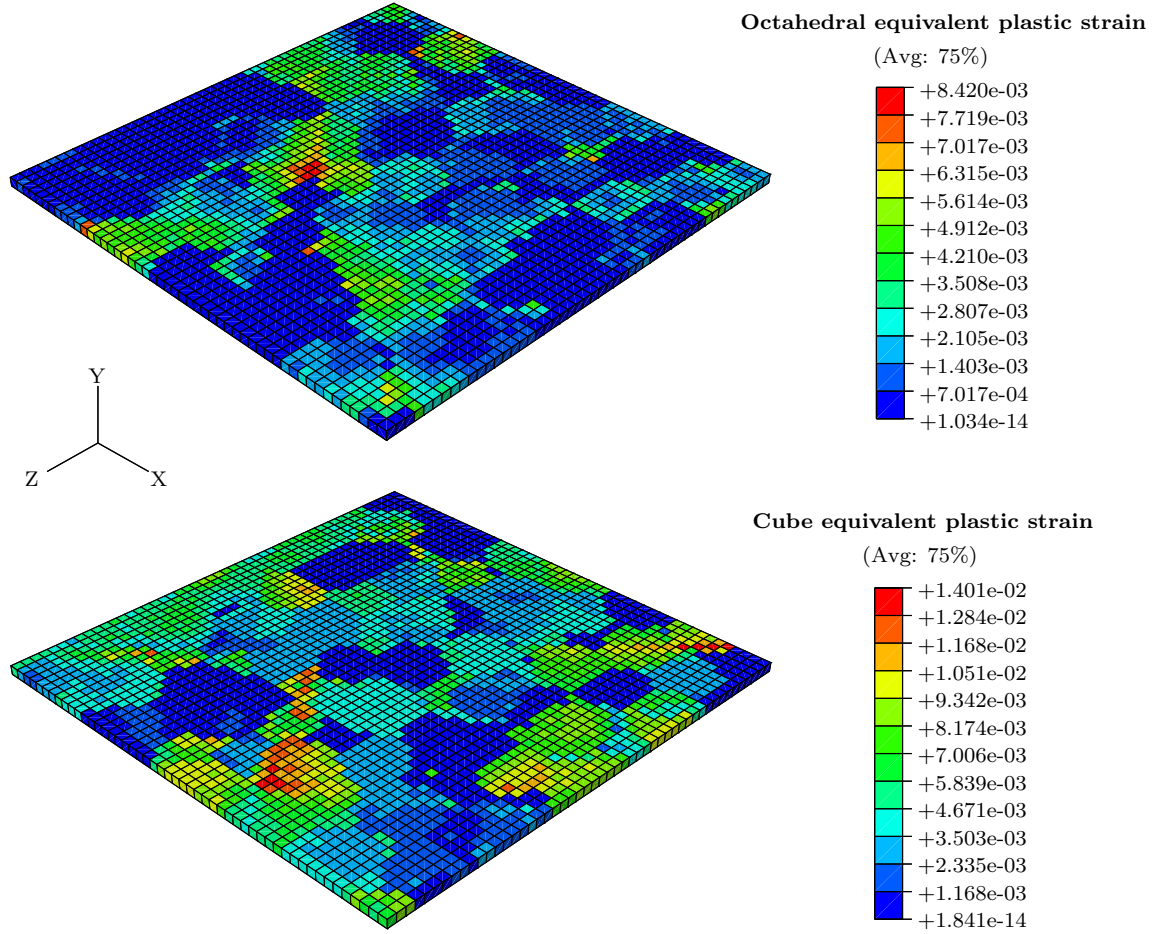
Figure 60: Equivalent plastic strains calculated with the contributions of either octahedral and cube slip.

to test the model would be to run EBSD analysis of deformed polycrystals and quantify the number of grains in which cube slip occurs by observing the crystallographic direction of the macroscopic slip bands. Then, the constants in the model (e.g., the ratio between the octahedral and the cube back stress thresholds) could be adjusted quantitatively to represent the macroscopic partition between octahedral and cube slip.

Another route to verification of the quality of the model relates to the cross-slip mechanism that provides the cube slip. In a recent publication, Tinga et al. [198] explained that in order to have cross-slip, the resolved shear stress on the octahedral planes should have the same direction on both planes, otherwise the γ' precipitates will impede further movement of dislocations. Hence, the direction of the resolved shear stress on pairs of octahedral

planes that lead to cube slip were compared, and on certain grains with non-zero cube slip, the stress showed opposite signs. In consequence, the model as presented and fit by Lin et al. [106] presents certain aphysical aspects, in spite of the overall apparent agreement with experimental data.

5.3.5 Improvements in the calibration of the constitutive model

The arguments in the previous section suggest that the constants of the crystal plasticity model need to be recalibrated in an attempt to make the threshold stress for the octahedral planes lower or at least equal to that for the cube planes. For the recalibration, the higher rate (0.5%/s) from [220] was not considered because it presented a softening behavior (in comparison with the other rates) that was not explained by the authors, cannot be justified by the physics of plastic deformation of superalloys, and perhaps raises concern about the accuracy of the experimental procedures. Hence, the constitutive model was recalibrated using only two strain rates 0.05%/s and 0.005%/s, aiming to lower the threshold stresses for the octahedral slip systems below that of the cube slip system. After many ($\sim$ 70) trial-and-error adjustments of the parameters, the results employing the constants in Table 6 were considered as "acceptable" to a first approximation.

For example, Figure 61 presents the experimental saturated loop for 0.05%/s strain rate compared to the results from the simulations used for calibration. Similarly, Figure 62 and Figure 63 present the peak load as a function of time for 0.05%/s and 0.005%/s strain rates, respectively. Finally, the validation of the model under dwell conditions is presented in Figure 64. To assess the convergence with increasing numbers of grains, Figures 61 to 64 include the results of more refined models with 5832 elements and about 170 grains randomly oriented. The refinement of the SVE only increased the stress by about 1-2.5%, which suggests that the model calibration represents the mean behavior. Indeed, these differences have a minor effect in the calculation of the FIP due to the uncertainty in determining the Fatemi-Socie constant k (Equation (9)).

Although the calibration of the crystal plasticity model could still be improved, the lack of slip transmission across GBs and the aphysical aspects in the model along with the scarce

Table 6: Parameters of the constitutive model the resulted from the recalibration procedure.

Parameter	Octahedral slip	Cube slip
F_0 $(kJmol^{-1})$	885	885
p	0.217	0.495
q	2.25	1.66
$\dot{\gamma}_0$ (s^{-1})	120	4
$\widehat{\tau}_0$ (MPa)	810	630
S_0 (MPa)	210	288
h_B (GPa)	40	50
h_S (GPa)	320	6.75
d_D (MPa)	1204.8	12
μ'_0 (GPa)	72.3	28.6
f_c	0.315	0.18

Other parameters: $C_{11} = 166.2 GPa$, $C_{12} = 66.3 GPa$, $C_{44} = 138.2 GPa$, $\lambda = 0.85$, $\mu_0 = 192 GPa$.

experimental data available limit the accuracy of the results. Therefore, this investigation assumes that the model describes the mean behavior of RR1000 alloy adequately, and continues with the analysis of cracks, pointing out that some limitations could arise.
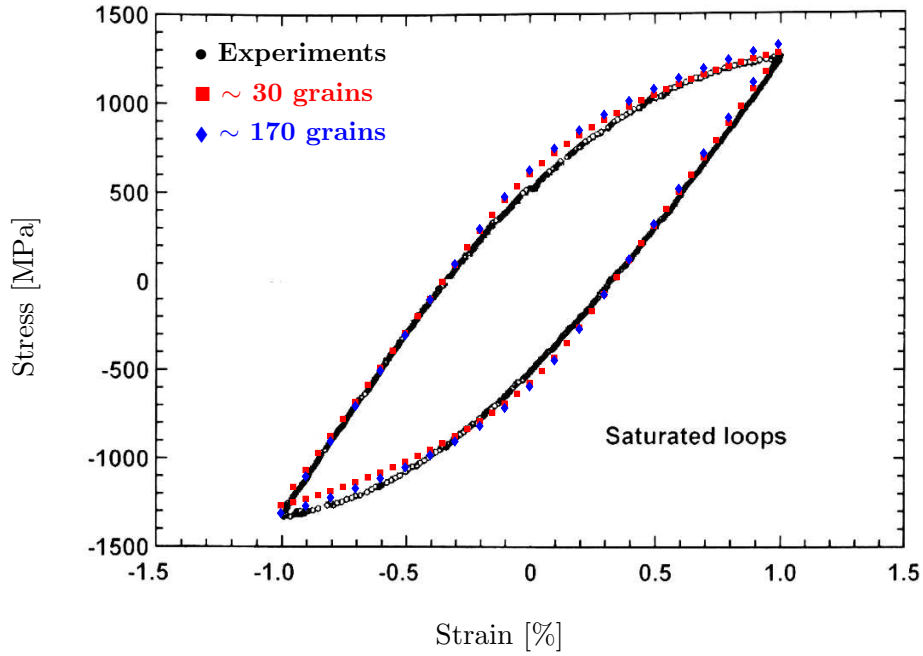
Figure 61: Stress-strain saturated hysteresis loop under displacement-controlled loading at 0.05%/s strain rate, comparing simulations. Symbol legend: ■ Simulations ∼ 30 grains, ♦ Simulations ∼ 170 grains, ● Experiments (black) [220].
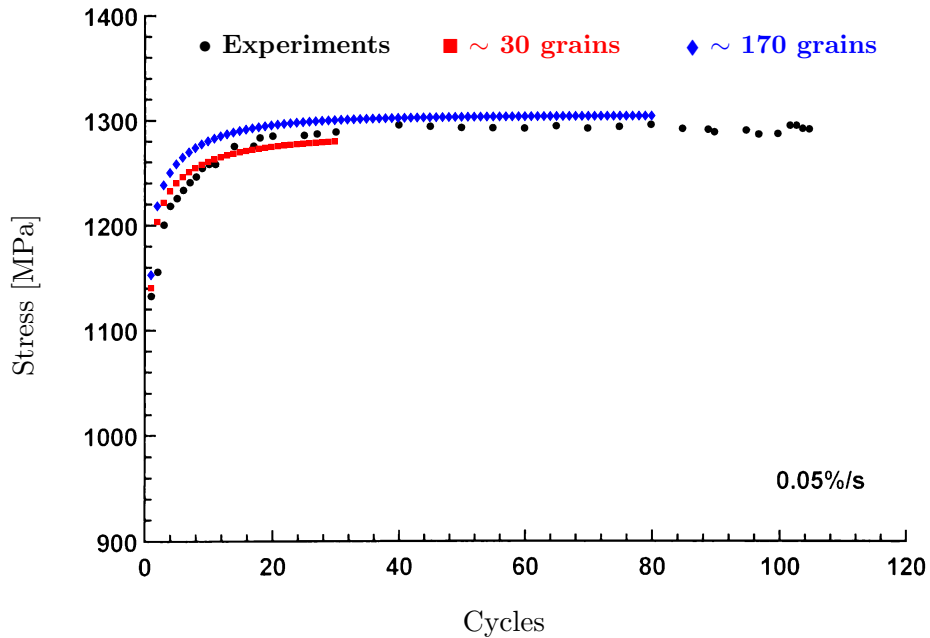
Figure 62: Stress vs. cycles results for the cube under cyclic displacement-controlled loading at 0.05%/s strain rate, comparing simulations. Symbol legend: ■ Simulations ∼ 30 grains, ♦ Simulations ∼ 170 grains, ● Experiments (black) [220].
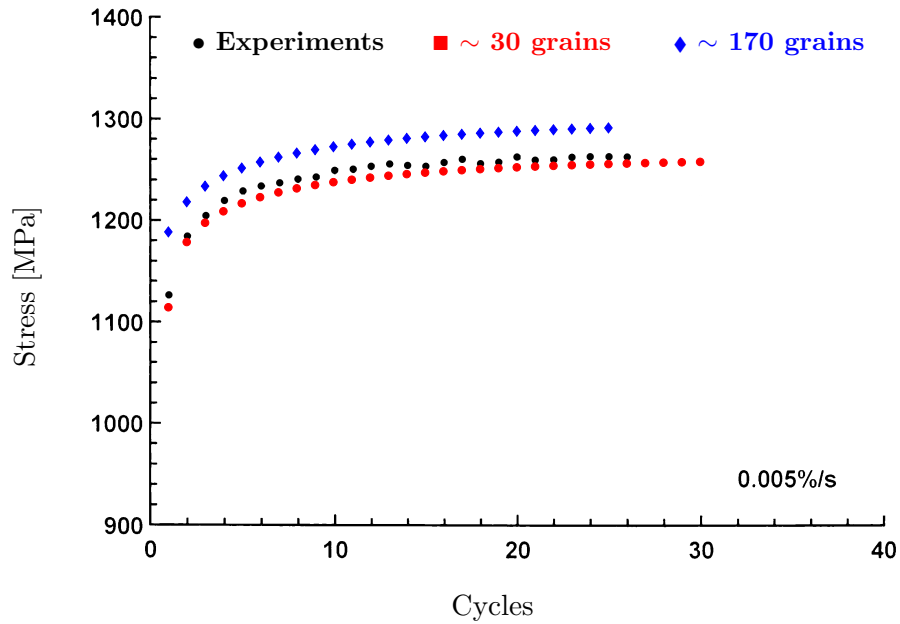
Figure 63: Stress vs. cycles results for the cube under cyclic displacement-controlled loading at 0.005%/s strain rate, comparing simulations. Symbol legend: ■ Simulations ~ 30 grains, ♦ Simulations ~ 170 grains, ● Experiments (black) [220].
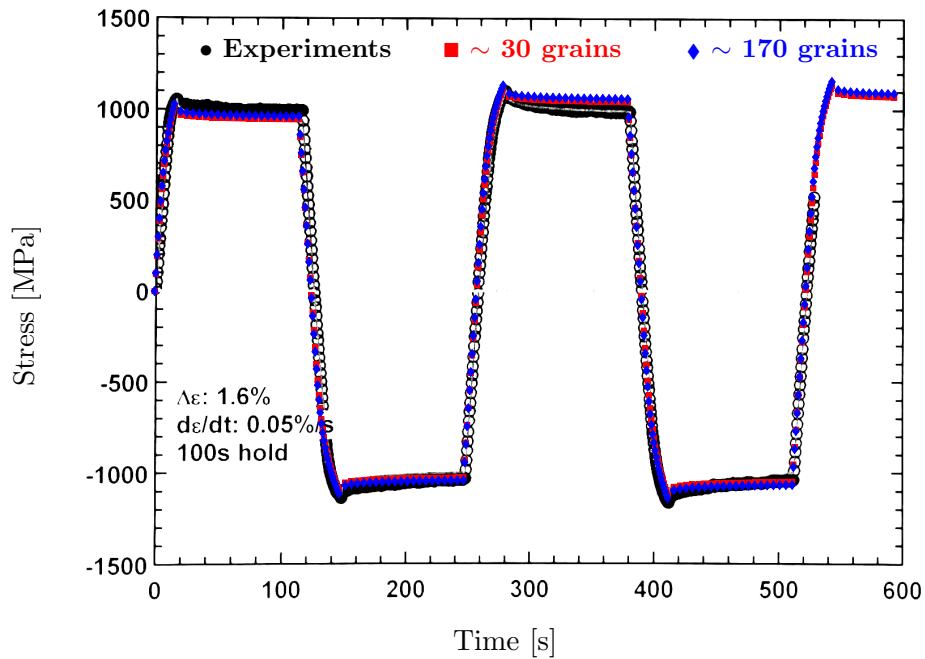
Figure 64: Stress vs. time results for the cube under cyclic with 100s dwell displacement-controlled loading, comparing simulations. Symbol legend: ■ Simulations ~ 30 grains, ♦ Simulations ~ 170 grains, ● Experiments (black) [220].

5.4 ΔCTD vs. FIP for RR1000

The response of the constitutive equation for RR1000 alloy is further explored with a set of simulations of single crystals with cracks, similar to those presented in Chapter 3. The simulations correspond to the circular crack tip introduced in Figure 10, using different stationary cracks lengths of $2\mu m$, $5\mu m$, $7.5\mu m$, $10\mu m$ and $15\mu m$. The simulations considered three loading cycles according to Figures 12 and 13, and the FIP was evaluated in the last half-cycle. The entire crystal obeyed the RR1000 constitutive model (i.e., homogeneous case with no explicit slip band) and the range of loading was expanded by including cases Shear4 and Mixed4 detailed in Table 7, while the rest of the loading cases were defined in Table 1. Similar to Chapter 3, the crystallographic planes are oriented so that one octahedral slip direction lies parallel to the plane of the crack.

Figure 65 presents the maximum FIP among all elements versus the ΔCTD for all the loading ranges simulated. On each plot two regimes can be distinguished: to the left the region in which elastic deformation dominates the driving forces, and to the right the region in which plastic deformation is significant. The change in regime occurs for values of ΔCTD about $10^{-2}\mu m$, which is significantly greater than the Burgers vector ($\sim 10^{-4}\mu m$ to $10^{-3}\mu m$), as would be expected. This discrepancy should be expected since the constitutive model was calibrated using cyclic stress-strain data loaded up to a 2% nominal strain range, which suggests that the model may not be accurate for simulations with limited plastic deformation. Hence, fatigue simulations should focus on the portion of the HCF regime that is farther from the fatigue threshold and closer to the HCF-LCF transition. The constitutive equation requires further calibration and refinement to be employed in the

Table 7: Displacements applied to the top face (in μm) for the additional case analyzed. The displacement of the bottom face had the same magnitude and opposite direction.

	Shear 4	Mixed 4
X axis	0.100	0.0707
Y axis	0	0.0707
Nominal peak strain	1%	1%

VHCF regime, i.e., regimes near the fatigue threshold.
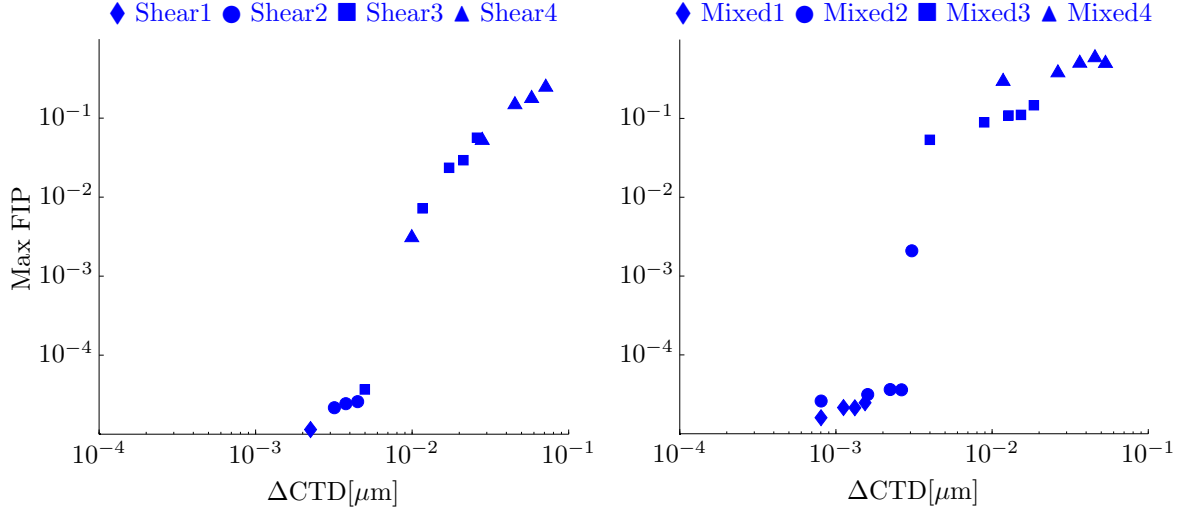
Figure 65: Maximum FIP versus the ΔCTD for shear (left) and mixed mode (right) loading.

Figure 66 compares the value of the ΔCTD with the FIP averaged over a $2\mu m$ band parallel to the crack (similar to that in Figure 10, Chapter 3). Similar to Figure 65, the averaged FIP presents a steep increment for ΔCTD of about $10^{-2}\mu m$, which is thought to be connected with the activation of plastic deformation in increasing numbers of elements within the band. Indeed, such steep increments are not present in Figure 67, which compares the ΔCTD with the total-strain FIP (elasticity included) averaged over bands. The correlation between both measures of the fatigue driving forces is significantly better for Shear than for Mixed loading. Such a disparity in the correlation quality with the loading mode is presumably caused by the averaging volume, which lies along the slip plane oriented for single slip. This fact suggests that the correlation could be improved by using multiple averaging volumes according to the slip plane activated.

To quantify the correlation, a linear regression analysis was performed including only data from Shear3 and Shear4 loading. Data from Shear1 and Shear2 loading were not considered because plastic deformation is very limited and requires further calibration of the constitutive model. Furthermore, mixed loading simulations were not included because, as argued, the quality of the correlation is significantly lower than that for Shear loading.
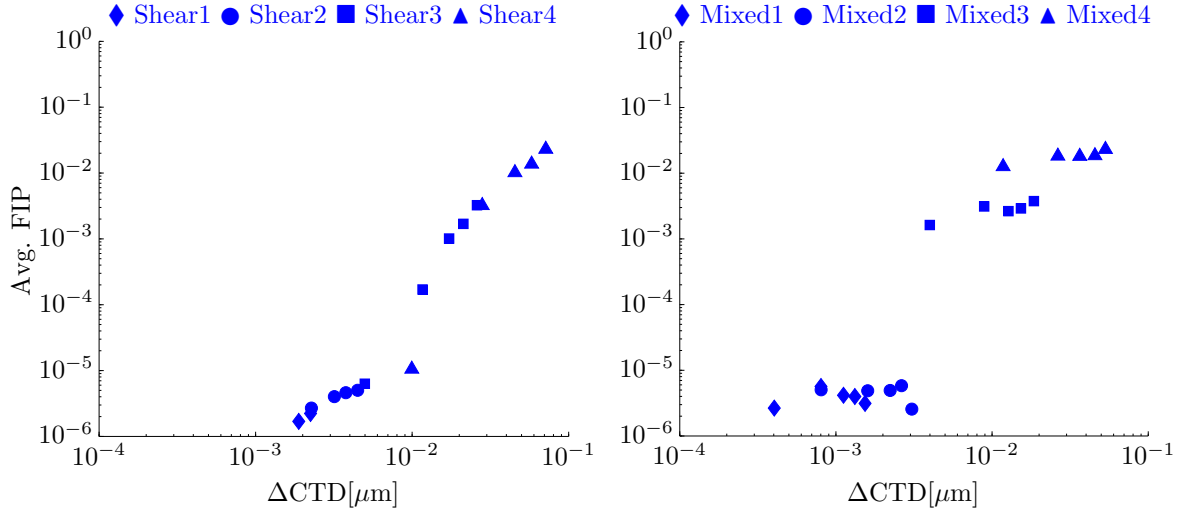
Figure 66: FIP averaged over bands versus the ΔCTD for shear (left) and mixed mode (right) loading.
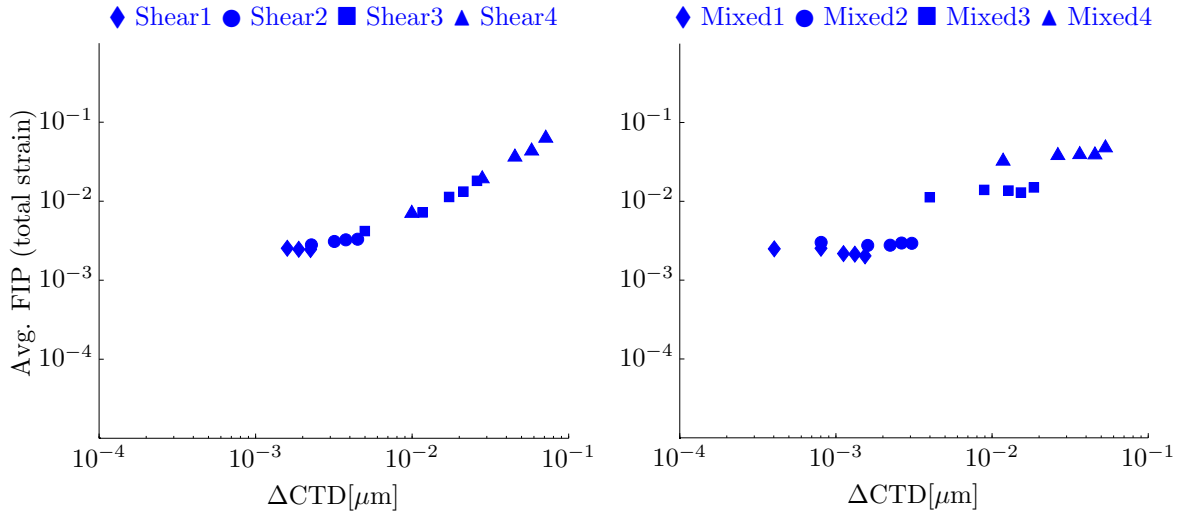
Figure 67: Averaged FIP versus the ΔCTD for shear (left) and mixed mode (right) loading.

The results are depicted by Figure 68, which shows an almost one-to-one relationship ($b \sim 1$) between both driving forces as a function of the Fatemi-Socie constant k. Overall, these results are in agreement with those presented for Cu in Chapter 3 (see Figure 24).
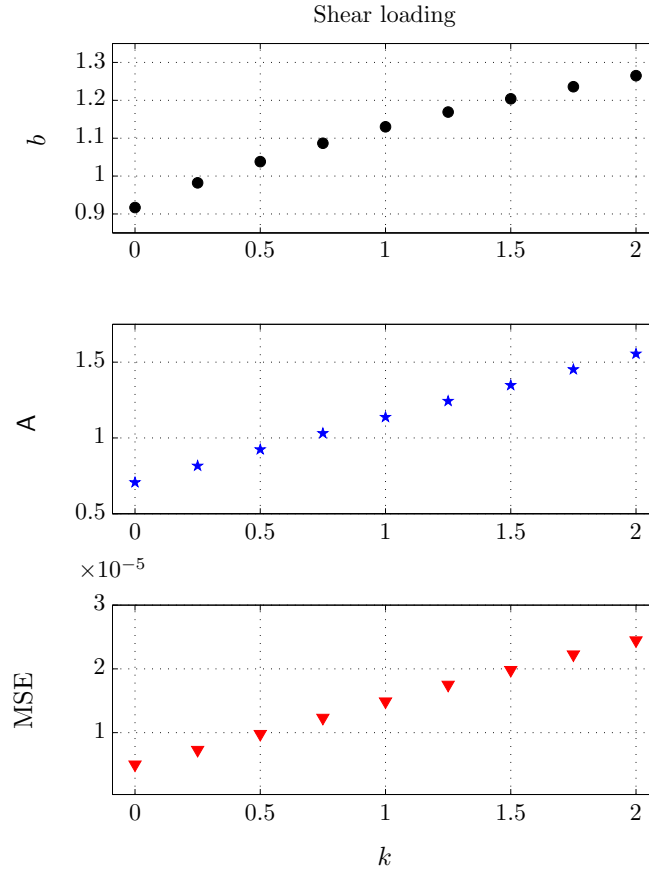
Figure 68: Linear regression of the averaged total-strain FIP vs ΔCTD for shear loading. Here, b and A correspond to Equation (8)

5.4.1 Multiple band analysis

The simulations of cracked single crystals for RR1000 (i.e., Figure 67) suggested that averaged FIP correlated better with ΔCTD under pure Shear rather than Mixed loading. One cause for this difference is, presumably, that the averaging volume was chosen to mimic one dominant slip band and not two. A natural extension would be to calculate a FIP based on the averages on multiple bands along different slip planes. Then, the results of the simulations were reanalyzed by assigning the elements in the meshes to bands (as shown in Figure 41) and averaging the FIP$^{(\alpha)}$ for each slip system on each band (i.e., for each band,

three different averaged FIPs). The equivalent FIP for the multiaxial case is calculated as

$$\mathbf{FIP} = \sum_i^N FIP_i^{(\alpha)} \mathbf{m}^{(\alpha)}, \tag{83}$$

in which $\mathbf{m}^{(\alpha)}$ is a vector that corresponds to the slip direction of slip plane α and $\mathrm{FIP}_i^{(\alpha)}$ are the values of the N higher band-averaged FIPs without repeating slip systems. Here, N refers to the number of slip systems considered and goes between 1 to 5. For each element, the FIP is calculated using Equation (9), in which $k = 0.5$ and $\Delta \gamma_p^\alpha$ is, for each slip plane α, the difference between the maximum and minimum accumulated plastic shear strain over the last cycle, i.e.,

$$\Delta \gamma_p^\alpha = \gamma_p^\alpha \Big|_{\text{over cycle}}^{max} - \gamma_p^\alpha \Big|_{\text{over cycle}}^{min} \tag{84}$$

Hence, the range of slip on system α is determined every cycle.

The magnitude of the ΔCTD in Equation (83) is compared to the magnitude of **FIP** in Figure 70, which presents in blue dots the sum of the contributions from the 5 most active systems. The correlation for Mixed loading has improved significantly, and it is comparable with that for shear loading. For completeness, Figure 70 also presents the calculations of the **FIP** magnitude using increasing numbers of bands that contribute, N from 1 to 5 in Equation (83), as marked with different colors. As expected, in Shear loading one band is enough to provide a good estimation of the ΔCTD. For mixed loading, the difference between using 1 or 3 bands can be up to a factor 2 or 3, while using 4 and 5 bands does not significantly affect the quality.

The comparison between Figures 66 and 70 suggests that selection of an appropriate direction for averaging volume has a central effect on the quality of the driving force, while, at least for the constitutive model employed, the number of bands employed exerts a second order influence. An additional note is that the calculations are based on non-uniform meshes, which introduces error, though small, in the estimations of FIPs.

Finally, the correlation between the FIP and the ΔCTD is evaluated by performing a regression analysis to the data in Figure 70. The regression considered the FIP from the sum of 5 bands (blue dots) from Shear3/Mixed3 (■) and Shear4/Mixed4 (▲) in which plastic deformation dominates the ΔCTD. The result of the correlation is presented in Figure 71,
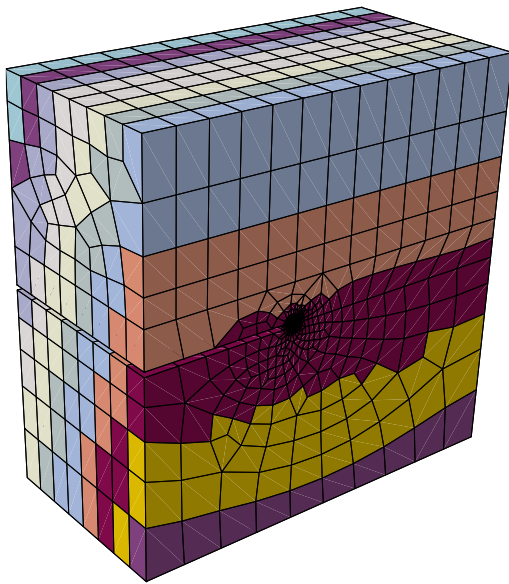
⟨1 1 1⟩
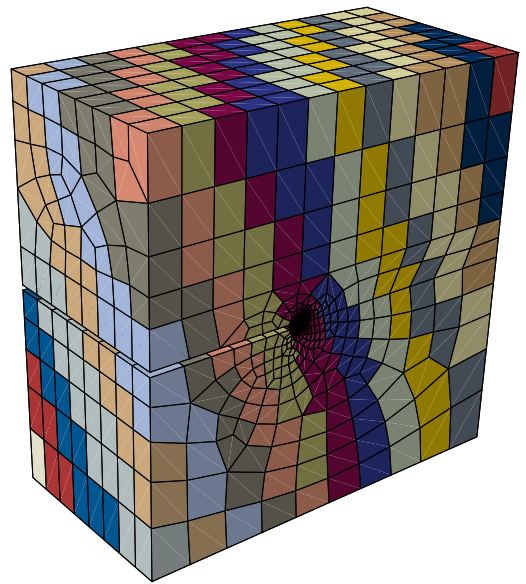
⟨-1 1 1⟩
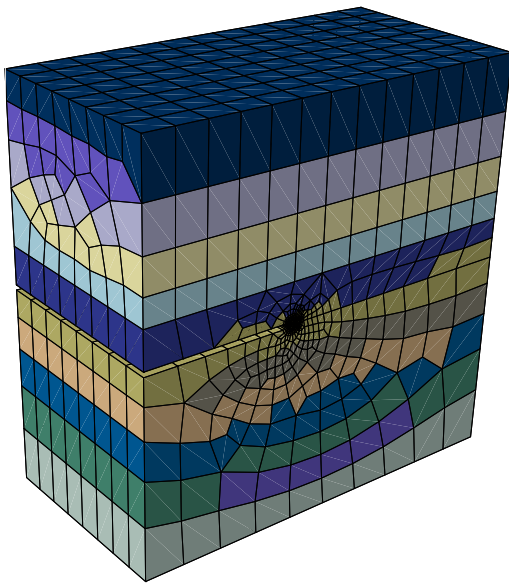
⟨-1 -1 1⟩
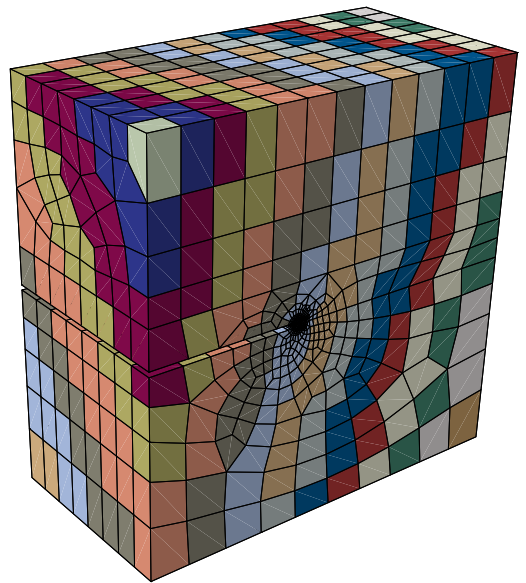
⟨1 -1 1⟩

Figure 69: Representation of the averaging volumes for different normal planes. Each color corresponds to a band. For further details about the crack tip shape refer to section 3.2.1 in Chapter 3.
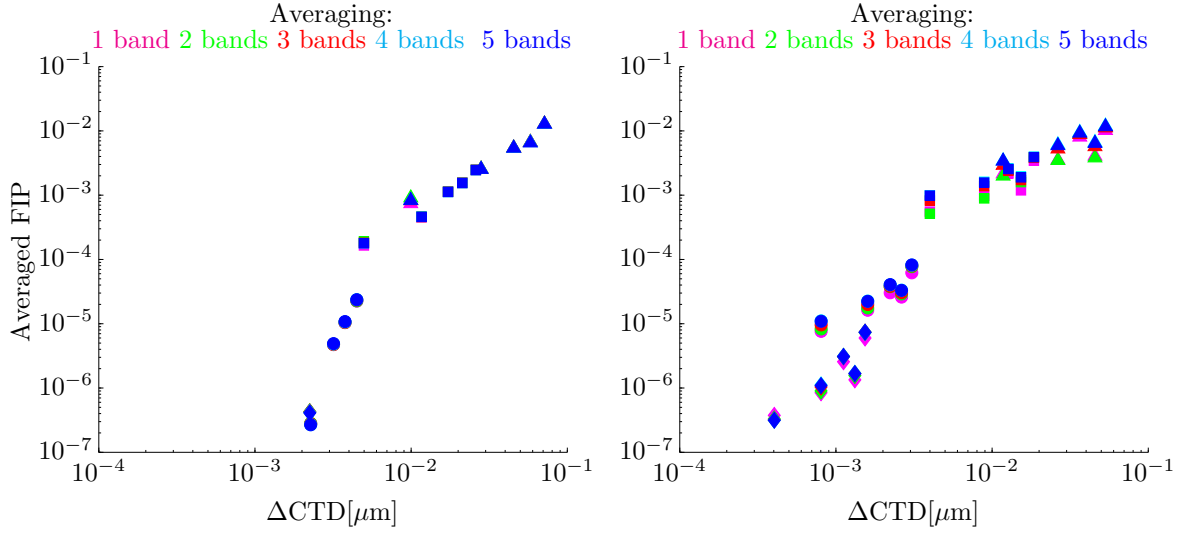
Figure 70: FIP calculated as a contribution different number of bands versus ΔCTD for shear (left) and mixed mode (right) loading.

which shows that both shear and mixed data support a one-to-one relation. The exponent $b = 1.16$ in the correlation (Eq. (8)) is close to that found in Figure 68 for k=0.5 ($b = 1.04$). The proportionality constant A differs in the previous analysis by about a factor of two due to the different methodologies employed to calculate the FIP. Moreover, the quality of the correlation is better than that for the correlations in Chapter 3, probably because only homogeneous data are employed here. Moreover, more scatter is observed towards the left of the figure, which reflects the influence of the dominant elastic deformation.

5.4.2 Non-local constitutive models

The results presented are based on calculations of the FIP for each element using a local constitutive model, subsequently averaged over finite volumes to produce non-local measurements of the driving force (averaged FIP). An additional possibility would be to develop non-local constitutive models that are able to develop regularized localization of strain and to determine the crack tip process zone. Non-local gradient theories are currently one of the topics of active research, but the complexities involved are significant. On the other hand, non-local integral constitutive models may become a viable and more physical approach that matches naturally into the formulation developed in this thesis. Indeed, the
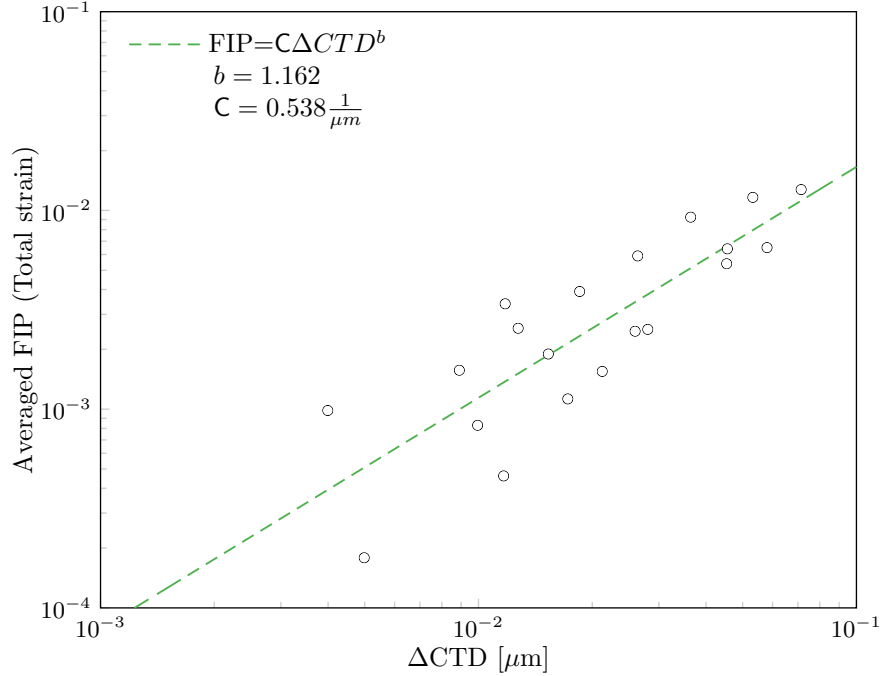
Figure 71: Linear regression of the averaged FIP vs ΔCTD using the data from Figure 70 with FIP greater than 10^{-4}.

constitutive model could be formulated so that the back stress or the slip resistance include a dependence on the averaged value along the band to which the element belong. This type of formulation would be consistent in some sense with the models of dislocation structures proposed by Ortiz and coworkers [158, 159] based on weak forms.

5.5   Preliminary Conclusions

The concepts discussed in the previous chapters regarding the study of early fatigue life and microstructure will next be applied in the study of RR1000 superalloy with dual microstructure. This chapter has described the nature of the RR1000 superalloy for turbine disk applications and introduced a crystal plasticity constitutive formulation showing the following:

- A crystal plasticity model for RR1000 was successfully implemented. The model considers cube slip to account for the zig-zag cross-slip mechanism and fits adequately to macroscopic stress-strain and stress-time experimental data. However, the model

may present some aphysical characteristics such as the dominance of cube slip plastic deformation or stresses incompatible with the zig-zag mechanism in spite of the macroscopic agreement. Furthermore, the GBs are treated in a simplified manner that does not account for slip transmission and the model does not have any intrinsic length scale.

- A new procedure was introduced in the implicit crystal plasticity scheme to enhance efficiency in ABAQUS.

- Modeling dual microstructures has special requirements to account for the moments of the grain size distribution. This work proposed to generate statistics with simulations based on SVE rather than a RVE, to be able to scale the quality of an estimation of the fatigue behavior with the computational effort. Furthermore, a Mesh Generator program has been developed to feed the FE solver with a complex microstructure that may include ALA grains.

- The analysis of single crystals with cracks has shown that the current calibration of the RR1000 constitutive model may not be accurate for VHCF loading type, but is good enough for studying the HCF regime and the transition to LCF. Moreover, for multiaxial loading, the sum of FIPs averages along multiple bands presents better correlation with ΔCTD than the maximum FIP average value.

- The correlation between the FIP and the ΔCTD for RR1000 is approximately one-to-one, which is similar to the results found for Cu in Chapter 3. Since the constitutive models for both metals are completely independent, the similarity in the correlation reinforces the fundamental relation between the FIP and the ΔCTD measures of the driving force .

CHAPTER VI

APPLICATION: FATIGUE MODEL FOR RR1000

The previous chapter presented simulations modeling the constitutive behavior of RR1000 alloy as a polycrystal or a cracked single crystal. This chapter introduces the fatigue model established in Chapter 4 as adapted for the study of RR1000 alloy, along with some details of the implementation in ABAQUS [1]. Because the disks for aircraft gas turbine engines undergo peak loads during takeoffs and landings, the most common test conditions correspond to peak strains between 1% and 2% under strain control with $R_\epsilon = 0.1$ and temperatures from 650°C to 725°C. These loading conditions are reproduced in this study of the effect of microstructure on fatigue early life and should result in nucleation lives on the order of 10^4 to 10^5 cycles.

6.1 Fatigue model implementation

The fatigue model has been implemented in ABAQUS FEM [1]. One drawback of using commercial FEM software is that access to the solver loop is constrained to a few fixed and predefined subroutines or stages. For example, under ABAQUS the constitutive model needs to be defined in the UMAT that is executed at a specific point in the solver loop. Similarly, the user-defined external database subroutine (UEXTERNALDB) is executed at each time increment once all the elements have converged, because it is intended for performing calculations in addition to the FEM computations. This subroutine could be employed when the parameters of the constitutive equation depend on an independent (i.e., decoupled) calculation such as a diffusion-controlled mechanism. Figure 72, adapted from ABAQUS documentation, presents a simplified flow chart describing the instances in which ABAQUS accesses the UEXTERNALDB subroutine during the solver loop.

In this research, the UEXTERNALDB subroutine plays a major role, since it contains an algorithm that deals with the information about microstructure and averaging volumes
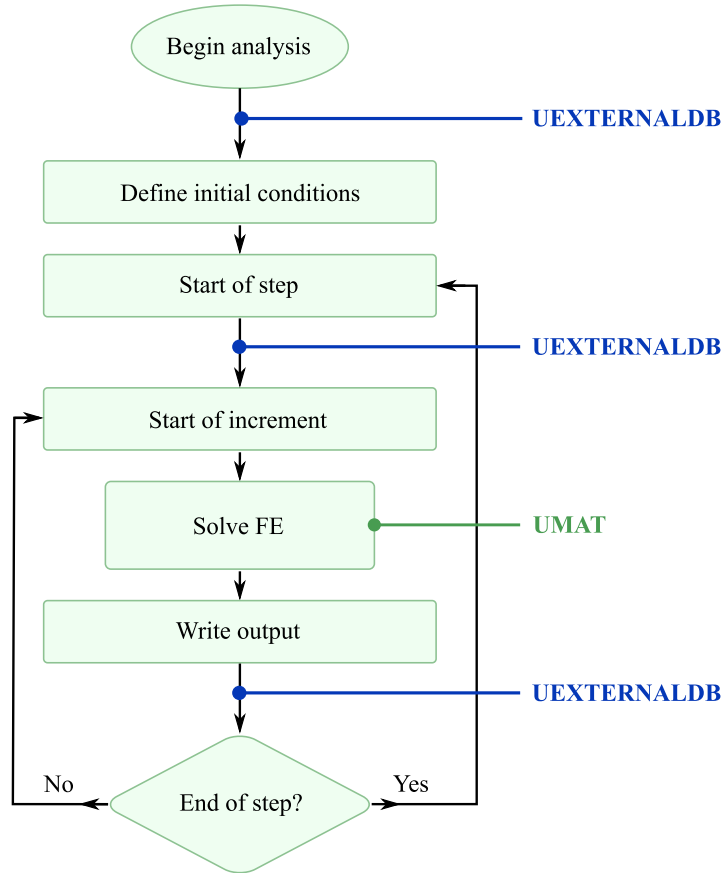
Figure 72: Simplified description of the steps executed by ABAQUS to solve the FE and the instances when the UEXTERNALDB is called. Adapted from ABAQUS documentation.

(e.g., which elements belong to each grain), calculates local and averaged values of FIPs, and estimates the fatigue life for each band among the most important tasks. Using the UEXTERNALDB subroutine allows seamless simulations that can predict whether cracks should grow in transgranular or intergranular fashion, accounting for the crack growth stress redistribution by adding damage to elements only if the crack undergoes opening loads. Additionally, as with any other subroutine in ABAQUS, the UEXTERNALDB subroutine is implemented in Fortran. For further details about the functioning of the UEXTERNALDB subroutine, refer to Appendix B.

6.1.1 Transgranular FIP calculation

The calculation of the FIP requires the evaluation of the cyclic plastic strains, which can be decomposed into reversed cyclic plasticity ($\Delta\epsilon_{\text{cyc}}^{\text{p}}$) and plastic ratcheting ($\Delta\epsilon_{\text{ratch}}^{\text{p}}$), as
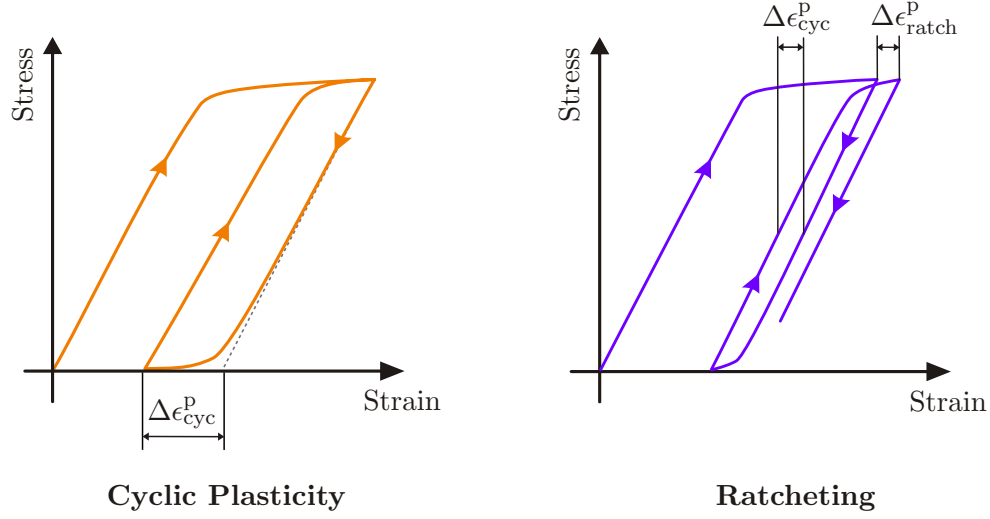
Figure 73: Schematic stress-strain curves depicting reversed cyclic plasticity and ratcheting.

exemplified in Figure 73. The former, also referred to as plastic shakedown, regards to the condition in which the material presents reversed plastic straining without a net accumulation of plastic deformation. The latter refers to cases in which the material accumulates a net amount of directional plastic strain in each cycle.

Following the arguments of McDowell [119], the processes of crack decohesion in slip bands (irreversible slip-driven crack growth) are better represented by the reversed cyclic plastic strain, based on a steady state cyclic behavior, rather than plastic ratcheting. Hence, the FIP$^\alpha$ in Equation (9) is calculated for each element and slip plane using the maximum plastic strain range developed on each slip system without the ratcheting component, as shown in Figure 74. In mathematical terms this is,

$$\Delta\gamma^\alpha\Big|_{\text{ratch}} = \gamma^\alpha\Big|_{\text{end of cycle}} - \gamma^\alpha\Big|_{\text{beginning of cycle}} \tag{85}$$

and

$$\Delta\gamma^\alpha\Big|_{cyc} = \Delta\gamma^\alpha\Big|_{\substack{\text{max} \\ \text{over cycle}}} - \Delta\gamma^\alpha\Big|_{\text{ratch}} \tag{86}$$

137
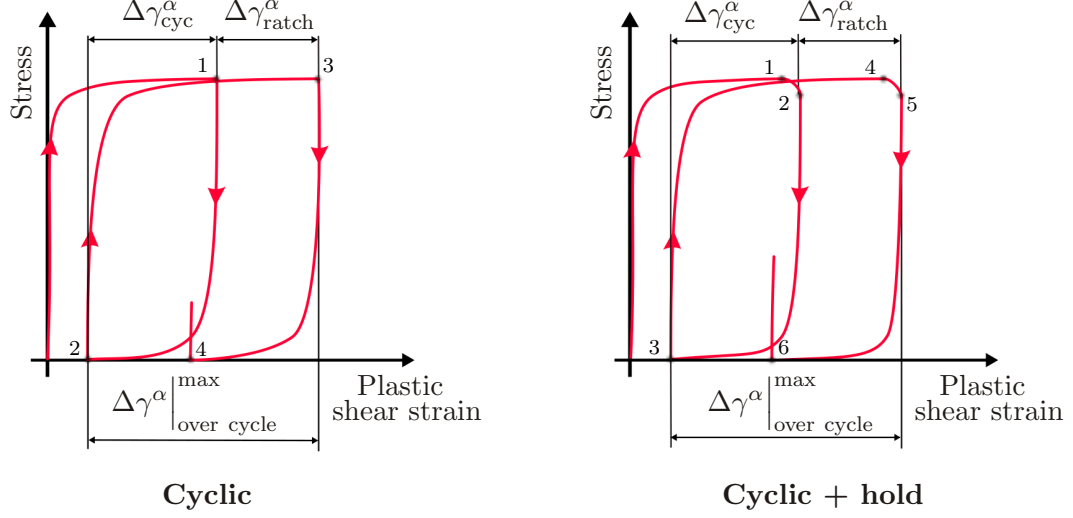
Figure 74: Plastic deformation employed to calculate the FIP with and without holding time. The numbers and dots correspond to a change in loading direction.

6.1.2 Intergranular FIP calculation

The FIP_{int} introduced in equation (16) requires calculate of the stress normal to the GB (σ_n^{GB}) using the stress tensor ($\boldsymbol{\sigma}$) as

$$\sigma_n^{GB} = \vec{\mathbf{m}} \cdot \boldsymbol{\sigma} \cdot \vec{\mathbf{m}} \tag{87}$$

in which $\vec{\mathbf{m}}$ represents the unit vector normal to the GB. Due to the discrete character of the mesh, the boundary is ill-defined, so the direction of the GB needs to be smoothed to compute the normal stress. Therefore, for each element neighboring a grain, the boundary is taken as the normalized sum of the unit vectors from faces shared with the other grain. This method is represented for a 2D case in Figure 75, and in mathematical terms becomes

$$\vec{\mathbf{m}} = \frac{\sum_i \vec{\mathbf{n}}_i}{|\sum_i \vec{\mathbf{n}}_i|}, \tag{88}$$

where $\vec{\mathbf{n}}_i$ corresponds to the unit vector normal to the faces of the elements shared by two grains. To inform the FE in ABAQUS about the GB locations, the Mesh Generator described in 5.2.1 produces and stores the information in a file, which indicates with the number ± 1 the faces of each element (coordinates 1 to 6) that belong to a boundary and its direction (i.e., sign indicates the direction with respect to global coordinates).

| One boundary | Two boundaries | Three boundaries |
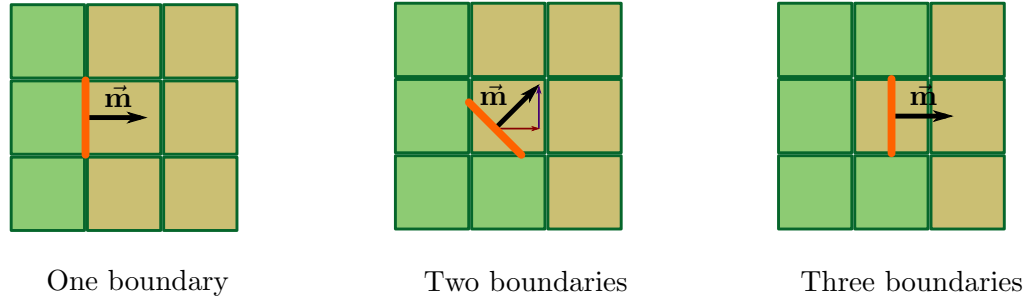
Figure 75: Schematic 2D representation of the equivalent direction of the GB for specific elements in the boundary. Each grain is represented with a different color.

6.1.3 Damage model implementation

The implementation of the elastic stiffness degradation model introduced in Chapter 4 requires interaction between the UEXTERNALDB and the UMAT subroutines. The former determines which elements should be cracked according to section 4.4 and for those elements sets, a value of 1 in a global variable representing $\tilde{d}$. The UMAT adjusts the degradation of the stiffness tensor to achieve convergence, in accordance to section 4.4.1. Figure 76 depicts an example of the effect of adding damage up to $\tilde{d} = 0.99$ on the maximum principal stresses. The damaged elements present stress below 100 MPa (in dark gray) while the neighboring elements present a low to moderate increase in the stress, which is less than a factor of two. For small cracks, the stress intensification does not resemble LEFM singularity models and is greatly affected by the microstructure.

To further verify and validate the damage model, a few realizations were carried out increasing the damage parameter $\tilde{d}$ up to a value of 0.999. The increment in damage increased the run time without any significant change in the FIP for the first grains to crack. Furthermore, for the particular example in Figure 76, the maximum principal stress showed the same distributions, with maximum values of approximately 2100 MPa, and the values for the damaged elements are less than 10 MPa. Hence, these results suggest that increasing $\tilde{d}$ up to 0.99 is an acceptable balance between accuracy and computational work.
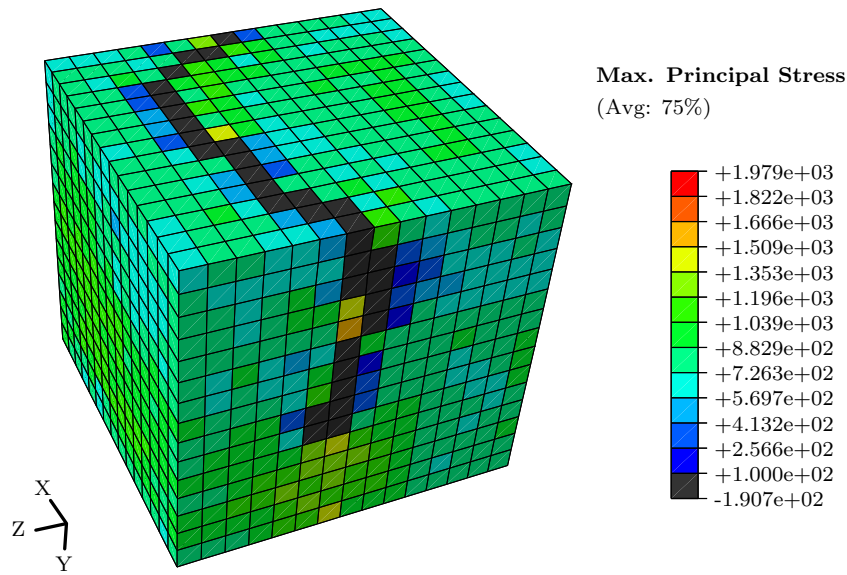
Figure 76: Example of the effect of adding damage to the bands with minimum life. This simulation corresponds to a cube with 52 grains loaded up to 1% strain along Z axis under periodic boundary conditions. The damage elements have much lower stresses (in dark gray), while some of the neighboring elements show an increment due to the local stress intensification (in yellow and orange).

6.2 Fatigue model for RR1000

6.2.1 Mechanical irreversibility factor

The mechanical irreversibility factor ϕ in Equation (12) is controlled by the environment, the type of loading, and the loading history. For Ni-base superalloys at low to moderate temperatures or high frequencies (e.g., higher than 10Hz), diffusion of foreign atoms will be limited, and the main source of irreversibility would be the interaction among defects, particles, etc. (pure mechanical irreversibility [45]); this type of mechanical irreversibility is present even in tests under vacuum. On the other hand, for higher temperatures or low frequencies (e.g., lower than 10^{-4} Hz), mechanical irreversibility may be controlled by a corrosive mechanism, for example, development of a layer of oxides and subsequent brittle fracture [45]. In between those temperature and frequency extremes, defects and foreign atoms contribute to nonlinear and coupled irreversible mechanisms that extend the crack.

To account for the effect of the shape of the loading cycle on the mechanical irreversibility factor, this research follows the work from Tong and coworkers [45, 226, 200]. In this series
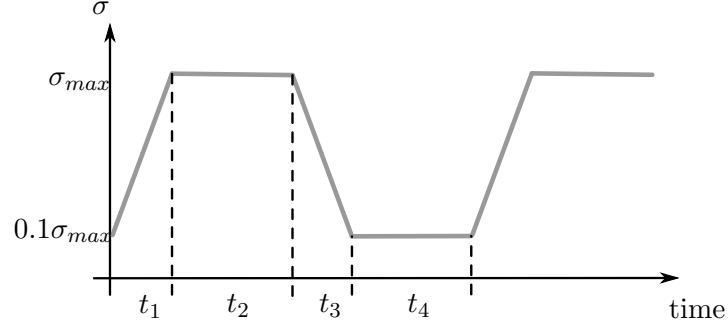
Figure 77: Definition of the loading periods that influence the mechanical irreversibility factor.

of papers, the authors analyzed the effect of different loading frequencies and dwell times in long cracks in RR1000 and showed that the loading half-cycle contributes more to crack extension than dwell or unloading half-cycles. Moreover, they introduced the equation

$$\frac{da}{dN} = C\exp\left(-\frac{Q}{RT}\right)(0.9t_1 + t_2 + 0.1t_3)^{(0.5-\xi)}\Delta K^m, \tag{89}$$

in which t_1, t_2 and t_3 correspond to periods of time in the loading cycle, as defined in Figure 77. Following the analysis in section 4.1.2.2, Equation 89 can be interpreted as the multiplication of two factors: the driving force (ΔK^m) and an irreversibility factor $\phi = C\exp\left(-\frac{Q}{RT}\right)(0.9t_1 + t_2 + 0.1t_3)^{(0.5-\xi)}$.

The modified Paris law in Equation 89 does not distinguish between intergranular and transgranular failure, but it attempts to characterize both failure mechanisms with a single correlation. This approach seems too ambitious since it fails to match the experimental data at very low or high accumulated time $0.9t_1 + t_2 + 0.1t_3$ (see black line in Figure 78, adapted from [200]), which corresponds to the cases of pure transgranular or intergranular failure, respectively. Hence, this investigation proposes that the irreversible factor ϕ depends on the sum $0.9t_1 + t_2 + 0.1t_3$, but the exponent $(0.5 - \xi)$ differs for transgranular or intergranular failure, resulting in a two-slope curve as shown schematically in orange (intergranular-dominated failure) and in blue (transgranular-dominated failure) colors, in Figure 78. A rough estimation of the slopes of the colored segments in Figure 78 results in $\xi_{trans} = 0.2$
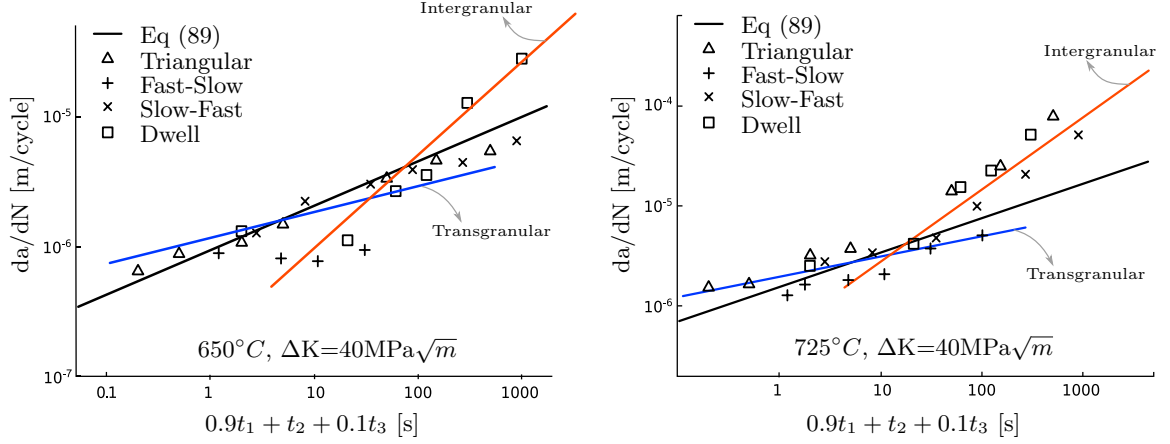
Figure 78: Crack growth rates as a function of $0.9t_1 + t_2 + 0.1t_3$. The black line corresponds to the model in Equation (89), while the blue and orange lines correspond to the proposed decoupling of transgranular and intergranular failure. Adapted from [200].

and $\xi_{int} = 0.05$. So the irreversible factors become, for transgranular failure,

$$\phi_{trans} = C \exp\left(-\frac{Q}{RT}\right)(0.9t_1 + t_2 + 0.1t_3)^{(\frac{1}{2}-0.2)}, \tag{90}$$

in which the factor $\exp\left(-\frac{Q}{RT}\right)$ carries an Arrhenius-type of the dependence with the temperature that represents the mobility of defects and foreign atoms. For intergranular failure, the Arrhenius dependence has the contribution from the maximum principal stress (PS) as proposed by Miller et al. [132]:

$$\phi_{int} = C_{int} \exp\left(-\frac{Q - B_{int}PS}{RT}\right)(0.9t_1 + t_2 + 0.1t_3)^{(\frac{1}{2}-0.05)}. \tag{91}$$

This formulation is equivalent to that proposed in Equation 17 since ϕ_{int} carries all the parameters besides the FIP_{int} in that equation.

6.2.1.1 Grain size influence on transgranular fatigue life

As mentioned in Chapter 4, the correlation between the FIP and the fatigue life depends on multiple microstructure attributes, among which grain size is dominant for superalloys. To account for this, the nucleation regime (Equation 11) depends on the microstructural length scale d_{gr}, which is usually associated with the mean grain size. However, superalloys have shown that neighboring grains with low disorientation (i.e., less than 15°) tend to cooperate as a single supergrain to nucleate cracks more easily [39, 127, 154]. To account for the effect

of clusters of low disorientation grains, the microstructural parameter d_{gr} is defined as the size of the current grain plus a contribution of the first neighbor grains that depends on the disorientation. The misorientation of each grain with its neighbor is calculated among all planes, and if the minimum of those values (the disorientation θ_{dis}) is lower than 20°, the disorientation factor (ω) is computed using

$$\omega = \left\langle 1 - \frac{\theta_{dis}}{20} \right\rangle \tag{92}$$

Thus, ω equals 1 when there is no disorientation (i.e., the grain and the neighbor have exactly the same orientation and should be a single grain), and it equals 0 if the disorientation is 20° or larger. The threshold of 20° was set based on the limit usually considered to distinguish between low and high angle GBs (10° to 20°). As a result, the calculation of the disorientation factor for randomly oriented grains showed non-zero values in fewer than 10% of the GBs.

Equation (92) is a linear approximation of the disorientation between grains employed to estimate the enhancement of plastic deformation at low disorientation GBs. Then, the microstructural length scale d_{gr} is calculated as

$$d_{gr} = D_{st} + \sum_i^n \omega^i {D_{nd}}^i, \tag{93}$$

in which D_{st} is related to the length of the band considered and ${D_{nd}}^i$ relates to the size of all the n neighboring bands. The values of D_{st} and ${D_{nd}}^i$ are calculated for each averaging band as the square root of the area of the band (similar to the approach by Murakami [145]), allowing differentiation among bands in grains that are not spherical and allowing the contribution from bands in neighboring grains that are only in direct contact. Equation (93) proposes a first order Taylor expansion of the dependence of d_{gr} on the ${D_{nd}}^i$ using ω^i as the proportionality coefficients without further evidence due to the lack of experimental data. Thus, the point is made that newer experimental data may allow a better representation of the effect of clusters of grains with low misorientation on fatigue life.

Following Equations (11) and (93) the nucleation life is written as

$$N_{nuc} = \frac{\alpha_g}{D_{st} + \sum_i^n \omega^i {D_{nd}}^i} (\mathrm{FIP}^\alpha)^{-2}, \tag{94}$$

143

The influence of the microstructure in the MSC regime has been defined as the $A(\beta_i)$ factors in Equation (13). The simplest contribution from the grain size can be introduced by defining

$$\beta = \Big(\frac{d_{gr}}{d_{gr}^{ref}}\Big)^{\eta},\tag{95}$$

which follows the dependence on grain size proposed by Alexandre et al. [4] and represents the effects of strain localization. Here d_{gr}^{ref} corresponds to a reference grain size related to the mean grain size of the material employed to calibrate the fatigue model, and η measures the intensity of the grain size effect and usually ranges between 1 and 2 superalloys. d_{gr} is calculated from Equation (93) for each band allowing us to distinguish crack growth paths within a grain and in neighboring bands with low angle misorientation.

The MSC regime is characterized by the MSC growth law

$$\frac{da}{dN}\Big|_{msc}^{\alpha} = \phi_{trans}\Big\langle \Big[\frac{D_{st} + \sum_i^n \omega^i D_{nd}{}^i}{d_{gr}^{ref}}\Big]^{\eta} \mathsf{A}(\mathrm{FIP}^{\alpha}) - \Delta\mathrm{CTD}_{\mathrm{th}}\Big\rangle,\tag{96}$$

which, combined with Equation 90, becomes

$$\frac{da}{dN}\Big|_{msc}^{\alpha} = C\exp\big(-\frac{Q}{RT}\big)(0.9t_1+t_2+0.1t_3)^{(\frac{1}{2}-0.2)}\Big\langle\Big[\frac{D_{st} + \sum_i^n \omega^i D_{nd}{}^i}{d_{gr}^{ref}}\Big]^{\eta}\mathsf{A}(\mathrm{FIP}^{\alpha}) - \Delta\mathrm{CTD}_{\mathrm{th}}\Big\rangle,\tag{97}$$

Note that, because the microstructural length scale d_{gr} is based on the cross section of the slip planes (D_{st} and $D_{nd}{}^i$), the fatigue model can assess the influence of the shape of grains, i.e., spherical versus elongated grains. Furthermore, the crystal plasticity model does not carry an intrinsic length scale, so the grain size effect introduced here accounts for the dependence of the bulk on the microstructure plus the the intensification of the driving force due to the localization of the strain discussed in Chapter 3.

6.3 Fatigue model calibration

6.3.1   U-notch beam specimens

The fatigue experimental data for RR1000 in the literature is limited and almost always refers to the bore microstructure with ALA grains about $10-20~\mu m$ [161, 160, 133]. Hence, the fatigue model will be calibrated using fatigue data from the bore region, so the model is expected to perform better for that microstructure. The calibration of the fatigue model
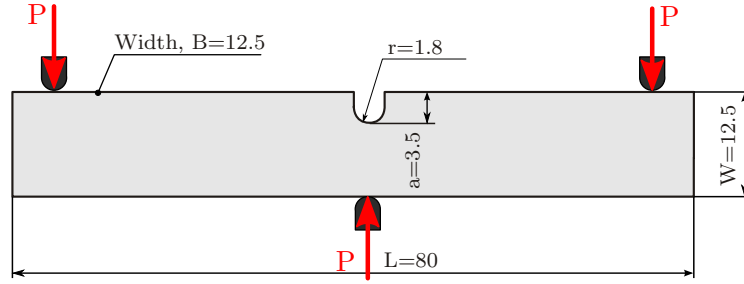
Figure 79: Three-point bending specimen with an U-notch employed by Pang [160] for experimental characterization of small fatigue cracks in RR1000. Dimensions are in mm.
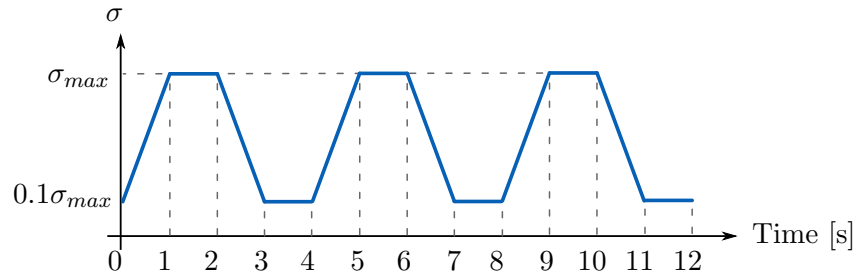
Figure 80: Applied load in experiments and simulations (1-1-1-1). Here, R=0.1 and the nominal applied maximum stress is about 840 MPa.

involves determining proportionality factors between the driving forces and fatigue damage evolution and represents the degree of mechanical irreversibility. The experimental data chosen for calibration belongs to Pang et al. [161, 160], who employed U-notch specimens shown in Figure 79 to measure fatigue life to nucleate a crack and the small crack regime. The load applied to the U-notch specimens corresponds to a nominal stress of about 840 MPa, undergoing (1-1-1-1) loading and R=0.1, as shown in Figure 80.

Figure 81 [160] presents experimental data at room temperature from Pang's work, which is used to calibrate the irreversibility constant in the nucleation regime. By assuming that the crack starts at an ALA grain of 16 μm, we can estimate the number of cycles to crack the first grain to be about 100000. This value is only a rough estimate applicable to Pang's specimens and loading conditions (Figure 82), and it may need to be refined to account for statistical variations. Experimental results at 650°C show a similar trend, and cracks formed after about 100000 cycles.

To quantify the FIPs that developed during the test, the experimental conditions were
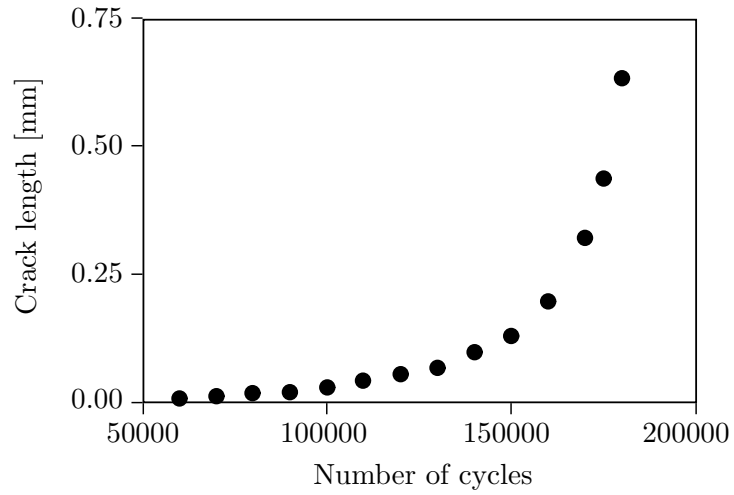
Figure 81: Crack growth of the fastest growing crack in RR1000 at room temperature (modified from [160]).
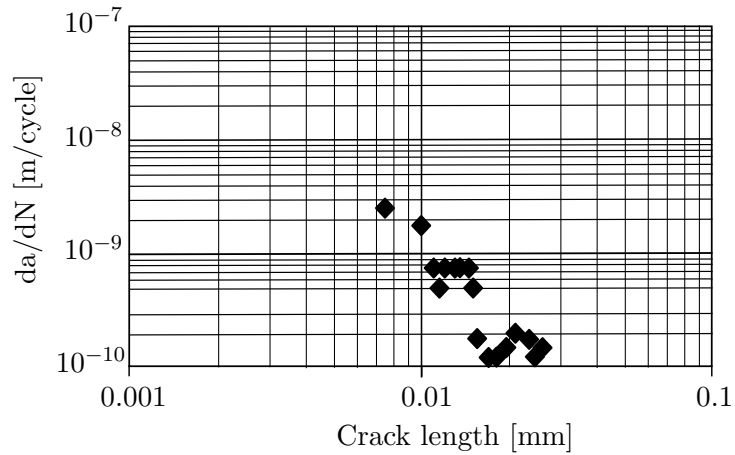
Figure 82: Crack growth of the fastest growing crack in RR1000 at room temperature (modified from [160]).

FEM model
Load applied 10400N in bending
Mean grain size $\sim 5~\mu m$ (1:1 scale)
Specimen scale 1:125
L=64μm
W=B=10μm
r=14.4μm
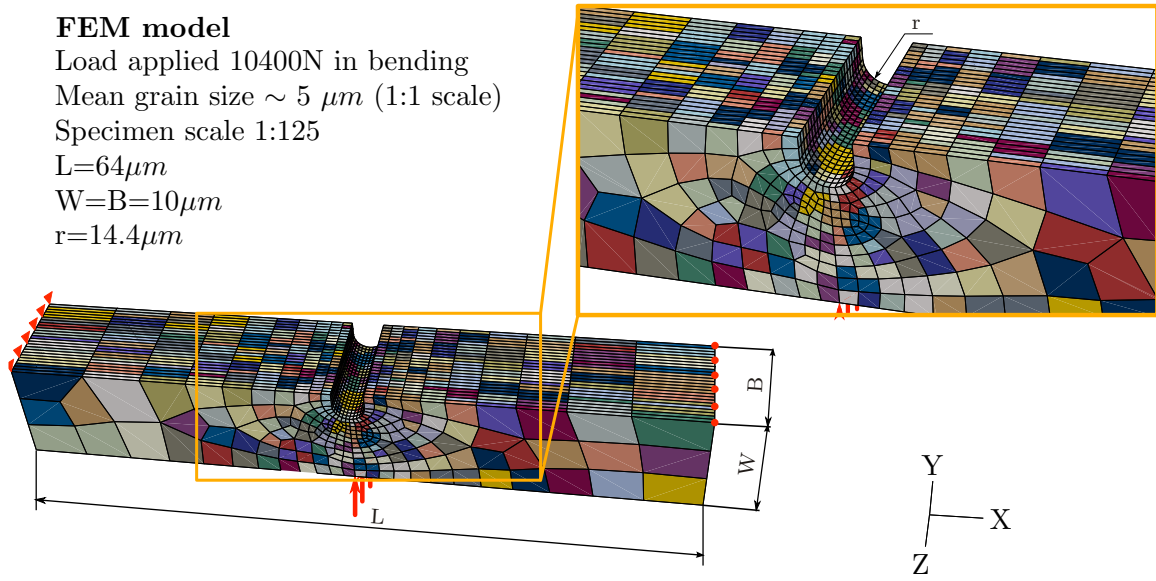
Figure 83: FEM model of the U-notch bending specimens with explicit grains colored and refinement towards the notch.

reproduced in a 1:125 scale FEM model, shown in Figure 83, but using a 1:1 scale for the grain size (the model has much larger grains in comparison to the specimen). The loading consisted in applying (1-1-1-1) type of cycles with R=0.1 and a peak force of 10400N in the Y-axis direction, distributed in 26 nodes along the Z-axis. One of the extremes of the specimen was not allowed any displacement while the other had displacement restriction along the Y-axis (Figure 83). The mesh is refined towards the notch, where it presents elements of aspect ratio close to 1 and side length of about 0.6 μm. The constitutive model corresponds to that presented in the previous chapter, with a grain distribution following a lognormal law [146] and with a mean grain size of about 5 μm and ALA grains about $10 - 20~\mu m$.

Since the computational model is 125 times smaller than the actual specimen, the number of grains sustaining high stresses and strains is 125 times smaller than in the real specimen (this scales with the length of the notch). Thus, to achieve equal highly stressed volumes in the simulations compared to that in the specimen, 125 realizations of the simulation were carried out. Figure 84 presents the stresses and strains resulting from one of the realizations after applying five loading cycles to the specimen. The peak stress is
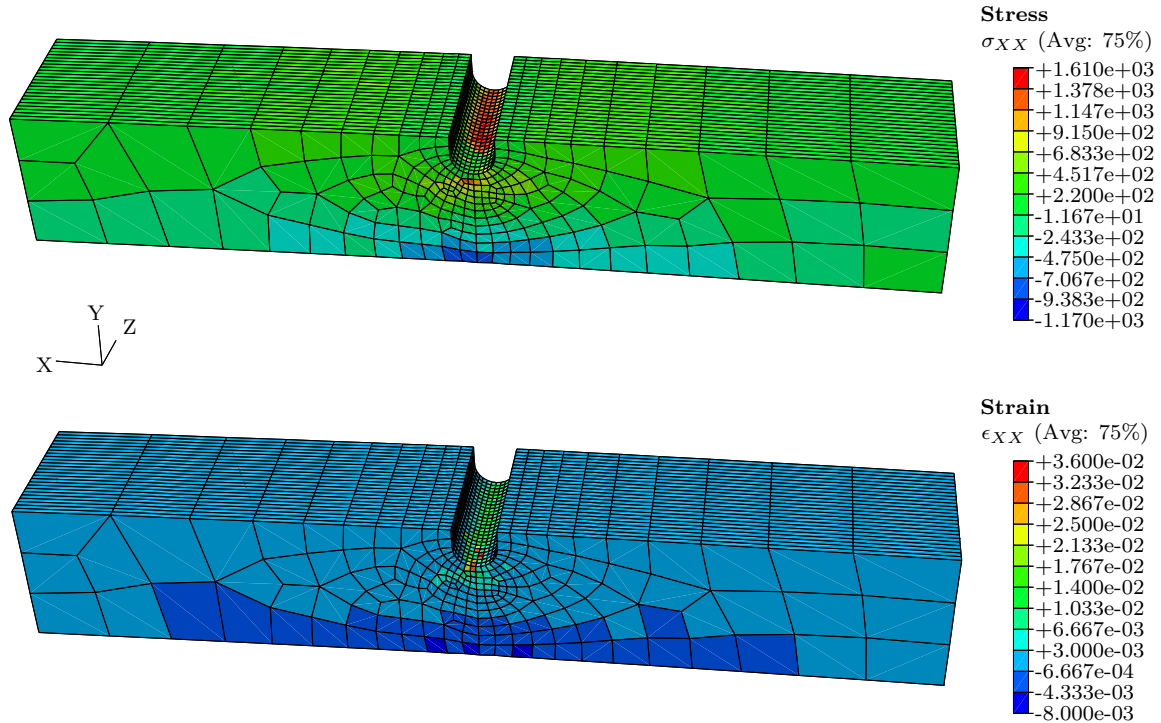
Figure 84: Stress and strain normal components along the X direction resulting from the U-notch bending specimen. The results match those presented by Pang et al. [160]

comparable to that resulting from Pang's simulations [160] using an elastic constitutive model. Since the grains in simulations are much larger with respect to the notch than in experiments, the model does not scale the stress gradient. Such difference may have some influence on the number of grains and elements under the stress intensification that will be neglected.

The fatigue simulations followed the procedure described in Figure 49, but due to the irregular mesh, d_{gr} is computed as the diameter of the grain and not the square root of the area of the bands. Note that the band that forms the crack and those that extend the crack in the MSC regime are determined based on the expected life and not the maximum FIP, so the fatigue calculations were redone after the entire fatigue model was calibrated. Based on the 125 simulations carried out after the calibration, Figure 85 presents a series of histograms showing the distribution of the FIPs for the first five grains to fail (nucleation grain plus four grains failed under the MSC regime). Note that these results represent the distribution of extreme values, since each simulation contributes a single value (the FIP of
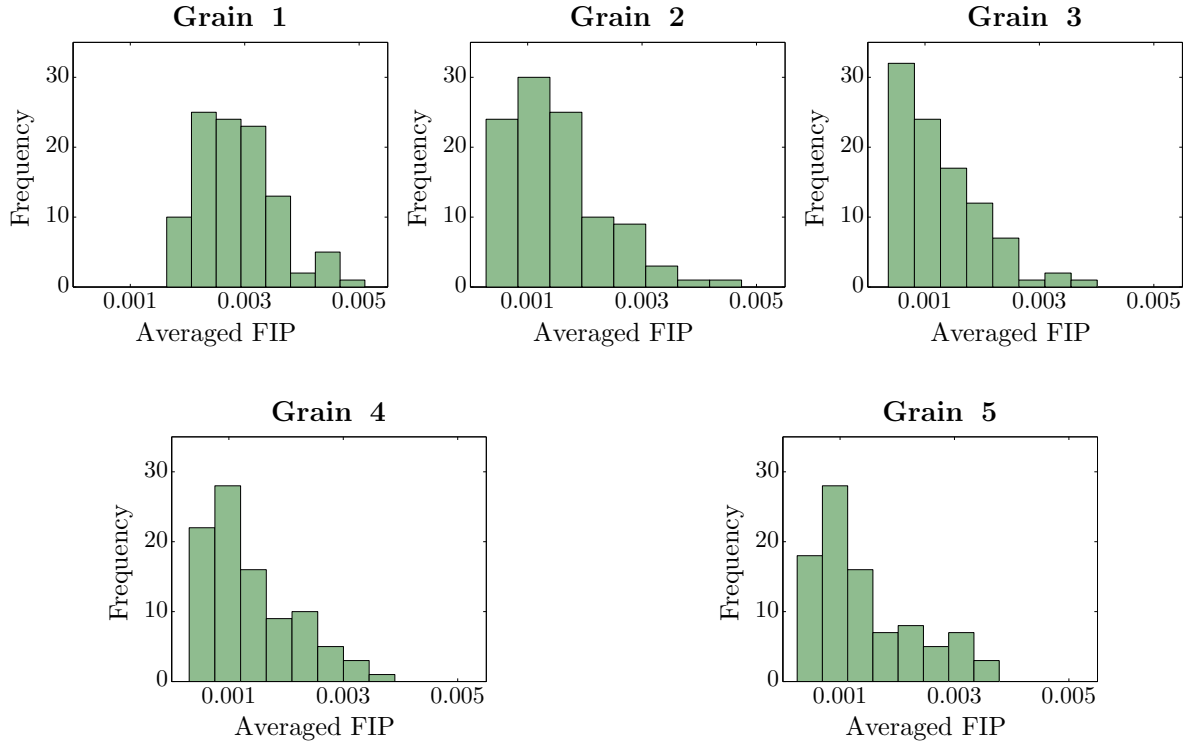
Figure 85: Distribution of maximum averaged FIP for the first five grains that failed (from left to right).

the grain that failed) to each histogram. In all cases, the distributions are not symmetric, though for the nucleation regime the distribution asymmetry seems to be less pronounced.

Because the tails of the FIP distributions dominate the fatigue problem, a quantitative comparison of the FIPs among grains 1 to 5 in Figure 85 cannot be based simply on mean values. Hence, this research employs boxplots, since they are a simple and an organized way of comparing data samples that do not need to fit data to an assumed distribution. For example, suppose a sample of variable X that ranges from X_{min} to X_{max} as shown to the right of Figure 86; a boxplot represents the lower ($Q1$) and upper ($Q3$) quartiles of the distribution of variable X with the bottom and top of a box, respectively, and the medium quartile ($Q2$) with a line near the middle of the box. The whisker length (dotted lines) satisfies that $Q3 + c(Q3 - Q1)$ and $Q1 - c(Q3 - Q1)$, with c usually between 1 and 2, and the data outside those limits correspond to the outliers and are represented with circles. The whisker extends up to the most extreme data value that is not an outlier. One final caveat is that the boxes sometimes are presented as fully colored boxes (not hollow), and
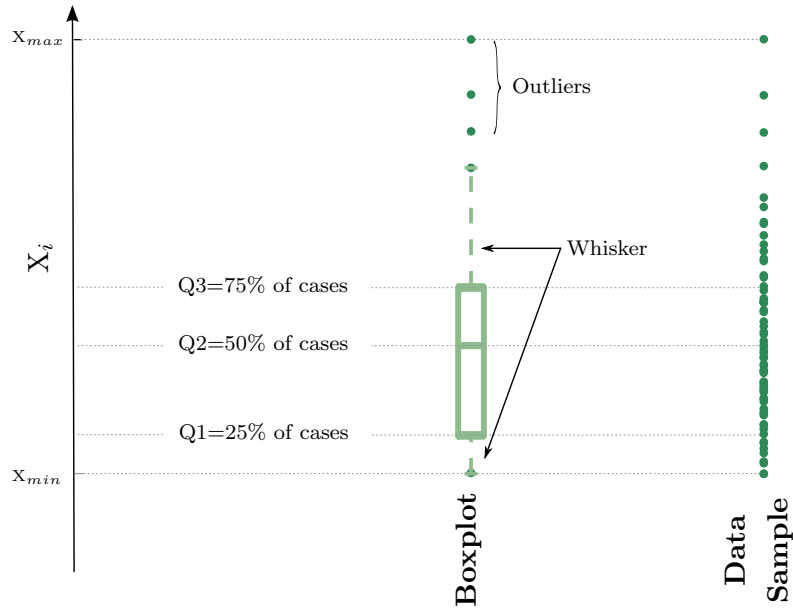
Figure 86: Example of a boxplot. The lower ($Q1$) and upper ($Q3$) quartiles of sample of X are represented with the bottom and top of the green box, respectively, and the medium quartile ($Q2$) with the line near the middle of the box. The whisker length (dotted lines) satisfies that $Q3 + c(Q3 - Q1)$ and $Q1 - c(Q3 - Q1)$, c usually between 1 and 2.

the second quartile extends outside the box. This alternative style will be employed to compare overlapping boxplots.

Figure 87 compiles the information from the histograms in Figure 85 using boxplots. The boxes (full lines) in Figure 87 describes the FIP distribution for grains 1 to 5. The whisker length (dotted lines) satisfies that $Q3 + 1.5(Q3 - Q1)$ and $Q1 - 1.5(Q3 - Q1)$, and the data outside those limits correspond to the outliers and are represented with circles. Clearly, the dispersion of the FIPs increases in the MSC regime and the lower, medium , and upper quartiles of the data decrease by about 40 % in the transition from cracking the first to the second grain (Nucleation to MSC regime). However, the data for the grains cracked in the MSC regime (grains 2, 3, 4 and 5) are comparable.

The importance of Figure 87 is that it shows that the driving force for fatigue crack growth decreases significantly after crossing the first GB. **This reduction is the consequence of a regularized "crack tip singularity effect" (i.e., effect of cracking the first grain on redistributing the stress) combined with the probability of**

finding a highly activated slip band in an adjacent grain connected to the one that failed in the first grain. In other words, cracking one grain does not affect the surrounding grains enough to reach, on average, the same driving force for the nucleation grain. These findings are in complete agreement with the crack growth rates measured by Pang at room temperature and 650°C [160], but they may not be completely general, since the geometry of the specimen may have an influence; indeed, simulations and experiments have shown that cracks tend to extend along the notch more easily than through the remaining ligament.

6.3.2 Estimation of constants

6.3.2.1 Transgranular nucleation regime

The constants of the mesoscale model can be calibrated using the experimental data introduced early in this chapter. Because the available information is limited, only an approximated calibration is attempted, and the results should match the order of magnitude of future experiments.

The irreversibility constant for the nucleation regime, α_g, is calculated following Equation (94),

$$\alpha_g = N_{nuc}\frac{D_{st} + \omega D_{nd}}{(\text{FIP}^\alpha)^{-2}},$$

(98)

by assuming that:

- $N_{nuc} = 100000$, as discussed based on Figure 81,

- $D_{st} = 16~\mu m$, which corresponds to the size of the ALA grain for the material testes and implies that the largest grains nucleate the crack,

- $\omega = 0$ since most of the time the disorientation is larger than $20°$ as estimated from simulation of random crystallographic orientation, and

- $\text{FIP}^\alpha = 0.0051$, which is the extreme value obtained for the grain that nucleates the crack in U-notch specimen simulations;

These assumptions result in $\alpha_g = 41.6$ cycles μm
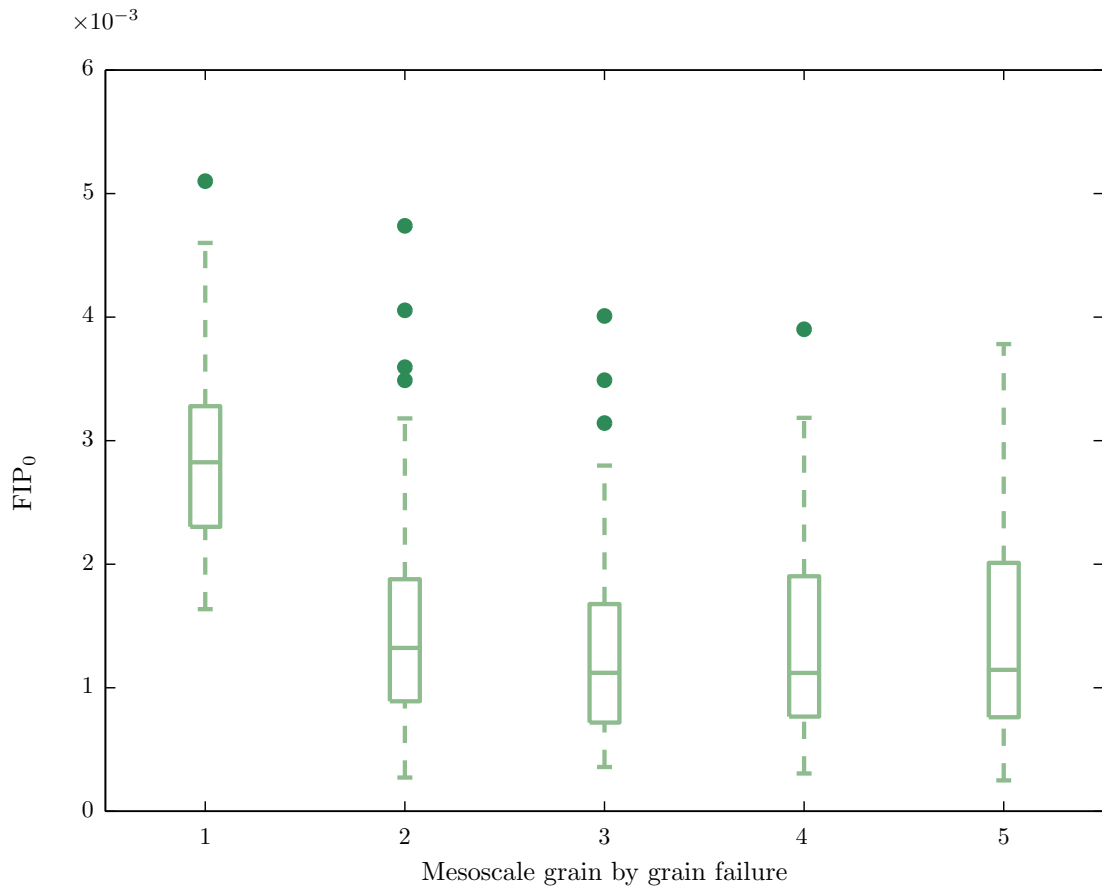
Figure 87: Boxplot compiling the FIP distributions for each grain in Figure 85. For each grain, the plot represents the lower ($Q1$) and upper ($Q3$) quartiles of their FIP distributions with the bottom and top of the green boxes, respectively, and the medium quartile ($Q2$) with the line near the middle of the box. The whisker length (dotted lines) satisfies that $Q3 + 1.5(Q3 - Q1)$ and $Q1 - 1.5(Q3 - Q1)$ and extends up to the most extreme data value in that range. The data outside those limits are represented with circles. Note how the FIP decreases significantly (about 40 %) after crossing the first GB.

The calibration of the MSC regime is based on the measurements of the crack growth rates in Figure 82. This Figure presents an initial decreasing crack growth rate that corresponds to the nucleation regime in the ALA grain. While the crack approaches the GBs (crack lengths about 11 μm, 17 μm, and 23 μm), the crack growth rate decreases by up to about $10^{-4}\mu m/cycle$. Upon crossing the boundaries, the crack growth rate jumps up to about $3\text{x}10^{-4}\mu m/cycle$ to $7\text{x}10^{-4}\mu m/cycle$. Thus, under the particular conditions analyzed, we may estimate the minimum crack growth rate to be about $10^{-4}\mu m/cycle$, and the average maximum rate, when a grain begins to crack, to be about $5\text{x}10^{-4}\mu m/cycle$.

The calibration of the constant C in Equation (97) assumes that:

- $D_{st} = 8$ μm, which corresponds to the mean grain size (d_{gr}^{ref}) in the material tested, making this value the most probable second grain to crack. This further implies that $\beta = 1$.

- $\mathsf{A} = 2$ μm and $b \sim 1$, based on the results in Figure 71. These constants scales the FIP with the ΔCTD.

- $Q = 241\frac{kJ}{mol}$, after Tong et al. [200].

- $\omega = 0$, since most of the time the misorientation is larger than $20°$ as estimated from simulation of random crystallographic orientation,

- $\Delta\text{CTD}_{th} = 5\text{x}10^{-4}\mu m$, which is about the dimension of the Burgers vector, assumed to be the minimum ΔCTD in the MSC regime, and

- $\text{FIP}^{\alpha} = 0.0035$ corresponds approximately to a 40% reduction in the FIP employed for calibrating the nucleation regime. Such a percentage corresponds to the average reduction of the FIP from nucleating in the first grain to growing in the MSC regime, as obtained from the U-notch simulations (Figure 87). Note that using the average proportion of the nucleation extreme FIP, and not the extreme value of the FIP for the second grain, moderates the variability due to the irregular mesh.

Because the mesoscale framework estimates the FIP$^\alpha$ before cracking the current grain, the driving force corresponds to the crack growth rate measured right after crossing a GB, and before it starts decreasing the elastic stiffness of the band that extends the crack. The constant C results from replacing the parameters mentioned in Equation (96),

$$C = 5\text{x}10^{-4}\frac{\mu m}{cycle}\left[\exp\left(\frac{-241}{8.31\ 923}\right)(0.9 + 1 + 0.1)^{(\frac{1}{2}-0.2)}[2\ \mu m\ 0.0051 - 5\text{x}10^{-4}\mu m]\right]^{-1},$$

$$C = 0.0645\frac{1}{cycle}. \tag{99}$$

Then, the transgranular irreversibility factor, including the temperature and loop shape influence becomes $\phi_{trans} = 0.077$, which is within the range measured by Shyam and Milligan [187]. Thus, approximately 1 out of 13 dislocations coming out of the crack tip do not return and annihilate after a loading cycle.

6.3.2.3   Intergranular failure

Since RR1000 experimental data are scarce for fully intergranular failure and almost nonexistent for small cracks, the model is expected to provide a rough estimation of the life. The calibration of the intergranular failure model requires that a value be set for constants λ_1 and λ_2 in Equation (16), and PS, B_{int} and C_{int} in Equation (91). Then, we assume that,

1. $\lambda_1 \sim \lambda_2 \sim 2$ and $B_{int} = 0.02\frac{m^3}{Kmol}$ after Miller et al. [132],

2. For the U-notch specimens simulated, the average intergranular crack growth rate should be about $5\text{x}10^{-5}\frac{\mu m}{cycle}$. This value is based on Figure 78, which shows that for (1 1 1 1) loading, the intergranular crack growth rate should be about an order of magnitude slower than that for transgranular failure (compare blue and orange lines), and

3. The average FIP$_{int}$ (using only non-null values) for all GBs was computed from U-notch specimens and resulted in FIP$_{int} = (2.7\text{x}10^{-4})^\lambda$. Similarly, the maximum principal stress presented a maximum value about $PS \sim 1600$ MPa.

Hence, following Equations (17) and (91),

$$C_{int} = 5\text{x}10^{-5}\frac{\mu m}{cycle}\left[\exp\left(-\frac{241-0.02\ 1600}{8.314\ 923}\right)(0.9+1+0.1)^{(\frac{1}{2}-0.05)}(2.7\text{x}10^{-4})^2\right]^{-1},$$

$$C_{int} = 8.01\frac{\mu m}{cycle} \tag{100}$$

6.3.3   Sub-grain evolution of the FIP

The mesoscale FIP ($\text{FIP}^{\alpha}_{\text{meso}} = \text{FIP}^{\alpha}_{o} \cdot g(a)$) introduced in Equation (23) in Chapter 4 estimates the evolution of the driving force as the crack grows through a grain. Contrary to LEFM, the study of small crack problems cannot employ a single function $g(a)$ for every possible alloy, microstructure, loading condition, etc. Thus, this research proceeds to characterize the function $g(a)$ for RR1000 alloy under the HCF loading regime by evaluating the change of the FIP while the crack extends inside the grains, here referred as the sub-grain evolution. The algorithm is designed to introduce damage only to one element in between loading cycles (i.e., not as a mesoscale framework that damages the entire grain at once) and to update the driving force on the remaining ligament of the grain. Figure 88 presents a schematic comparison of the subgrain and mesoscale methodologies to extend the crack along bands within grains. The subgrain methodology can assess the evolution of the FIP as the crack extends through the grain, but it demands a larger number of loading cycles that result in a significantly increase in computational work.

Figure 89 summarizes the algorithm for the subgrain methodology. The crack extends one element per two cycles until a predefined number of loading cycles is reached (maximum number of loading cycles). The prediction of the band along which the crack extends does not change within each grain and is based on the values of the FIP before cracking the grain, but the next element to crack is defined based on the local values of the FIP. The purpose of applying two loading cycles each time the crack extends is to redistributed stress and strain fields.
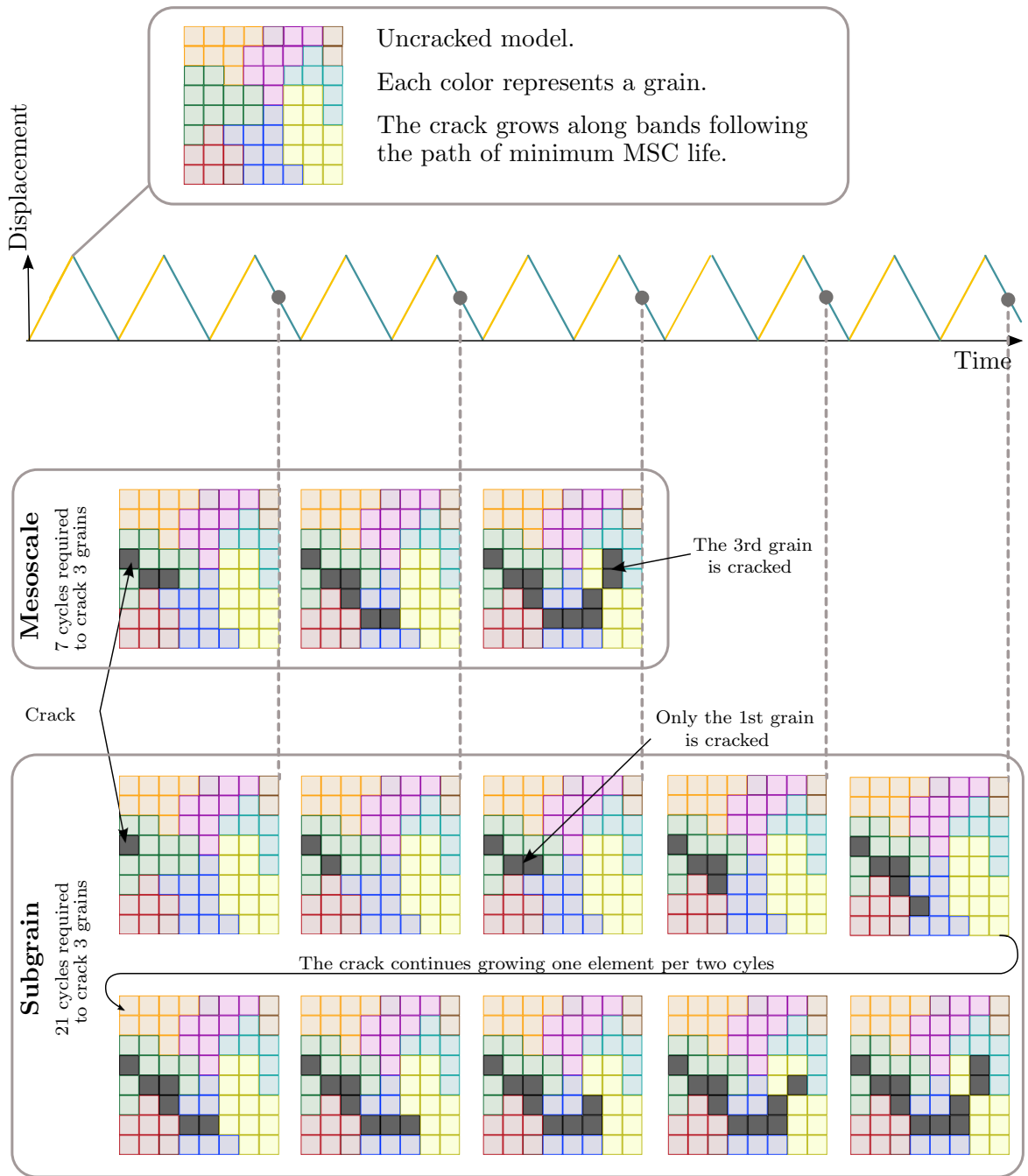
Figure 88: Schematic 2D representation of crack growth under the mesoscale and subgrain models. The crack (dark gray) extends along the elements by decreasing the elastic stiffness tensor.
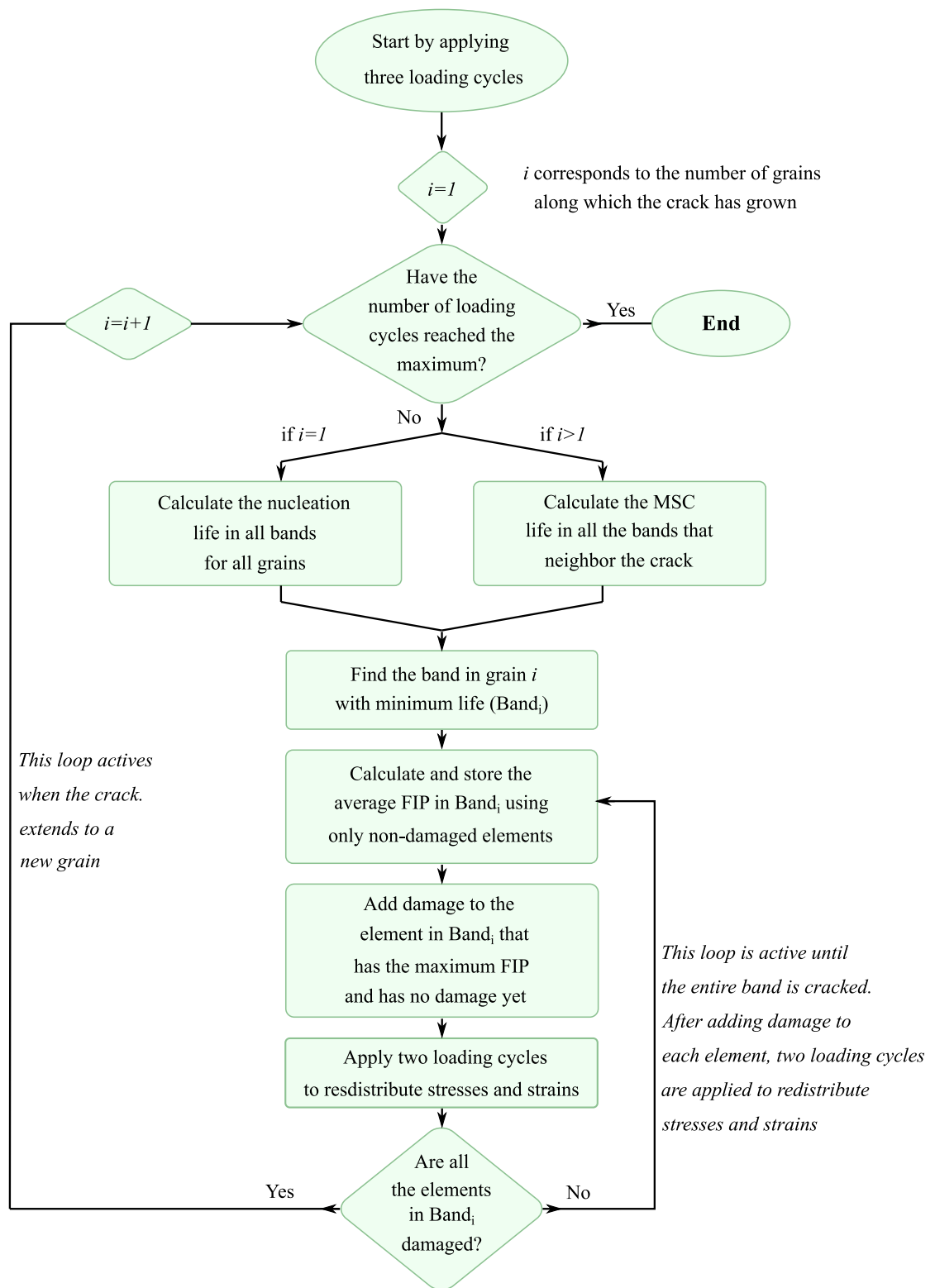
Figure 89: Algorithm showing the tasks performed by the UEXTERNALDB subroutine developed to evaluate subgrain crack growth.

Because the mesh of the U-notch specimen is not regular, the number of elements in bands within grains varied significantly, so only those simulations that had damaged a minimum of 12 elements along the bands that failed were considered in the sub-grain analysis. Figure 90 presents the sub-grain evolution of the driving force for the first five grains that cracked in about 50 realizations of U-notch specimen simulations. The magnitude ã is the number of cracked grains in a sequence and is defined by

$$\tilde{\mathrm{a}} = i - \mathrm{a}_i \tag{101}$$

where a_i is the fraction of the area cracked (between 0 to 1) in the ith grain to fail. For example, when three grains are fully cracked and the 4th grain is half-cracked, $i = 4$ and $a_i = 0.5$, resulting in $\tilde{\mathrm{a}} = 3.5$.

The results show that the FIP$^\alpha$ at ã=0 (i.e., FIP$_0^\alpha$ in Equation (23) used to predict the minimum nucleation life of each band) presents a narrow range (less than a factor of 3) compared to the variability of the initial FIP$^\alpha$ on the subsequent grains (i.e., FIP$_0^\alpha$ in Equation (23) that corresponds to the FIP @ ã=1.0, 2.0, 3.0 ...). Such a fact suggests that the variability in the small crack regime depends significantly on the extension to subsequent grains rather than cracking the first grain.

The sub-grain evolution of the FIP$^\alpha$ was nondimensionalized using the initial value of the FIP$^\alpha$ before cracking each grain (i.e., FIP$_0^\alpha$); note that the nondimensionalization parameter changes for every new grain cracked. The results in Figure 91 depict a decreasing evolution of the driving force within each grain, except maybe for the first grain (ã between 0 and 1), which presented in some simulations a temporary increase of the driving force. Indeed, the black lines in Figure 91 attempt to represent the mean and boundary values for the driving force following the equation,

$$\frac{\mathrm{FIP}^\alpha}{\mathrm{FIP}_0^\alpha} = g(a) = \left(1 - P_g \mathrm{a}_i^m\right), \tag{102}$$

which is inspired after Equations (18) and (19); the simulations seem to validate this type of average evolution.

The constant P_g in Equation (102) can be computed either as a fixed value that represents the mean sub-grain behavior, or as a value that varies according to statistical distributions. However, as shown in section 6.3.5, the mesoscale model requires the exponent m to be a fixed value to be able to compute the life of a grain and not only the crack growth rate. Therefore, both constants will be treated as constants.
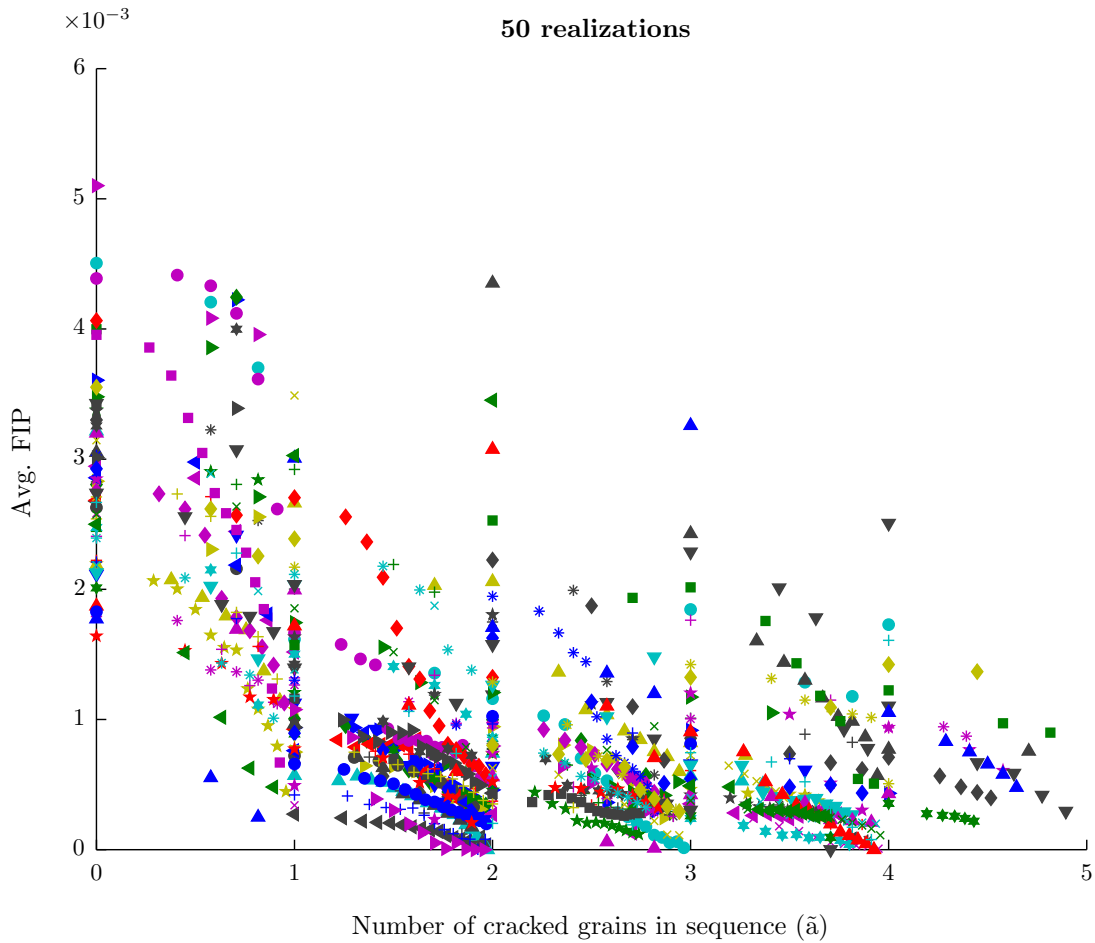
Figure 90: Evolution of the FIP as a crack grows within a grain for U-notch specimen for 50 realizations. Each data point represents that the crack extended by one element, while the value of the FIP corresponds to the average over the remaining undamaged elements of the band.
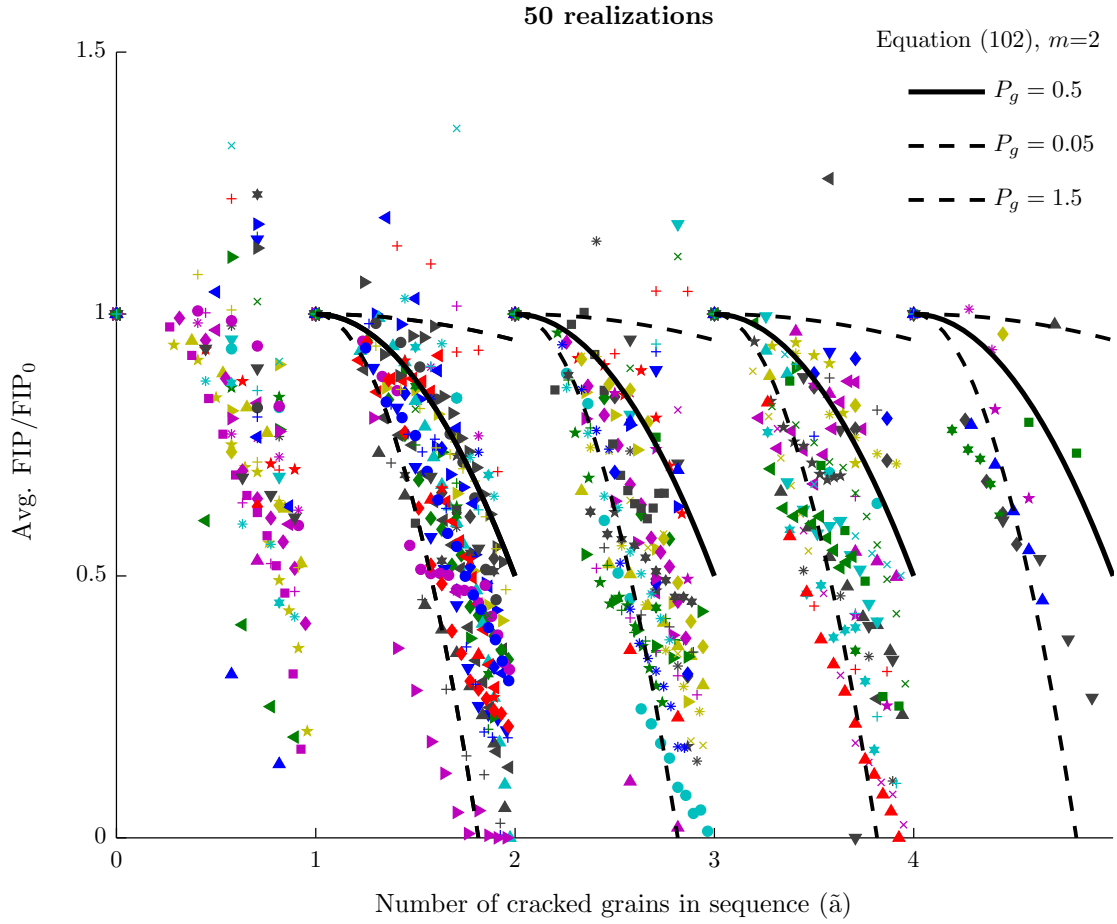
Figure 91: Evolution of the nondimensionalized FIP as a crack grows within a grain with the proposed subgrain estimation superimposed for U-notch specimens. Data is equivalent to that in Figure 90, which corresponds to 50 realizations.

6.3.4 Regular mesh with periodic boundary conditions

The evolution of the FIP is assessed using cubic regular meshes created with the Mesh Generator. The models have 3375 elements, 52 grains undergoing 0.9% range, strain-controlled triangular cyclic loading, $R_\epsilon = 0.1$, and periodic loading conditions. The loading periodicity is achieved by requiring that the sum of forces and moments on opposite faces be equal to zero, but these are not truly periodic boundary conditions, since grain distributions on opposite faces are not identical.

Figure 92 summarizes the statistics of the FIP_0 averaged along bands and computed using the mesoscale model (the entire grain is cracked simultaneously). The whisker length (doted lines) are proportionally shorter in this case ($Q3 + 1.0(Q3 - Q1)$ and $Q1 - 1.0(Q3 - Q1)$) since the distributions have a narrower scatter, which is attributed to the regular mesh and refined grains. Similar to the results for the U-notch specimen in Figure 87, the dispersion of the FIPs in Figure 92 increases in the MSC regime. Moreover the three quartiles of the MSC data (grains 2, 3, 4 and 5) decrease by about 40 % with respect to the first grain (Nucleation). **Figure 92 demonstrates that the driving force for fatigue crack growth decreases after crossing the first GB due to a regularized crack effect and limited plastic slip in band adjacent to the crack**.

6.3.4.1   Sub-grain evolution using a regular mesh

Although the subgrain evolution in U-notch simulations resemble the experimental data, the non-regular mesh and the notch itself can affect the results and introduce an abnormal variability of the FIPs. Hence, the subgrain evolution analysis was reproduced employing the regular mesh previously described. Figure 93 presents the resulting evolution of the FIP as the crack grew inside the grains out of 30 realizations. Similar to Figure 90, the FIP that minimizes the nucleation life (i.e., ã=0) presents a very narrow range (less than a factor of 2), while the initial values of the FIP on the subsequent grains can vary orders of magnitude. These results demonstrates that the variability of the small crack regime depends more on the extension to subsequent grains than on the nucleation on the first grain.
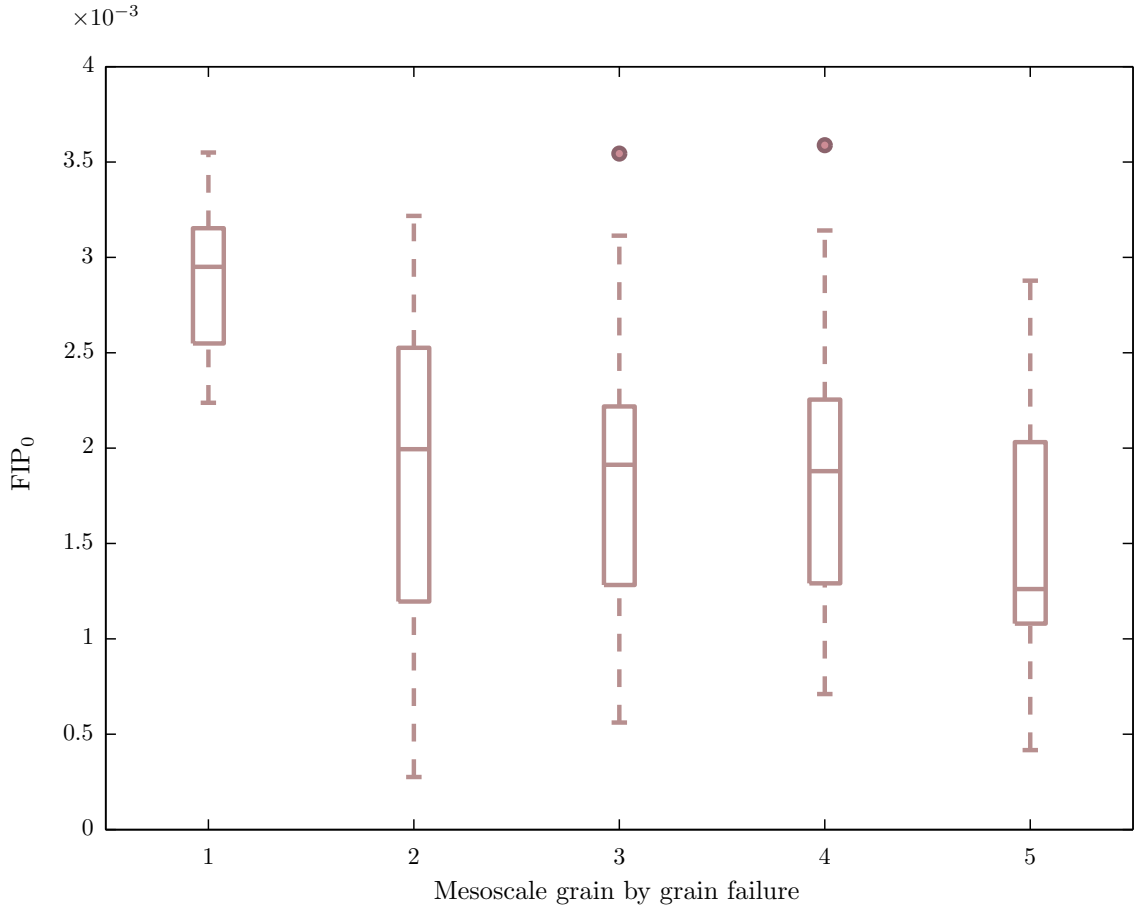
Figure 92: Boxplot compiling the FIPs computed from models with regular meshes. The lower ($Q1$) and upper ($Q3$) quartiles correspond to the bottom and top of the green boxes, respectively, and the medium quartile ($Q2$) corresponds to the line near the middle of the box. The whisker length (dotted lines) satisfies that $Q3+1.0(Q3-Q1)$ and $Q1-1.0(Q3-Q1)$ and extends up to the most extreme data value in that range. The data outside those limits are represented with circles. Note how the FIP decreases significantly (about 40 %) after crossing the first GB.

Figure 94 presents in more detail some of the evolutions of the FIP in Figure 93 (same colors and markers for each simulation) along with additional simulations in the black data points that are identical except that the damage parameter d_1 increased up to a value of 0.999 (demanding more computational work). The agreement among both colored and black data points further shows that limiting the increment of the damage parameter d_1 up to 0.99 does not affect the quality of the results.
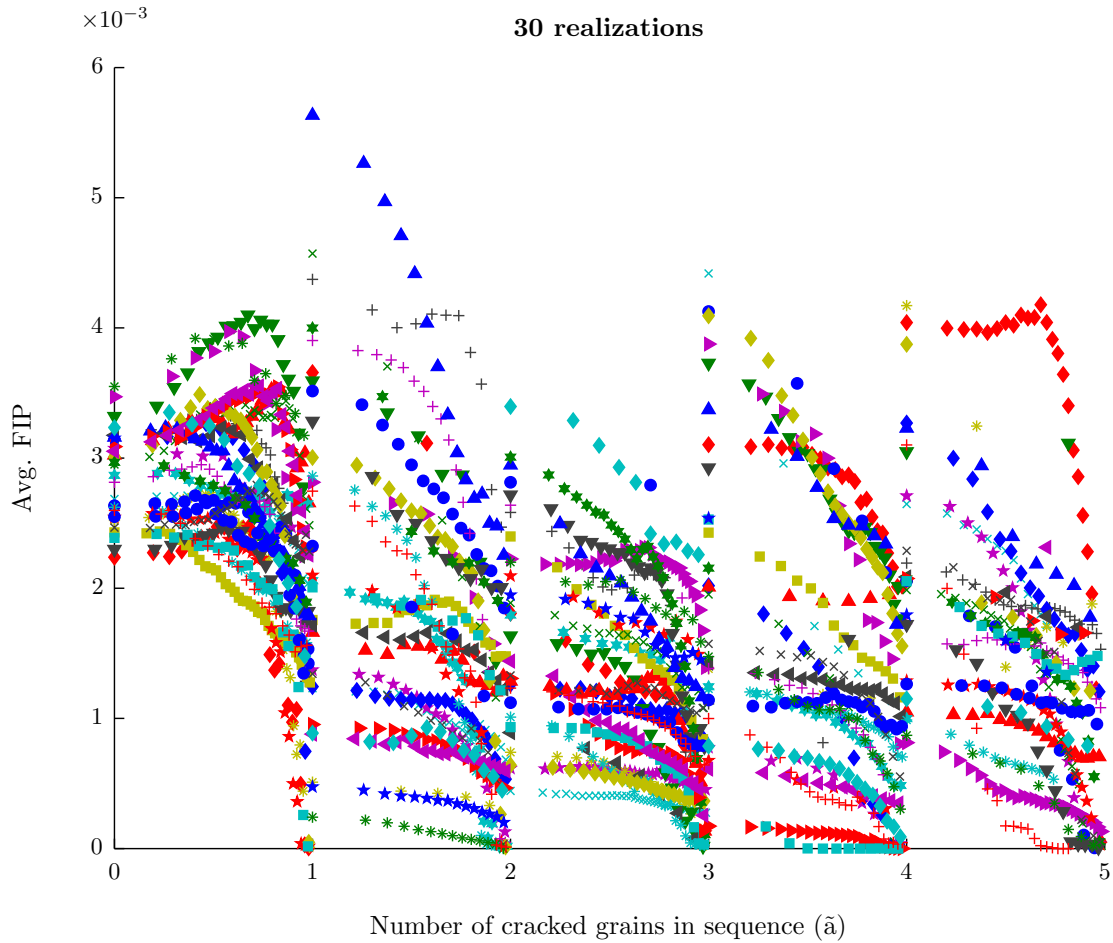
Figure 93: Evolution of the FIP as a crack grows within a grain for 30 realizations. Each data point represents that the crack extended one by element and the FIP is averaged over the remaining elements of the band with minimum life.

Figure 95 presents the evolution of the FIP in Figure 93 (same colors and markers for each simulation), nondimensionalized by the value of the FIP before cracking, which changes for every new grain cracked. The results present a significant difference between the first grain to crack ($\tilde{a}$ between 0 and 1) and the following grains, showing that the life estimation for the first grain to crack needs to be calculated differently from the subsequent grains to fail, which follow a more predictable behavior. The black continuous line in Figure 95 follows Equation (102), using $P_g = 0.5$ and $m = 2$, which is proposed to describe the
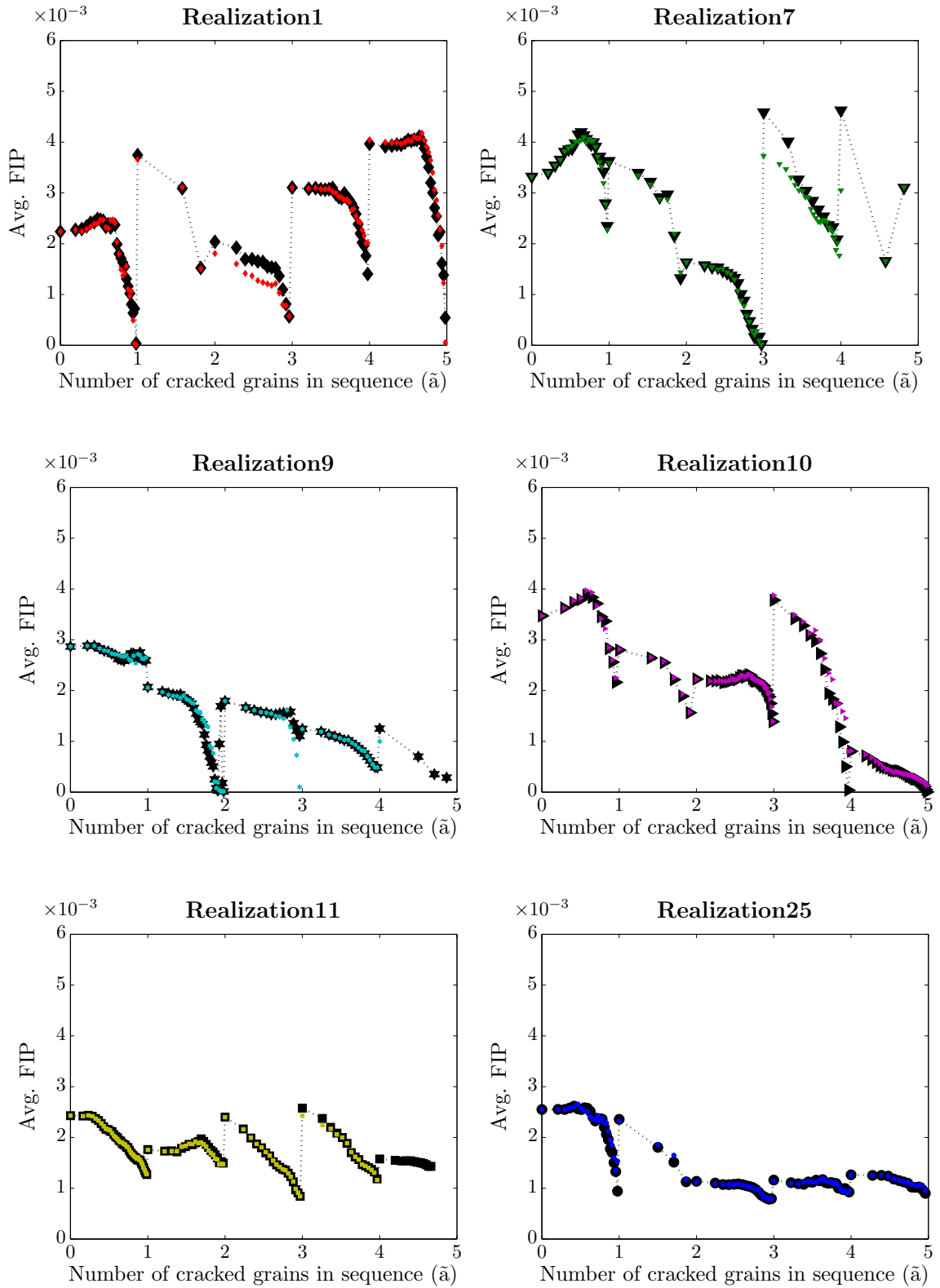
Figure 94: Overview of a few cases of the evolution of the FIP in Figure 93. Black data points correspond to simulations of the same microstructure, but damage incrementation up to 0.999, which results in almost exactly the same sub-grain evolution of the FIP.

mean behavior of the subgrain evolution of the FIP in the MSC regime. To evaluate such an assumption, Equation (102) was fit to the evolution of the FIP within each grain, and the resulting values of the constants P_g and the exponent m were analyzed in Figure 96 and Figure 97, respectively. These Figures present histograms of the values of P_g and m for each grain that failed and show, again, that the nucleation regime stands out with a different behavior from the subsequent grains to fail. Overall, the P_g presents a relatively planar distribution between 0 and 1, while the mean value of m is about 2 to 3. Note that best-fitting was carried out, limiting the values of P_g and m between 0 and 10, which results in a negative concavity for the sub-grain FIP evolution.
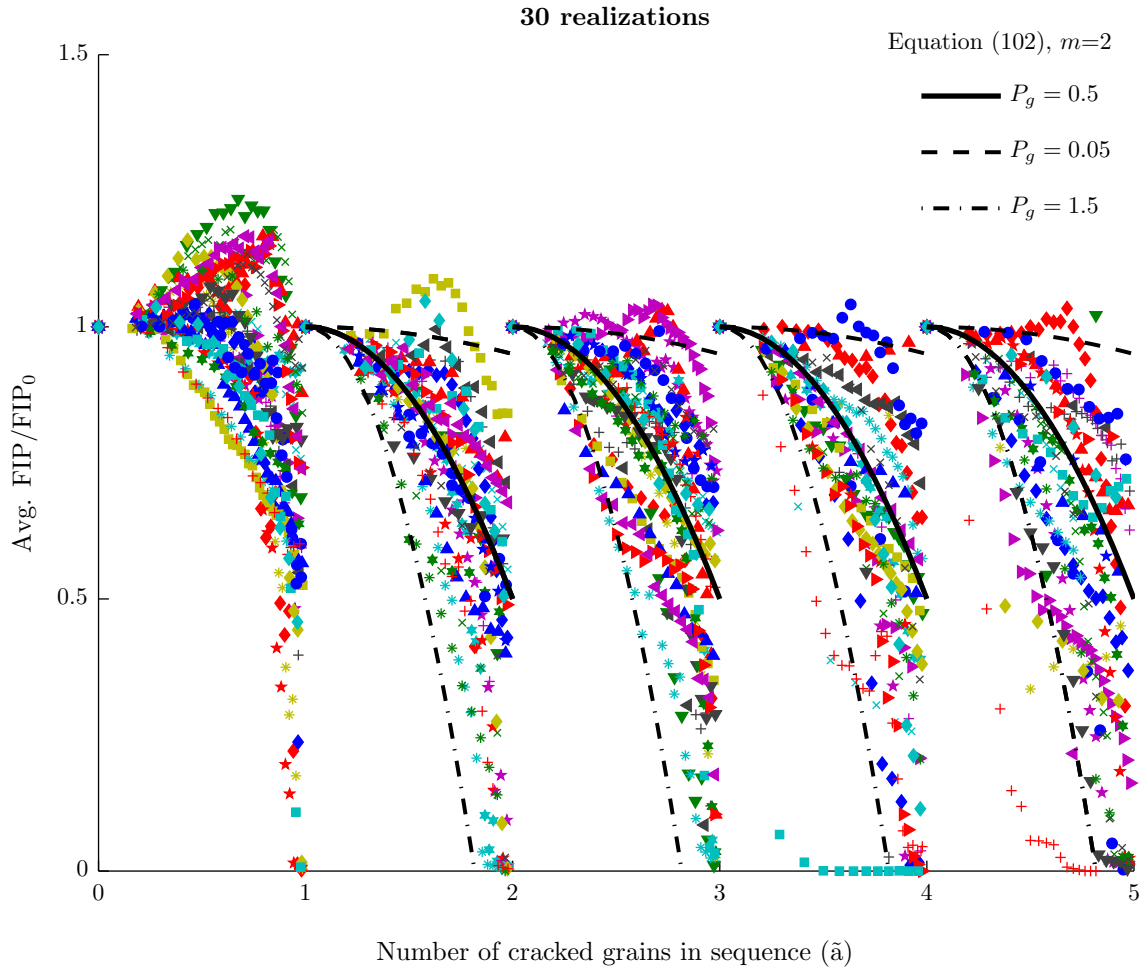
Figure 95: Evolution of the nondimensionalized FIP as a crack grows within a grain with the proposed subgrain estimation superimposed. Data is equivalent to that in Figure 90.
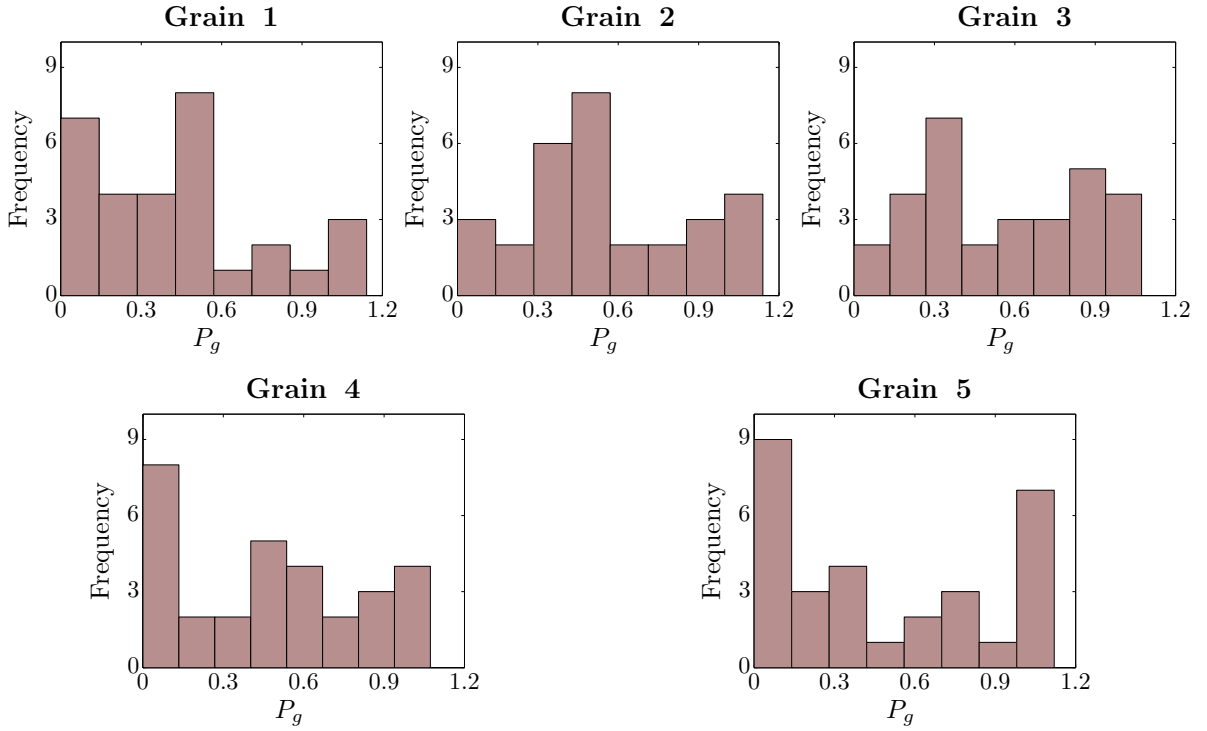
Figure 96: Distribution of the coefficient Pg in Equation (102) for the first five grains cracked.
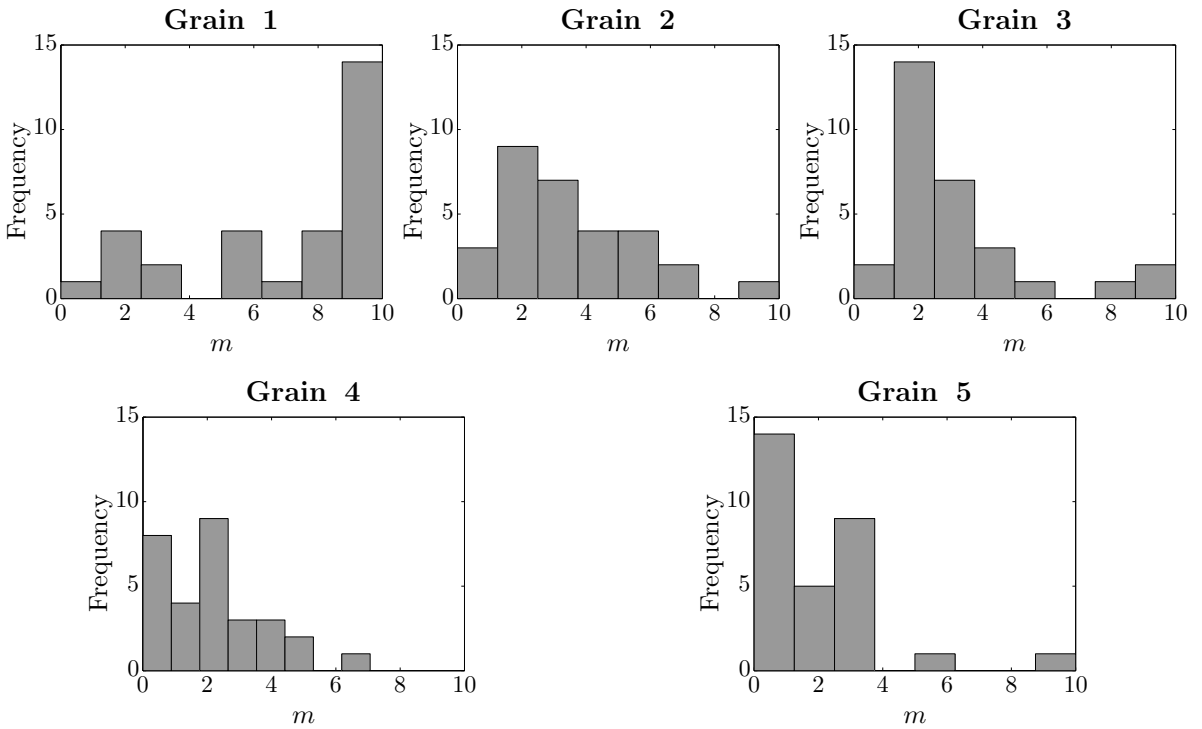
Figure 97: Distribution of the exponent m in Equation (102) for the first five grains cracked.)

To further explore the nature of the approximation introduced by Equation (102) in the mesoscale model, the simulations in section 6.3.4 were reproduced using the mesoscale model to estimate the failure of the first five grains, followed by a subgrain analysis. Figure 98 presents the non-dimensionalized behavior of the FIP; the first five grains to fail are calculated using the mesoscale model with Equation (102) and $P_g = 0.5$ and $m = 2$, while the following grains show the subgrain evolution that is approximated with the same evolution law. Even after the crack has extended over 10 grains, the average subgrain behavior seems to consistently follow Equation (102).

For each grain, the value of the FIP before a new grain is damaged (FIP_0) has a central importance, since it controls the fatigue life prediction. Hence, Figure 99 presents the boxplot with the distributions of the FIP_0 calculated with the sub-grain or mesoscale methodologies from the simulations in Figure 95 (hollow boxplot) and Figure 98 (full boxplots). Both methodologies predict exactly the same distributions for the nucleation regime (1st grain), since the grains are not cracked yet and for the following grains show negligible differences; indeed, for grains two to five, sub-grain and mesoscale results have almost identical lower and medium quartiles of the FIP distributions, and only the upper quartile appears to be slightly higher for the sub-grain model. Accordingly, grains 6 to 10 also have slightly high upper quartiles and extreme values when compared to the first grains.

The significance of Figure 99 is that **the subgrain and the mesoscale models result in statistical distributions of FIP_0 that are almost identical, supporting the use of Equation (102) to model the average subgrain evolution**. Since the nucleation calculation is the same for both methods, the location of the crack is identical, but the extension to the second, third and fourth grain occurred exactly through the same grains in 83%, 66% and 53% of the cases, respectively. These values do not consider the fact that the same grains in both methods might be cracked in different sequences, which reduces the differences in the crack paths between sub-grain and mesoscale models to about a third of the cases after five grains cracked.
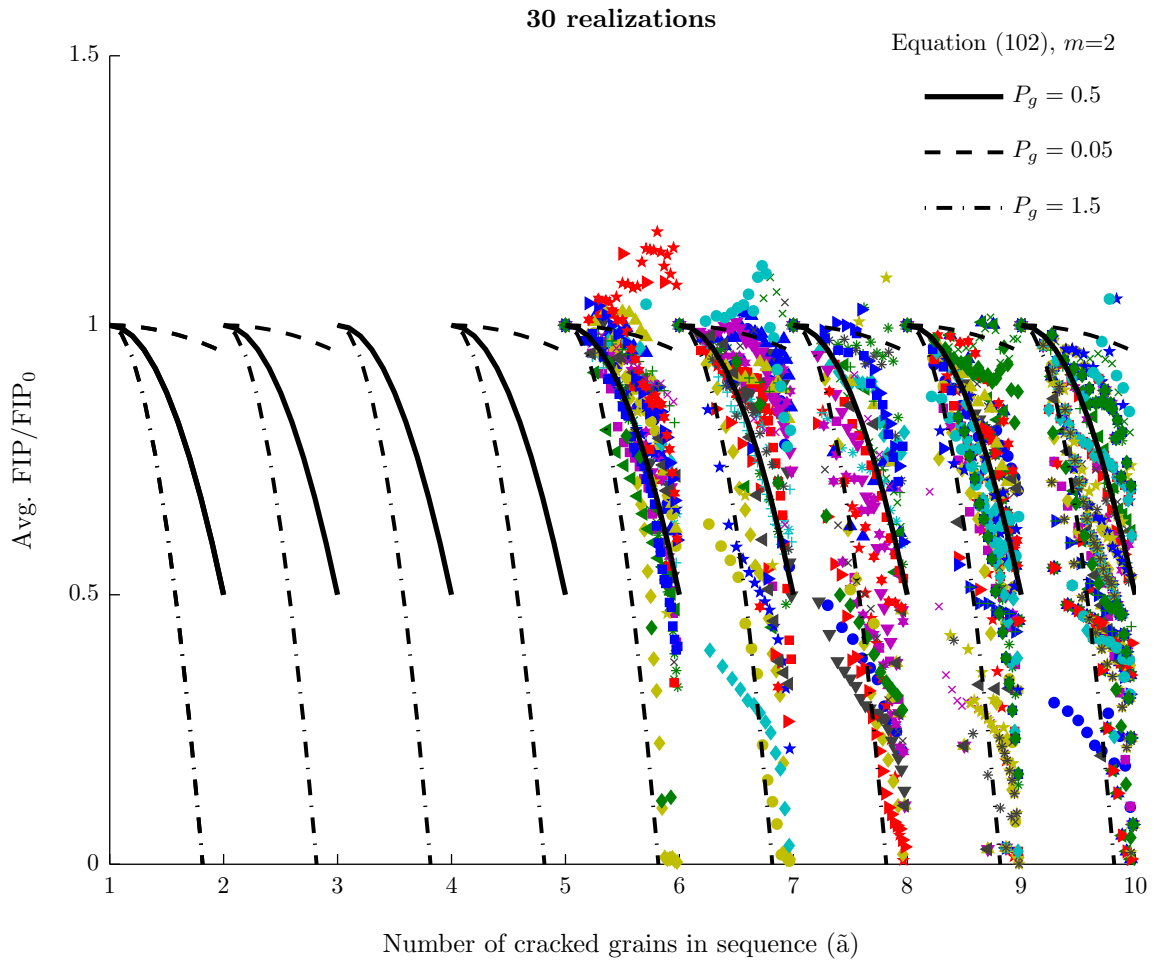
Figure 98: Evolution of the normalized FIP within a grain as a crack grows after the fifth grain, and the proposed subgrain estimation in black line. The first four grains to crack were computed using the mesoscale model.
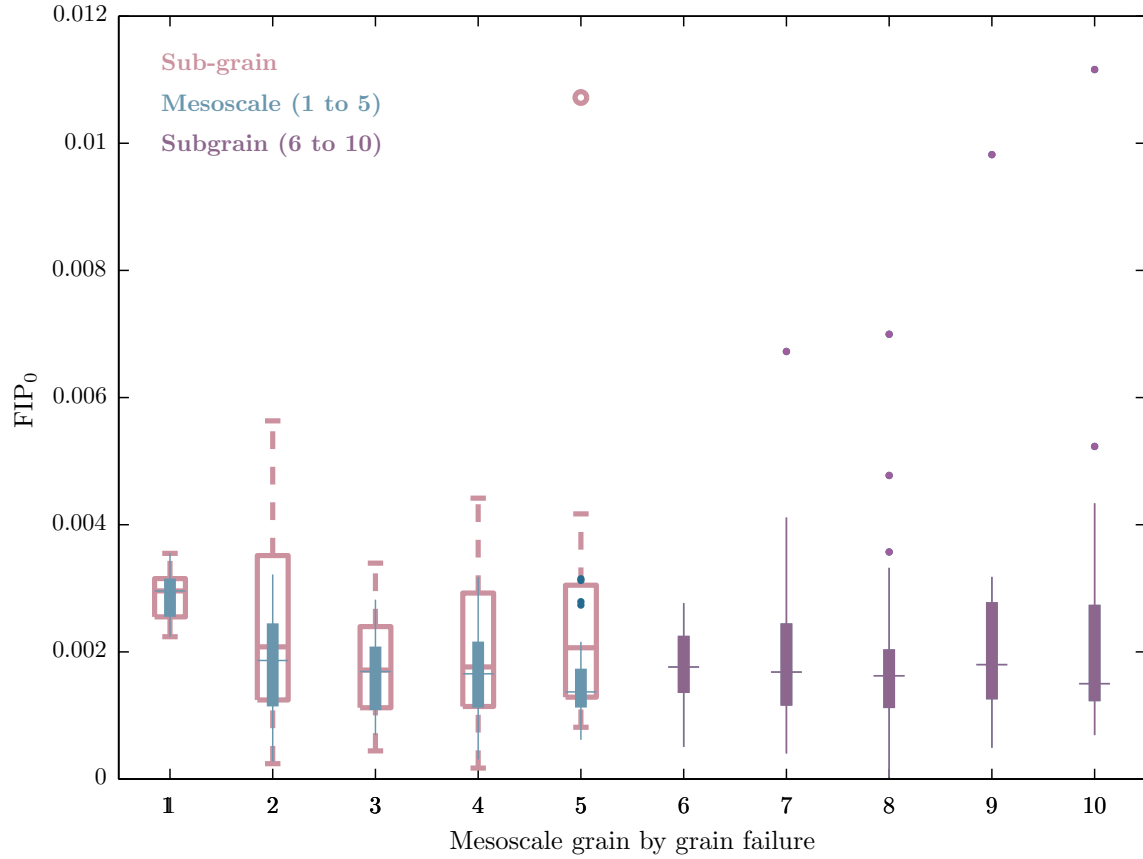
Figure 99: Boxplot compiling the data from sub-grain and mesoscale simulations. The lower ($Q1$) and upper ($Q3$) quartiles correspond to the bottom and top of the green boxes, respectively, and the medium quartile ($Q2$) corresponds to the line near the middle of the box. The whisker length satisfies that $Q3 + 1.5(Q3 - Q1)$ and $Q1 - 1.5(Q3 - Q1)$ and extends up to the most extreme data value in that range. The data outside those limits are represented with circles. Note the good agreement in the distributions from sub-grain (hollow boxes) and mesoscale (full boxes) simulations for grains 2 to 5.

6.3.5 Life estimation in the MSC regime

The number of cycles to nucleate a crack is estimated by Equation (94), but for the MSC regime the mesoscale model computes the crack growth rate within each grain. To complete the formulation for life estimation, the crack growth rate needs to be integrated with respect to the crack length.

In the case of transgranular failure, the crack growth rate depends on the normalized crack length a_i that varies between zero and one (from uncracked to fully cracked grains). After combining Equations (97) and (102), the crack growth rate depends on a_i, m and P_g

$$\frac{da_i}{dN}\bigg|_{msc}^{\alpha} = \phi_{trans}\left\langle \frac{D_{st} + \sum_i^n \omega^i {D_{nd}}^i}{d_{gr}^{ref}} 2\mathrm{FIP}_0^{\alpha}(1 - P_g(a_i)^m) - \Delta\mathrm{CTD_{th}}\right\rangle. \tag{103}$$

To integrate this equation, the sub-grain parameters in Equation (102) are considered as constants, $m = 2$ and $P_g = 0.5$. An alternative approach could compute P_g based on a statistical distribution, however, m should still be considered a constant to facilitate the analytical integration of Equation (103), for example:

$$\int_0^1 \frac{da_i}{dN}\bigg|_{msc}^{\alpha} = \frac{1}{\sqrt{c_1 c_2}}\mathrm{atan}\left(D_{st}\sqrt{\frac{c_2}{c_1}}\right) \tag{104}$$

where,

$$c_1 = \phi_{trans}\frac{D_{st} + \sum_i^n \omega^i {D_{nd}}^i}{d_{gr}^{ref}} 2\mathrm{FIP}_0^{\alpha} - \Delta\mathrm{CTD}_{th} \tag{105}$$

and

$$c_2 = \frac{1}{2}\phi_{trans}\frac{D_{st} + \sum_i^n \omega^i {D_{nd}}^i}{d_{gr}^{ref}} 2\mathrm{FIP}_0^{\alpha}\left(D_{st} + \sum_i^n \omega^i {D_{nd}}^i\right) \tag{106}$$

Equation (104) estimates the MSC life for transgranular failure for each slip direction in each band. Hence, the path followed by the crack is defined by the band that has the minimum life among all the bands that have at least one element neighboring the current crack perimeter; this is referred as being in contact with the crack.

In a scenario in which a crack has passed completely through a grain and is extending on its neighboring grains, it is possible that transgranular crack growth occurs in multiple grains, simultaneously. To account for this situation, the simulations keeps a record of the number of cycles undergone since the crack first reached the ith GB ($N_{History}$). This history

is then subtracted to the life predicted for each band that is connected to the ith GB, since it is assumed that the crack has started growing before, but some other grain cracked faster. Hence, for each band the simulation computes,

$$N\Big|_{msc}^{\alpha} = N_{Computed}\Big|_{msc}^{\alpha} - N_{History} \tag{107}$$

This strategy keeps track of the life consumed by those grains that neighbor the crack but did not crack, rendering them more prone to failure.

Similarly, the estimation of intergranular life requires the integration of the crack growth rate in Equation 17. However, as discussed before, due to the distributed nature of the Zener-Stroh mechanism the life is calculated for each element, and only afterwards averaged over the GB sector. Consequently, the integral assumes that the FIP_{int} is constant along the element (does not depend on the length of the crack), which implies that the rate can be approximated by a discrete difference. Hence,

$$N\Big|_{msc}^{inter} = l_{element}\left[\phi_{int}exp\left\{-\frac{Q - B\langle\sigma_{max}^{GB}\rangle}{RT}\right\}\Delta t^{(1/2-\xi)}FIP_{int}\right]^{-1}, \tag{108}$$

in which $l_{element}$ is the size of the element. Thus, the expected intergranular life of each portion of GB is calculated by averaging the life $N\Big|_{msc}^{inter}$ for all the elements in one grain that are in contact with another grain.

Figure 100 presents a summary of the algorithm that computes the intergranular and transgranular MSC lives. Before predicting the MSC life of the following grain to crack, the FIPs are updated by applying two loading cycles.
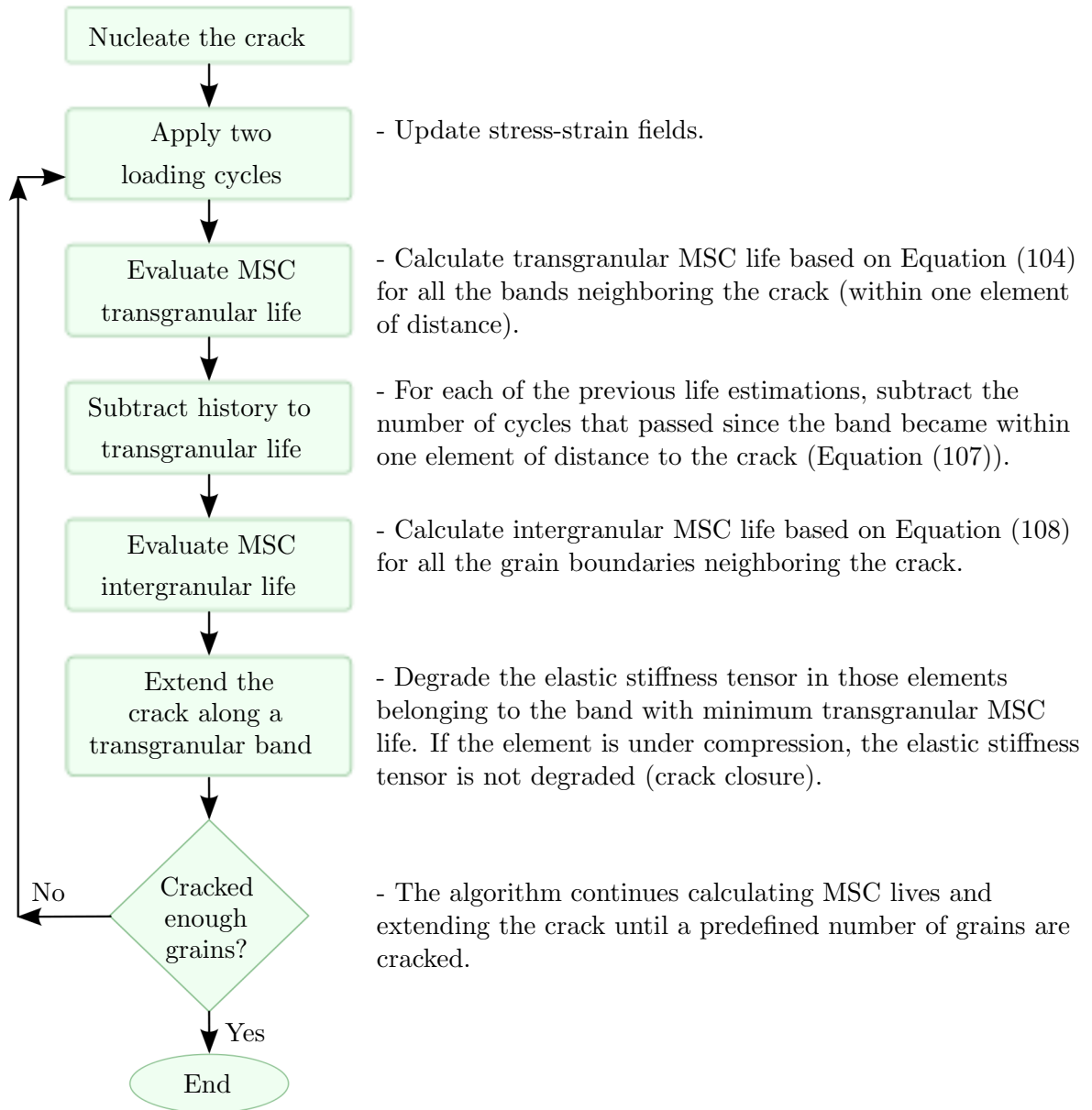
Figure 100: Summary of the MSC life calculation algorithm for transgranular and intergranular failure.

6.4 Assessment of the effect of annealing twins on FIPs

The experimental fatigue literature shows extensive evidence that twins can be, but not always, favorable sites for fatigue crack nucleation [24, 172, 58]. In the particular case of FCC metals and alloys with low SFE, coherent symmetric $\Sigma 3$ annealing twins are the most prone to enhance the fatigue crack initiation driving force [128, 129]. This type of twin corresponds to a rotation of the lattice orientation of 60° with respect to the $\langle 1\,1\,1 \rangle$ plane, which forms a 180° rotation of the lattice about the twin plane normal. Heinz and Neumann [72] studied the effects of twin boundaries in FCC alloys developing anisotropic elastic models and found that twins can be the source of a local stress concentration effect. In the case of twin laminae, the stress concentration displaces dislocations along the slip plane and leads to stronger strain localization, which increases the probability of nucleating a crack at a twin.

This section assess the effect of $\Sigma 3$ twin on the driving force to nucleate a crack. The algorithms developed to average FIPs along bands was adapted to introduce explicit $\Sigma 3$ twins in grains; a twin is defined by adding a rotation (that depends on the type of twin boundary) to the Euler angles on those elements along one or multiple bands. This is, the Euler angles of the twin are deduced from the rotation matrix of the twin, $\left[R_{twin} \right]$, which is computed by multiplying the rotation matrix for a 60° rotation along the $\langle 1\,1\,1 \rangle$ direction $\left[R_{60°@\langle 1\,1\,1 \rangle} \right]$ by the rotation matrix resulting from the original Euler angles for the lattice $\left[R_{lattice} \right]$, i.e.,

$$\left[R_{twin} \right] = \left[R_{lattice} \right] \left[R_{60°@\langle 1\,1\,1 \rangle} \right] \tag{109}$$

The rotated Euler angles are then employed for defining the initial orientation of the lattice in elements within the twins.

6.4.1 Twins in Single crystals

A set of simulations was designed to assess twins in single crystals. The simulations render 3D single crystal cubes loaded under shear, and the lattice orientation is such that the $\langle 1\,1\,1 \rangle$ vector lies along the X axis (see Figure 101). The model contains 21952 elements,
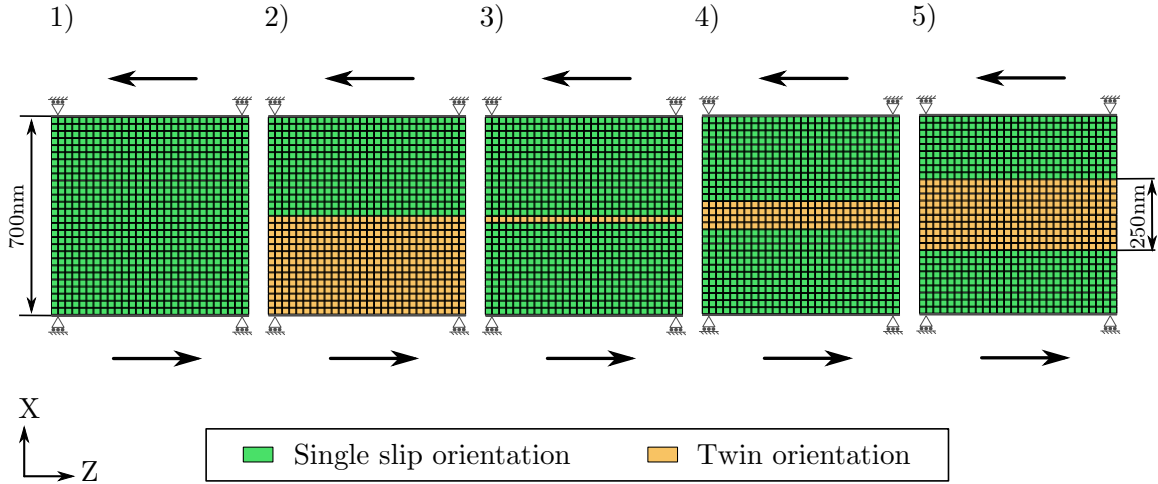
Figure 101: Schematic representation of the five cases analyzed. Some elements in bands associated with the $\langle 1\ 1\ 1 \rangle$ slip plane normal (horizontal) have a crystallographic orientation that simulate twins. The simulations are fully 3D, and the upper and lower boundary layers are displaced along the Z axis, but they are constrained not to move along the X and Y axes. The other faces of the cubic mesh are free to displace and have no boundary constraint Cases: 1) no twin, 2) grain corner twin, 3) one band is a complete-parallel twin, 4) four bands form a complete-parallel twin, 5) ten bands form a complete-parallel twin.

representing a 700 nm-side cube subdivided in bands of 25nm. Since the bands are aligned with the slip planes, the bands associated with the $\langle 1\ 1\ 1 \rangle$ slip plane normal divide the cubic mesh in 28 planes along the X axis (see Figure 101).

The loading consisted in displacing the upper and lower boundary surfaces of the crystal 7 nm in opposite directions along the Z axis. These surfaces are not allowed to move in the X and Y axes, while the other faces of the cubic mesh are free to displace and have no boundary constraint. A total of five strain-controlled triangular cycles were applied with a fatigue ration of $R_\epsilon = 0.1$.

Five cases were analyzed as presented in Figure 101:

- No twin: the entire crystal is oriented for single slip,

- Grain corner twin: half crystal is oriented for single slip, and half as a $\Sigma 3$ twin,

- One band is a complete-parallel twin: only one band is oriented as a $\Sigma 3$ twin,

- Four bands form a complete-parallel twin: four bands are oriented as a $\Sigma 3$ twin.

- Ten bands form a complete-parallel twin: ten bands are oriented as a Σ3 twin.

These cases are based on the twin configurations described by Meyer and Murr [126], for twins that extend along the entire cross-section of grains. Table 6.4.1 summarizes the orientation of the slip plane normal and slip directions before and after rotating the orientation for single slip and twin orientation. Note that slip plane 1 has a slip direction along the z axis, so it should be the most activated plane in models without twins. The FIPs and their averages for each slip system on each band are evaluated after 4 loading cycles using the methodology described in section 6.1.1.

Figure 102 presents the averaged FIP for each band on simulations without twins (Case 1). The slip plane number is indicated above the barplot, and as expected, the first slip plane dominates plastic deformation. Note that for such slip plane, the applied boundary conditions modulate the FIP with a slight negative concavity, which suggests that a crack would initiate in the middle of the crystal. Figure 103 presents the averaged FIP for each band on simulations in which a half crystal is twinned (Case 2), and shows a change in the planes activated (the twin activates plane 3), but also a significant increment in the FIPs magnitudes in the twinned region. The boundary conditions exert a slight influence on the FIP distribution that may affect the locations of cracks.

Figure 104 presents the averaged FIP for each band on simulations in which only one band is twinned (Case 3). Compared to Figure 103, slip plane 1 has FIPs slightly higher, but these are still below the FIP for the twin in slip plane 3. Note that the latter is lower than in Figure 104, which suggests that the width of the twin plays a role. The effect of the boundary conditions is consistent with the previous cases.

Figures 105 and 106 present the averaged FIP for each band on simulations in which four bands and ten bands are twinned, respectively (Cases 4 and 5). Compared to Figure 103, Figures 105 and 106 present comparable FIPs for slip plane 1 within the twin, but below the FIPs for slip plane 3. Note that the latter have values slightly higher than those in Figure 104. The effect of the boundary conditions is consistent with the previous cases, but the borders of the twins seem to have a higher driving force.

The simulations of single crystals with twins showed that FIPs tend to increase by a

176

Table 8: Summary of the slip plane normal and slip directions, and the corresponding magnitudes after being rotated for single slip and the double rotation for the twin lattice.

Slip plane	Initial slip normal	Rotated slip normal	Initial slip direction	Rotated slip direction	Twin slip normal	Twin slip direction
1	⟨1 1 1⟩	⟨1 0 0⟩	[0 1 -1]	[0 0 -1]	⟨1 0 0⟩	[0 -0.866 -0.5]
2	⟨1 1 1⟩	⟨1 0 0⟩	[-1 0 -1]	[0 0.866 0.5]	⟨1 0 0⟩	[0 0.866 -0.5]
3	⟨1 1 1⟩	⟨1 0 0⟩	[1 -1 0]	[0 -0.866 0.5]	⟨1 0 0⟩	[0 0 1]
4	⟨1 -1 -1⟩	⟨-0.333 -0.943 0⟩	[0 -1 1]	[0 0 -1]	⟨-0.333 -0.471 0.817⟩	[0 0.866 0.5]
5	⟨1 -1 -1⟩	⟨-0.333 -0.943 0⟩	[-1 0 -1]	[-0.817 0.289 -0.5]	⟨-0.333 -0.471 0.817⟩	[0.817 -0.577 0]
6	⟨1 -1 1⟩	⟨-0.333 -0.943 0⟩	[1 1 0]	[0.817 -0.289 -0.5]	⟨-0.333 -0.471 0.817⟩	[0.817 0.289 -0.5]
7	⟨-1 1 -1⟩	⟨-0.333 0.471 -0.817⟩	[0 1 1]	[0.817 -0.577 0]	⟨-0.333 -0.471 -0.817⟩	[0 0.866 -0.5]
8	⟨-1 1 -1⟩	⟨-0.333 0.471 -0.817⟩	[1 0 -1]	[0 -0.866 -0.5]	⟨-0.333 -0.471 -0.817⟩	[0 -0.866 0.5]
9	⟨-1 1 -1⟩	⟨-0.333 0.471 -0.817⟩	[-1 -1 0]	[-0.817 0.289 0.5]	⟨-0.333 -0.471 -0.817⟩	[-0.817 0.577 0]
10	⟨-1 -1 1⟩	⟨-0.333 0.471 0.817⟩	[0 -1 -1]	[-0.817 -0.577 0]	⟨-0.333 0.943 0⟩	[-0.817 -0.289 0.5]
11	⟨-1 -1 1⟩	⟨-0.333 0.471 0.817⟩	[1 0 1]	[0.817 -0.289 0.5]	⟨-0.333 0.943 0⟩	[0.817 0.289 0.5]
12	⟨-1 -1 1⟩	⟨-0.333 0.471 0.817⟩	[-1 1 0]	[0 0.866 -0.5]	⟨-0.333 0.943 0⟩	[0 0 -1]

177
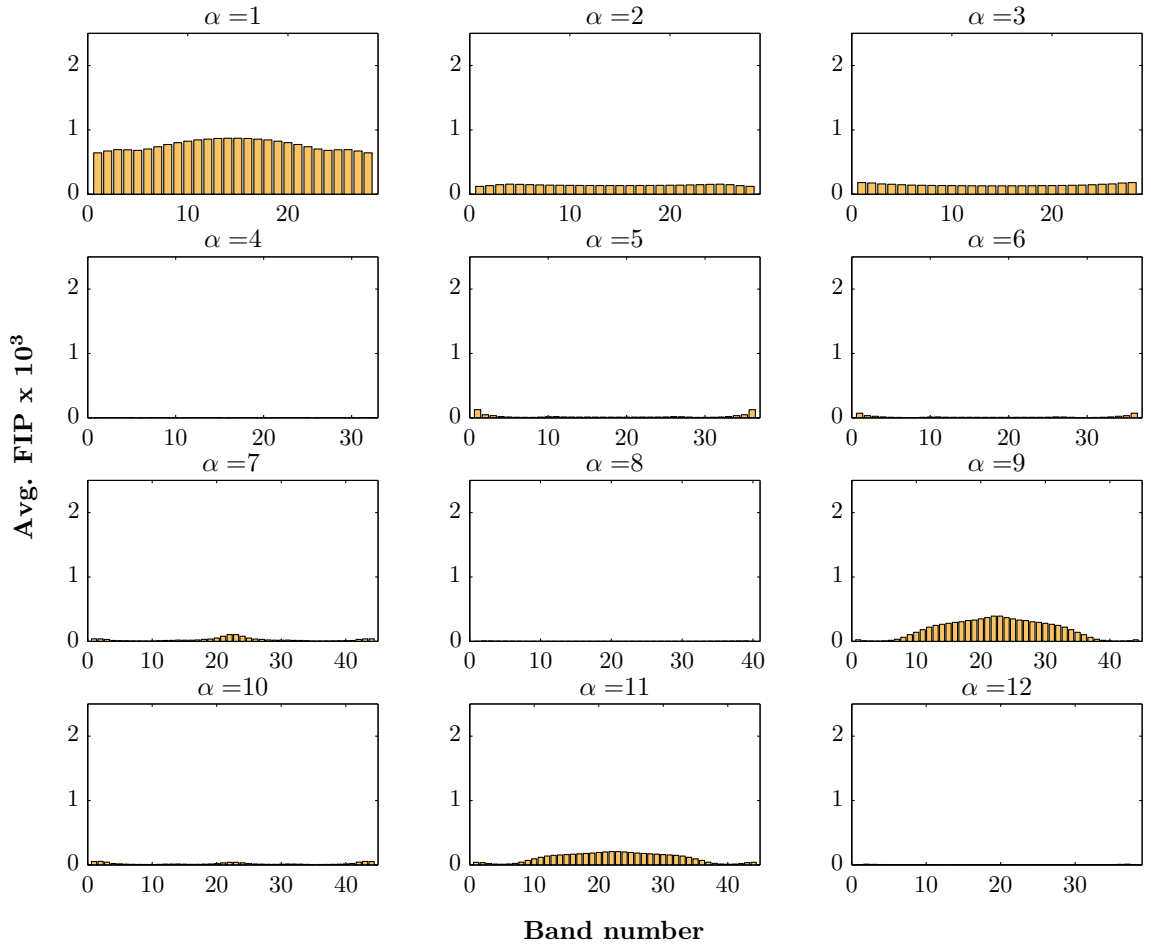
Figure 102: Bar plots of the averaged FIP for 12 octahedral slip systems corresponding to case 1 (no twin). Note that the first slip plane dominates plastic deformation.
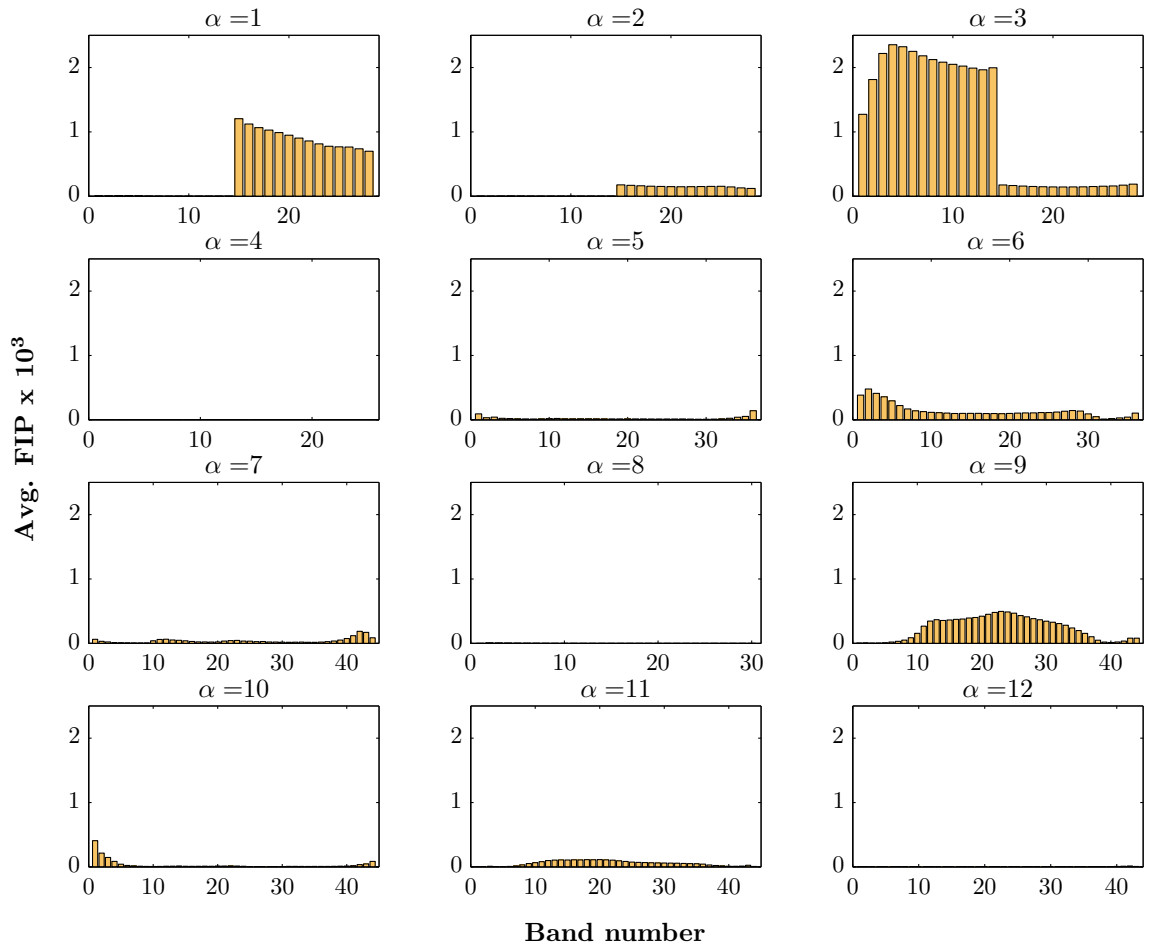
Figure 103: Bar plots of the averaged FIP for 12 octahedral slip systems corresponding to case 2 (half crystal twinned).

179
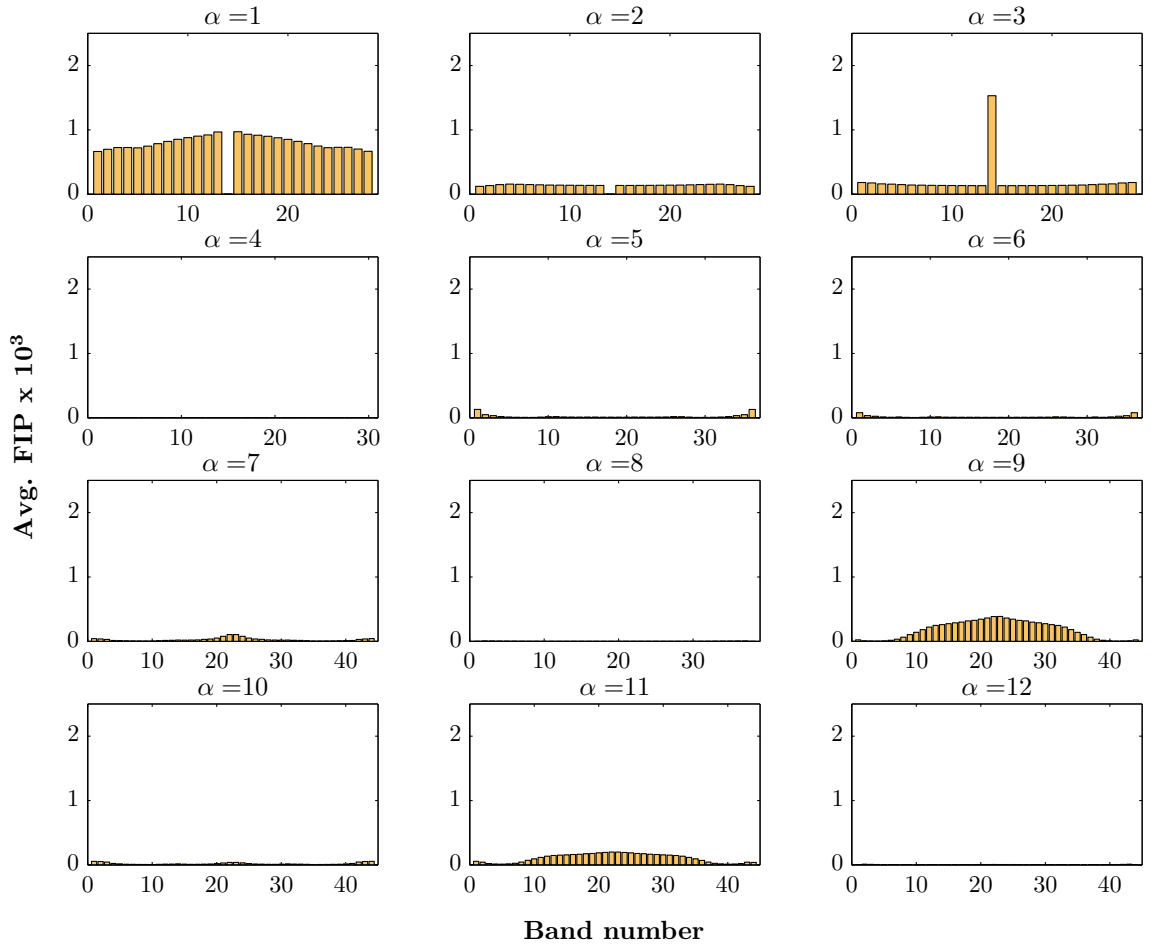
Figure 104: Bar plots of the averaged FIP for 12 octahedral slip systems corresponding to case 3 (only one band twinned).
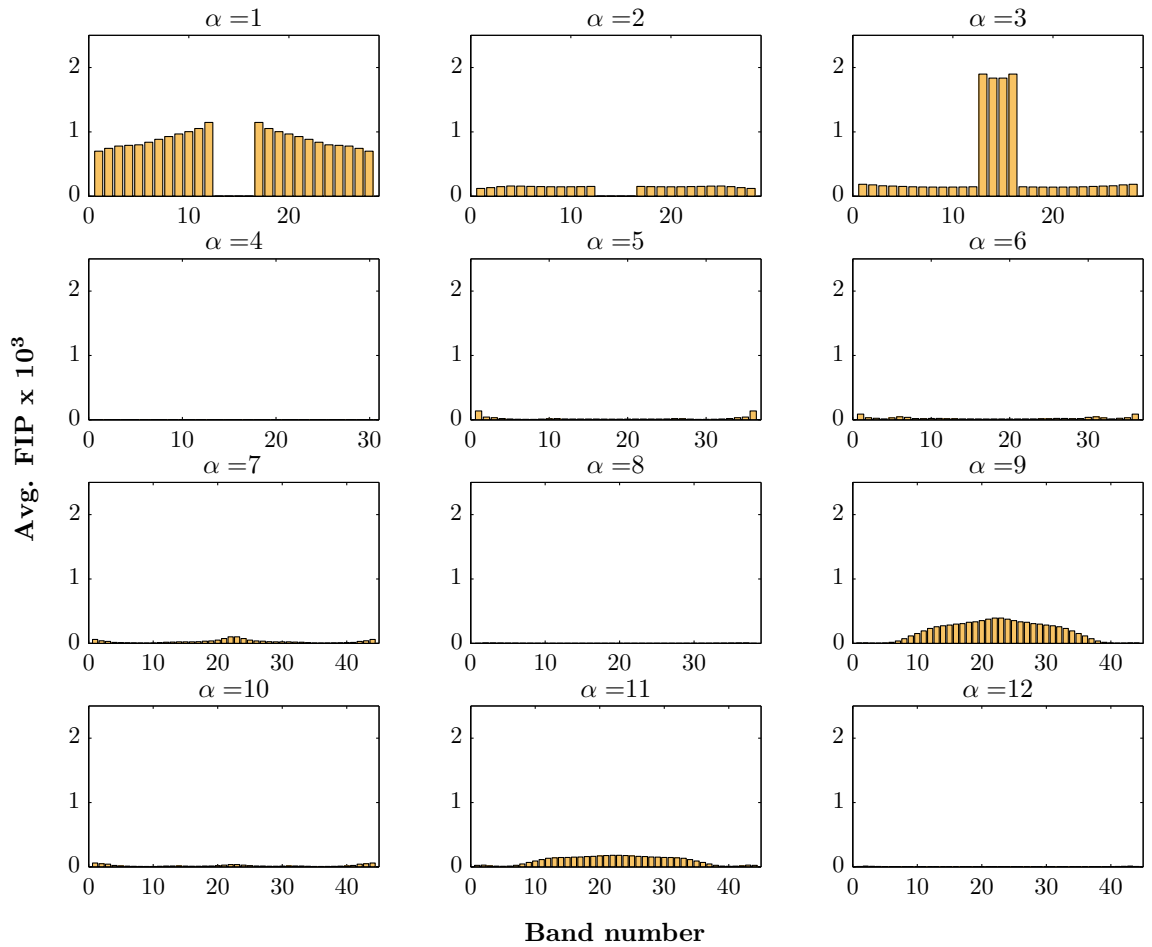
Figure 105: Bar plots of the averaged FIP for 12 octahedral slip systems corresponding to case 4 (four bands twinned).

181
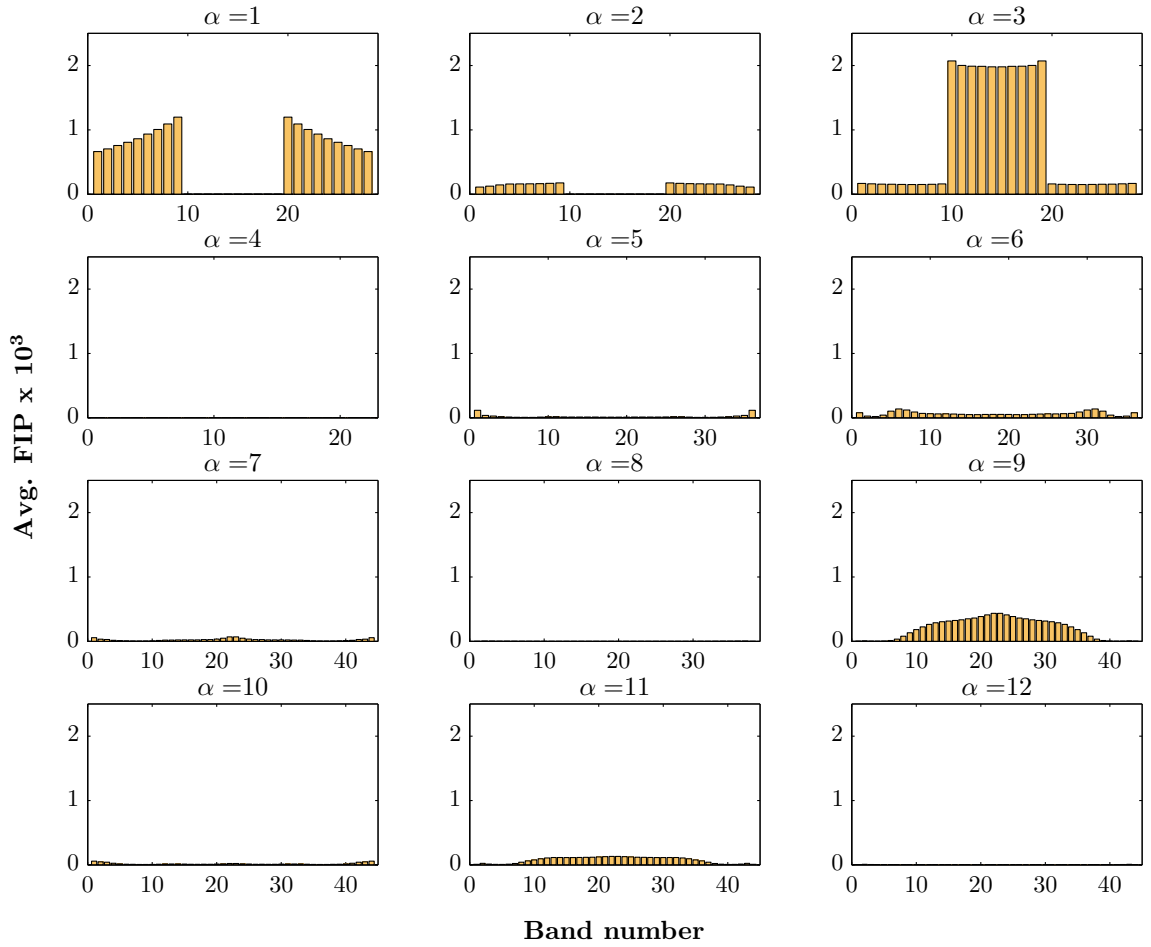
Figure 106: Bar plots of the band averaged FIP for each of the 12 slip systems corresponding to case 5 (ten bands twinned).

factor of 2 or less within the twins. Secondly, the width of the twins affects the FIPs; very thin twins intensify the FIP less than wider twins, with the worst case being when half a crystal is twinned. These results suggest that deformation twins have a less detrimental effect on fatigue life than annealing twins, since the latter are usually much wider. Furthermore, the borders of the twins show a local increment of the driving force, which has been found in experiments [149]. However, the loading boundary conditions may influence the location of the maximum FIP.

6.4.2   Twins in polycrystals

The effect of twins in FIP distributions in polycrystals is analyzed by including twins to the polycrystalline models considered in sections 6.3.4. Each simulation contains 10 grains (out of 52) with twins in half the grain volume. The twins were introduced by adding a rotation of $60°$ along the [1 1 1] axis to the crystallographic direction of each twinned grain. The results are based on the analysis of the grains that contained twinned bands. The average FIPs on each slip system on each band are evaluated by the end of the third loading cycle. A total of 30 equivalent realizations were modeled, corresponding to 1560 grains. For comparison, exactly the same models were reproduced without the twins (that corresponds to FIP results after nucleating a crack in sections 6.3.4); these simulations allow comparison of the FIP on bands with twins or their neighbors. To avoid considering bands that undergo essentially elastic deformation, only bands with expected nucleation lives below 10^9 cycles were considered.

Figure 107 presents two histograms with the distributions of FIPs for the bands within the twin, and the same bands on simulations without twins but exact same microstructure. The data suggest that the twin enhances the driving force along the bands, and the enhancement is less than an order of magnitude. Similarly, Figure 108 depicts the distributions of FIPs for bands that are not twinned (but within grains that have twins), and the same bands on simulations without twins; the data show almost no influence of the twins. Overall, these results are in agreement with the trends found in single crystal simulations.

The histograms in Figures 107 and 108 show the general trends of the FIP averaged along
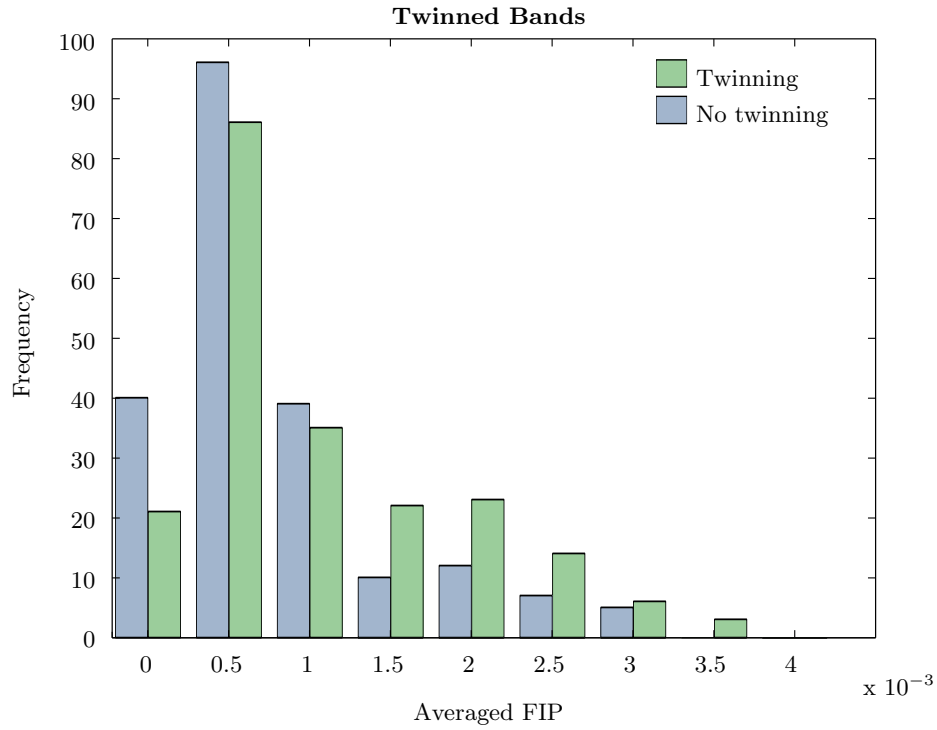
Figure 107: Distribution of the FIP for those bands containing a twin, and the corresponding band on simulations without twins.
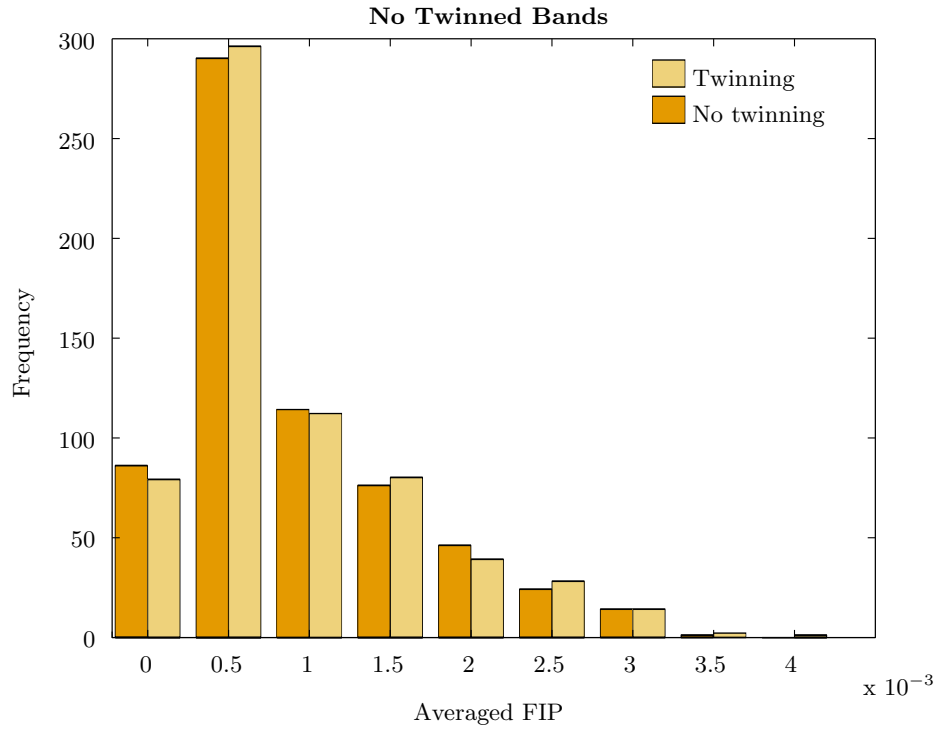
Figure 108: Distribution of the FIP for non-twinned bands that are neighbors to twins, and the corresponding band on simulations without twins.
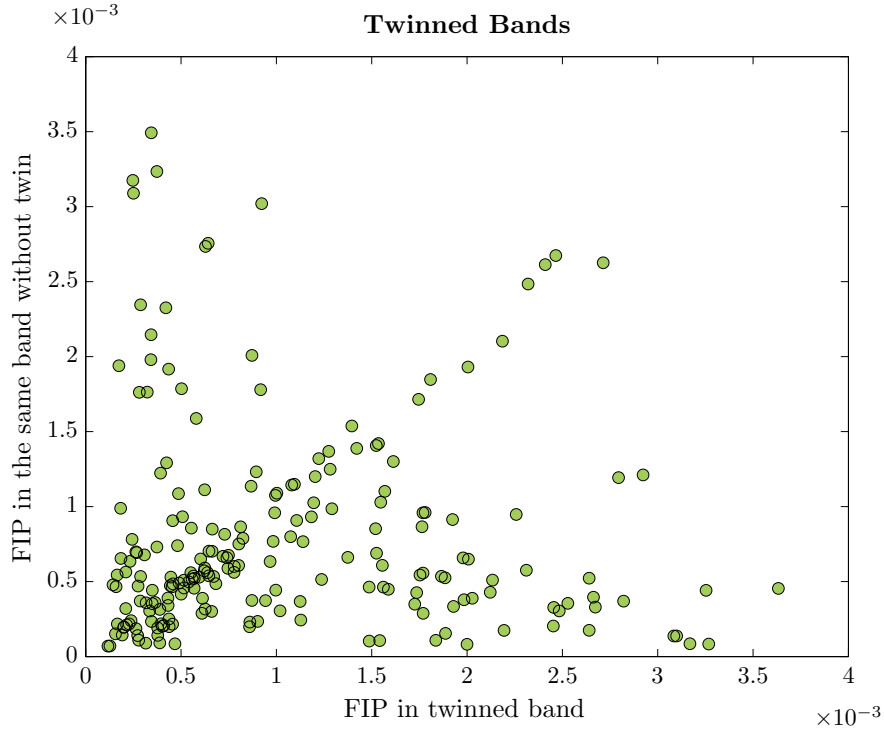
Figure 109: Comparison between the FIP in bands with twins and the FIP of the exact same band in simulations with the exact same microstructure but without twins.

bands. However, they cannot show the relation between the FIP of a band in simulations with twins, and the FIP of the exact same band in simulations with identical microstructure but without twins. Thus, Figure 109 plots the FIP from a band that is twinned versus the FIP of the exact same band in simulations without twins. The correlation between both FIPs is poor, which suggests that simulations with explicit twins may predict crack initiation in bands that present much lower FIPs in simulations with the same microstructure, but without twins.

Similarly, Figure 110 plots the FIPs from bands that are non-twinned, but belong to a grain with twins versus the FIP of the exact same band in simulations without twins. In this case, the FIPs show a linear correlation, which implies that simulations without explicit twins can predict the accurately the FIPs of those bands that are not be twinned, but belong to grains with twins.

To conclude the analysis of twins, the results have shown that FIPs are intensified by twins, and wider twins have a more pronounced effect. The FIPs were intensified by less
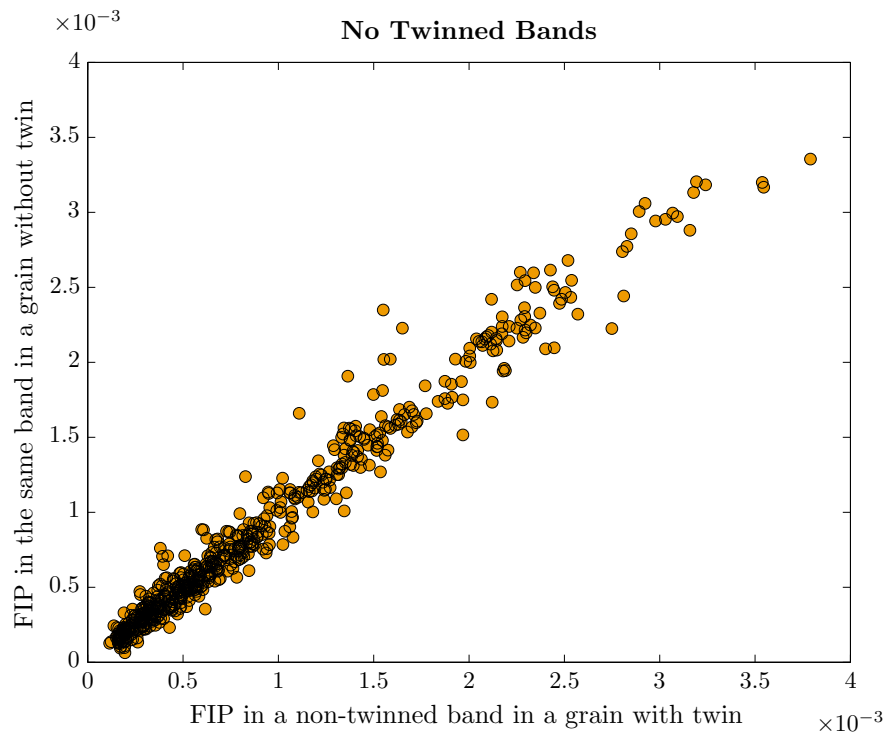
Figure 110: Comparison between the FIP in bands without twins, but in a grain with twins, and the FIP of the exact same band in simulations with the exact same microstructure but without twins.

than an order of magnitude, which is lower than the intrinsic variability found in the FIP. Therefore, this research will treat the effects of twins as a special case of strain localization, which is considered in the mesoscale model by Equation (95). If twins are not explicitly modeled, this methodology should adequately predict the magnitudes of the FIPs, although the location of a crack may be inaccurate.

6.5 Preliminary conclusions

This Chapter adopts the general framework for fatigue crack formation and MSC growth introduced before and works out the details of the formulation for RR1000 superalloy, including a first order calibration of the parameters involved. The most important findings include,

- The introduction of damage only exerts a moderate influence on the neighboring elements. This fact suggests that for small cracks, the stress intensification on a grain due to crack growth is moderate, does not resemble the LEFM model, and is greatly affected by the microstructure.

- The calibration of the fatigue model can be attempted using limited experimental data belonging to small fatigue cracks and long cracks, which are essentially employed to calibrate the proportionality factor between crack growth rate and FIPs.

- When considering multiple realizations, the values of the fatigue driving force that nucleates cracks presents a very narrow range (about a factor of two), while it can vary orders of magnitude on the subsequent grains. This finding suggests that the variability of the small crack regime depends more on the extension to subsequent grains than on the nucleation within the first grain.

- The analysis of the sub-grain evolution showed that the mean behavior of the fatigue driving force presents a decreasing trend that can be approximated by $\text{FIP}^\alpha = \text{FIP}_0^\alpha \left(1 - P_g \text{a}_i^2\right)$, a_i representing the fraction of the grain that has been cracked.

187

- When the subgrain and mesoscale analyses were applied to the same set of microstructures the distributions of FIP_0 showed minimum differences, which were a fraction of the overall variability of the fatigue process. This results validate the mesoscale framework as a modeling technique that requires lower computational work.

- The analysis of twins showed that, the wider the twin, the more intensified the FIP becomes. The FIPs were intensified by less than an order of magnitude, which can be considered as a special case of strain localization. However, models without explicit twins may not predict the location of a crack accurately.

CHAPTER VII

APPLICATION: FATIGUE ANALYSIS OF RR1000 MICROSTRUCTURES WITH ALA GRAINS

Having built, verified and validated a computational tool to assess fatigue initiation and early crack growth, this thesis proceeds to apply that tool to study the early fatigue life of RR1000 microstructures containing ALA grains [133, 63]. This chapter introduces multiple realizations of models with one ALA grain surrounded by smaller grains. The parametric study includes changing the size of the ALA grain, the assessment of the transgranular and intergranular failure and the transition between fatigue Stage I/Stage II.

7.1 Running the computational tool

The simulations have been developed under Linux-based ABAQUS V6.9, running in Ubuntu 10.04 (Lucid Lynx) on an 8-core Intel machine with 12GB RAM and Linux Intel FORTRAN compiler ifort V11. Such a system is able to perform mesoscale simulations comfortably up to about 8000 elements, requiring less than 24 hours in simulations that apply about 30 loading cycles up to 1% strain range. However, most of the simulations in this Chapter were actually run at Georgia Tech Partnership for Advanced Computing Environment (PACE), which has hundreds of CPUs and GBs in RAM available. The PACE facility allowed the computer algorithm to be tested, at least partially, using ABAQUS Linux-based versions V6.7, V6.10 and V6.11 with successful results. The models were also evaluated under Windows environments, which showed notably less efficiency in the administration of the RAM.

In general, the simulations showed robust and consistent convergence speed, and the few cases in which ABAQUS aborted simulations correspond to either a crack arrest (the crack extension takes over 10^9 cycles) or a prolonged hold period. This latter case required the reduction of the maximum allowable time increment, at least for the loading steps

with constant applied strain. Because the study of microstructures containing ALA grains requires a statistical analysis, the target size for the models is chosen between 1000 and 6000 elements. This range provided the best balance between accuracy of the simulations and computational speed in order to achieve between 30 to 60 realizations for each type of microstructure. This task resulted in thousands of computing hours that required the use of computer clusters to run even relatively low-demand simulations. The same type of simulations conducted explicitly over the summed volume with cycle-by-cycle growth would likely require a supercomputer.

7.2   *Models for ALA grain analysis*

The simulation of microstructures with ALA grains was performed by models produced with the Mesh Generator (introduced in section 5.2.1), in which one ALA grain [133, 63] is centered in a cubic mesh with periodic boundary conditions undergoing strain controlled triangular loading. The periodic boundary conditions increase the constraints on the mesh and mitigate the boundary effects, but they also affect the loading after some crack extension (due to stress redistribution), so the crack growth should be limited to a few grains.

The microstructures employ three ALA grain sizes, 70 μm, 106 μm and 142 μm surrounded by grains about 10 μm to 30 μm, and a reference microstructure composed only of grains about 10 μm to 30 μm. To make the comparison of FIPs equivalent among microstructures, all the meshes possess elements of 9 μm size; hence, with increasing ALA grain size, the number of bands in the ALA grain increase, but they all represent the same length scale. Furthermore, the surrounding grains have the same refinement for all microstructures, and they usually contain between 1 and 10 elements.

Table 9 presents the parameters employed to create the microstructure models containing one ALA grain, shown in Figure 111. All the meshes correspond to cubes with periodic conditions, as in the case of Bore 15 μm, but for the sake of clarity, only the ALA grains in orange and a few of the surrounding grains are represented. A strain history is applied by displacing the cube face with normal along the Z direction and periodic loading conditions. As discussed in section 6.3.4 the loading is periodic, but it does not have truly periodic

190

Table 9: Model parameters to create the models for studying microstructures with ALA grains and the resulting mesh attributes in bold. The remaining parameters in the Mesh Generator kept their default values, which are based on the calibration of the model.

	Bore 15 μm	ALA 70 μm	ALA 106 μm	ALA142 μm
Cube X, Y, Z length [μm]	90	90	126	162
Large grain 1 [μm]	0	70	106	142
Large grain 2 and 3 [μm]	0 (only one ALA grain)			
d gr ref [μm]	8			
Band period [μm]	9			
Mesh size [μm]	9			
Band jump [μm]	9.05			
Grain size [μm]	10, resulting in 10 μm to 30 μm grains			
μ (lognorm dist.)	-0.1			
σ (lognorm dist.)	0.4			
Max. applied strain [%]	1			
Applied strain rate [%/s]	0.5			
R_ϵ	0.1			
$t_2 = t_4$ [s] (see Figure 77)	0 for triangular or 100 for trapezoidal loading			
Number of elements	**1000**	**1000**	**2274**	**5832**
Number of grains	**174**	**174**	**478**	**1015**

boundary conditions since grain distributions on opposite faces are not identical. Note that for increasing ALA grain size, the volume not occupied by the ALA grain increases and so does the number of grain surrounding, since the grain size is constant. Furthermore, the size of the cubic mesh (first row in Table 9) is big enough to fit at least one grain in between the outside limits and the ALA grain. This characteristic attempts to shield the effects of the periodic boundary conditions on the ALA grain.

Figure 112 presents bar plots for the grain sizes calculated based on spherical grains with equivalent volume for the Bore 15 μm and ALA 70 μm microstructures generated with the Mesh Generator application. Both distributions have a total of 8700 grains from

Bore 15μm

ALA 70μm

ALA 106μm

ALA 142μm
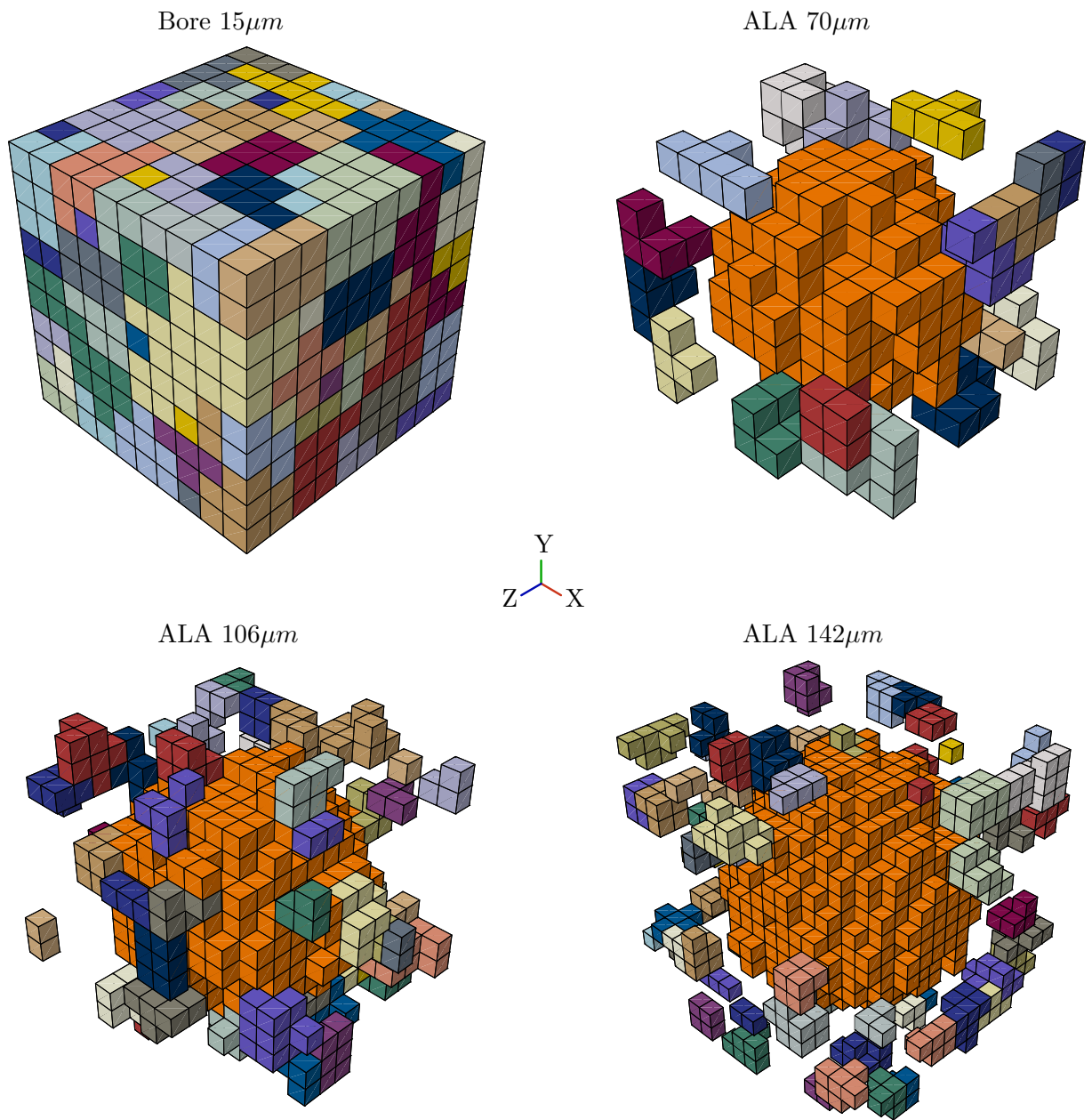
Figure 111: Different microstructures simulated. All models correspond to cube meshes with periodic boundary conditions strained along Z axis, but some grains were removed for clarity. In all the models the element size is equivalent to 9 μm, and the ALA grain (in orange) is surrounded by $10 - 20$ μm grains, similar to Bore 15 μm.

50 realizations and start at 9 μm, which corresponds to the element size. ALA 106 μm and ALA 142 μm microstructures present distributions similar to that for ALA 70 μm, and they are therefore omitted. Because the mesh is discrete, the grain size can only take a finite number of values that become closer with increasing grain size. This characteristic causes the granularity of the data (note the empty spaces in between bars) and the decreasing distance between bars.

7.2.1 Subgrain FIP evolution in ALA grains

Equation 102 is the basis for the mesoscale model, but it was validated only for microstructures with unimodal distributions of grain size. Hence, 30 simulations were developed using the ALA 106 μm microstructure and the sub-grain evolution algorithm explained in Figure 89. The resulting nondimensionalized evolution of the FIP is presented in Figure 113. Note that only 6 simulations out of 30 actually cracked an ALA grain, as shown by the dense-color lines between 0 and 1, and their evolution is in agreement with the results in Figure 95. Although non-ALA grains usually have less than 10 elements and the evolution of the FIP is not well resolved, the cloud of points lies around the black lines that represent Equation 102. These results demonstrate that the mesoscale model is adequate to evaluating ALA grains, and that the subgrain model in Equation 102 introduces a refined evolution of FIP without the need for refined meshes. Hence, the strategy is to use meshes with low refinement to estimate the FIP_0 and later to impose the subgrain evolution that has been deduced using more refined meshes.
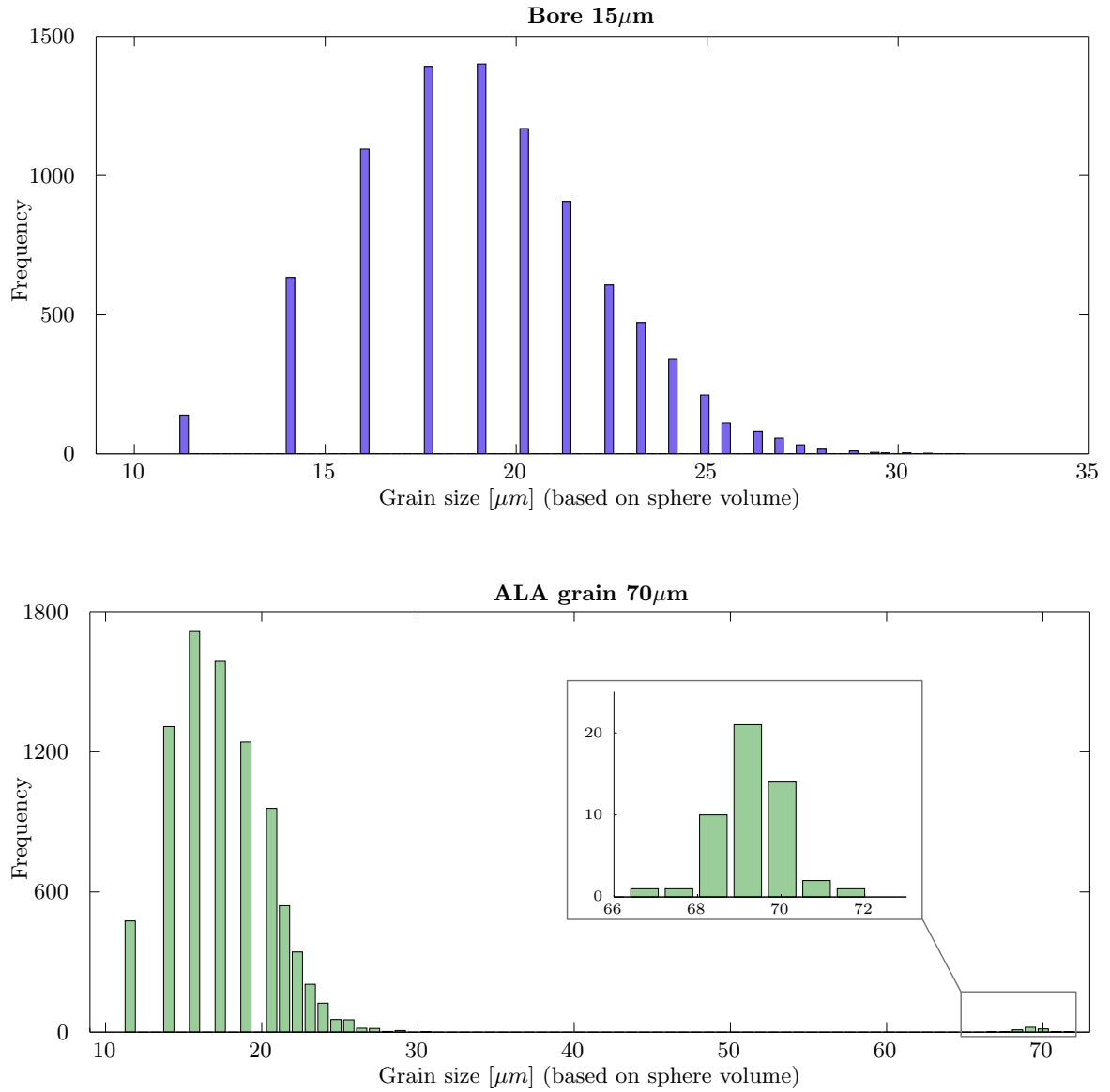
Figure 112: Bar plots presenting grain size distributions for Bore 15 μm and ALA 70 μm microstructures generated with the Mesh Generator application, which employs a lognormal distribution. The size is calculated based on spherical grains with equivalent volume out of 50 realizations, each with 174 grains. ALA 106 μm and ALA 142 μm microstructures present similar distributions to that for ALA 70 μm.
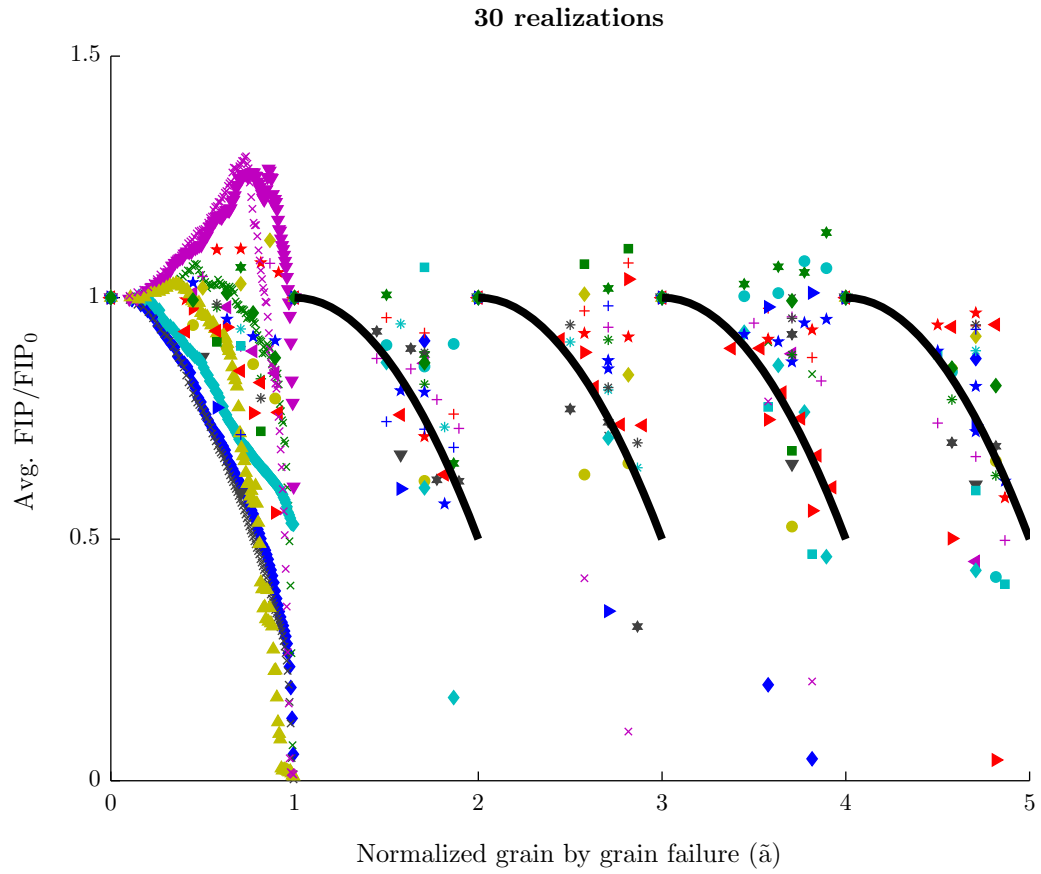
Figure 113: Evolution of the nondimensionalized FIP as a the crack growth within a grain for a microstructure with ALA grains about 106 μm after 30 realizations. Black lines correspond to the subgrain estimation proposed by Equation (102), with $P_g = 0.5$ and $m = 2$. Results are equivalent to those in Figure 95. ALA grains failure result in more refined curves than for the surrounding grains.

7.3 Transgranular fatigue life assessment of ALA grains

Having verified the adequacy of Equation (102), a total of 50 realizations, using the mesoscale model, assessed the early fatigue life of each microstructure in Figure 111 and each loading condition in Table 9. Figure 114 presents the resulting crack length vs. life; each data point corresponds to an extension of the crack by one grain, and the total crack length is computed as the square root of the meandering cracked area. Furthermore, the dotted lines connect data points belonging to the crack extension in the same realization, and the slopes represent the crack growth rate. The cases in which the slope is almost vertical correspond to cracks growing simultaneously on neighboring grains, as considered in section 6.3.5, Equation (104) in particular.

The data for the Bore $15\mu m$ lie in a single cloud of points in Figure 114, but the simulations containing ALA grains present the data divided in two clouds: on top lie the simulations that have nucleated a crack in the ALA grain while at the bottom are those that nucleated in the surrounding grains. These two groups show similar minimum nucleation lives, since they are both dominated by the size of the ALA grain, either because the crack nucleates in it, or because the ALA has low misorientation with the grain that nucleates the crack and enhances the driving force.

Overall, we observe that fatigue life variability is controlled by nucleating the crack or extending it to the first or second grain (after this, the average slope is consistent among the realizations). Indeed, despite the nucleation and MSC regimes that follow different correlations with the FIP, they both play a role in controlling the minimum life. Furthermore, the life in the MSC regime for the first or second grains shows significant differences with that for the subsequent grains, even though they share the fatigue correlation. Hence, **these results shows that not only the nucleation, but the extension of the crack to the first few grains has an important role in controlling the fatigue life**. A similar finding was pointed out in the previous chapter with regard to the variability of the FIP.

Another interesting fact is that, even though the local driving force on each grain is assumed to decrease with increasing crack length, the collective growth along the first

grains presents an increasing crack growth rate with the crack length. **This suggests that it is the increase in the number of grains sampled by the crack front rather than in the driving force that is responsible for the monotonically increasing dependence of the macroscopic crack growth rate on crack length**. Indeed, the FIP has been characterized as proportional to the macroscopic crack length [120, 130, 185], which is equivalent to say that the driving force is proportional to the crack tip perimeter for circular or penny-shaped cracks. The results are consistent with the work of Navarro and de los Rios [147] and the concept of reaching similitude in Fracture Mechanics, but further characterization of the evolution of the driving force would require the study of longer cracks using a specific specimen geometry (i.e., rather than periodic boundary conditions).

Figure 115 compares the results for all microstructures in a single semilog plot, and shows clearly that the larger the ALA grain, the lower the fatigue life. Furthermore, the gray lines present a rough extrapolation of the minimum life until the crack reaches 120 μm. The confidence interval is obtained from using the ranges of slopes from the results. Table 10 and Figure 116 summarize some of the most important statistics from Figure 115. As expected, the minimum nucleation life always occurs for ALA grains and decreases with increasing ALA size. However, the maximum nucleation life in an ALA grain out of 50 realizations is roughly constant, which explains how the wider dispersion of life results in microstructures with ALA grains. Similarly, the maximum nucleation life corresponds to the grains surrounding the ALA grain and decreases with increasing ALA size due to the neighboring grain contributions. Note that the number of simulations that have nucleated in an ALA grain is limited and further simulations would be required for a significant statistical assessment of the life distribution.

7.3.1 Influence of mesh refinement on transgranular fatigue life estimation

Because the element size is 9 μm in all cases in Figure 111, the microstructures show very refined ALA grains composed of hundreds of elements surrounded by coarse bore-type grains composed of 2 to 10 elements. To assess the quality of the life estimation of the coarse grains, a new set of models was developed, similar to Bore 15 μm, but using elements of
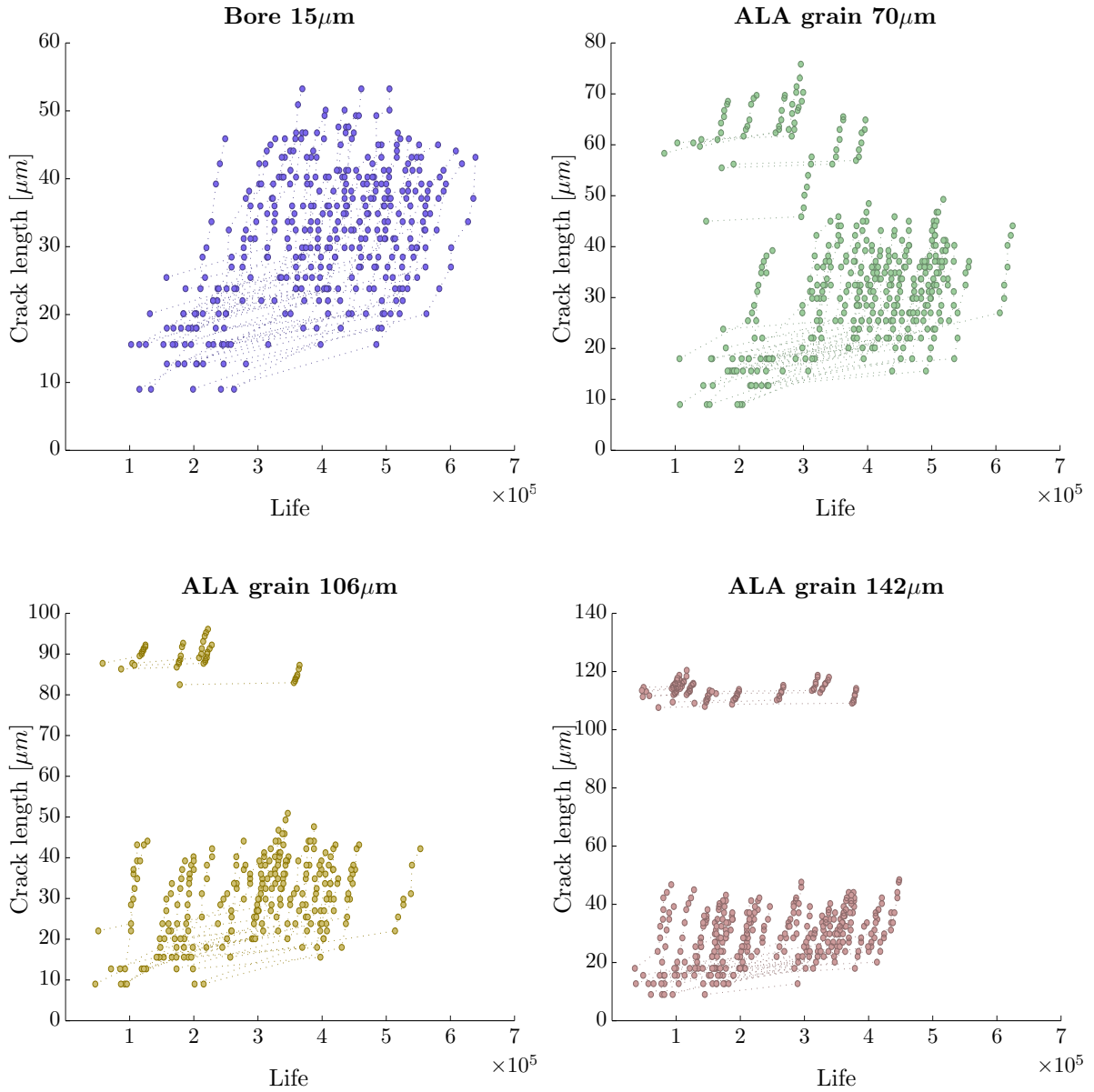
Figure 114: Life vs crack length for the four microstructures analyzed, each with 50 realizations. The upper group of points in ALA grain simulations correspond to realizations in which the crack nucleated in the ALA grain.
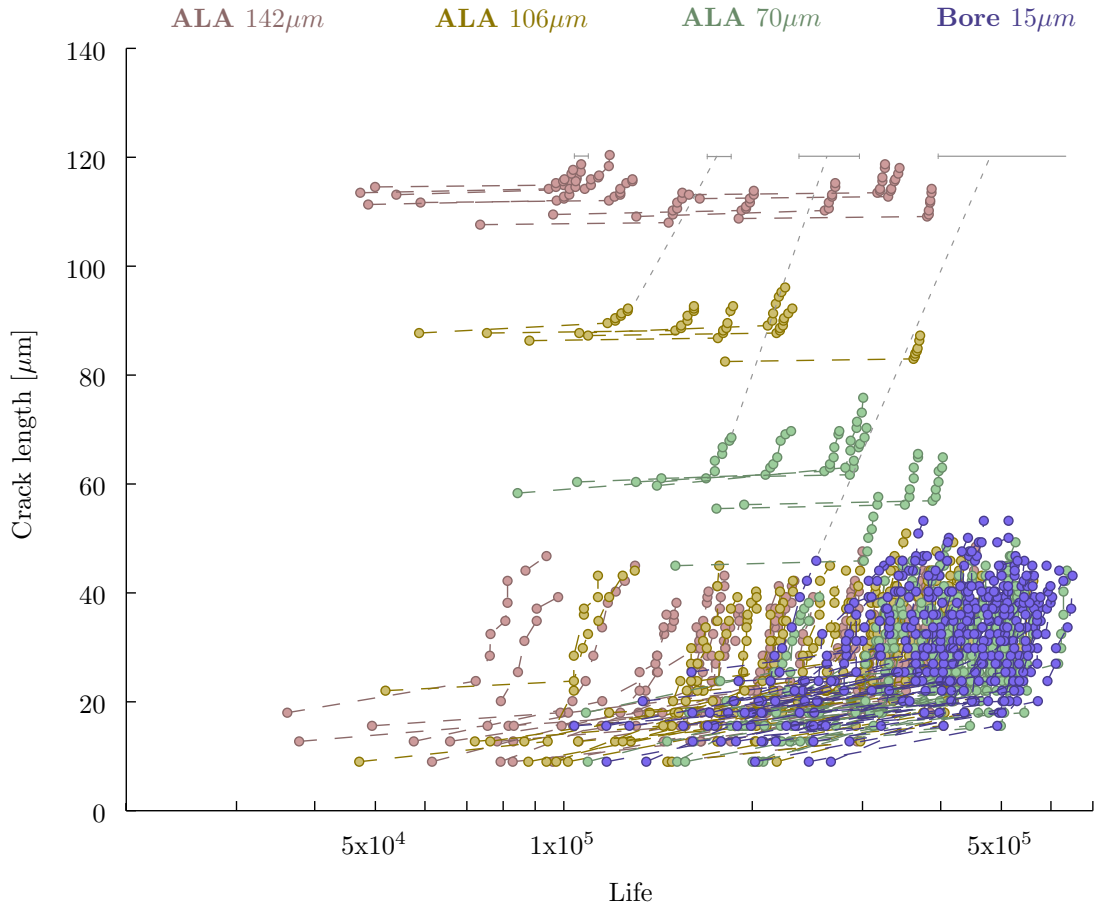
Figure 115: Comparison of the life vs crack length for the four microstructures analyzed, each with 50 realizations. Data correspond to that presented in Figure 114, but now on a single plot in semilog scale. Dotted lines correspond to an engineering linear extrapolation to reach a crack of 120 μm using a the range of slopes from the different realizations.

Table 10: Statistics for nucleating a crack out of 50 realizations for each microstructure.

	Bore 15 μm	ALA 70 μm	ALA 106 μm	ALA142 μm
Min. nuc. life	102217	82984	46350	35574
Max. nuc. life in ALA grain	-	190952	178010	177492
Max. nuc. life in any grain	281278	303060	256844	217362
5% probability of nucleation	115050	105000	54405	41845
Number of cracked ALA grain	0	7	6	11

199
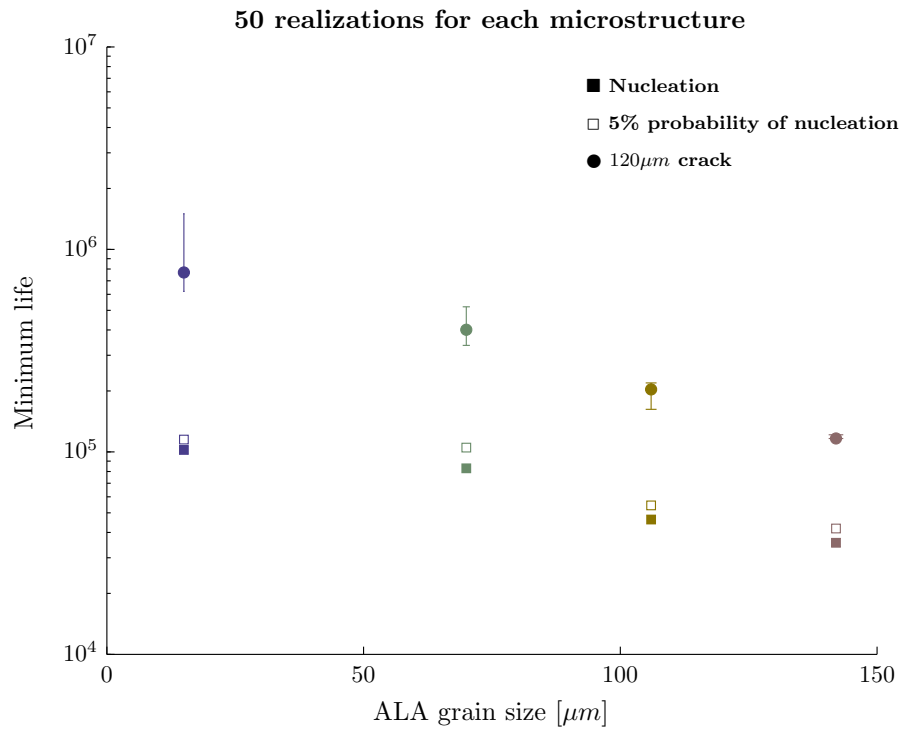
Figure 116: Minimum life to nucleate a crack (■), 5% probability to nucleate a crack (□) and an engineering estimation of the life to reach a crack length of 120 μm (●) for different microstructures, based on 50 realizations each. The error bars correspond to linear extrapolation using a variety of slopes from different realizations.
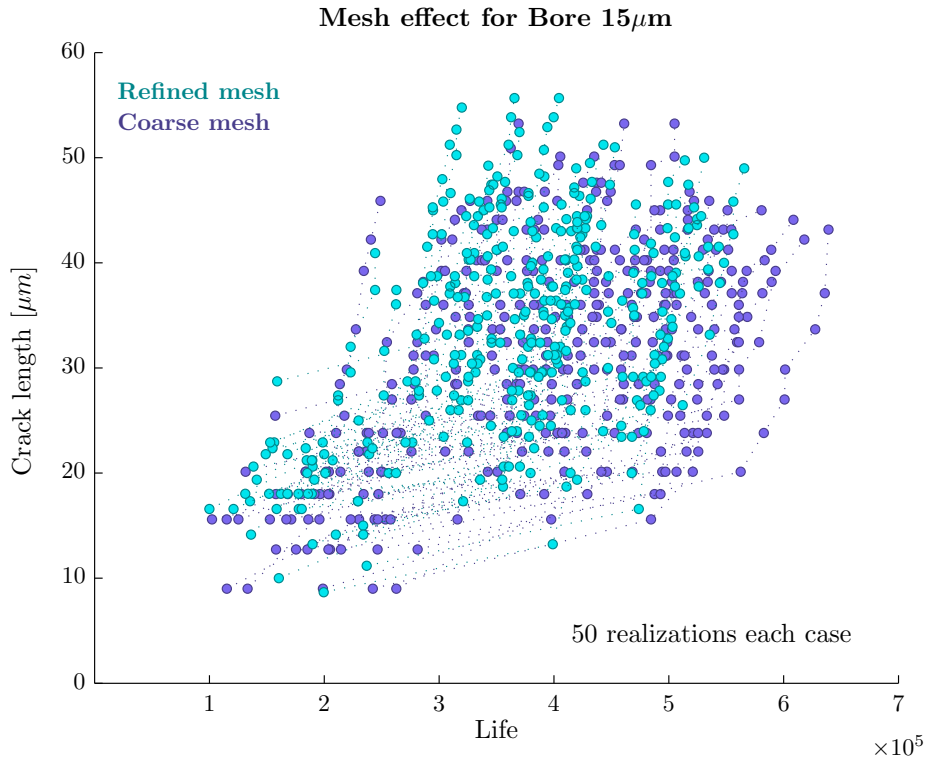
Figure 117: Comparison between coarse and refined meshes for Bore 15 μm microstructures after 50 realizations each. Both clouds of data points overlap and share similar minimum nucleation lives. The refined mesh seems to have a slightly wider distribution of results.

5 μm in size. The input parameters for the Mesh Generator are similar to the Bore 15 μm in Table 9, except for the band period, mesh size and band jump, which are all equivalent to 5 μm. Furthermore, the models have 174 grains, and a total of 5832 elements (compared to 1000 elements).

Figure 117 compares the life computations for 50 realizations of the coarse and refined Bore 15 μm microstructures and shows no major differences among both clouds of data points. The results for the refined mesh seem to present a slightly narrower spread of results for longer lives, but further statistical analysis would be required to ascertain this fact. More important, both distributions exhibit similar minimum nucleation lives and early MSC growth, which supports the use of the coarse mesh in the study of microstructures with ALA grains.

7.4   Stage I-Stage II transition

One of the assumptions of the mesoscale model is that transgranular-dominated fatigue cracks grow along a single crystallographic plane inside a grain, which was proposed based on experimental evidence. To assess the validity of such hypothesis, multiple parameters could be computed to measure the tendency of the transition to Stage II, for example:

- *Crack orientation*: determine the normal direction of the bands that fail and compare them with the loading direction. The alignment of the normals with the loading direction implies a transition into Stage II,

- *Multislip*: compare the life (FIP) of the band that fails with the life (FIPs) of the bands in the same grain, but with different normals. If the latter are much smaller (larger) than the former, then the crack could change into another slip plane inside the grain (i.e., Stage II),

7.4.1   Crack orientation

As shown in Figure 3, after the crack has grown along many grains, it tends to rotate into mode I loading (opening mode). To evaluate this behavior, a set of simulations was designed with 8000 elements, 239 grains undergoing 1% range, strain-controlled triangular cyclic loading, $R_\epsilon = 0.1$, and periodic loading conditions. On each simulation, between 20 and 40 grains are cracked, which demanded days of computational work; therefore, the number of realizations is limited. The orientation of the macroscopic crack is defined by the local orientation of multiple cracked bands. Hence, the angle between the loading direction and the macroscopic crack for each grain needs to be integrated or averaged over multiple grains. Figure 118 A) presents the evolution of the angle between the loading direction and the cracked band plane normal for one simulation, and Figure 118 B) to F) presents the smoothed results using moving averages with the specified window.

Figure 118 shows a tendency towards the opening mode, which would be a zero angle between the loading and the crack normal. The angle decreases at an approximate average slope between 0.25° to 0.5° per cracked grain, which implies that a fully Stage II crack
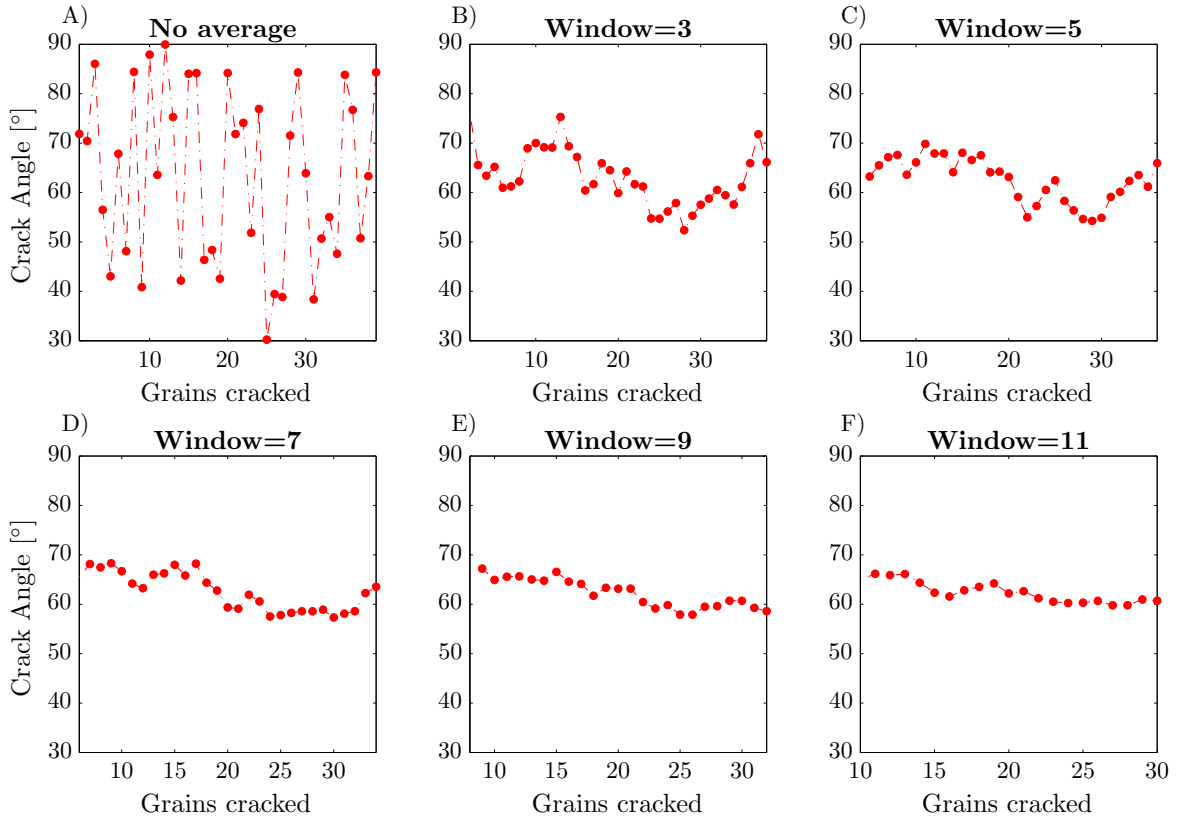
Figure 118: The evolution of the angle between the loading direction and the cracked band plane normal for one simulation, and the smoothed results using moving averages with the specified window.

would develop after cracking between 200 to 400 grains. These results should be considered as a qualitative description more than a quantitative one, since further statistics would be required. Furthermore, simulations showed that the orientation can be affected by the periodic boundary conditions, especially if the crack nucleates or approaches the boundary.

To exemplify the growth of a crack, Figure 119 presents the mesh employed for calculating the results in Figure 118. To the left of Figure 119 about 20 of the bands that form the crack are presented; each band from each grain has a different color. This Figure shows the complexity of the crack growth pattern, the degree of refinement of the grains, and how easily a crack can approach the boundary, which affects the orientation of the crack.
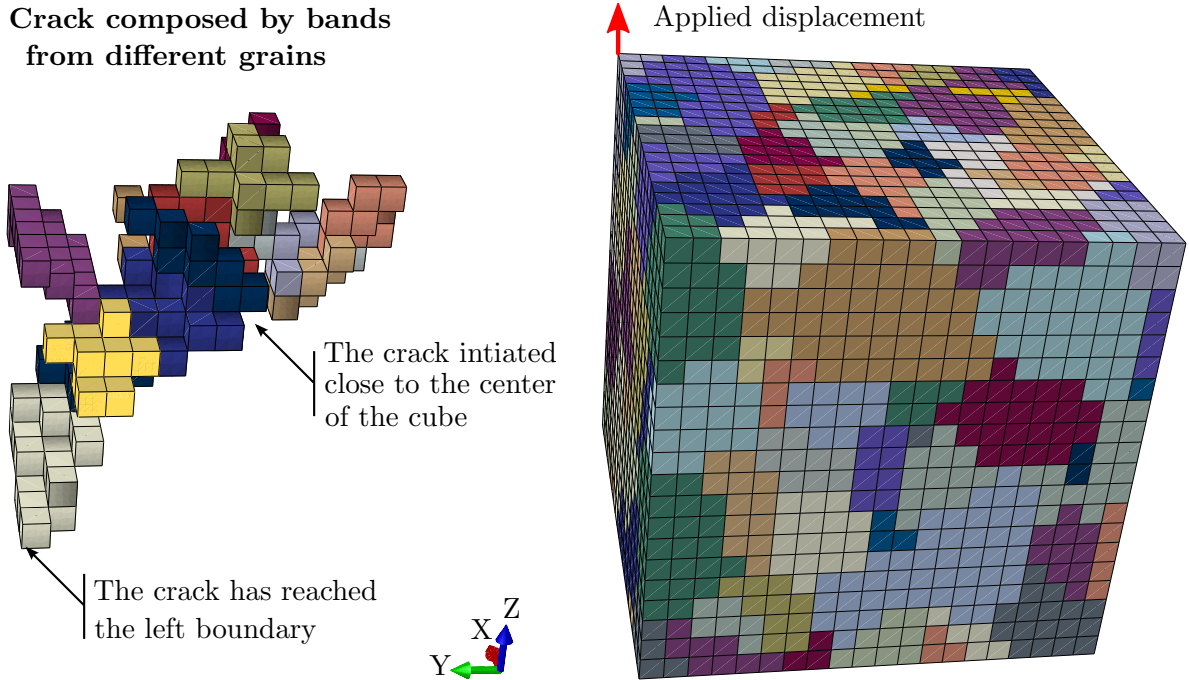
Figure 119: Mesh employed in the assessment of the crack orientation. On the left, the crack composed by bands in multiple grains (each grain in a different color). On the right, the entire mesh.

7.4.2 Multislip

The rotation of the normal plane directions into opening mode usually takes several grains to develop and does not indicate the transition inside a grain, but a macroscopic transition; hence this is not the best methodology to assess whether a crack would shift to another plane within a grain. In contrast, the comparison of FIPs or fatigue lives of bands can measure the transition withing a grain, but the latter is preferred since it includes grain size and strain localization effects.

To test the hypothesis in the mesoscale model that cracks do not deviate from one slip plane, the life of the actual band along which the crack grows in a grain is divided by the minimum life among every other band in the same grain. This calculation is performed for every new grain cracked in the MSC regime, once it has been determined along which grain the crack extends, but before adding any damage. Indeed, because the crack extends along bands that must be connected to the crack, another band in the grain, not connected to the

crack, may result in shorter life predictions. For grain i, the stage ratio (SR) is defined as

$$\text{SR}_i = \frac{\text{Life of the band that failed in grain } i}{\text{Minimum life of every other band in grain } i}, \tag{110}$$

with the additional condition that the bands should belong to a grain that failed in the MSC regime and should not have the same normal direction. Hence, a stage ratio larger than one means that there is another band in the grain that has a lower MSC life estimation, but it does not neighbor the crack, which prevents the crack from growing along that band.

Figure 120 presents four boxplots, each corresponding to a different microstructure, with the distributions of stage ratios for the first seven grains to fail. For clarity, values larger than 5 were omitted, and the number of those cases is indicated for each microstructure. Similarly, the first grain is not considered because the model nucleates the crack in the band with minimum life, making SR always below 1. For the remaining grains, the upper quartile has values below 2, which implies that in at least the 75% of the cases, the minimum life of any band in the grain that cracked differs by less than a factor of two with the actual life computed for the band that failed. A SR value larger than one would not imply directly that the predictions of the mesoscale model are inaccurate, since the transition into multiple slip planes would take a certain number of additional cycles. Hence, the relatively low percentage of cases that have SR values significantly larger than 1 suggests that the hypothesis that cracks follow a single slip plane is adequate.

Figure 121 now compares the effect of mesh refinement on SR by overlapping two boxplots (hollow and full boxes) with the distributions for the first grains to fail. The refined meshes show narrower distributions of SR, and significant lower upper quartiles, which are constantly below a value of 1.20 and have a lower number of outliers. Therefore, the refinement of the mesh intensifies the Stage I character that is imposed by the mesoscale model.
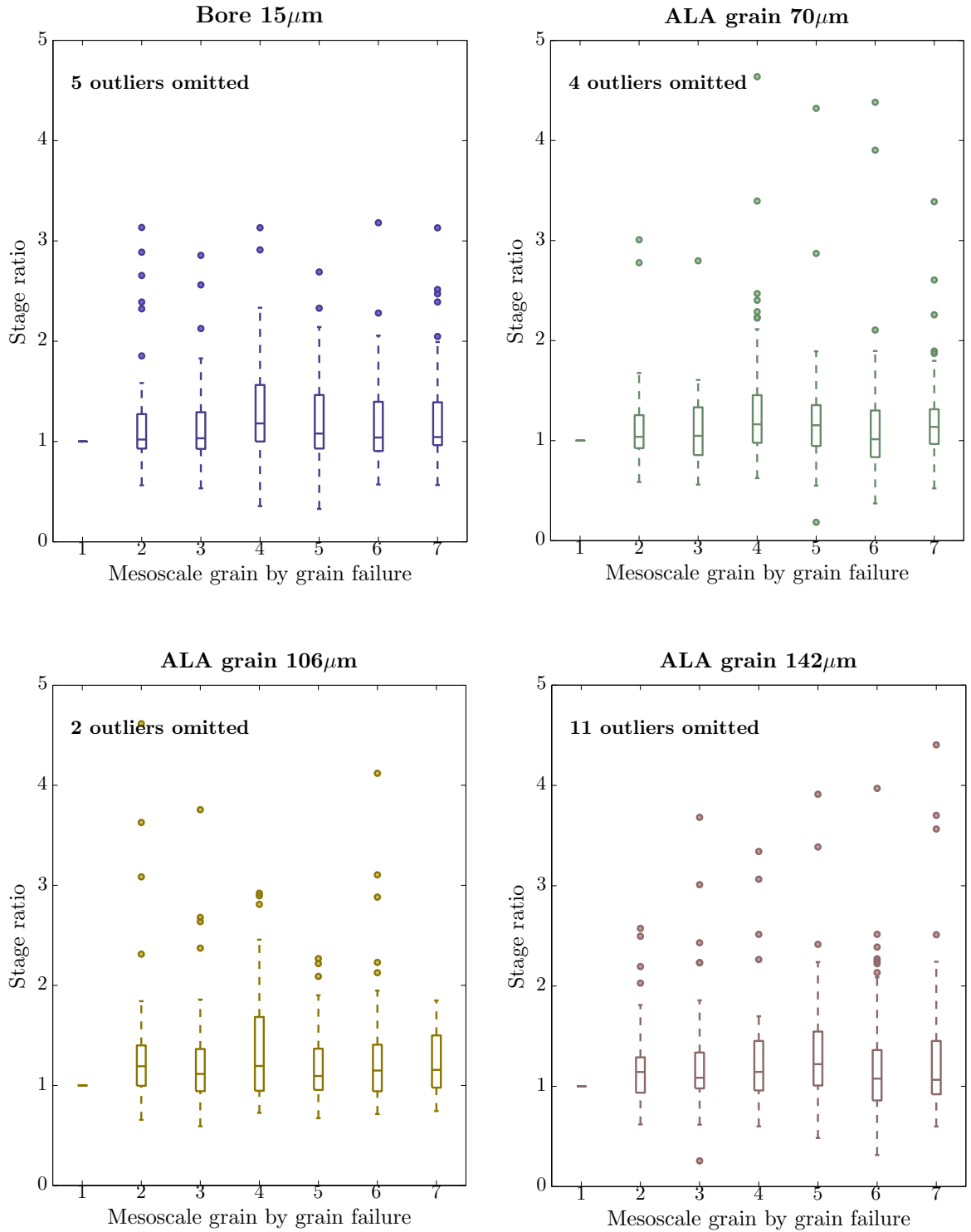
Figure 120: Boxplots showing the stage ratios for the first seven grains to fail in the microstructures analyzed. Although some outliers have values larger than 2, they correspond to a relatively small number of cases. Values larger than 5 were omitted, and the number of cases is indicated for each microstructure.
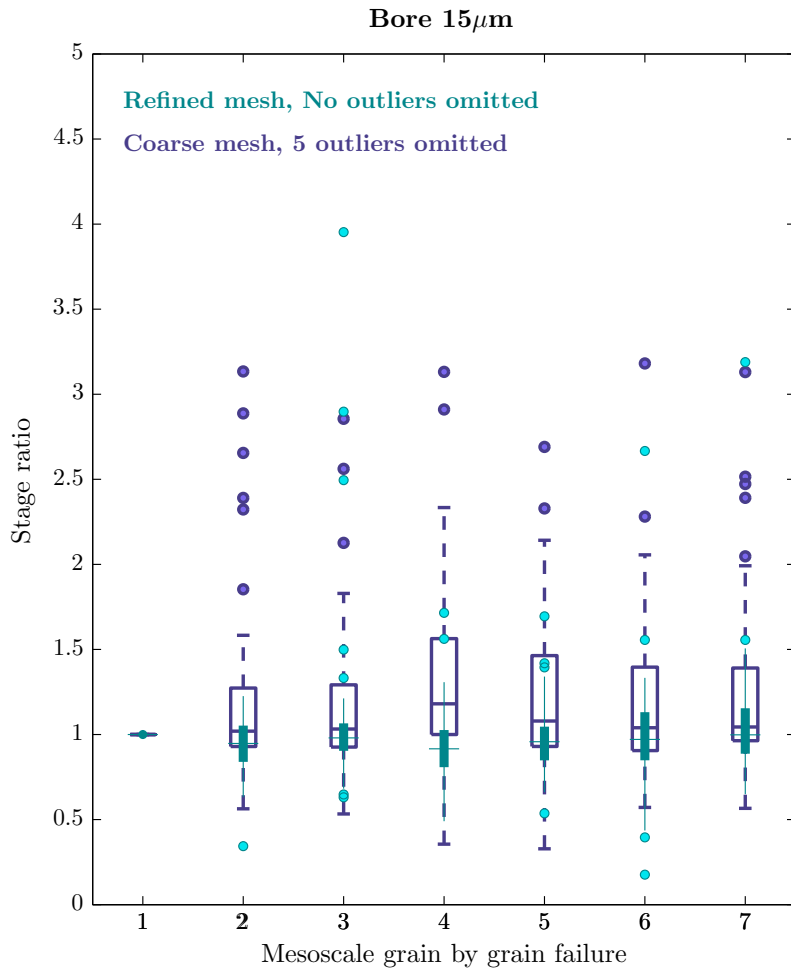
Figure 121: Comparison of SR between coarse (hollow boxes) and refined meshes (full boxes) for Bore 15 μm microstructures. The refined mesh shows a stronger Stage I character that is actually imposed by the mesoscale model.

7.5 Intergranular fatigue life assessment of ALA grains

The intergranular fatigue life in the MSC regime was also assessed for microstructures with ALA grains. As mentioned in the description of the mesoscale model, the intergranular life is computed after the crack is nucleated, and considers only the GB sectors neighboring the crack, which extends only along transgranular paths. For each GB sector, the intergranular life is calculated, and the minimum of those is considered as the intergranular life for the current crack length. Because the transgranular lives of grains are on the order of 10^3 to 10^4 cycles, only intergranular lives below $2x10^5$ were considered.

Figure 122 presents the evolution of the minimum intergranular fatigue life for those grains neighboring the crack as a function of transgranular crack length. Dark points correspond to those cases in which the minimum intergranular life of the GBs sectors neighboring the crack are below the minimum transgranular life to extend the crack by a grain; hence, the transition into intergranular failure is expected to occur for the dark points. Although the calibration of the actual lives could be somewhat inaccurate, we can still learn from the distributions of lives. For example, all the microstructures simulated tend to transition into intergranular failure only after a few grains have cracked, regardless of the length of the crack. These results suggest that the transition into intergranular failure is not dominated by the length of the crack but by the intergranular life of the boundaries. Hence, if the life of any boundary on grains neighboring the crack is above about 10^4 cycles, the transition into intergranular failure tends to be suppressed. An additional observation is that even though the formulation does not carry any intrinsic length scale, the intergranular life decreases with increasing ALA grains.

7.5.1 Influence of mesh refinement on intergranular fatigue life estimation

Figure 123 compares the evolution of the minimum intergranular fatigue life for refined and coarse meshes. Light gray and dark points correspond, for refined and coarse meshes respectively, to cases in which the minimum intergranular life is below the minimum transgranular life to extend the crack by a grain. These results show that the refined and coarse mesh simulations provide similar estimates of the intergranular life transition.
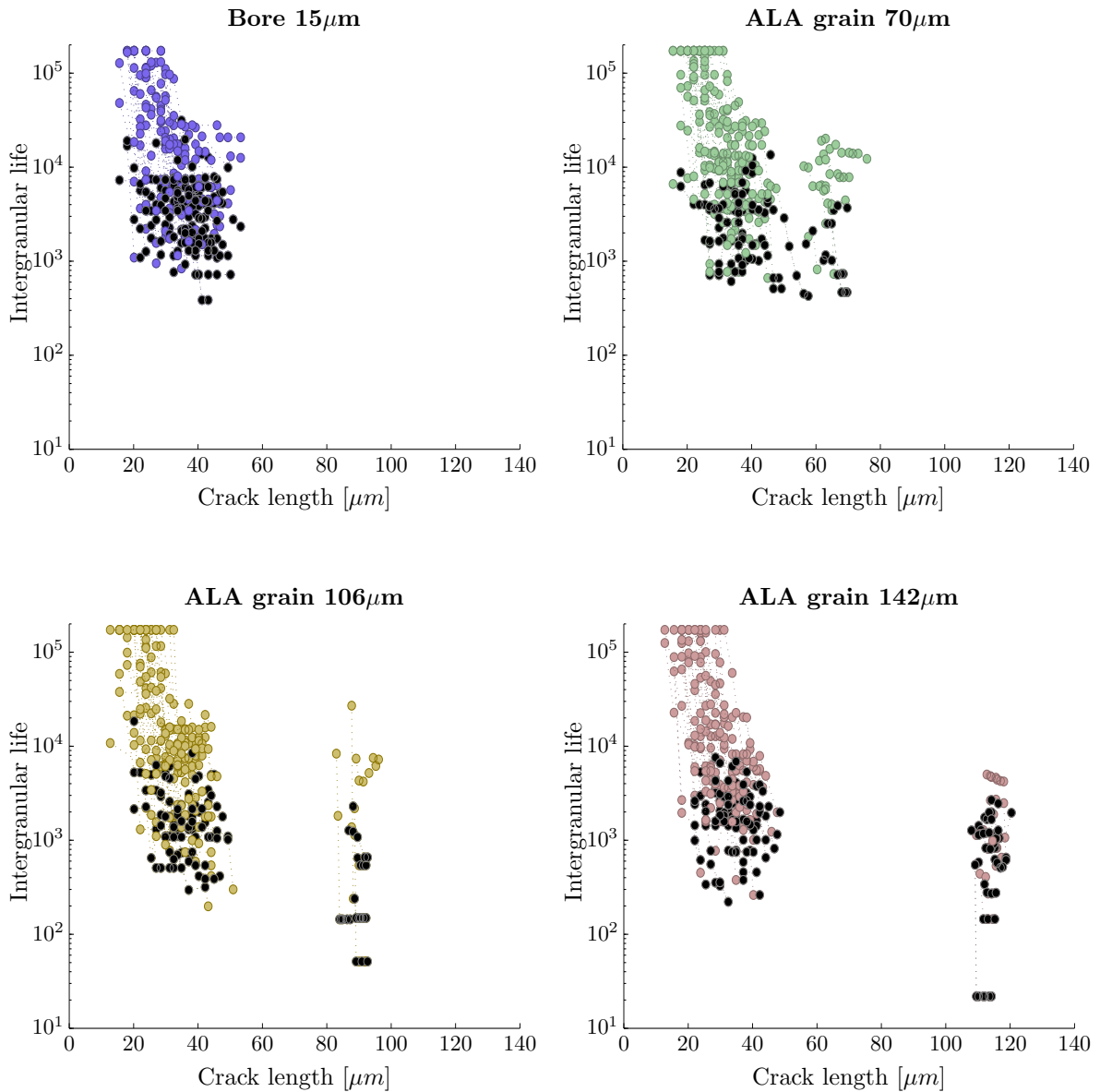
Figure 122: Minimum intergranular life as a function of transgranular crack length. Dark points correspond to those cases in which the minimum intergranular life of the GBs sectors neighboring the crack is below the minimum transgranular life, suggesting the tendency for transition of failure mode. Only intergranular lives below 2×10^5 were considered.
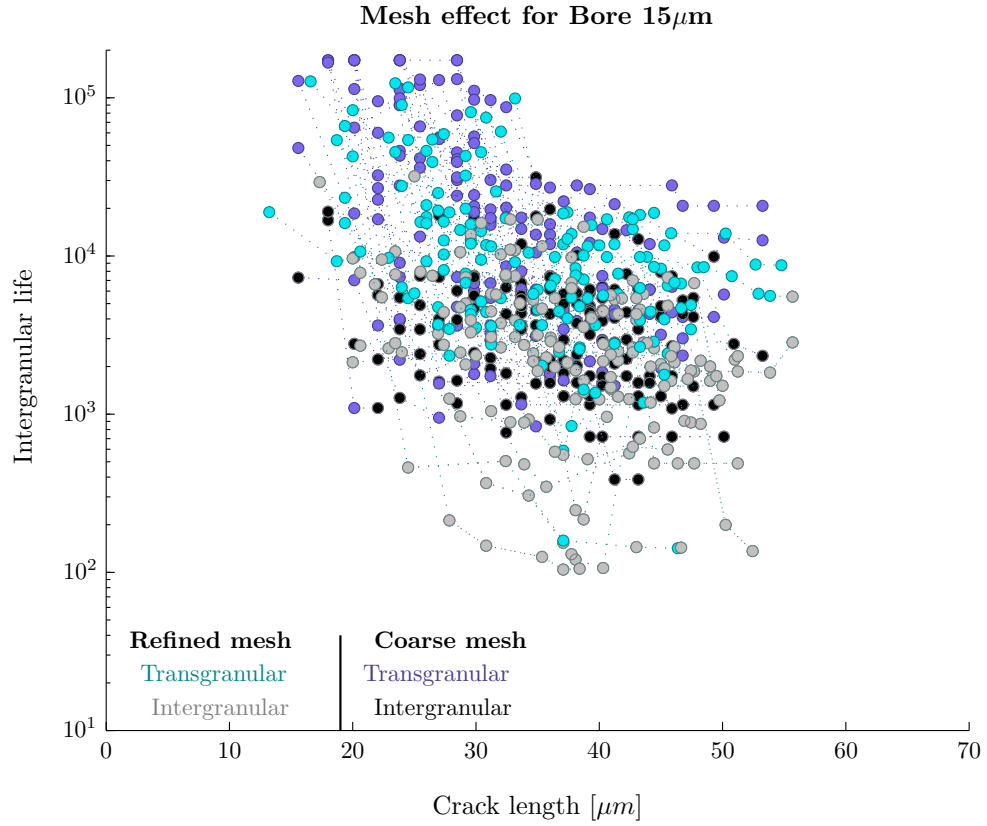
Figure 123: Comparison of the minimum intergranular life between coarse and refined meshes for Bore 15 μm microstructures. Light gray (dark) points correspond to those cases in which the minimum intergranular life of the GBs sectors neighboring the crack is below the minimum transgranular life of the refined (coarse) mesh, suggesting the tendency for transition of failure mode. Only intergranular lives below $2\text{x}10^5$ were considered.

7.6 100s hold time effect

Finally, this section presents the results corresponding to ALA 106 μm undergoing 1% strain controlled trapezoidal loading (1-100-1-100) and R_ϵ=0.1. A total of 30 realizations were performed, and the results are presented in Figure 124, which shows a significant decrease in the life when compared to the triangular loading results without hold. The transgranular fatigue life seems to have been reduced by about 20%, mainly in the MSC regime, which presents slopes (crack growth rates) that are steeper. Furthermore, the nucleation of the crack and the extension into the first or second grain still control the fatigue life.

Figure 125 presents the intergranular life for ALA 106 μm with 100s hold time compared to the results from triangular loading without hold time. Here, most of the simulations tend to transition into intergranular failure, which is observed to start when the GBs have intergranular lives about $2x10^3$ cycles. These results are in agreement with the expected detrimental effects of hold times in superalloys.
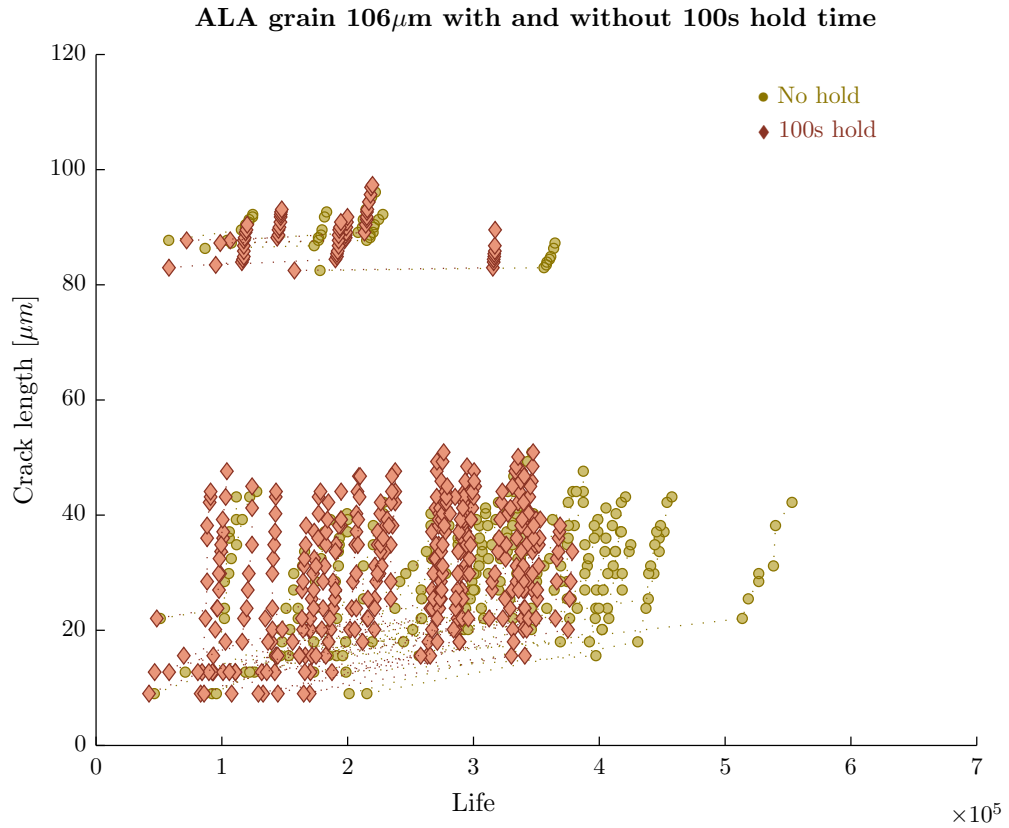
Figure 124: Life vs. crack length for ALA 106 μm without ($\bullet$) and with ($\blacklozenge$) 100s hold time for 30 realizations. Note that the slopes are more steep in the case with hold time due to the increase of irreversibility.
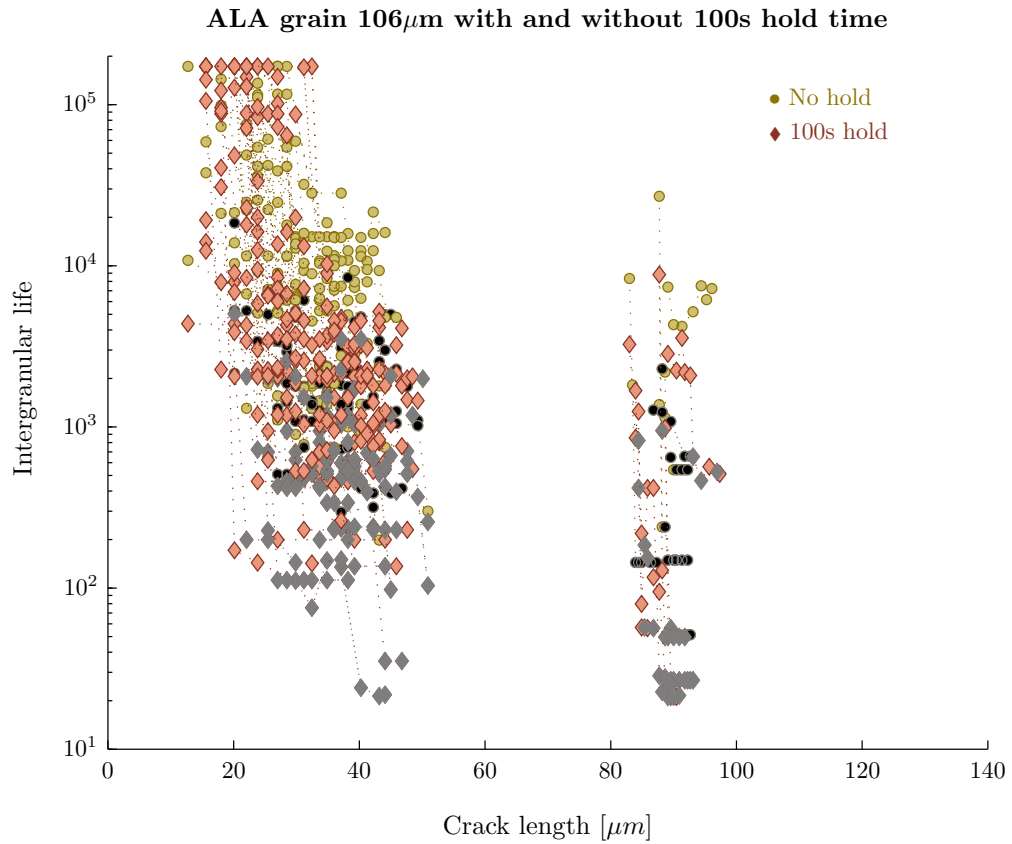
Figure 125: Minimum intergranular life ALA 106 μm without ($\bullet$) and with ($\blacklozenge$) 100s hold time as a function of transgranular crack length for 30 realizations. Dark points correspond to those cases in which the minimum intergranular life of the GBs sectors neighboring the crack is below the minimum transgranular life, suggesting the tendency for transition of failure mode. Only intergranular lives below 2×10^5. were considered.

7.7 Preliminary conclusions

This chapter employed computational tools based on the mesoscale model to study the formation and MSC growth of fatigue cracks in microstructures containing one ALA grain of different sizes and a reference microstructure without ALA grains. The results support the following conclusions.

- The FIP within an ALA grain still follows the sub-grain evolution proposed in the previous chapter, providing further evidence that the mesoscale model can be employed for analyzing microstructures with ALA grains.

- Crack formation and early growth is controlled by the ALA grain, either because the crack nucleates in such a grain or because ALA grains assist in the plastic deformation of neighboring grains.

- The nucleation regime and the MSC regime for the first few grains control the fatigue life. Afterwards, crack growth rates increase and cracks tend to grow within multiple grains simultaneously. Furthermore, ALA grains tend to influence more strongly the lower tail of the nucleation distribution lives rather than the tail of maximum values.

- The transition from fatigue Stage I to Stage II was assessed, and the results showed that in the majority of the cases the Stage I hypothesis in the mesoscale model is adequate for the cases analyzed. Furthermore, the refinement of the mesh intensifies the Stage I character, which is actually a feature imposed by the mesoscale model to coarse meshes.

- Intergranular life was also assessed, and the results showed that the transition from transgranular to intergranular failure occurs when the GB sectors presented lives below a certain value.

- The detrimental effects of a hold period during loading were quantified as transgranular and intergranular failures, and they are in agreement with the expected behavior for superalloys.

CHAPTER VIII

SUMMARY AND CONCLUSIONS

The formation and early growth of fatigue cracks in the high cycle fatigue regime is influenced by microstructural features such as grain size and morphological and crystallographic texture. However, most fatigue models do not predict the influence of the microstructure on early stages of crack formation, or they employ parameters that should be calibrated with experimental data from specimens with microstructures of interest. These *post facto* strategies are adequate to characterize materials, but they are not fully appropriate to aid in the design of fatigue-resistant engineering alloys. Indeed, the prediction of fatigue life associated with the growth of MSCs is still an open challenge that impacts mechanical design.

The review of the current understanding of the development of small fatigue crack argued that traditional homogeneous-based fracture mechanics cannot describe the early behavior of fatigue cracks because they are based on far-homogenized field magnitudes and not local measurements. The alternative is to employ fatigue driving forces based on the crack tip local fields. The ΔCTD is one such local driving force that can be directly linked to the mechanically irreversible mechanisms at the crack tip. Since, the computation of the ΔCTD is experimentally and computationally complex, a variety of alternatives for the driving forces have been proposed.

The Fatemi-Socie based FIPs showed experimentally good correlation for ascertaining the early fatigue life of metals with low to medium SFE and planar slip. In spite of this fact, the quality and foundations of these FIPs have received limited attention. Therefore, the first objective considered was to evaluate the role of FIPs as fatigue crack driving force for cracks in single crystals with and without idealized slip band heterogeneities. For this analysis, simulations of Cu were employed, since it is the most studied material in fatigue damage. The comparison between the ΔCTD and the Fatemi-Socie FIP was performed

explicitly for several multiaxial loading conditions, and the results demonstrate that the ΔCTD correlates almost linearly Fatemi-Socie FIP. Furthermore, the crack tip geometry exerted only a secondary influence on the driving forces as well as the mesh refinement.

Mesh refinement can affect the value of computed FIPs to a greater extent than ΔCTD, and the effect seems more intense for mixed loading. To mitigate such problems as well as the variability of the mesh, averaged FIPs along slip bands demonstrate reduced variability and dependence on the mesh refinement than local maximum magnitudes.

A notable result is that the shape of the correlation was not significantly affected by introducing slip bands. Indeed, specimens with slip bands followed a similar trend from that shown by homogeneous specimens, with the driving force enhanced. Such a localization of plastic strain in a slip band can exert significant influence on the ΔCTD, particularly for higher values, and appears to affect the threshold ΔCTD. These findings are a fundamental support for simulations of small fatigue cracks using FIPs, since they justify that ΔCTD and Fatemi-Socie FIPs averaged along bands are correlated measures of the driving force, but the latter is computationally less demanding.

Chapter 4 introduced local correlations between crack growth rates and FIPs based on the hierarchical approach to fatigue modeling, which allows the estimation of the life consumed in different stages as the crack extends. Since this formulation does not have an intrinsic length scale, the computation of the fatigue driving force could be performed for every element, demanding intense numerical work.

The local model was extended as a mesoscale framework that is able to calculate fatigue life over hundreds of microns. To limit the computational demands, the mesoscale scheme takes the grain as the minimum unit to crack (instead of an element) and assumes that the evolution of the driving force inside the grains follows a function $g(a)$ that depends on the length of the crack within the grain, a. The scaling factor is calculated after only a few loading cycles, which requires that the microstructure does not change significantly throughout the fatigue life.

Once the crack has extended over a grain or more, the stress and strain redistribution can affect the driving force on the neighboring uncracked grains. To account for this effect,

various strategies were reviewed among which the damage approach was preferred. This methodology degrades the elastic stiffness tensor without affecting the crystal plasticity calculations, and it is based on a 4th rank damage tensor that guarantees that the stress tensor is symmetric. Although the formulation describes correctly the behavior of an equivalent cracked element, the implementation in FE simulations may present additional complexities, in particular regarding the convergence of the strongly anisotropic damaged stiffness tensor.

The concepts discussed in the previous chapters regarding the study of early fatigue life and microstructure were later applied in the study of RR1000 superalloy with dual microstructure fatigue crack formation. Such task required discussing the nature of the RR1000 superalloy for turbine disk applications and the details of the crystal plasticity constitutive formulation for RR1000. This analysis pointed out that crystal plasticity models for superalloys that consider cube slip to account for the zig-zag cross slip mechanism may fit adequately to macroscopic stress-strain and stress-time experimental data, but they can still present non-physical behavior such as the dominance of cube slip plastic deformation or stresses incompatible with zig-zag mechanism.

The modeling of dual microstructures needs to account for a larger number of moments of the grain size distribution than unimodal distributions. Hence, this work proposed to perform a statistical analysis using SVE. This allows the quality of an estimation of the fatigue behavior to be scaled with the computational effort. Furthermore, a Mesh Generator application has been developed to feed the FEM solver with a complex microstructure that may include ALA grains.

Similar to the previous analysis using Cu, the correlation between the FIP and the ΔCTD for RR1000 is approximately one-to-one. Since the constitutive models for both metals are completely independent, the similarity in the correlation suggests a fundamental relation between the driving force measurements.

The general framework for fatigue life estimation is later applied for estimating the early life of RR1000 superalloy. Simulations showed that the fully anisotropic damage models can introduce numerical instabilities that are overcome by employing a simplified

isotropic degradation of the stiffness tensor adjusted dynamically according to the increase of damage. The introduction of damage only exerts a moderate influence on the neighboring elements, which suggests that for small cracks, the stress intensification on a grain due to crack growth is moderate, does not resemble singularity models and is greatly affected by the microstructure.

Multiple realizations of equivalent unimodal microstructures showed that the fatigue driving force for nucleating cracks presents a very narrow range (about a factor of two) while it can vary by orders of magnitude for extending the crack on the subsequent grains. Thus, the variability of the small crack regime depends more on the extension to subsequent grains than on the nucleation of the first grain. Furthermore, the analysis of sub-grain evolution showed that the mean behavior of the fatigue driving force presents a decreasing trend that can be approximated by a power law of the fraction of the grain that has been cracked.

The comparison of sub-grain and mesoscale analyses using similar microstructures showed negligible differences in the driving forces employed to estimate fatigue lives, validating the mesoscale framework as a modeling technique that requires lower computational work. Furthermore, the analysis of crystals with annealing twins showed that, the larger the twin, the more intensified the FIP becomes. The FIPs were intensified by less than an order of magnitude, which can be considered as a special case of strain localization. Hence, models without explicit twin may not predict the location of a crack accurately.

The work presented in Chapters 2 to 6 is the basis that justifies the life estimations for RR1000 dual microstructures in Chapter 7. The Mesh Generator application generated the models analyzed with the mesoscale model to study the early fatigue life of microstructures containing one ALA grain of different sizes and a reference microstructure without ALA grains. The results showed that the shape of the sub-grain evolution does not strongly depend on the microstructure, and that ALA grains still follow the sub-grain evolution proposed, justifying the use of the mesoscale model for analyzing microstructures with ALA grains.

The early fatigue lives is controlled by the ALA grain, either because the crack nucleates

in such a grain or because ALA grains assist in the plastic deformation of neighboring grains. Furthermore, both the nucleation and the MSC regimes for the first couple of grains present the lowest crack growth rates and take a central portion of the fatigue life. Afterwards, crack growth rates are increased and cracks tend to grow on multiple grains simultaneously. Furthermore, ALA grains tend to affect the minimum nucleation lives more than the maximum values.

Intergranular life was also assessed, and the results showed that the transition from transgranular to intergranular failure occurs when the GB sectors presented lives below a certain value, regardless of the size of the crack. The detrimental effects of a hold period during loading were quantified for transgranular and intergranular failure.

8.1 Most significant innovative aspects of this work

The key innovations achieved in this work are summarized below:

- The Fatemi-Socie based FIP correlates almost linearly with the ΔCTD in single crystals under multiple loading conditions. This relation was found for two unrelated FCC constitutive models, which supports that the magnitudes have a fundamental relation.

- The localization of plastic strain in a slip band influences the fatigue driving force. However, the shape of the correlation between the FIP and the ΔCTD is not significantly affected by introducing slip bands, which supports the validity of using homogenized constitutive models for estimating the driving force.

- The use of averaged FIPs along bands oriented with the slip planes reduced the variability and mesh dependence of the fatigue driving force compared to pointwise measures.

- The evolution of the fatigue driving force within a band in a grain decreases as the crack grows in the grain, which is in agreement with other simplified models and experimental results in the literature. This characterization provides a definition of the Microstructrual Fracture Mechanics fatigue driving force.

- The mesoscale framework developed is capable of calculating fatigue life over hundreds of microns using a crystal plasticity constitutive model containing explicit grains. The model divides the grains in bands that are the minimum unit that crack, and the comparison of results with more detailed models validated the results from the mesoscale framework.

- The fatigue driving force for nucleating cracks presents a very narrow range (about a factor of two) while it can vary orders of magnitude for extending the crack on the subsequent grains. Thus, the variability of the fatigue small crack regime depends more on the extension of a fatigue crack to subsequent grains rather than on the nucleation of a fatigue crack on the first grain.

- Crystal plasticity models for superalloys that consider cube slip to account for the zig-zag cross slip mechanism may fit adequately to macroscopic stress-strain and stress-time experimental data, but they can still present non-physical behavior such as the dominance of cube slip plastic deformation or stresses incompatible with zig-zag mechanism.

- The algorithms developed are capable of predicting the early fatigue life for idealized microstructures in 3D under multiaxial loading. This tool pioneers the modeling of 3D growth of MSCs in polycrystalline microstructures.

- ALA grains control the early fatigue lives, either because the crack nucleates in such a grain or because ALA grains assist in the plastic deformation of neighboring grains. Furthermore, both nucleation and MSC regime for the first couple of grains present the lowest crack growth rates and take a central portion of the fatigue life.

8.2   Open issues and further improvements

This research has successfully constructed a multi-stage methodology from fundamentals up to the application for industrial needs. For the sake of covering this wide range, some matters were overlooked by assuming certain simplifications. Among the most important subjects are improving the constitutive model and the fatigue model.

The crystal plasticity formulation (and most models available) may not reproduce accurately the partition of strain among the slip planes. This problem affects the quantification of the fatigue driving force because plastic strain tends to spread in multiple planes, even worse when considering cube slip that results from the zig-zag mechanisms. Furthermore, the transition into multiple slip (Stage I to Stage II) is controlled by the activation of multiple slip planes, which affects the evaluation of the transition between stages. A possible solution is to limit the number of planes that can be activated at a time, but the selection rule may introduce significant complexities.

A second deficiency of the constitutive model is the lack of strain localization in smooth specimens (i.e., not caused by geometric stress concentrators). To compensate for this problem, the fatigue model considers a dependence of the driving force on the grain size (Equation 95) that models the strain localization effects. However, this model is a simple correction of a complex problem, which requires further experimental and theoretical characterization.

One of the difficulties with modeling strain localization is the need for an intrinsic length scale, which is not currently included in the constitutive model. However, the definition of the bands in which the FIPs are averaged introduces a length scale into the fatigue model that could be extended to the constitutive formulation. Therefore, a natural extension of this work would explore non-local (integral) constitutive equations in which the bands are the integral volumes. This type of formulation may consider integral ISVs that describe the evolution of the bands as one entity. This would be particularly well fitted for modeling slip bands.

APPENDIX A

ALTERNATIVE FIP CALCULATION

In order to compute the value of the FIP, the range of plastic strains should be estimated over one loading cycle. Chapter 3 computed the FIP based on the range of the plastic strain tensor and in section 3.3.3 compared the results with the FIP computed using the methodology by McDowell and coworkers [171]. For completeness, this appendix introduces the details of the latter calculation.

McDowell and coworkers [171] calculated the maximum plastic shear strain, γ_{max}^p, at the peak point in the loading cycle using that,

$$\gamma_{max}^p = \left| \epsilon_1^p \big|_{max} - \epsilon_3^p \big|_{max} \right| \, \text{sgn}(\epsilon_1^p|_{max}), \tag{111}$$

in which $\epsilon_1^p \big|_{max}$ $\epsilon_3^p \big|_{max}$ are the maximum and minimum ordered principal plastic strains at peak load, respectively. Each eigenvalue has associated two respective eigenvectors $\boldsymbol{\nu}_1$ and $\boldsymbol{\nu}_3$, which define the plane of maximum plastic strain at peak load $\boldsymbol{\pi}$ as,

$$\boldsymbol{\pi} = \frac{\boldsymbol{\nu}_1 + \boldsymbol{\nu}_3}{||\boldsymbol{\nu}_1 + \boldsymbol{\nu}_3||} \tag{112}$$

This plane locates at an angle of 45° to the eigenvectors.

For proportional loading, if it is assumed that the ordered principal plastic strains at the minimum point of the loading cycle have eigenvectors coincident with $\boldsymbol{\nu}_1$ and $\boldsymbol{\nu}_3$ (this is not generally true for non-proportional loading), then the minimum plastic shear strain on the same plane is given by

$$\gamma_{min}^p = \left| \epsilon_1^p \big|_{min} - \epsilon_3^p \big|_{min} \right| \, \text{sgn}(\epsilon_3^p|_{min}), \tag{113}$$

Here the subscript *min* refers the point in the loading cycle with minimum load. Equations (111) and (113) are different because the sign of the eigenvalues can change with the fatigue ratio R. Note that general loading conditions requires to compute the plastic strain ranges on each multiple planes to estimate the value of the maximum range.

Then, the range of plastic strain is computed as,

$$\Delta\gamma^p = \gamma^p_{max} - \gamma^p_{min} =$$

$$= \left|\epsilon^p_1\big|_{max} - \epsilon^p_3\big|_{max}\right| \operatorname{sgn}(\epsilon^p_1|_{max}) - \left|\epsilon^p_1\big|_{min} - \epsilon^p_3\big|_{min}\right| \operatorname{sgn}(\epsilon^p_3|_{min}), \tag{114}$$

which requires computing four eigenvalues. As mentioned in section 3.2.4.2, the methodology employed in Chapter 3 only computes two eigenvalues belonging to the plastic strain tensor range.

The external database user subroutine (UEXTERNALDB) is in charge of performing all the calculations that are connected with the fatigue model, and it runs after every step has converged. This subroutine performs the following tasks:

- Reads the information about the mesh generated along with the input file by the Matlab scripts and translates it into arrays that can be interpreted in ABAQUS,

- Calculates the value of the fatigue indicators locally and over averaged volumes,

- Calculates the number of cycles to transgranular failure for each band using the adequate life law (i.e, nucleation, MSC),

- Calculates the intergranular life for each grain boundary sector,

- Keeps track of the neighboring grains that are candidates to crack next and allows only them to fail.

B.1 UEXTERNALDB subroutine functioning

The simulation starts by initializing the variables that contain the additional information (beside ABAQUS input file) regarding the geometry; i.e., the Neighbor_grains.txt, Boundary_el.txt and Boundaries_dir.txt files are read and saved as arrays in global memory. Since information is exchanged between the UMAT and the UEXTERNALDB subroutines, the initialization lasts for two time increments and comprises the if-loop for which `time(2).eq.0.0`. Later, on the second time increment of the first step (`(kinc.eq.2).and.(kstep.eq.1)`), the code reads the files Min_dist.txt and Grains.txt and writes the files disAngle.txt.

At the beginning of each even number step, the extreme values of the accumulated plastic strains (variables `gamma_cum_element_min` and `max`) are set to zero, and the values of the

latest even-step plastic strains are replaced with the current values. This calculation is done by the end of the first time increment after the crack has been extended to a new grain, and its objective is to account for the ratcheting effect. The subroutine continues calculating the averaged FIPs for all steps after the second time increment (if loop `kinc.gt.2`). This calculation is performed for every time increment, which allows the maximum and minimum plastic strains to be determined over the cycle, whose difference results in the maximum plastic strain range $\Delta\gamma^\alpha\Big|_{\text{over cycle}}^{\text{max}}$ in Figure 74.

To limit the computational work, lives are computed only by the end of certain loading cycles; this is when the remaining time to complete the loading step is less than half the current time increment. The computation of the nucleation life is performed under if `kstep.eq.Eval_Nuc`, while the MSC lives are computed if `(kstep.gt.Eval_Nuc).and.` `(mod((kstep-1),(int(Eval_MSC))/2).eq.0)`. Once the simulation has concluded, the following text files will be found on the running folder:

- FIP.txt: This files summarizes the values of the FIP_0, employed for computing the life of the bands that failed. The columns describe FIP and the number of elements cracked.

- life.txt: This file summarizes the life of the first grain to fail under the nucleation regime, and the subsequent grains under the MSC regime (MSC1, MSC2, etc.). The content has four columns: the expected life, the number of the grain that contains the band that failed, the number of the bands and the slip direction failed.

- life Nuc.txt: This file summarizes the life to nucleate a crack in all grains. The content has five columns: expected life of the bands (only of those shorter than 10^8), the number of the grain that contains the band failed, the number of band, the slip direction and the value of the band-averaged FIP.

- life MSCi.txt: This file summarizes the life to grow a crack along the ith grain to fail in the MSC regime. Similar to the previous file, the content has five columns: expected life of the bands in grains neighboring those that have already failed, the number of

the grain that contains the band failed, the number of band, the slip direction and the value of the band-averaged FIP.

- disAngle.txt: Lists the contributions from neighboring grains. The misorientation (3rd column) between two grains (1st and 2nd columns) lead to a neighboring grain contribution (D_{nd}) in the 4th column.

- d_gr_nd.txt: Similar to disAngle.txt, lists the contributions from neighboring grains, but for each band. Columns 1, 2 and 3 state the grain, the band number and the slip plane, and the 4th column states the neighboring grain contribution (D_{nd}).

B.2 Variables and arrays

To store and access information at different times from different subroutines, ABAQUS indicates that the FORTRAN common block should be employed. Thus, a series of global variables (i.e., static memory) were defined in named common blocks in the Common_Block.txt file. This file is called from the UMAT and the UEXTERNALDB subroutines, which assures that all the subroutine use the exact same definition for the common block. Indeed, FORTRAN requires the definition of these variable to be done carefully, in decreasing order of memory size.

Since global variables can be the source of multiple errors, this appendix presents a list of the global variables employed by the algorithms. Below "Name" refers to the name of the common block in which the variable is allocated, while the amount of space allocated in memory is indicated in between brackets.

Name: **KUEXT0**

Elem_pos(num_elem,5): *[integer*4]* For all normal vectors, Elem_pos(i,1 to 4) stores the number of band that contains the ith element. Elem_pos(i,5) stores the grain that contains the ith element.

Name: **KUEXT1**

`Cnum(num_grains,max_num_layers,4)`: *[real*4]* Contains, for each band of each grain, the number of elements in it. The third coordinate indicates to the four normal vectors of the octahedral slip planes.

`Cnum_fail(num_grains_fail+1)`: *[real*4]* Contains the number of the grains that have been cracked. A total of `num_grains_fail+1` grains fail in the MSC regime.

Name: **KUEXT2**

`gamma_dot_element(num_elem,num_octa_sys)`: *[real*8]* The shear rate calculated as a local variable in the UMAT is made available as a global variable.

`gamma_cum_element(num_elem,num_octa_sys)`: *[real*8]* The accumulated shear strain for each slip plane calculated in the UMAT is made available as a global variable.

`gamma_cum_element_max(num_elem,num_octa_sys)`: *[real*8]* The maximum value of the accumulated shear strain.

`gamma_cum_element_min(num_elem,num_octa_sys)`: *[real*8]* The minimum value of the accumulated shear strain.

`gamma_cum_init_even_step(num_elem,num_octa_sys)`: *[real*8]* The accumulated shear strain at the beginning of the cycle used to discount the ratcheting effect.

`sigma_gl(num_elem,num_octa_sys)`: *[real*8]* The normal stress on each slip plane calculated as a local variable in the UMAT is made available as a global variable.

`dam_elem(num_elem)`: *[real*8]* Global damage variable that determines if the grains are damaged (value=1) or undamaged (value=0)

Name: **KUEXT3**

`N_nuc(num_grains,max_num_layers,num_octa_sys)`: *[integer*8]* Stores the expected life to nucleate a crack for all bands and slip directions.

`N_msc(num_grains,max_num_layers,num_octa_sys)`: *[integer*8]* Stores the expected life to currently grow a MSC crack for all bands and slip directions.

`N_history(num_grains,num_grain_fail)`: *[integer*8]* Stores the consumed life once the band becomes in contact with the crack. It has a zero value if the band is not in contact

with the crack.

`N_msc_min(4,num_grain_fail)`: [integer*8] Stores the minimum life to grow a MSC crack and the corresponding grain, band and slip direction.

`NGrain_failed(num_grain_fail+1)`: *[integer*8]* The maximum number of grain failures that will be analyzed.

`Nstep_failed(num_grain_fail+1)`: *[integer*8]* Stores in which step the crack has extended to the next grain.

`N_nuc_min(4)`: *[integer*8]* Stores the minimum life to nucleate crack.

`Nfailed`:*[integer*8]* Correspond to the number of grains currently cracked.

Name: **KUEXT4**

`Neighbor1(num_grains*2*num_grains)`: *[integer*8]* Temporary variable.

`Neighbor_grains(num_grains,num_grains)`: *[integer*8]* `Neighbor_grains(i,j)` stores the number of the neighboring grain j, around grain i.

`Neighbor_num(num_grains)`: *[integer*8]* The number of grains (meaning quantity) that neighbor the ith grain.

Name: **KUEXT5**

`N_El_GB(num_elem,6)`: *[integer*8]* For each of the six faces of the element, stores the number of the neighboring grain. If the face neighbors the same grain, it stores a value of zero.

Name: **KUEXT5b**

`N_int(num_grains,num_grains)`: [integer*8] `N_int (i,j)` stores the intergranular life of grain i, on the boundary with grain j, using the elements that neighbor on grain i (Note that it is not symmetric).

`N_int_local(num_elem)`: [integer*8] Stores the intergranular life of each element. If it is not a boundary element, it stores 1^9.

Name: **KUEXT5c**

`Nun_int(num_grains,num_grains)`: *[integer*8]* `Num_int (i,j)` stores the number of elements in grain i that neighbor grain j.

Name: **KUEXT7**

`Spk2_gl(num_elem,3,3)`: *[real*8]* Corresponds to the 2nd Piola-Kirchhoff stress passed as a global variable.

`GB_dir(num_elem,6)`: *[real*8]* For each face on each element, stores the direction of the grain boundary.

`S_prin_max(num_elem)`: *[real*8]* Maximum principal stress.

Name: **KUEXT8**

`Min_dist(num_grains,num_grains,max_num_layers,max_num_layers,4,4)`: *[real*8]* Stores the data in the Min_dist.txt file and corresponds to the connectivity among bands.

Name: **KUEXT9**

`disAngle(num_grains,num_grains)`: *[real*8]* Stores the misorientation angle among grains.

`disAngleMax(num_grains,num_grains)`: *[real*8]* Temporary variable to stores the misorientation angle among grains.

`Grs(num_grains,4)`: *[real*8]* Temporary variable used to calculate the misorientation angle among grains.

Name: **KUEXT10**

`d_gr_nd(num_grains,max_num_layers,num_octa_sys)`: *[real*8]* Contribution of the neighboring grains on the current band size.

Name: **CONSTANTS**

This block defines constants that are defined at the beginning of the simulations, such as temperature, Boltzmann constant, the initial values and constants for the constitutive model.

APPENDIX C

MESH GENERATOR APPLICATION

The Mesh Generator introduced in Chapter 5 has been tested under ABAQUS V6.7, V6.9 and Matlab 7.9 R2009b, both in Linux and Windows systems. Because the application employs ABAQUS python commands to create meshes, ABAQUS should be installed in the system. The expected time required to create the default model (3375 elements) is approximately 200 seconds, but it can take hours for models with more than 10000 elements.

The application runs in Matlab, which prompts a graphic user interface similar to that shown in Figure 126. This interface allows defining the parameters described below, whose default quantities (shown inside the boxes in the GUI) correspond to RR1000 Bore microstructure. The parameters required in the mesh generator GUI (default values are in brackets) are as follows:

Name for ABAQUS input file: Name of the input file to be created.

Header lines[8]: This corresponds to the number of lines in the header of the input file. This can change with ABAQUS version. For ABAQUS 6.9 it should be equal to 9 while for ABAQUS 6.7 it should be equal to 8.

Model parameters

Definition of mesh attributes

Cube X length [15 μm]: Dimensions of the cube to model in microns along the X axis.

Cube Y length [15 μm]: Dimensions of the cube to model in microns along the Y axis.

Cube Z length [15 μm]: Dimensions of the cube to model in microns along the Z axis.

Band period [1 μm]: Thickness of the bands over which transgranular FIPs will be averaged. This value should be equal or larger than the mesh size.
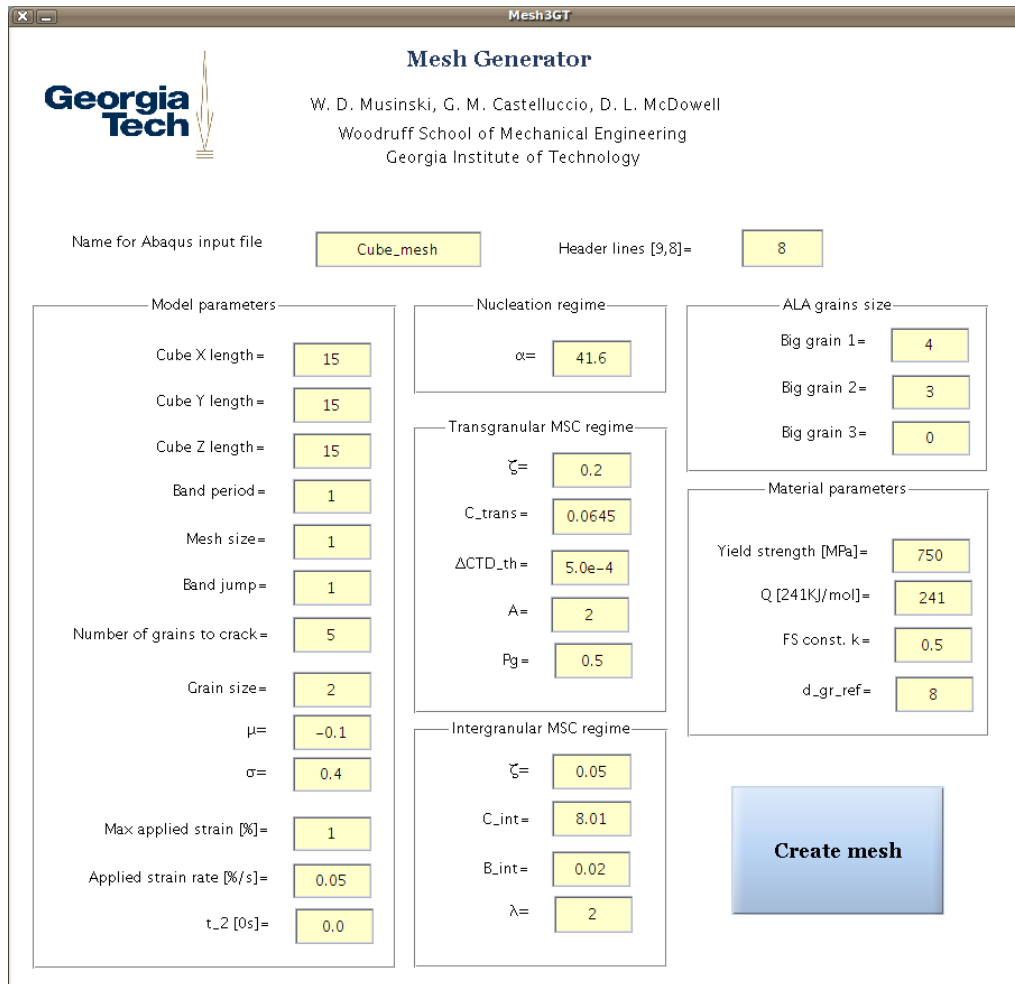
Figure 126: Graphic user interface of the Mesh Generator application.

Mesh size [1 μm]: Size to seed the part in microns. This value depends on the number of elements attempted for the whole model.

Band jump [1 μm]: Maximum distance between bands used to consider them as connected. This value should be equal or larger than the mesh size.

Number of grains to crack [5]: Total number of grains that are cracked in sequence.

Lognormal distribution of grains to be created

Grain size [2 μm]: Approximate grain size radius in microns. Note that the actual value of the grain distributions is larger due to the addition of unassigned elements.

μ [-0.1]: Mean of the lognormal grain size distribution.

σ [0.4]: Standard deviation of the lognormal grain size distribution.

Loading

Max. applied strain [1 %]: Nominal cyclic strain applied in percentage.

Applied strain rate [0.05 %/s]: Nominal cyclic strain rate applied in percentage per second.

t_2 [0]: Corresponds to the hold time. A zero value corresponds to triangular loading while another value will result in trapezoidal loading with such value as the holding time.

Definition of parameters for the nucleation regime

α [41.6]: Irreversibility factor employed in the nucleation regime.

Definition of parameters for the transgranular MSC regime

ξ_{trans} [0.2]: Irreversibility exponent for transgranular failure.

C [0.0645]: Irreversibility constant for transgranular failure.

ΔCTD_{th} [5.0 10^{-4} μm]: ΔCTD threshold.

A_{fs}[2]: Proportionality factor employed in the transgranular failure model.

P_g [0.5]: Constant employed in estimating subgrain FIP evolution.

Definition of parameters for the intergranular MSC regime

ξ_{int} [0.05]: Irreversibility exponent for intergranular failure.

C_{int} [8.01]: Irreversibility constant for intergranular failure.

B_{int} [0.02]: Constant employed in the intergranular failure model,

λ [2]: Intergranular failure coefficient for the FIP_{int}.

ALA grains size

This box specifies the diameter of grains 1, 2 and 3 (center, bottom and right respectively) without following the lognorm distribution. Thus, this option allows defining three arbitrarily big grains surrounded by finer grains that follow the lognorm distribution. When a value "0" is specified on any of the three grains, the program does not employ this option and the volume is filled with grains following the lognorm distribution.

Big grain 1 [4 μm]: Diameter of the grain centered in the cube.

Big grain 2 [3 μm]: Diameter of the grain centered below Big grain 1.

Big grain 3 [0 μm]: Diameter of the grain centered to the right of Big grain 1.

Material parameters
Definition of global mechanical properties
Yield strength [750MPa]: Yield strength
$Q = 241 \frac{kJ}{mol}$: Activation energy.
Fatemi-Socie constant, k [0.5]: Constant multiplying the normal stress in the FIP for transgranular failure.
d_gr_ref [8 μm]: Reference grain size.

REFERENCES

[1] ABAQUS, "FEM software V6.9, Simulia Corp., Providence, RI, USA," 2009.

[2] ABU AL-RUB, R. K. and VOYIADJIS, G. Z., "On the coupling of anisotropic damage and plasticity models for ductile materials," *International Journal of Solids and Structures*, vol. 40, no. 11, pp. 2611–2643, 2003.

[3] AHMED, J., WILKINSON, A. J., and ROBERTS, S. G., "Electron channelling contrast imaging characterization of dislocation structures associated with extrusion and intrusion systems and fatigue cracks in copper single crystals," *Philosophical Magazine A*, vol. 81, no. 6, pp. 1473–1488, 2001.

[4] ALEXANDRE, F., DEYBER, S., and PINEAU, A., "Modelling the optimum grain size on the low cycle fatigue life of a Ni based superalloy in the presence of two possible crack initiation sites," *Scripta Materialia*, vol. 50, no. 1, pp. 25–30, 2004.

[5] AMARO, R., *Thermomechanical Fatigue Crack Formation in a Single Crystal Ni-base Superalloy*. PhD thesis, Georgia Institute of Technology, 2010.

[6] ANDERSON, T. L., *Fracture Mechanics: Fundamentals and Applications*. CRC Press, 3rd ed., 2004.

[7] ANDREEV, G. A., SMIRNOV, B. I., and MIZERA, E., "Vacancy generation and bulk density change in crystals as a result of platic deformation," in *Proc. of the 7th Int. School, Szczyrk, Poland*, Defects in Crystals, 1985.

[8] ANTONOPOULOS, J. G., BROWN, L. M., and WINTER, A. T., "Vacancy dipoles in fatigued copper," *Philosophical Magazine*, vol. 34, no. 4, pp. 549–563, 1976.

[9] ASARO, R. J., "Crystal plasticity," *Journal of Applied Mechanics*, vol. 50, no. 4B, pp. 921–934, 1983.

[10] ASARO, R. J. and NEEDLEMAN, A., "Overview 42. Texture development and strain-hardening in rate dependent polycrystals," *Acta Metallurgica*, vol. 33, no. 6, pp. 923–953, 1985.

[11] ASLANIDES, A. and PONTIKIS, V., "Atomistic study of dislocation cores in aluminium and copper," *Computational Materials Science*, vol. 10, no. 1-4, pp. 401–405, 1998.

[12] AUSTRALIAN TRANSPORT SAFETY BUREAU, "Investigation AO-2010-089 Inflight engine failure - Qantas, Airbus A380, VH-OQA, overhead Batam Island, Indonesia, 4 November 2010. http://www.atsb.gov.au/publications/investigation_reports/2010/aair/ao-2010-089.aspx," Feb. 2012.

[13] AWATANI, J., KATAGIRI, K., and KOYANAGI, K., "Study on the effect of stacking-fault energy on fatigue crack-propagation as deduced from dislocation patterns," *Metallurgical Transactions A*, vol. 10, no. 4, pp. 503–507, 1979.

[14] BAMMANN, D. J., CHIESA, M. L., HORSTEMEYER, M. F., and WEINGARTEN, L. I., "Failure in ductile materials using finite element methods," in *Structural Crashworthiness and Failure* (JONES, N. and WIERZBICKI, T., eds.), pp. 1–54, 1993.

[15] BANNANTINE, J. A., COMER, J. J., and HANDROCK, J. L., *Fundamentals of Metal Fatigue Analysis*. Englewood Cliffs N.J.: Prentice Hall, 1989.

[16] BARSOM, J. and ROLFE, S., *Fracture and Fatigue Control in Structures*. Butterworth-Heinemann, 3rd ed., 1999.

[17] BASINSKI, Z. S., PASCUAL, R., and BASINSKI, S. J., "Low amplitude fatigue of copper single crystals- 1 the role of the surface in fatigue failure," *Acta Metallurgica*, vol. 31, no. 4, pp. 591–602, 1983.

[18] BAZANT, Z. and JIRASEK, M., "Nonlocal integral formulations of plasticity and damage: Survey of progress," *Journal of Engineering Mechanics*, vol. 128, no. 11, pp. 1119–1149, 2002.

[19] BENNETT, V. P. and McDOWELL, D. L., "Cyclic crystal plasticity analyses of stationary, microstructurally small surface cracks in ductile single phase polycrystals," *Fatigue & Fracture of Engineering Materials & Structures*, vol. 25, no. 7, pp. 677–693, 2002.

[20] BENNETT, V. P. and McDOWELL, D. L., "Crack tip displacements of microstructurally small surface cracks in single phase ductile polycrystals," *Engineering Fracture Mechanics*, vol. 70, no. 2, pp. 185–207, 2003.

[21] BERVEILLER, M., MULLER, D., and KRATOCHVIL, J., "Nonlocal versus local elastoplastic behaviour of heterogeneous materials," *International Journal of Plasticity*, vol. 9, no. 5, pp. 633–652, 1993.

[22] BETTGE, D. and OSTERLE, W., "Cube slip in near-[111] oriented specimens of a single-crystal nickel-base superalloy," *Scripta Materialia*, vol. 40, no. 4, pp. 389–395, 1999.

[23] BLOCHWITZ, C., HEINRICH, D., and FRENZEL, R., "Microcrack propagation in fatigued F.C.C. monocrystals. 1. Crack-depth distribution and propagation rate," *Materials Science and Engineering A*, vol. 118, pp. 71–81, 1989.

[24] BLOCHWITZ, C. and TIRSCHLER, W., "Twin boundaries as crack nucleation sites," *Crystal Research and Technology*, vol. 40, no. 1-2, pp. 32–41, 2005.

[25] BOZEK, J. E., HOCHHALTER, J. D., VEILLEUX, M. G., LIU, M., HEBER, G., SINTAY, S. D., ROLLETT, A. D., LITTLEWOOD, D. J., MANIATTY, A. M., WEILAND, H., and ET AL., "A geometric approach to modeling microstructurally small fatigue crack formation: I. probabilistic simulation of constituent particle cracking in AA 7075-T651," *Modelling and Simulation in Materials Science and Engineering*, vol. 16, no. 6, p. 065007, 2008.

[26] BROCKS, W., CORNEC, A., and SCHEIDER, I., "3.03 Computational aspects of nonlinear fracture mechanics," in *Comprehensive Structural Integrity*, vol. 3, Elsevier, 2003.

[27] BROWN, L. M., OGIN, S., BILBY, B., MILLER, H., and WILLIS, J., "Role of internal stresses in the nucleation of fatigue cracks," in *Fundamentals of Deformation and Fracture*, pp. 501–528, Cambridge, UK: Cambridge University Press, 1985.

[28] BROWN, M. W. and MILLER, K. J., "High temperature low cycle biaxial fatigue of two steels," *Fatigue and Fracture of Engineering Materials*, vol. 1, no. 2, pp. 217–229, 1979.

[29] BUCHINGER, L., CHENG, A. S., STANZL, S., and LAIRD, C., "The cyclic stress-strain response and dislocation structures of Cu 16 at.%Al alloy III: single crystals fatigued at low strain amplitudes," *Materials Science and Engineering*, vol. 80, no. 2, pp. 155–167, 1986.

[30] BUSSO, E. P., *Cyclic deformation of monocrystalline nickel aluminide and high temperature coatings.* PhD thesis, Massachusetts Institute of Technology, 1990.

[31] CAROL, I., JIRASEK, M., and BAZANT, Z., "A thermodynamically consistent approach to microplane theory. Part I. Free energy and consistent microplane stresses," *International Journal of Solids and Structures*, vol. 38, no. 17, pp. 2921–2931, 2001.

[32] CAROL, I. and BAZANT, Z. P., "Damage and plasticity in microplane theory," *International Journal of Solids and Structures*, vol. 34, no. 29, pp. 3807–3835, 1997.

[33] CAUVIN, A., *Damage mechanics: Basic variables in continuum theories.* PhD, Columbia University, 1997.

[34] CAUVIN, A. and TESTA, R. B., "Damage mechanics: basic variables in continuum theories," *International Journal of Solids and Structures*, vol. 36, no. 5, pp. 747–761, 1999.

[35] CHABOCHE, J. L., "Constitutive equations for cyclic plasticity and cyclic viscoplasticity," *International Journal of Plasticity*, vol. 5, no. 3, pp. 247–302, 1989.

[36] CHAN, K. S., "A microstructure-based fatigue-crack-initiation model," *Metallurgical and Materials Transactions A*, vol. 34, no. 1, pp. 43–58, 2003.

[37] CHAN, K. S., LANKFORD, J., and DAVIDSON, D. L., "A comparison of crack-tip field parameters for large and small fatigue cracks," *Journal of Engineering Materials and Technology*, vol. 108, no. 3, pp. 206–213, 1986.

[38] CHAN, K., TIAN, J., YANG, B., and LIAW, P., "Evolution of slip morphology and fatigue crack initiation in surface grains of Ni200," *Metallurgical and Materials Transactions A*, vol. 40, no. 11, pp. 2545–2556, 2009.

[39] CHAN, K. S., "Roles of microstructure in fatigue crack initiation," *International Journal of Fatigue*, vol. 32, no. 9, pp. 1428–1447, 2010.

[40] CHEREPANOV, G. P., "Interface microcrack nucleation," *Journal of the Mechanics and Physics of Solids*, vol. 42, no. 4, pp. 665–680, 1994.

[41] CORDEBOIS, J. P. and SIDOROFF, F., "Endommagement anisotrope en elasticite et plasticite.," *Journal de Mecanique Theorique et Appliquee*, vol. Numero Special, pp. 45–60, 1982.

[42] CRETEGNY, L. and SAXENA, A., "AFM characterization of the evolution of surface deformation during fatigue in polycrystalline copper," *Acta Materialia*, vol. 49, no. 18, pp. 3755–3765, 2001.

[43] CUITINO, A. M. and ORTIZ, M., "Computational modelling of single crystals," *Modelling and Simulation in Materials Science and Engineering*, vol. 1, no. 3, pp. 225–263, 1993.

[44] CUITINO, A. M. and ORTIZ, M., "Ductile fracture by vacancy condensation in FCC single crystals," *Acta Materialia*, vol. 44, no. 2, pp. 427–436, 1996.

[45] DALBY, S. and TONG, J., "Crack growth in a new nickel-based superalloy at elevated temperature. Part II," *Journal of Materials Science*, vol. 40, no. 5, pp. 1217–1228, 2005.

[46] DAVIDSON, D. L., TRYON, R. G., OJA, M., MAT, R., and RAVI CHANDRAN, K. S., "Fatigue crack initiation in WASPALOY at 20C," *Metallurgical and Materials Transactions A*, vol. 38, no. 13, pp. 2214–2225, 2007.

[47] DEPRES, C., ROBERTSON, C. F., and FIVEL, M. C., "Low-strain fatigue in 316L steel surface grains: a three dimension discrete dislocation dynamics modelling of the early cycles. Part 2: persistent slip markings and micro-crack nucleation," *Philosophical Magazine*, vol. 86, no. 1, pp. 79–97, 2006.

[48] DESHPANDE, V. S., NEEDLEMAN, A., and VAN DER GIESSEN, E., "Discrete dislocation modeling of fatigue crack propagation," *Acta Materialia*, vol. 50, no. 4, pp. 831–846, 2002.

[49] DUNNE, F. P. E., WILKINSON, A. J., and ALLEN, R., "Experimental and computational studies of low cycle fatigue crack nucleation in a polycrystal," *International Journal of Plasticity*, vol. 23, no. 2, pp. 273–295, 2007.

[50] ENGLER, O. and RANDLE, V., *Introduction to Texture Analysis: Macrotexture, Microtexture, and Orientation Mapping, Second Edition*. CRC Press, 2009.

[51] ESSMANN, U., GOSELE, U., and MUGHRABI, H., "A model of extrusions and intrusions in fatigued metals. 1. Point-defect production and the growth of extrusions," *Philosophical Magazine A*, vol. 44, no. 2, pp. 405–426, 1981.

[52] EWING, J. A. and HUMFREY, J. C. W., "The fracture of metals under repeated alternations of stress," *Philosophical Transactions of the Royal Society of London Series A*, vol. 200, pp. 241–250, 1903.

[53] FAN, H., "Interfacial Zener-Stroh crack," *Journal of Applied Mechanics*, vol. 61, no. 4, pp. 829–834, 1994.

[54] FARKAS, D., WILLEMANN, M., and HYDE, B., "Atomistic mechanisms of fatigue in nanocrystalline metals," *Physical Review Letters*, vol. 94, no. 16, pp. 165502 1–4, 2005.

[55] FATEMI, A. and KURATH, P., "Multiaxial fatigue life predictions under the influence of mean-stresses," *Journal of Engineering Materials and Technology*, vol. 110, no. 4, pp. 380–388, 1988.

[56] FATEMI, A. and SOCIE, D. F., "A critical plane approach to multiaxial fatigue damage including out-of-phase loading," *Fatigue & Fracture of Engineering Materials & Structures*, vol. 11, no. 3, pp. 149–165, 1988.

[57] FERRIE, E. and SAUZAY, M., "Influence of local crystallographic orientation on short crack propagation in high cycle fatigue of 316LN steel," *Journal of Nuclear Materials*, vol. 386-388, pp. 666–669, 2009.

[58] FIGUEROA, J. C. and LAIRD, C., "Crack initiation mechanisms in copper polycrystals cycled under constant strain amplitudes and in step tests," *Materials Science and Engineering*, vol. 60, no. 1, pp. 45–58, 1983.

[59] FINNEY, J. M. and LAIRD, C., "Strain localization in cyclic deformation of copper single-crystals," *Philosophical Magazine*, vol. 31, no. 2, pp. 339–366, 1975.

[60] FORSYTH, P. J. E., "A two-stage process of fatigue crack growth," in *Proceedings of the Crack Propagation Symposium*, (The College of Aeronautics, Cranfield UK), pp. 76–94, 1961.

[61] FU, L. S., "Creep crack growth in technical alloys at elevated temperature–A review," *Engineering Fracture Mechanics*, vol. 13, no. 2, pp. 307–330, 1980.

[62] GABB, T. P., KANTZOS, P. T., TELESMAN, J., GAYDA, J., SUDBRACK, C. K., and PALSA, B. S., "Fatigue resistance of the grain size transition zone in a dual microstructure superalloy disk," Technical Memorandum E-17305, NASA Glenn Research Center, 2010.

[63] GABB, T. P., KANTZOS, P. T., TELESMAN, J., GAYDA, J., SUDBRACK, C. K., and PALSA, B. S., "Fatigue resistance of the grain size transition zone in a dual microstructure superalloy disk," *International Journal of Fatigue*, vol. 33, no. 3, pp. 414–426, 2011.

[64] GALL, K., SEHITOGLU, H., and KADIOGLU, Y., "A methodology for predicting variability in microstructurally short fatigue crack growth rates," *Journal of Engineering Materials and Technology*, vol. 119, no. 2, pp. 171–179, 1997.

[65] GAO, Y. F. and BOWER, A. F., "A simple technique for avoiding convergence problems in finite element simulations of crack nucleation and growth on cohesive interfaces," *Modelling and Simulation in Materials Science and Engineering*, vol. 12, no. 3, p. 453, 2004.

[66] GERDES, C., GYSLER, A., LUTJERING, G., DAVIDSON, D. L., and SURESH, S., "Fatigue crack growth threshold concepts," in *International Symposium on Fatigue Crack Growth Threshold Concepts*, (Warrendale, Pa.), Metallurgical Society of AIME, 1984.

[67] GINER, E., SUKUMAR, N., TARANCON, J. E., and FUENMAYOR, F. J., "An Abaqus implementation of the extended finite element method," *Engineering Fracture Mechanics*, vol. 76, no. 3, pp. 347–368, 2009.

[68] GROEBER, M., *Development of an automated characterization-representation framework for the modeling of polycrystalline materials in 3D*. PhD thesis, 2007.

[69] GURTIN, M. E., *Topics in Finite Elasticity*. CBMS-NSF Regional Conference Series in Applied Mathematics, Society for Industrial Mathematics, 1987.

[70] HEALY, J. C., GRABOWSKI, L., and BEEVERS, C. J., "Short-fatigue-crack growth in a nickel-base superalloy at room and elevated temperature," *International Journal of Fatigue*, vol. 13, no. 2, pp. 133–138, 1991.

[71] HEINO, S. and KARLSSON, B., "Cyclic deformation and fatigue behaviour of 7Mo-0.5N superaustenitic stainless steel–slip characteristics and development of dislocation structures," *Acta Materialia*, vol. 49, no. 2, pp. 353–363, 2001.

[72] HEINZ, A. and NEUMANN, P., "Crack initiation during high cycle fatigue of an austenitic steel," *Acta Metallurgica et Materialia*, vol. 38, no. 10, pp. 1933–1940, 1990.

[73] HOBSON, P. D., "The formulation of a crack-growth equation for short cracks," *Fatigue of Engineering Materials and Structures*, vol. 5, no. 4, pp. 323–327, 1982.

[74] HOBSON, P. D., BROWN, M. W., and DE LOS RIOS, E. R., "Two phases of short crack growth in a medium carbon steel," in *The behaviour of short fatigue cracks* (MILLER, K. J. and DE LOS RIOS, E. R., eds.), pp. 441–459, London: Mechanical Engineering Publications, 1986.

[75] HOCHHALTER, J. D., LITTLEWOOD, D. J., CHRIS, R. J., VEILLEUX, M. G., BOZEK, J. E., INGRAFFEA, A. R., and MANIATTY, A. M., "A geometric approach to modeling microstructurally small fatigue crack formation: II. physically based modeling of microstructure-dependent slip localization and actuation of the crack nucleation mechanism in AA 7075-T651," *Modelling and Simulation in Materials Science and Engineering*, vol. 18, no. 4, p. 045004, 2010.

[76] HORTON, J. A. and OHR, S. M., "TEM observations of the motion of crack tip produced dislocations during cyclic loading in aluminum," *Scripta Metallurgica*, vol. 16, no. 5, pp. 621–626, 1982.

[77] HSIUNG, L. M. and STOLOFF, N. S., "A point defect model for fatigue crack initiation in Ni_3Al + B single crystals," *Acta Metallurgica et Materialia*, vol. 38, no. 6, pp. 1191–1200, 1990.

[78] HU, Y. M. and WANG, Z. G., "Fatigue crack initiation and early growth in a copper bicrystal with a grain boundary perpendicular to stress axis," *Scripta Materialia*, vol. 35, no. 8, pp. 1019–1025, 1996.

[79] HUNSCHE, A. and NEUMANN, P., "Quantitative measurement of persistent slip band profiles and crack initiation," *Acta Metallurgica*, vol. 34, no. 2, pp. 207–217, 1986.

[80] HUNSCHE, A., NEUMANN, P., FONG, J., and FIELDS, R., "Crack nucleation in persistent slip bands," in *Basic Questions in Fatigue: Volume I.*, STP 924, pp. 26–38, ASTM, 1988.

[81] HUSSAIN, K., "Short fatigue crack behaviour and analytical models: A review," *Engineering Fracture Mechanics*, vol. 58, no. 4, pp. 327–354, 1997.

[82] HUTCHINSON, J. and TVERGAARD, V., "Edge-cracks in single crystals under monotonic and cyclic loads," *International Journal of Fracture*, vol. 99, no. 1, pp. 81–95, 1999.

[83] JEZERNIK, N., KRAMBERGER, J., LASSEN, T., and GLODEZ, S., "Numerical modelling of fatigue crack initiation and growth of martensitic steels," *Fatigue and Fracture of Engineering Materials and Structures*, vol. 33, no. 11, pp. 714–723, 2010.

[84] JIRASEK, M., "Comparative study on finite elements with embedded discontinuities," *Computer Methods in Applied Mechanics and Engineering*, vol. 188, pp. 307–330, July 2000.

[85] JIRASEK, M., "Lecture notes from *Modeling of Localized Inelastic Deformation* course, Czech Technical University, Prague." Sept. 2010.

[86] KAMAYA, M., "Influence of grain boundaries on short crack growth behaviour of IGSCC," *Fatigue & Fracture of Engineering Materials & Structures*, vol. 27, no. 6, pp. 513–521, 2004.

[87] KANDIL, F. A., BROWN, M. W., and MILLER, K. J., "Biaxial low cycle fatigue failure of 316 stainless steel at elevated temperatures," in *Metal Society book 280*, (Varese, Italy), pp. 203–210, Metal Society of London, 1982.

[88] KATAGIRI, K., OMURA, A., KOYANAGI, K., AWATANI, J., SHIRAISHI, T., and KANESHIRO, H., "Early stage crack tip dislocation morphology in fatigued copper," *Metallurgical Transactions A*, vol. 8, no. 11, pp. 1769–1773, 1977.

[89] KHAN, A. and HUAN, S., *Continuum theory of plasticity*. New York: Wiley, 1995.

[90] KIRANE, K. and GHOSH, S., "A cold dwell fatigue crack nucleation criterion for polycrystalline Ti-6242 using grain-level crystal plasticity FE model," *International Journal of Fatigue*, vol. 30, no. 12, pp. 2127–2139, 2008.

[91] KIRANE, K., GHOSH, S., GROEBER, M., and BHATTACHARJEE, A., "Grain level dwell fatigue crack nucleation model for Ti alloys using crystal plasticity finite element analysis," *Journal of Engineering Materials and Technology*, vol. 131, no. 2, pp. 021003 1–14, 2009.

[92] KLESNIL, M. and LUKAS, P., "Dislocation structure associated with fracture surface of fatigued copper single crystals," *Philosophical Magazine*, vol. 17, no. 150, pp. 1295–1298, 1968.

[93] KNOWLES, D. and HUNT, D., "The influence of microstructure and environment on the crack growth behavior of powder metallurgy nickel superalloy RR1000," *Metallurgical and Materials Transactions A*, vol. 33, no. 10, pp. 3165–3172, 2002.

[94] KOCKS, U. F., ARGON, A., and ASHBY, M. F., "Thermodynamics and kinetics of slip," *Progress in Materials Science*, vol. 19, 1975.

[95] KOLBE, M., "The high temperature decrease of the critical resolved shear stress in nickel-base superalloys," *Materials Science and Engineering A*, vol. 319-321, pp. 383–387, 2001.

[96] KRUPP, U., KANE, W. M., LAIRD, C., and MCMAHON, C. J., "Brittle intergranular fracture of a Ni-base superalloy at high temperatures by dynamic embrittlement," *Materials Science and Engineering A*, vol. 387-389, pp. 409–413, 2004.

[97] LAIRD, C. and BUCHINGER, L., "Hardening behavior in fatigue," *Metallurgical Transactions A*, vol. 16, no. 12, pp. 2201–2214, 1985.

[98] LAIRD, C., FINNEY, J. M., and KUHLMANN-WILSDORF, D., "Dislocation behavior in fatigue VI: variation in the localization of strain in persistent slip bands," *Materials Science and Engineering*, vol. 50, no. 1, pp. 127–136, 1981.

[99] LANSEY, J., "Matlab *logfit* subroutine. Last access, July 2011. www.mathworks.com/matlabcentral/.," 2010.

[100] LARSEN, J. M., JIRA, J. R., and WEERASOORIYA, T., "Crack opening displacement measurements on small cracks in fatigue," in *Fracture Mechanics: Eighteenth Symposium*, STP 945, pp. 896–912, ASTM, 1985.

[101] LEE, H., LI, G., and LEE, S., "The influence of anisotropic damage on the elastic behavior of materials," (Moret-sur-Loing, France), pp. 79–90, 1986.

[102] LEMAITRE, J., "A continuous damage mechanics model for ductile fracture," *Journal of Engineering Materials and Technology*, vol. 107, no. 1, pp. 83–89, 1985.

[103] LEMAITRE, J. and CHABOCHE, J., *Mechanics of Solid Materials.* Cambridge University Press, 1994.

[104] LI, Y. and LAIRD, C., "Cyclic response and dislocation structures of AISI 316L stainless steel. Part 1: single crystals fatigued at intermediate strain amplitude," *Materials Science and Engineering A*, vol. 186, no. 1-2, pp. 65–86, 1994.

[105] LIN, B., ZHAO, L. G., TONG, J., and CHRIST, H. J., "Crystal plasticity modeling of cyclic deformation for a polycrystalline nickel-based superalloy at high temperature," *Materials Science and Engineering A*, vol. 527, no. 15, pp. 3581–3587, 2010.

[106] LIN, B., ZHAO, L., and TONG, J., "A crystal plasticity study of cyclic constitutive behaviour, crack-tip deformation and crack-growth path for a polycrystalline nickel-based superalloy," *Engineering Fracture Mechanics*, vol. 78, no. 10, pp. 2174–2192, 2011.

[107] LIN, T. H. and ITO, Y. M., "Mechanics of a fatigue crack nucleation mechanism," *Journal of the Mechanics and Physics of Solids*, vol. 17, no. 6, pp. 511–523, 1969.

[108] LUKAS, P. and KUNZ, L., "Threshold stress intensity and dislocation structures surrounding fatigue cracks in polycrystalline copper," *Materials Science and Engineering*, vol. 62, no. 2, pp. 149–157, 1984.

[109] LUKAS, P. and KUNZ, L., "Role of persistent slip bands in fatigue," *Philosophical Magazine*, vol. 84, no. 3-5, pp. 317–330, 2004.

[110] LUO, J. and BOWEN, P., "Small and long fatigue crack growth behaviour of a PM Ni-based superalloy, Udimet 720," *International Journal of Fatigue*, vol. 26, no. 2, pp. 113–124, 2004.

[111] MA, B. T. and LAIRD, C., "Overview of fatigue behavior in copper single-crystals. 2 population, size distribution and growth kinetics of stage I cracks for tests at constant strain amplitude," *Acta Metallurgica*, vol. 37, no. 2, pp. 337–348, 1989.

[112] MA, F., DENG, X., SUTTON, M. A., NEWMAN, J. C., MILLER, K., and McDOW-ELL, D. L., "A CTOD-based mixed-mode fracture criterion," in *Mixed-Mode Crack Behavior*, STP 1359, pp. 86–110, ASTM, 1999.

[113] MAN, J., KLAPETEK, P., MAN, O., WEIDNER, A., OBRTLIK, K., and POLAK, J., "Extrusions and intrusions in fatigued metals. Part 2. AFM and EBSD study of the early growth of extrusions and intrusions in 316L steel fatigued at room temperature," *Philosophical Magazine*, vol. 89, no. 16, pp. 1337–1372, 2009.

[114] MAN, J., OBRTLIK, K., BLOCHWITZ, C., and POLAK, J., "Atomic force microscopy of surface relief in individual grains of fatigued 316L austenitic stainless steel," *Acta Materialia*, vol. 50, no. 15, pp. 3767–3780, 2002.

[115] MANONUKUL, A. and DUNNE, F. P. E., "High- and low-cycle fatigue crack initiation using polycrystal plasticity," *Proceedings of the Royal Society of London Series A*, vol. 460, no. 2047, pp. 1881–1903, 2004.

[116] MAY, A. N., "Model of metal fatigue," *Nature*, vol. 185, no. 4709, pp. 303–304, 1960.

[117] McDOWELL, D. L., "Basic issues in the mechanics of high cycle metal fatigue," *International Journal of Fracture*, vol. 80, no. 2-3, pp. 103–145, 1996.

[118] McDOWELL, D. L., "Mutiaxial fatigue strength," in *ASM handbook on Fatigue and Fracture*, vol. 19, pp. 263–273, Metals Park, OH: American society of metals, 1996.

[119] McDOWELL, D. L., "Simulation-based strategies for microstructure-sensitive fatigue modeling," *Materials Science & Engineering A*, vol. 468, pp. 4–14, 2007.

[120] McDOWELL, D. L. and BERARD, J. Y., "A ΔJ-based approach to biaxial fatigue," *Fatigue & Fracture of Engineering Materials & Structures*, vol. 15, no. 8, p. 719741, 1992.

[121] McDOWELL, D. L. and DUNNE, F. P. E., "Microstructure-sensitive computational modeling of fatigue crack formation," *International Journal of Fatigue*, vol. 32, no. 9, pp. 1521–1542, 2010.

[122] McDOWELL, D. L., GALL, K., HORSTEMEYER, M. F., and FAN, J., "Microstructure-based fatigue modeling of cast A356-T6 alloy," *Engineering Fracture Mechanics*, vol. 70, no. 1, pp. 49–80, 2003.

[123] McGINTY, R. D., *Multiscale representation of polycrystalline inelasticity*. PhD thesis, Georgia Institute of Technology, Atlanta, GA, USA, 2001.

[124] McNARY, M., *Implementation of the extended finite element method (XFEM) in the Abaqus software package*. Masters thesis, 2009.

[125] MEISSONNIER, F. T., BUSSO, E. P., and O'DOWD, N. P., "Finite element implementation of a generalised non-local rate-dependent crystallographic formulation for finite strains," *International Journal of Plasticity*, vol. 17, no. 4, pp. 601–640, 2001.

[126] MEYERS, M. A. and MURR, L. E., "A model for the formation of annealing twins in F.C.C. metals and alloys," *Acta Metallurgica*, vol. 26, no. 6, pp. 951–962, 1978.

[127] MIAO, J., *Very High Cycle Fatigue Behavior of Nickel-based Superalloy Rene 88 DT*. PhD, University of Michigan, 2010.

[128] MIAO, J., POLLOCK, T. M., and JONES, J. W., "Crystallographic fatigue crack initiation in nickel-based superalloy ren 88DT at elevated temperature," *Acta Materialia*, vol. 57, no. 20, pp. 5964–5974, 2009.

[129] MIAO, J., POLLOCK, T. M., and WAYNE JONES, J., "Microstructural extremes and the transition from fatigue crack initiation to small crack growth in a polycrystalline nickel-base superalloy," *Acta Materialia*, no. In preprint, 2012.

[130] MILLER, K., PIASCIK, R. S., and NEWMAN, J. C., "The three thresholds for fatigue crack propagation," in *Fatigue and Fracture Mechanics: 27th volume*, ASTM STP 1296, pp. 267–286, ASTM, 1997.

[131] MILLER, K. J. and AKID, R., "The application of microstructural fracture mechanics to various metal surface states," *Proceedings of the Royal Society A*, vol. 452, no. 1949, pp. 1411–1432, 1996.

[132] MILLER, M. P., MCDOWELL, D. L., and OEHMKE, R. L. T., "A creep-fatigue-oxidation microcrack propagation model for thermomechanical fatigue," *Journal of Engineering Materials and Technology*, vol. 114, no. 3, pp. 282–288, 1992.

[133] MITCHELL, R. J., LEMSKY, J. A., RAMANATHAN, R., LI, H. Y., PERKINS, K. M., and CONNOR, L. D., "Process development and microstructure and mechanical property evaluation of a dual microstructure heat treated advanced nickel disc alloy," in *Superalloys 2008*, The Minerals, Metals & Materials Society, 2008.

[134] MITCHELL, R. J., PREUSS, M., TIN, S., and HARDY, M. C., "The influence of cooling rate from temperatures above the γ' solvus on morphology, mismatch and hardness in advanced polycrystalline nickel-base superalloys," *Materials Science and Engineering A*, vol. 473, no. 1-2, pp. 158–165, 2008.

[135] MITCHELL, R. J., RAE, C. M. F., and TIN, S., "Grain boundary transformations during isothermal exposure of powder metallurgy nickel base superalloys for turbine disc applications," *Materials Science and Technology*, vol. 21, no. 1, pp. 125–138, 2005.

[136] MOES, N. and BELYTSCHKO, T., "Extended finite element method for cohesive crack growth," *Engineering Fracture Mechanics*, vol. 69, no. 7, pp. 813–833, 2002.

[137] MORRISON, D. J. and AUBIN, V., "Cyclic stress-strain response of polycrystalline nickel," *Materials Science and Engineering A*, vol. 177, no. 1-2, pp. 29–42, 1994.

[138] MORRISON, D. J. and MOOSBRUGGER, J. C., "Effects of grain size on cyclic plasticity and fatigue crack initiation in nickel," *International Journal of Fatigue*, vol. 19, no. 93, pp. 51–59, 1997.

[139] MOTOYASHIKI, Y., BRCKNER-FOIT, A., and SUGETA, A., "Investigation of small crack behaviour under cyclic loading in a dual phase steel with an FIB tomography technique.," *Fatigue & Fracture of Engineering Materials & Structures*, vol. 30, no. 6, pp. 556–564, 2007.

[140] MUGHRABI, H., "Cyclic hardening and saturation behavior of copper single-crystals," *Materials Science and Engineering*, vol. 33, no. 2, pp. 207–223, 1978.

[141] MUGHRABI, H., WANG, R., DIFFERT, K., and ESSMANN, U., "Fatigue crack initiation by cyclic slip irreversibilities in high-cycle fatigue," in *Fatigue Mechanisms: Advances in Quantitative Measurement of Physical Damage*, STP 811, pp. 5–45, ASTM, 1983.

[142] MURA, T., "A theory of fatigue crack initiation," *Materials Science and Engineering A*, vol. 176, no. 1-2, pp. 61–70, 1994.

[143] MURAKAMI, S., "Notion of continuum damage mechanics and its application to anisotropic creep damage theory," *Journal of Engineering Materials and Technology*, vol. 105, no. 2, pp. 99–105, 1983.

[144] MURAKAMI, S., "Mechanical modeling of material damage," *Journal of Applied Mechanics*, vol. 55, no. 2, pp. 280–286, 1988.

[145] MURAKAMI, Y., *Metal fatigue: effects of small defects and nonmetallic inclusions.* Oxford & Boston: Elsevier, 2002.

[146] MUSINSKI, W., *Novel methods for microstructure-sensitive probabilistic fatigue notch factor.* Masters thesis, Georgia Institute of Technology, Atlanta, GA, USA, 2010.

[147] NAVARRO, A. and DE LOS RIOS, E. R., "A model for short fatigue crack propagation with an interpretation of the short-long crack transition," *Fatigue & Fracture of Engineering Materials & Structures*, vol. 10, no. 2, pp. 169–186, 1987.

[148] NEUMANN, P., FUHLROTT, H., VEHOFF, H., and FONG, T., "Experiments concerning brittle, ductile, and environmentally controlled fatigue crack growth," in *Fatigue Mechanisms*, STP 675, pp. 371–395, ASTM, 1979.

[149] NEUMANN, P. and TONNESSEN, A., "Crack initiation at grain boundaries," in *proceedings of the 8th International Conference on the Strength of Metals and Alloys*, (Tampere, Finland), pp. 743–748, Oxford; Pergamon Press, 1988.

[150] NEWMANN, P., TONNESSEN, A., RITCHIE, R. O., and LANKFORD, J., "Fatigue crack formation in copper," in *Small Fatigue Cracks*, pp. 41–47, TMS (The Minerals, Metals & Materials Society), 1986.

[151] NISHIMURA, K. and MIYAZAKI, N., "Molecular dynamics simulation of crack growth under cyclic loading," *Computational Materials Science*, vol. 31, no. 3-4, pp. 269–278, 2004.

[152] NISITANI, H., GOTO, M., and KAWAGOISHI, N., "A small-crack growth law and its related phenomena," *Engineering Fracture Mechanics*, vol. 41, no. 4, pp. 499–513, 1992.

[153] Ohr, S. M., "An electron microscope study of crack tip deformation and its impact on the dislocation theory of fracture," *Materials Science and Engineering*, vol. 72, no. 1, pp. 1–35, 1985.

[154] Oja, M., Ravi Chandran, K. S., and Tryon, R. G., "Orientation imaging microscopy of fatigue crack formation in waspaloy: crystallographic conditions for crack nucleation," *International Journal of Fatigue*, vol. 32, no. 3, pp. 551–556, 2010.

[155] Okada, M., Tsutsumi, M., Kitamura, T., and Ohtani, R., "Initiation and growth of small cracks in directionally solidified MAR-M247 under creep-fatigue. II. Effect of angle between stress axis and solidification direction," *Fatigue & Fracture of Engineering Materials & Structures*, vol. 21, no. 6, pp. 751–760, 1998.

[156] Oliver, J., "Modelling strong discontinuities in solid mechanics via strain softening constitutive equations. part .2. numerical simulations," *International Journal for Numerical Methods in Engineering*, vol. 39, no. 21, pp. 3601–3623, 1996.

[157] Ortiz, M., Leroy, Y., and Needleman, A., "A finite element method for localized failure analysis," *Computer Methods in Applied Mechanics and Engineering*, vol. 61, no. 2, pp. 189–214, 1987.

[158] Ortiz, M. and Repetto, E. A., "Nonconvex energy minimization and dislocation structures in ductile single crystals," *Journal of the Mechanics and Physics of Solids*, vol. 47, no. 2, pp. 397–462, 1999.

[159] Ortiz, M., Repetto, E. A., and Stainier, L., "A theory of subgrain dislocation structures," *Journal of the Mechanics and Physics of Solids*, vol. 48, no. 10, pp. 2077–2114, 2000.

[160] Pang, H. T., *Effect of microstructure variation on turbine disc fatigue live.* PhD thesis, University of Southampton, Southampton, UK, 2003.

[161] Pang, H. T. and Reed, P. A. S., "Fatigue crack initiation and short crack growth in nickel-base turbine disc alloys-the effects of microstructure and operating parameters," pp. 1089–1099, 2003.

[162] Pippan, R., Berger, M., and Stuwe, H. P., "The influence of crack length on fatigue crack growth in deep sharp notches," *Metallurgical Transactions A*, vol. 18, no. 3, pp. 429–435, 1987.

[163] Pippan, R., Riemelmoser, F. O., and Kreuzer, H., "Effect of the discrete nature of plasticity on fatigue crack propagation," *Journal de Physique IV France*, vol. 11, pp. Pr5–77–Pr5–84, 2001.

[164] Polak, J., "On the role of point-defects in fatigue crack initiation," *Materials Science and Engineering*, vol. 92, pp. 71–80, 1987.

[165] Polak, J., "Resistivity of fatigued copper Single-Crystals," *Materials Science and Engineering*, vol. 89, pp. 35–43, 1987.

[166] Polak, J., "Personal communication," July 2011.

[167] POLAK, J., HELESIC, J., and OBRTLIK, K., "Nucleation stress for persistent slip bands in fatigued copper single crystals," *Materials Science and Engineering A*, vol. 101, pp. 7–12, 1988.

[168] POLAK, J., OBRTLIK, K., and HELESIC, J., "Cyclic strain localization in polycrystalline copper at room temperature and low temperatures," *Materials Science and Engineering A*, vol. 132, pp. 67–76, 1991.

[169] POLAK, J. and SAUZAY, M., "Growth of extrusions in localized cyclic plastic straining," *Materials Science and Engineering A*, vol. 500, no. 1-2, pp. 122–129, 2009.

[170] POTIRNICHE, G. P., HORSTEMEYER, M. F., and LING, X. W., "An internal state variable damage model in crystal plasticity," *Mechanics of Materials*, vol. 39, no. 10, pp. 941–952, 2007.

[171] PRZYBYLA, C., PRASANNAVENKATESAN, R., SALAJEGHEH, N., and McDOWELL, D. L., "Microstructure-sensitive modeling of high cycle fatigue," *International Journal of Fatigue*, vol. 32, no. 3, pp. 512–525, 2010.

[172] QU, S., ZHANG, P., WU, S., ZANG, Q., and ZHANG, Z., "Twin boundaries: Strong or weak?," *Scripta Materialia*, vol. 59, no. 10, pp. 1131–1134, 2008.

[173] REDDY, S. C., FATEMI, A., MITCHELL, M. R., and LANDGRAF, R. W., "Small crack growth in multiaxial fatigue," in *Advances in Fatigue Lifetime Predictive Techniques*, STP1122, pp. 276–298, ASTM, 1992.

[174] REPETTO, E. A. and ORTIZ, M., "A micromechanical model of cyclic deformation and fatigue-crack nucleation in fcc single crystals," *Acta Materialia*, vol. 45, no. 6, pp. 2577–2595, 1997.

[175] RICE, J. R., "Inelastic constitutive relations for solids: An internal-variable theory and its application to metal plasticity," *Journal of the Mechanics and Physics of Solids*, vol. 19, no. 6, pp. 433–455, 1971.

[176] RICHTER, R., TIRSCHLER, W., and BLOCHWITZ, C., "In-situ scanning electron microscopy of fatigue crack behaviour in ductile materials," *Materials Science and Engineering A*, vol. 313, no. 1-2, pp. 237–243, 2001.

[177] RIEMELMOSER, F. O., PIPPAN, R., and STUWE, H. P., "A comparison of a discrete dislocation model and a continuous description of cyclic crack tip plasticity," *International Journal of Fracture*, vol. 85, no. 2, pp. 157–168, 1997.

[178] RITCHIE, R. O. and SURESH, S., "The fracture mechanics similitude concept: questions concerning its application to the behavior of short fatigue cracks," *Materials Science and Engineering*, vol. 57, no. 2, pp. L27–L30, 1983.

[179] ROSENBLOOM, S. N. and LAIRD, C., "Fatigue-crack nucleation based on a random slip process. 1. Computer-model," *Acta Metallurgica et Materialia*, vol. 41, no. 12, pp. 3473–3482, 1993.

[180] SANGID, M. D., EZAZ, T., SEHITOGLU, H., and ROBERTSON, I. M., "Energy of slip transmission and nucleation at grain boundaries," *Acta Materialia*, vol. 59, no. 1, pp. 283–296, 2011.

[181] Sangid, M. D., Maier, H. J., and Sehitoglu, H., "A physically based fatigue model for prediction of crack initiation from persistent slip bands in polycrystals," *Acta Materialia*, vol. 59, no. 1, pp. 328–341, 2011.

[182] Sangid, M. D., Sehitoglu, H., Maier, H. J., and Niendorf, T., "Grain boundary characterization and energetics of superalloys," *Materials Science and Engineering A*, vol. 527, no. 26, pp. 7115–7125, 2010.

[183] Sauzay, M. and Gilormini, P., "Influence of surface effects on fatigue of microcracks nucleation," *Theoretical and Applied Fracture Mechanics*, vol. 38, no. 1, pp. 53–62, 2002.

[184] Shenoy, M. M., Tjiptowidjojo, Y., and McDowell, D. L., "Microstructure-sensitive modeling of polycrystalline IN100," *International Journal of Plasticity*, vol. 24, no. 10, pp. 1694–1730, 2008.

[185] Shenoy, M. M., Zhang, J., and McDowell, D. L., "Estimating fatigue sensitivity to polycrystalline Ni-base superalloy microstructures using a computational approach," *Fatigue & Fracture of Engineering Materials & Structures*, vol. 30, no. 10, pp. 889–904, 2007.

[186] Shih, C. F., "Relationships between the J-integral and the crack opening displacement for stationary and extending cracks," *Journal of the Mechanics and Physics of Solids*, vol. 29, no. 4, pp. 305–326, 1981.

[187] Shyam, A. and Milligan, W. W., "A model for slip irreversibility, and its effect on the fatigue crack propagation threshold in a nickel-base superalloy," *Acta Materialia*, vol. 53, no. 3, pp. 835–844, 2005.

[188] Socie, D. F. and Marquis, G. B., *Multiaxial Fatigue.* SAE International, 1999.

[189] Stocker, C., Zimmermann, M., Christ, H. J., Zhan, Z. L., Cornet, C., Zhao, L. G., Hardy, M., and Tong, J., "Microstructural characterisation and constitutive behaviour of alloy RR1000 under fatigue and creep-fatigue loading conditions," *Materials Science and Engineering A*, vol. 518, no. 1-2, pp. 27–34, 2009.

[190] Stroh, A. N., "The formation of cracks as a result of plastic flow," *Proceedings of the Royal Society of London. Series A*, vol. 223, no. 1154, pp. 404–414, 1954.

[191] Stroh, A. N., "The formation of cracks in plastic flow. II," *Proceedings of the Royal Society of London. Series A*, vol. 232, no. 1191, pp. 548–560, 1955.

[192] Suresh, S., *Fatigue of materials.* Cambridge solid state science series, Cambridge University Press, 2nd ed., 1998.

[193] Taira, S., Tanaka, K., and Nakai, Y., "Model of crack-tip slip band blocked by grain-boundary," *Mechanics Research Communications*, vol. 5, no. 6, pp. 375–381, 1978.

[194] Tanaka, K. and Akiniwa, Y., "Propagation and non-propagation of small fatigue cracks," in *Advances in Fracture Research*, vol. 2, (Houston, Texas,), pp. 869–887, 1989.

[195] TANAKA, K., HOSHIDE, T., and SAKAI, N., "Mechanics of fatigue crack-propagation by crack-tip plastic blunting," *Engineering Fracture Mechanics*, vol. 19, no. 5, pp. 805–825, 1984.

[196] TANAKA, K. and MURA, T., "A dislocation model for fatigue crack initiation," *Journal of Applied Mechanics*, vol. 48, no. 1, pp. 97–103, 1981.

[197] TEN THIJE, R. H. W., AKKERMAN, R., and HUETINK, J., "Large deformation simulation of anisotropic material using an updated lagrangian finite element method," *Computer Methods in Applied Mechanics and Engineering*, vol. 196, no. 33-34, pp. 3141–3150, 2007.

[198] TINGA, T., BREKELMANS, W. A. M., and GEERS, M. G. D., "Cube slip and non-Schmid effects in single crystal ni-base superalloys," *Modelling and Simulation in Materials Science and Engineering*, vol. 18, no. 1, p. 015005, 2010.

[199] TOKAJI, K., OGAWA, T., MILLER, K. J., and DE LOS RIOS, E. R., "The growth behaviour of microstructurally small fatigue cracks in metals," in *Short Fatigue Cracks - ESIS 13*, pp. 85–99, London: Mechanical Engineering Publications, 1992.

[200] TONG, J., DALBY, S., and BYRNE, J., "Crack growth in a new nickel-based super-alloy at elevated temperature. Part III," *Journal of Materials Science*, vol. 40, no. 5, pp. 1237–1243, 2005.

[201] VALLE, R., OCTOR, H., and STOHR, J. F., "Investigation of the production of vacancies in fatigue and of their possible role in fatigue fracture using a unidirectionally solidified composite," *Philosophical Magazine A*, vol. 65, no. 1, pp. 177–193, 1992.

[202] VEHOFF, H., LAIRD, C., and DUQUETTE, D., "The effects of hydrogen and segregation on fatigue crack nucleation at defined grain boundaries in nickel bicrystals," *Acta Metallurgica*, vol. 35, no. 12, pp. 2877–2886, 1987.

[203] VENKATARAMAN, G., CHUNG, Y. W., NAKASONE, Y., and MURA, T., "Free energy formulation of fatigue crack initiation along persistent slip bands: calculation of S-N curves and crack depths," *Acta Metallurgica et Materialia*, vol. 38, no. 1, pp. 31–40, 1990.

[204] VISWANATHAN, G. B., KARTHIKEYAN, S., SAROSI, P. M., UNOCIC, R. R., and MILLS, M. J., "Microtwinning during intermediate temperature creep of polycrystalline ni-based superalloys: mechanisms and modelling," *Philosophical Magazine*, vol. 86, no. 29, pp. 4823–4840, 2006.

[205] VLADIMIROV, I. N., REESE, S., and EGGELER, G., "Constitutive modelling of the anisotropic creep behaviour of nickel-base single crystal superalloys," *International Journal of Mechanical Sciences*, vol. 51, no. 4, pp. 305–313, 2009.

[206] VOYIADJIS, G. Z. and KATTAN, P. I., *Advances in Damage Mechanics: Metals and Metal Matrix Composites With an Introduction to Fabric Tensors*. Elsevier Science, 2nd ed., 2006.

[207] VOYIADJIS, G. Z. and PARK, T., "Anisotropic damage effect tensors for the symmetrization of the effective stress tensor," *Journal of Applied Mechanics*, vol. 64, no. 1, pp. 106–110, 1997.

[208] WALTER, S., "A history of fatigue," *Engineering Fracture Mechanics*, vol. 54, no. 2, pp. 263–300, 1996.

[209] WALTERSDORF, J. and VEHOFF, H., "Initiation of corrosion fatigue cracks at defined grain boundaries in bicrystals," *Scripta Metallurgica*, vol. 23, no. 4, pp. 513–518, 1989.

[210] WANG, H., JI, H., SUN, Y., and MIAO, H., "Discussion on convergence issues in ABAQUS/Standard while carrying out damage and fracture analysis," *Advanced Materials Research*, vol. 189 - 193, no. Manufacturing Process Technology, pp. 2247–2250, 2011.

[211] WANG, R., MUGHRABI, H., McGOVERN, S., and RAPP, M., "Fatigue of copper single crystals in vacuum and in air I: persistent slip bands and dislocation microstructures," *Materials Science and Engineering*, vol. 65, no. 2, pp. 219–233, 1984.

[212] WANG, Z., "Cyclic deformation response of planar-slip materials and a new criterion for the wavy-to-planar-slip transition.," *Philosophical Magazine*, vol. 84, no. 3-5, pp. 351–379, 2004.

[213] WINTER, A. T., "Model for fatigue of copper at low plastic strain amplitudes," *Philosophical Magazine*, vol. 30, no. 4, pp. 719–738, 1974.

[214] WITMER, D. E., FARRINGTON, G. C., and LAIRD, C., "Changes in strain localization behavior induced by fatigue in inert environments," *Acta Metallurgica*, vol. 35, no. 7, pp. 1895–1909, 1987.

[215] WOHUA, Z., YUNMIN, C., and YI, J., "Effects of symmetrisation of net-stress tensor in anisotropic damage models," *International Journal of Fracture*, vol. 109, no. 4, pp. 345–363, 2001.

[216] WORTHEM, D. W., ROBERTSON, I. M., LECKIE, F. A., SOCIE, D. F., and ALTSTETTER, C. J., "Inhomogeneous deformation in INCONEL 718 during monotonic and cyclic loadings," *Metallurgical Transactions A*, vol. 21, no. 12, pp. 3215–3220, 1990.

[217] WUSATOWSKA-SARNEK, A. M., GHOSH, G., OLSON, G. B., BLACKBURN, M. J., and AINDOW, M., "Characterization of the microstructure and phase equilibria calculations for the powder metallurgy superalloy IN100," *Journal of Materials Research*, vol. 18, no. 11, p. 26532663, 2003.

[218] XIAO, L., CHEN, D. L., and CHATURVEDI, M. C., "Shearing of γ" precipitates and formation of planar slip bands in inconel 718 during cyclic deformation," *Scripta Materialia*, vol. 52, no. 7, pp. 603–607, 2005.

[219] YAN, B., CHENG, A., BUCHINGER, L., STANZL, S., and LAIRD, C., "The cyclic stress–strain response of single crystals of Cu 16 at.%Al alloy I: cyclic hardening and strain localization," *Materials Science and Engineering*, vol. 80, no. 2, pp. 129–142, 1986.

[220] ZHAN, Z., *A Study of Creep-Fatigue Interaction in a New Nickel-Based Superalloy.* PhD, University of Portsmouth, UK, 2004.

[221] ZHAN, Z. L. and TONG, J., "A study of cyclic plasticity and viscoplasticity in a new nickel-based superalloy using unified constitutive equations. Part I: evaluation and determination of material parameters," *Mechanics of Materials*, vol. 39, no. 1, pp. 64–72, 2007.

[222] ZHANG, J., PRASANNAVENKATESAN, R., SHENOY, M. M., and McDOWELL, D. L., "Modeling fatigue crack nucleation at primary inclusions in carburized and shot-peened martensitic steel," *Engineering Fracture Mechanics*, vol. 76, no. 3, pp. 315–334, 2009.

[223] ZHANG, M., *Crystal plasticity modeling of Ti-6Al-4V and its application in cyclic and fretting fatigue analysis.* PhD thesis, Georgia Institute of Technology, Atlanta, GA, USA, 2008.

[224] ZHANG, X. P., WANG, C. H., YE, L., and MAI, Y. W., "In situ investigation of small fatigue crack growth in polycrystal and single crystal aluminium alloys," *Fatigue and Fracture of Engineering Materials*, vol. 25, pp. 141–150, 2002.

[225] ZHANG, Z. F. and WANG, Z. G., "Grain boundary effects on cyclic deformation and fatigue damage," *Progress in Materials Science*, vol. 53, no. 7, pp. 1027–1099, 2008.

[226] ZHAO, L. G. and TONG, J., "Crack growth in a new nickel-based superalloy at elevated temperature. Part II," *Journal of Materials Science*, vol. 40, no. 5, pp. 1229–1235, 2005.

[227] ZHAO, L. G., TONG, J., and HARDY, M. C., "Prediction of crack growth in a nickel-based superalloy under fatigue-oxidation conditions," *Engineering Fracture Mechanics*, vol. 77, no. 6, pp. 925–938, 2010.

[228] ZHOU, D., MOOSBRUGGER, J. C., and MORRISON, D. J., "Finite element simulation of PSB macroband nucleation and propagation in single crystal nickel cycled at low plastic strain amplitudes," *International Journal of Plasticity*, vol. 22, no. 7, pp. 1336–1366, 2006.

VITA

Gustavo Castelluccio hails from Argentina, where he received a degree in mechanical engineering in 2005 and a master's degree in materials science in 2006 from the Instituto Balseiro. For his master's he chose a joint academic-industrial program with the Tenaris Group. In January 2008 he started his PhD at Georgia Tech after being awarded a Roberto Rocca Scholarship for two years, and the following two summers. His doctoral studies on modeling fatigue of metals complements with his previous experience in experimental fracture mechanics. His areas of expertise span the various mechanical properties of metals and their applications in manufacturing.